

Ferroelectric Phase Transitions in Oxide Perovskites Studied
by XAFS

by

Bruce D. Ravel

A dissertation submitted in partial fulfillment of the requirements for the degree of

Doctor of Philosophy

University of Washington

1997

Approved by _____
(Chairperson of Supervisory Committee)

Program Authorized
to Offer Degree _____

Date _____

In presenting this dissertation in partial fulfillment of the requirements for the Doctoral degree at the University of Washington, I agree that the Library shall make its copies freely available for inspection. I further agree that extensive copying of this dissertation is allowable only for scholarly purposes, consistent with "fair use" as prescribed in the U. S. Copyright Law. Requests for copying or reproduction of this dissertation may be referred to University Microfilms, 1490 Eisenhower Place, P. O. Box 975, Ann Arbor, MI 49106, to whom the author has granted "the right to reproduce and sell (a) copies of the manuscript in microform and/or (b) printed copies of the manuscript made from microform."

Signature_____

Date_____

University of Washington

Abstract

Ferroelectric Phase Transitions in Oxide Perovskites Studied by XAFS

by Bruce D. Ravel

Chairperson of Supervisory Committee: Professor Edward A. Stern
Department of Physics

Temperature dependent x-ray absorption fine structure (XAFS) measurements on several titanium oxide perovskites are presented in this thesis. Measurements on PbTiO_3 and BaTiO_3 are presented at temperatures spanning their structural and ferroelectric phase transitions. Using these XAFS data, I provide direct evidence for order-disorder behavior in the local structures of PbTiO_3 and BaTiO_3 . The local structure of PbTiO_3 is shown to be tetragonally distorted at all temperatures, while that of BaTiO_3 is approximately rhombohedrally distorted at all temperatures. As the temperature is raised in these materials, long range correlations between the local distortions change, resulting in the observed sequences of macroscopic phase transitions. The extended x-ray absorption fine structures (EXAFS) of these materials are analyzed for quantitative evidence of the order-disorder behavior. The details of the EXAFS analysis techniques are provided. X-ray absorption near edge structure (XANES) measurements on these materials demonstrate further evidence of the order-disorder behavior.

A newly developed computer program, XANES, is presented for *ab initio* calculations of near edge structures. XANES computes the near edge spectrum simultaneously with local electronic densities of state within the one-electron, full multiple scattering formalism using a fast, separable representation of the free electron propagator and scattering matrices computed using fully relativistic, Dirac-Fock, muffin tin potentials. The calculation is made in a real space basis with no assumption of structural symmetry or periodicity. After testing XANES on several sample compounds, I demonstrate the applicability of the code to PbTiO_3 and use it to interpret the near edge spectrum of PbTiO_3 in terms of its local structure. By combining simulations of XANES spectra with XANES and EXAFS measurements, a structural interpretation

of absorption spectra is presented using nearly the entire information content of the XAFS signal.

TABLE OF CONTENTS

List of Figures	iv
List of Tables	vii
Chapter 1: Introduction	1
1.1 XAFS Studies of Ferroelectric Phase Transitions	1
1.2 Full Multiple Scattering XANES Calculations	5
1.3 A Note on Presentation	6
Chapter 2: The EXAFS Equation and EXAFS Analysis	8
2.1 Heuristic Development of the EXAFS Equation	9
2.1.1 Single Scattering EXAFS	9
2.1.2 Multiple Scattering EXAFS	12
2.1.3 Other Corrections to the EXAFS Equation	12
2.2 Background Removal	14
2.3 Fitting EXAFS Data	15
2.4 Interpreting Reduced Chi-Square	18
Chapter 3: XAFS Experiments	21
3.1 Data Collection	21
3.1.1 The Monochromator	21
3.1.2 The Slits	23
3.1.3 The Ion Chambers	24
3.1.4 Collection Geometries	26
3.1.5 Measurements at Low and High Temperature	29
3.2 Sample Preparation	33
3.2.1 Powder Samples for Transmission	34
3.2.2 Single Crystal Samples for Fluorescence	36

Chapter 4:	EXAFS Measurements on PbTiO₃	40
4.1	The Phase Transition of PbTiO ₃	40
4.2	PbTiO ₃ EXAFS Measurements	42
Chapter 5:	EXAFS Measurements on BaTiO₃	59
5.1	The Phase Transitions of BaTiO ₃	59
5.2	BaTiO ₃ EXAFS Measurements	62
Chapter 6:	EXAFS Measurements on EuTiO₃	74
6.1	EuTiO ₃ EXAFS Measurements	74
6.2	Thermal Distortion Parameter	80
Chapter 7:	XANES Measurements on BaTiO₃, PbTiO₃, and EuTiO₃	85
7.1	Symmetry and the XANES Spectrum	85
7.2	Measuring the Area of the Near Edge Peak	87
7.3	The Temperature and Polarization Dependence of the XANES Spectra of BaTiO ₃	89
7.4	Relating the <i>3d</i> Peak to the Local Distortion in PbTiO ₃ , BaTiO ₃ , and EuTiO ₃	94
7.4.1	Polycrystalline PbTiO ₃	94
7.4.2	Polycrystalline BaTiO ₃ and EuTiO ₃	96
7.4.3	Summary of Polycrystalline Results and Comparison with XANES Calculations	97
7.4.4	PbTiO ₃ Single Crystal Data	99
Chapter 8:	Theory of XANES	107
8.1	The Multiple Scattering Path Formalism	108
8.2	The Full Multiple Scattering Formalism	111
8.2.1	The Scattering Matrix	111
8.2.2	The Free Propagator Matrix	112
8.2.3	Matrix Algebra	115
8.2.4	Computing χ and μ	117
8.2.5	Local Electronic Densities of State	119
8.2.6	Computing the Fermi Energy and Charge Transfer	120
8.2.7	Limitations of the FMS Method	121

Chapter 9: XANES Simulations	123
9.1 Copper	123
9.2 Sulfur Hexafluoride	127
9.3 Boron Nitride	130
9.4 Lead Titanate	133
Chapter 10: Summary and Future Work	143
10.1 The Implications of this Work to Ferroelectricity	143
10.2 The Role of FMS XANES Calculations in XAFS Research	146
10.3 Future Work	147
Bibliography	153
Appendix A: Crystallography Based Fitting Models in FEFFIT	168
A.1 A Fitting Model for Tetragonal PbTiO ₃	169
A.1.1 Evaluating the Path Parameters for PbTiO ₃	170
A.1.2 Evaluating the Effect of non-collinearity in PbTiO ₃	177
A.2 A Fitting Model for Rhombohedral BaTiO ₃	181
A.3 A Fitting Model for Cubic EuTiO ₃	184
Appendix B: ATOMS: Handling Crystalline Materials in XAFS Theory and Experiment	189
B.1 The Crystallographic Algorithm	189
B.2 Calculations Using the McMaster Tables	194
B.2.1 The Density and Absorption Lengths	194
B.2.2 The McMaster Correction	195
B.2.3 The I_0 Correction	196
B.2.4 The Self-Absorption Correction	197
Appendix C: The Operation of the Computer Program XANES	200
C.1 Running XANES	200
C.2 Five Steps to a Successful XANES Run	203
C.3 Using FEFF with XANES	206
C.3.1 New FEFF Keywords	206
C.3.2 FEFF Tricks	207

LIST OF FIGURES

1.1	Schematic of displacive and order–disorder transitions	3
1.2	The perovskite crystal structure	5
3.1	Schematic of an XAFS experiment	21
3.2	Full schematic of the transmission XAFS furnace	31
3.3	Schematic of the transmission XAFS furnace main body	32
3.4	Comparison of polycrystalline and single crystal PbTiO ₃ data	38
4.1	Ti <i>K</i> edge spectrum of PbTiO ₃	43
4.2	Ti <i>K</i> edge $\chi(k)$ for PbTiO ₃	44
4.3	Fit to the Ti edge in PbTiO ₃ at 10 K	50
4.4	Fit to the Ti edge in PbTiO ₃ at 300 K	51
4.5	Fit to the Ti edge in PbTiO ₃ at 850 K	51
4.6	Axis lengths in PbTiO ₃	54
4.7	Titanium–oxygen bond lengths in PbTiO ₃	55
4.8	Titanium–lead bond lengths in PbTiO ₃	56
4.9	Distortion parameter in PbTiO ₃	57
4.10	Fit to 850 K PbTiO ₃ data using the cubic model	58
5.1	Ti <i>K</i> and Ba <i>L</i> _{III} edges of BaTiO ₃	63
5.2	Ba <i>K</i> edge spectrum of BaTiO ₃	64
5.3	Ba <i>K</i> edge $\chi(k)$ for BaTiO ₃	65
5.4	Fit to the Ba edge in BaTiO ₃ at 35 K	68
5.5	Fit to the Ba edge in BaTiO ₃ at 200 K	69
5.6	Fit to the Ba edge in BaTiO ₃ at 300 K	69
5.7	Fit to the Ba edge in BaTiO ₃ at 750 K	70
6.1	Absorption edges of EuTiO ₃	75
6.2	$\chi(k)$ for the EuTiO ₃ Ti <i>K</i> edge	76
6.3	$\chi(k)$ for the EuTiO ₃ Eu <i>L</i> _{III} edge	76

6.4	Determination of S_0^2 for Ti in EuTiO_3	78
6.5	Fit to the Ti edge in EuTiO_3 at 15 K	81
6.6	Fit to the Ti edge in EuTiO_3 at 300 K	81
6.7	Fit to the Eu edge in EuTiO_3 at 15 K	82
6.8	Fit to the Eu edge in EuTiO_3 at 300 K	82
7.1	Schematic of a dipole interaction in a crystal	86
7.2	Example use of PHIT for BaTiO_3 XANES	88
7.3	Temperature dependence of the BaTiO_3 Ti XANES spectrum	90
7.4	Polarization dependence of the BaTiO_3 Ti XANES spectrum	90
7.5	Polarization dependence of the PbTiO_3 Ti XANES spectrum	91
7.6	Cartoon depiction of displacive and order-disorder local structures	92
7.7	Temperature dependence of the PbTiO_3 Ti XANES spectrum	95
7.8	$3d$ peak areas in PbTiO_3 as functions of temperature	96
7.9	Temperature dependence of the EuTiO_3 Ti XANES spectrum	97
7.10	Effect of local distortions on the Ti K edge XANES of EuTiO_3	100
7.11	Temperature dependence of the $\hat{\epsilon} \parallel c$ PbTiO_3 Ti XANES spectrum	101
7.12	Temperature dependence of the $\hat{\epsilon} \perp c$ PbTiO_3 Ti XANES spectrum	102
7.13	Difference spectra of the single crystal PbTiO_3 Ti XANES spectra	104
9.1	FEFF calculation of FCC copper	124
9.2	XANES calculation of FCC copper	126
9.3	Eigenvalues of G^0t in FCC copper	127
9.4	Sulfur XANES of SF_6	129
9.5	Sample FEFF input file	130
9.6	Sulfur XANES of SF_6	131
9.7	Boron XANES of BN	131
9.8	Boron s and p DOS in BN	134
9.9	Nitrogen s and p DOS in BN	135
9.10	Ti K edge XANES and calculations on 1–6 shells	138
9.11	Effect of local distortions on the Ti K edge XANES of PbTiO_3	139
9.12	Unconvolved Ti $\chi(E)$ of PbTiO_3	139
9.13	Ti p DOS of PbTiO_3	140
9.14	Calculations of tetragonal and cubic PbTiO_3	141
9.15	Calculations of single crystal PbTiO_3	142

10.1	Ti <i>K</i> edge XANES of several Ti perovskite	152
A.1	The <code>atoms.inp</code> file for PbTiO_3	171
A.2	Crystallographic information for PbTiO_3 in <code>FEFFIT</code>	172
A.3	Bond length information for PbTiO_3 in <code>FEFFIT</code>	173
A.4	Single scattering paths for PbTiO_3 in <code>FEFFIT</code>	174
A.5	<code>Set</code> and <code>guess</code> variables for PbTiO_3 in <code>FEFFIT</code>	175
A.6	A collinear multiple scattering path for PbTiO_3 in <code>FEFFIT</code>	176
A.7	Computing non-collinearity angle for PbTiO_3 in <code>FEFFIT</code>	179
A.8	A non-collinear multiple scattering path for PbTiO_3 in <code>FEFFIT</code>	180
A.9	The <code>files.dat</code> file used for non-collinear paths in PbTiO_3	182
A.10	The <code>atoms.inp</code> file for BaTiO_3	183
A.11	Crystallographic information for BaTiO_3 in <code>FEFFIT</code>	183
A.12	Oxygen bond lengths for BaTiO_3 in <code>FEFFIT</code>	185
A.13	Oxygen path paragraphs for BaTiO_3 in <code>FEFFIT</code>	186
A.14	Titanium and barium bond lengths for BaTiO_3 in <code>FEFFIT</code>	187
A.15	A scattering path of EuTiO_3 in <code>FEFFIT</code>	188
B.1	Example <code>atoms.inp</code> file.	190
B.2	Example <code>feff.inp</code> file from <code>ATOMS</code>	192
B.3	Unnormalized absorption spectrum for PbTiO_3	195
C.1	Sample <code>FEFF</code> input file	201
C.2	Sample XANES configuration file	203
C.3	Sample <code>CORRECT</code> configuration file	204

LIST OF TABLES

4.1	The phase transitions of PbTiO ₃	41
4.2	Background removal parameters for PbTiO ₃	44
4.3	Multiplicities and bond lengths in the phases of PbTiO ₃	45
4.4	Structural fitting parameters used in the PbTiO ₃ fits	46
4.5	Fitting and statistical parameters for the PbTiO ₃ fits	47
4.6	E_0 corrections in the PbTiO ₃ fits.	49
4.7	Values of structural fitting parameters in PbTiO ₃ fits	53
5.1	The phase transitions of BaTiO ₃	60
5.2	Background removal parameters for BaTiO ₃	63
5.3	Multiplicities and bond lengths in the phases of BaTiO ₃	66
5.4	Fitting and statistical parameters for the BaTiO ₃ fits	67
5.5	Fitting parameters used in BaTiO ₃ fits	67
5.6	Einstein temperatures in BaTiO ₃	70
5.7	χ^2_{ν} for different average structures in BaTiO ₃	71
5.8	Comparison of σ^2 for different fitting models	72
6.1	Background removal parameters for EuTiO ₃	75
6.2	Fitting parameters and statistics for the EuTiO ₃ fits	77
6.3	Fitting parameters for EuTiO ₃	79
6.4	Thermal distortion parameter in EuTiO ₃	84
7.1	$3d$ peak areas in EuTiO ₃ XANES spectra	98
7.2	Proportionality constants between \mathcal{A} and d^2	99
7.3	Fraction of rotated cells in PbTiO ₃ measured by peak areas	104
7.4	Fraction of rotated cells in PbTiO ₃ measured by axis lengths	106
9.1	Parameters for XANES runs	125
9.2	Charge distribution in the ground state of BN	133
A.1	FEFFIT path parameters	169

C.1	Output files from FEFF used in XANES.	200
C.2	Output files from XANES	202

ACKNOWLEDGMENTS

My first and largest “Thank you!” is to my mentors, Ed Stern and John Rehr. Today I am a physicist because these gentlemen are fine teachers. I also am grateful to my many colleagues who have contributed to my knowledge and success in physics. In particular I thank Matt Newville, Dani Haskel, Julie Cross, Shelly Kelly, Larry Sorensen, Bob Ingalls, Mehmet Sarikaya, Fatih Dogan, Chuck Bouldin, and Alex Ankudinov.

To my mother Frances, my father Ira, my brother Jeff, my sister-in-law Cristelle Baskins, and the cutest nephew in the world Gabriel: I love you all very much.

I thank my dearest friends, Cecilia Bitz, Alison Eisenger, Mark Wilber, Eric Sorenson, Daria Ross, John Neergaard, Victor Kress, Dawn Meekhof, Diane Markoff, Ed Mulligan, Mitch Kaplan, and Bruce Thompson for their warmth and generosity.

Chapter 1

INTRODUCTION

This thesis describes in detail the two avenues of research I have pursued as a student at the University of Washington. The first research interest presented here is a structural analysis using the X-ray Absorption Fine Structure technique of the ferroelectric perovskites PbTiO_3 and BaTiO_3 through their ferroelectric and structural phase transitions. I present new evidence for a crucial order-disorder component to these nominally displacive phase transitions. My second research interest has been the development of a real-space, full multiple scattering computer program for the *ab initio* calculation of X-ray Absorption Near Edge Structure and local electronic densities of state. This technique is particularly applicable to the study of ferroelectric materials.

1.1 XAFS Studies of Ferroelectric Phase Transitions

In the first part of this thesis, I apply the XAFS technique to the study of the structural and ferroelectric phase transitions in two ferroelectric materials, PbTiO_3 and BaTiO_3 , and also to the structurally related but non-ferroelectric EuTiO_3 . The aim of this research is to understand the nature of the local structure in these materials through their structural and ferroelectric phase transitions.

A ferroelectric crystal, such as PbTiO_3 or BaTiO_3 , possesses a dipole moment in its low temperature phase that is correlated across the entire length of the crystal. This polarization can be redirected by application of an electric field. The presence of an inherent dipole moment in a ferroelectric crystal can be understood from its atomic structure. When atoms within the unit cell of the crystal are displaced from sites of point centrosymmetry, the electron density within the unit cell is redistributed to accommodate the displacement. The enhanced electron density in some regions of the unit cell and diminished density elsewhere induces a dipole moment within the cell. When these displacements within the unit cells are correlated in direction from cell to cell across the length of the crystal, so are the dipole moments. Then the crystal

possesses a net polarization and is ferroelectric. At some temperature this macroscopic polarization vanishes and the material transforms into a phase with an average crystallographic structure lacking the displacements which cause ferroelectricity.

PbTiO_3 and BaTiO_3 are end members of solid solutions with PbZrO_3 , SrTiO_3 and others forming materials of considerable technological interest. Applications include electro-mechanical and electro-chemical transducers, optical elements, sensors, storage devices, pyroelectric devices, and others. The relatively simple structure of perovskite ferroelectrics makes them attractive for both basic experimental and theoretical investigation.

There are two canonical models commonly used to describe the structural phase transitions observed in PbTiO_3 and BaTiO_3 , the *displacive* and the *order-disorder*. In a displacive transition, the potential surface in which the atoms rest changes with increasing temperature. At low temperature, the atoms populate a potential minimum which is displaced from a point of centrosymmetry. As the temperature rises, the potential minimum moves towards the point of centrosymmetry. Finally, in the high temperature phase, the minimum resides at a point of centrosymmetry. This is shown schematically in Fig. 1.1a. In the order-disorder model, the shape of the potential surface remains unchanged with temperature. As the temperature is raised, the hopping rate between adjacent minima in the potential surface increases, leading to a disordered structure. In the high temperature phase, the hopping rate is such that the equivalent sites are equally populated. This is shown in Fig. 1.1b.

It is possible for these two models to yield very similar results for certain kinds of measurements. For example, a measurement of Bragg peaks without consideration of the diffuse part of the diffraction spectrum may not distinguish between these two models above the phase transition. The measurement of Bragg peak positions averages the possible displacements depicted in Fig. 1.1b as *vectors*. Since these local displacements are equal in magnitude but opposite in sign, their average is zero. Consequently the positions of the Bragg peaks are insensitive to the differences between these two models above T_c . A diffraction measurement may lack the resolution to distinguish between thermal disorder and the structural disorder introduced by the disordering of the local displacements. Likewise, if the hopping rate between the two potential minima in the order-disorder model is significantly faster than the time scale of the lattice dynamics, then many hopping events will happen within the time scale of the excitation in the Raman measurement. The sensitivity of this measurement to the lower symmetry of the disordered local structure will thus be lost.

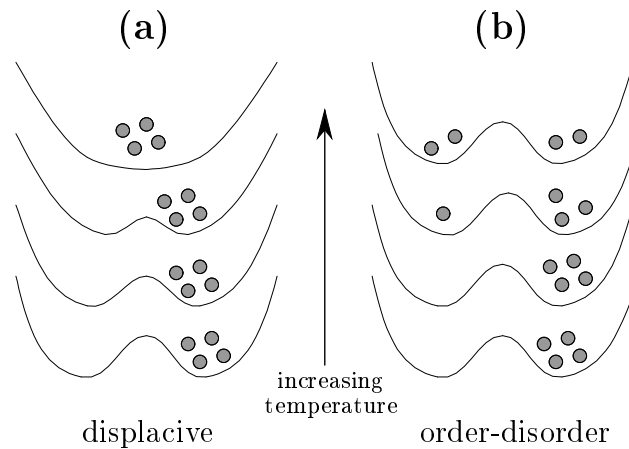


Figure 1.1: Schematic of displacive and order–disorder transitions showing the temperature dependence of the local displacements in the two models. (a) shows the shrinking of the potential barrier between two local potential wells which may be occupied by an atom as predicted by the displacive model. These wells represent the possible positions of some atom in a structurally distorted phase and the barrier between them is located at a site of point centrosymmetry. As the temperature rises, the minimum of the potential well and therefore the atomic displacements moves towards the central position. Above T_c the potential minimum is located at a centrosymmetric site. (b) shows the disordering of local displacements among equivalent sites. As the temperature increases, the hop rate over the potential barrier also increases. Finally the local displacements become totally disordered but the shape of the potential surface remains unchanged.

The perovskite structure, shown in Fig. 1.2, is cubic and of space group $Pm\bar{3}m$. Its stoichiometry is ABO_3 , where the A and B cations are usually metals and the O anion is usually oxygen or fluorine. As shown in the schematic, an A cation occupies each of the corners of the cubic unit cell, the B cation occupies the cell center, and an anion occupies each of the faces. The anions form a rigid octahedron whose motion tends to be a key component in the phase transitions of perovskite compounds. The various lower symmetry phases of $PbTiO_3$ and $BaTiO_3$ involve distortions to this structure.

In the non–cubic, ferroelectric phases of these materials, the macroscopic polarization points in a direction consistent with the symmetry of the structural phase. In the tetragonal, ferroelectric phase of $PbTiO_3$, the macroscopic polarization points along a $\langle 001 \rangle$ crystal axis. In the rhombohedral phase of $BaTiO_3$ the macroscopic

polarization points along a $\langle 111 \rangle$ crystal axis. In the orthorhombic and tetragonal phases of BaTiO_3 the polarization points along $\langle 011 \rangle$ and $\langle 001 \rangle$ axes, respectively.

The structural symmetries of these crystals as measured by Raman spectroscopy [1, 2] and by diffraction [3, 4] follow the behavior of the polarization, which is the macroscopic order parameter. Both measure titanium displacements in directions parallel to the macroscopic polarization in the ferroelectric phases of both materials. In the high temperature phase, wherein the polarization vanishes, diffraction observes cubic symmetry.

Both PbTiO_3 and BaTiO_3 display thermodynamic properties consistent with many features of the classic theory of displacive phase transitions [5]. Both show underdamped, zone centered soft modes of diminishing frequency as the transition temperature to the lower symmetry, ferroelectric phase is approached from above, which is characteristic of the displacive type of transition. Both have large Curie–Weiss constants, which relate the dielectric susceptibility to the temperature and transition temperature, characteristic of displacive ferroelectrics [6]. Because of these thermodynamic properties, the measurements of the diffraction and Raman spectra, and the behavior of the macroscopic order–parameter, it has long been assumed that the local structure behaves identically to the average structure. That is, the microstructure of these materials is presumed to share the symmetry elements of the macroscopic order parameter. This simple but physically incomplete model suffices to explain many of the properties of the material which rely upon long–range correlations.

In recent years a wide variety of techniques have suggested the possibility that perovskite type materials display order–disorder character, including infrared reflectivity measurements [7], cubic phase x–ray diffraction[8], electron spin resonance[9], impulsive stimulated Raman scattering[10, 11] and others. Also direct evidence of order–disorder character in perovskite materials which were traditionally considered to be of the displacive sort has been demonstrated using XAFS. These include KNbO_3 [12], $\text{KTa}_{0.91}\text{Nb}_{0.09}\text{O}_3$ [13–15], NaTaO_3 [16], $\text{Na}_{0.82}\text{K}_{0.18}\text{TaO}_3$ [16] and PbZrO_3 [17]. Some of the results of this thesis on order–disorder behavior in PbTiO_3 were previously presented in Refs.[18] and [19].

XAFS is an ideal technique for studying the microstructure of these materials. As mentioned above, both diffraction and Raman can fail to resolve differences between the two models in certain cases. When measuring only Bragg peak positions and widths, diffraction can lack the resolution necessary to distinguish thermal and structural disorder. In contrast, XAFS naturally possesses a high degree of spatial

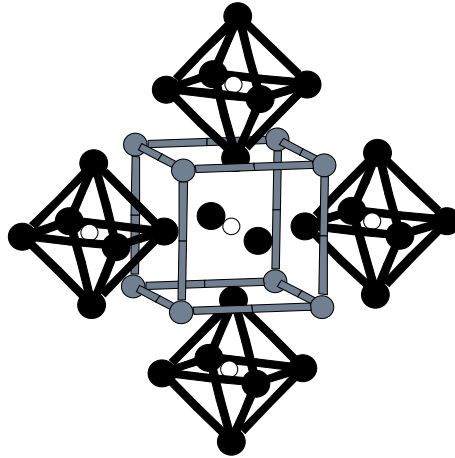


Figure 1.2: The ABO_3 perovskite crystal structure. The A cation (grey ball) is at the corner of the cubic unit cell. The B cation (white ball) is at the center of both the oxygen (black ball) octahedron and the cubic unit cell. In this thesis, the A cation is one of lead, barium or europium and the B cation is titanium.

resolution and it is sensitive only to local and not to long-range correlations in structure. Furthermore, the time scale of the XAFS measurement is far shorter than the time scale of the lattice vibrations. XAFS can resolve a disordered structure in a case where an atom is hopping between two or more positions displaced from sites of point centrosymmetry on a time scale that may be averaged by a Raman measurement. Consequently XAFS is capable of resolving behavior of the local, short-range correlations in a material which differs from the behavior of the macroscopic order parameter.

In this thesis I analyze both the extended x-ray absorption fine structure (EXAFS) and the x-ray absorption near edge structure (XANES) of $PbTiO_3$ and $BaTiO_3$. From this I verify the existence of an order-disorder component to the local structure of the phase transitions in these materials.

1.2 Full Multiple Scattering XANES Calculations

In the second part of this thesis, Chs. 8 and 9, I present the theory and results of a recently developed computer program for calculating the X-ray Absorption Near Edge Structure (XANES) employing a real-space, full multiple scattering (FMS) approach.

XANES is an enticing spectroscopy as it can provide local chemical and structural information even in complex and disordered systems. As such it is applicable to a wide variety of materials of interest to many different scientific disciplines. The fundamental physics of the multiple scattering approach to XANES calculations has been well established for many years [20–24]. Still calculations are of limited accuracy for complex materials, particularly near the absorption edge, the region presumably containing the local chemical information avidly sought in so many systems. Even in the case of crystalline materials, band structure approaches [25, 26] to the XANES problem are unsatisfactory as they usually neglect the effect of the core–hole. Recent advances in multiple scattering theory have seen considerable success when applied to the Extended XAFS (EXAFS) spectrum [27, 28].

The XANES code presented here applies recently developed algorithms and extensions which have proven successful in application to the extended part to the XAFS spectrum. These include relativistic Dirac–Fock atomic potentials [27, 29] and an efficient and quickly convergent expansion of the free electron propagator [30]. In recent years the speed and computational power of computers has risen dramatically. At the same time the cost of processors and computer memory has plummeted. Today calculations are tractable on desktop computers that only five years ago required access to a supercomputer. As FMS techniques are computationally expensive, requiring significant CPU, memory, and storage capacity, the prospect of approaching an old problem with new resources is attractive.

Using the FMS technique, my program simultaneously calculates XANES and local electronic densities of states as well as chemical quantities such as Fermi energies and charge transfer within solids. After presenting the theory of the FMS technique and demonstrating the utility of the code on a variety of simple physical systems, I tie together the two portions of this thesis by presenting XANES calculations on PbTiO_3 . The XANES spectrum of ferroelectric oxides such as those presented in the first portion of this thesis are well understood in terms of the local structure of these materials.

1.3 A Note on Presentation

To aid in the legibility of this thesis, I have adopted certain typographic conventions. Following common convention, normal text is set in computer modern roman and mathematical text is set in *mathematical italics*. Additionally I have adopted the following type faces:

Monospaced type is used to indicate the names of computer files or verbatim transcriptions of the contents of computer files.

SMALL CAPS are used to indicate the names of computer programs.

Sans-serif type is used to indicate matrix quantities. One special matrix, the full multiple scattering matrix, is set in blackboard bold: \mathbb{G} . Matrix quantities denoted by Greek characters are set in bold face: δ , ρ

I made extensive use of a number of software tools while preparing this thesis and feel I should acknowledge them. The thesis was typeset using the L^AT_EX [31] typesetting system and the University of Washington thesis style package [32]. The text was composed using the EMACS [33] text editor along with the AUC T_EX [34], REFTEX [35], and BIB-CITE [36] packages of editing utilities. The bibliography was compiled using BIBT_EX [37]. Figures in this thesis were created using the programs GNPLOT [38], XMGR [39], XFIG [40], and XMOL [41].

Chapter 2

THE EXAFS EQUATION AND EXAFS ANALYSIS

X-Ray Absorption Fine Structure (XAFS) spectroscopy is used to determine local atomic structure from the oscillatory portion of the x-ray absorption cross section of a material. The physical process measured in the XAFS experiment is the promotion by an incident photon of a deep core electron belonging to some atom in the material into a state above the Fermi level of the material. Because each element has a different set of electron binding energies, the absorption cross section due to a particular element within the material can be probed by tuning the x-ray source to an absorption energy associated with that element. By measuring the cross-section above a binding energy associated with a particular element, the local configurational environment about each such atom can be determined.

The XAFS spectrum is traditionally divided into two regions. The measurement of the absorption spectrum in a region between the Fermi energy and about 30 eV above the Fermi energy is referred to as the X-Ray Absorption Near Edge Spectrum (XANES). Above that energy is the Extended XAFS (EXAFS) region. In Ch. 7 – 9 I discuss measurements and calculations of XANES spectra. In this chapter and in Ch. 3 – 6 I discuss measurement and analysis of EXAFS data.

For an isolated atom, for instance a monoatomic gas, the cross section measures the probability of promoting a deep core electron into a continuum state. The measured spectrum looks roughly like a decaying step function¹. This step function is broadened by the lifetimes of the core hole and of the excited photoelectron as well as by the energy resolution of the experimental apparatus. When an atom is in condensed matter, this broadened, decaying step function is modulated by an oscillatory fine structure associated with the presence of the surrounding atoms. This oscillatory structure can be isolated and analyzed to yield information about the local configurational environment within which the absorbing atom sits.

In the first part of this chapter, I derive a heuristic expression for this oscillatory

¹ This statement assumes a one-electron picture and neglects many-body effects. Structure associated with multi-electron excitations can be observed in the absorption spectra of many elements. See, for example, Ref. [42].

structure and provide a physical basis for its analysis. The derivation presented here is a plane wave approach to the EXAFS equation. This approach is conceptually transparent and incorporates much of the essential physics. However, the effects of curved waves and self energy are neglected by the plane wave approach. The places where curved wave and other effects are critical to a proper development of the EXAFS formalism are carefully noted. See any of Refs. [24, 27, 43–46] for a formal development of modern EXAFS theory. In the rest of the chapter I outline the analytical procedures used to extract the structural information. Finally I discuss sources of measurement error in an EXAFS experiment.

2.1 *Heuristic Development of the EXAFS Equation*

2.1.1 *Single Scattering EXAFS*

When a deep core electron is promoted to a state above the Fermi energy, the outgoing wave function may be expressed as an outwardly propagating photoelectron wave of the form e^{ikr}/r , where k is the wavenumber of the photoelectron. In condensed matter, other atoms are encountered by this photoelectron within the lifetimes of the core hole and the photoelectron. These surrounding atoms are scattering sites and these scattered waves interfere with the outwardly propagating photoelectron. This quantum interference is the source of the oscillatory fine structure in the measurement of the x-ray cross section. Starting with this simple picture of a propagating photoelectron and backscattering wave, I derive an expression for the fine structure χ . This is a K shell, single scattering (SS) derivation within the small atom approximation which is simple and underscores the essential physics of the interference phenomenon. Towards the end of the derivation, I discuss the many improvements to the small atom model, which is inadequate for rigorous, quantitative analysis of EXAFS data. In the following section I discuss multiple scattering.

Consider the interference between the photoelectron and the backscattering from an atom at \mathbf{r}_i . The backscattered wave is a spherical wave of the form

$$\frac{e^{ik|\mathbf{r}-\mathbf{r}_i|}}{|\mathbf{r}-\mathbf{r}_i|} \quad (2.1)$$

as it propagates from a center at atom i . The photoelectron wave-number k is related

to the Fermi energy by

$$k = \sqrt{\frac{2m(E - E_F)}{\hbar^2}}. \quad (2.2)$$

In discussions of EXAFS analysis, the Fermi energy E_F is often called E_0 . For the remainder of this chapter I will use the latter notation.

The amplitude of the backscattered wave depends on two factors, 1) a dimensionless scattering amplitude for atom i and 2) the value of the outwardly propagating photoelectron at the position \mathbf{r}_i . Putting these pieces together, placing the absorbing atom at the origin so that $\mathbf{r}_0 = 0$, and taking the real part, I obtain an expression of the form

$$\chi_i(k) \approx \text{Im} \left(F_i(k) \frac{e^{2ikr_i}}{(kr_i)^2} \right). \quad (2.3)$$

There are phase shifts associated with the electron propagating into and out of the potentials of the scattering site and of the absorbing site (see for example page 405 of Ref. [47]). There is also a phase shift of $\frac{\pi}{2}$ for an outwardly propagating K shell spherical wave. Including these yields

$$\chi_i(k) \approx \text{Im} \left(F_i(k) \frac{e^{2ikr_i + \phi_i(k) - \pi/2}}{(kr_i)^2} \right) \quad (2.4)$$

$$\approx \frac{F_i(k)}{(kr_i)^2} \sin(2ikr_i + \phi_i(k)). \quad (2.5)$$

Eq. (2.5) is only an approximate equality, even within the small atom approximation, because it neglects two important amplitude factors. The first is a thermal attenuation. At finite temperature, the bond between atom i and the central atom deviates from its average length $\langle |\mathbf{r}_i - \mathbf{r}_0| \rangle$ due to thermal motion. Assuming this thermal motion is Gaussian and denoting the root mean square deviation in bond length as σ_i , the probability of finding the atom at \mathbf{r}_i is

$$\mathcal{P}_i = \frac{1}{\sqrt{2\pi\sigma_i^2}} \exp\left(-\frac{|\mathbf{r}_i - \bar{\mathbf{r}}_i|^2}{2\sigma_i^2}\right). \quad (2.6)$$

The effect of this distribution is to attenuate the signal by a factor $\exp(-2k^2\sigma_i^2)$, which is similar in form to the crystallographic Debye–Waller factor.

The second amplitude attenuation is due to the finite lifetime of the core hole and of the photoelectron. Both of these effects as well as any experimental broadening can be expressed as a mean free path $\lambda(k)$ and included in the expression for $\chi(k)$ as $\exp(-2r/\lambda)$.

Finally the EXAFS equation within the small atom approximation is written as

$$\chi_i(k) = \frac{F_i(k)}{(kr_i)^2} \sin(2ikr_i + \phi_i(k)) e^{-2k^2\sigma_i^2} e^{-2r_i/\lambda(k)}. \quad (2.7)$$

To consider the effect of all single scatterings from the surrounding atoms, a summation over all different kinds of scattering sites i is performed

$$\begin{aligned} \chi(k) &= \sum_i \chi_i(k) \\ &= \sum_i \frac{N_i S_0^2 F_i(k)}{(kr_i)^2} \sin(2ikr_i + \phi_i(k)) e^{-2k^2\sigma_i^2} e^{-2r_i/\lambda(k)}. \end{aligned} \quad (2.8)$$

In this equation N_i is the number of equivalent atoms at distance r_i . I have also explicitly included an important many-body contribution to the EXAFS equation, S_0^2 , the passive electron reduction factor which is due to the relaxation of the remaining electrons in the absorbing atom after the creation of the core hole [48].

Eq. (2.7) is not appropriate for EXAFS analysis. The small atom approximation is too severe of an approximation for quantitative analysis of EXAFS data. Much more appropriate is a ‘‘spherical wave approximation’’ [43] in which the form of Eq. (2.7) is preserved but $F_i(k)$ is replaced by $F_i^{eff}(k, R)$ and the calculation is made using a complex momentum p . The curved nature of the propagating photoelectron and the finite size of the scatterers introduce the R dependence in the calculation of F_i^{eff} . The complex momentum is given by [28]

$$p = \sqrt{2(E - V_{int}(E)) + i\Gamma/2}. \quad (2.9)$$

$V_{int}(E)$ is the potential of the muffin tin interstice. The calculation of the muffin tin includes the energy dependent self-energy, so V_{int} is energy dependent and complex. Γ is the line width of the core-hole state.

Considering these effects is essential for obtaining accurate quantitative results from EXAFS analysis. Ref. [28] prescribes a method for considering these curved wave and self-energy effects while still casting the EXAFS equation in the form of Eq. (2.7).

2.1.2 Multiple Scattering EXAFS

Many interesting problems require consideration of atoms beyond the first shell where a single scattering formulation of EXAFS is often insufficient. Consideration of multiple scattering (MS) events, i.e. the scattering of the photoelectron from two or more of the surrounding atoms, is required for detailed resolution of local structures in many materials. The multiple scattering code FEFF presents a particularly convenient solution [27, 30] to the MS problem.

The conceptual key to the approach of FEFF is to consider *scattering geometries* rather than bond lengths. The relevant length scale of each scattering geometry j is its half path length r_j , i.e. half of the sum of the lengths of the legs of the scattering path. For a single scattering path, the half path length is the same as the bond length, $r_j^{ss} = r_i^{ss}$. The effects of the scattering amplitudes of each atom in a path as well as the scattering angles are included into an effective scattering amplitude $F_j^{eff}(k)$. The phase shifts, including their angular dependencies, of each atom in the path is included into an effective phase shift $\phi_j^{eff}(k)$. Using the half path lengths and the effective amplitudes and phase shifts, FEFF is able to express the MS EXAFS equation in a form analogous to Eq. (2.8)

$$\chi(k) = \sum_{\frac{1}{2}pt|allpaths\ j} \frac{N_j S_0^2 F_j^{eff}(k)}{(kr_j)^2} \sin(2ikr_j + \phi_j^{eff}(k)) e^{-2k^2\sigma_j^2} e^{-2r_j/\lambda(k)} \quad (2.10)$$

Here the sum is over all scattering geometries j . The term $F_j^{eff}(k)$ is the source of the name FEFF. Note that $F_j^{eff}(k)$ depends on path length and properly considers curved wave and self-energy effects for all orders of scattering.

There are many analytical advantages to the path formalism introduced by FEFF. As is discussed later in this thesis, Eq. (2.10) is conveniently parameterized by variables which can be optimized in the data analysis. Another advantage is that structural disorder is handled in a transparent manner. All effects in χ due to structural disorder are included automatically by the summation of paths without the need to consider the algebra introduced in Refs. [48] and [49] to handle structural disorder.

2.1.3 Other Corrections to the EXAFS Equation

In Eq. (2.10), k is the real momentum referenced to the Fermi energy. In analysis it is common to adjust the energy scale of the calculation to match that of the data. A

shift of the energy scale δE_0 enters Eq. (2.10) as

$$k' = \sqrt{k^2 - \delta E_0 \left(\frac{2m_e}{\hbar^2} \right)} \quad (2.11)$$

where m_e is the electron mass. k is computed from energy reference of the experiment by Eq. (2.2) and k' is inserted into Eq. (2.10).

At least one δE_0 parameter is always needed when fitting EXAFS data using fitting standards from FEFF. This is because the absolute energy scale of the FEFF calculation must be adjusted to the calibration of the monochromater used in the experiment. For many materials, the use of neutral atomic spheres in the construction of the muffin tin potential in FEFF may result in significant disagreement between the experiment and the phase shifts $\phi_j^{eff}(k)$ calculated by FEFF. As discussed in Ref. [50], one *ad hoc* way of resolving this disagreement is to allow the possibility of different δE_0 shifts for each type of backscatterer. This results in different δE_0 corrections for each path in Eq. (2.10). In this case Eq. (2.11) is used on a path-by-path basis.

At high temperatures or in the case of anharmonic bonds, the assumption in Eq. (2.6) that the deviation around some bond length \mathbf{r}_i is described by a Gaussian distribution is inadequate. Higher cumulants of the distribution may be added to Eq. (2.10) by correcting the phase of each term in the sum by $-4ik^3 C_{3,j}/4$ and the amplitude by $e^{-2k^4 C_{4,j}/3}$. $C_{3,j}$ and $C_{4,j}$ are the third and fourth cumulants of the distribution for path j . These are defined for SS paths in Ref. [51]. In materials where the Gaussian distribution is inadequate, neglecting $C_{3,j}$ and $C_{4,j}$ results in errors in the determination of structural parameters such as path length and σ^2 . Anharmonic effects are negligible in the materials presented in this thesis.

Because of experimental resolution or because of errors in the determination of the self-energy used to calculate $F_j^{eff}(k)$ in FEFF, it may be necessary to modify the mean free path λ . In FEFFIT, this correction is done on an energy scale using the same complex momentum used in the FEFF calculation. The details of this correction to the amplitude of the path are presented in Ch. 6 of the FEFFIT document [52]. Amplitude corrections in the form of mean free path corrections were used in the the analysis presented in this thesis.

2.2 Background Removal

The absorption cross section μ is conveniently separated [53] into the atomic background μ_0 and the scattering contribution χ by

$$\mu(E) = \mu_0(E)(1 + \chi(E)) \quad (2.12)$$

Background removal is the process of approximating the functional form of $\mu_0(E)$ and subtracting it from $\mu(E)$ to isolate $\chi(E)$. The background removals in this thesis were performed by the program AUTOBK [54]. Other approaches to background removal are given in Refs. [55, 56].

$\mu_0(E)$ in Eq. (2.12) is the absorption cross section of an *embedded atom*, i.e. the absorbing atom in the potential environment of its neighbors but without the contribution of the scattering from its neighbors. Consequently, this $\mu_0(E)$ is different from the cross section of the free atom. Often $\mu_0(E)$ shows low frequency oscillatory structure due to scattering of the photoelectron from the edge of the embedded atom potential [57, 58]. Knowledge of the form of $\mu_0(E)$ thus requires detailed knowledge not only of the embedded atom potential but of multi-electron effects and of the experimental setup, including the energy response of the detectors, the energy dependence of the attenuation due to air and other objects in the experimental path, the harmonic content of the beam, and others. Because experimental effects are difficult to know *ab initio*, it is usually necessary to rely upon empirical methods of determining $\mu_0(E)$. The algorithm used by AUTOBK uses the information content of the $\mu(E)$ signal and, optionally, a fitting standard from Feff to distinguish the background from $\chi(E)$.

AUTOBK uses a set of b-splines [59] to approximate the functional form of $\mu_0(E)$. The knots of the spline are placed evenly in photoelectron wavenumber k . The number of knots are determined by the information content of the background portion of the spectrum. As suggested by Eq. (2.10), the photoelectron wavenumber k and the path length $2R$ are Fourier conjugate variates. The shortest path length thus sets a lower limit on the contribution to the frequency content of $\mu(E)$ due to scattering from the neighboring atoms. Thus the low frequency portion of $\mu(E)$ is due to $\mu_0(E)$ while the high frequency portion is due to $\chi(E)$. The cutoff frequency between these two regimes is $2R_{bkg}$, where R_{bkg} corresponds to a distance smaller than nearest neighbor bond length. If the functional form of $\mu_0(E)$ is to be approximated in some energy range ΔE corresponding to a wavenumber range Δk , then the number of knots $N_{kn} = 2R_{bkg}\Delta k/\pi$ used in the spline is determined from the information content [60]

of that portion of the signal. The evenly spaced knots are separated by the spacing between independent points. In practice, the swiftly varying part of the background function near E_0 is excluded from the optimization in AUTOBK. The high frequency components of the swiftly varying part of $\mu_0(E)$ can difficult to distinguish from the frequency content of $\chi(E)$. By excluding that part of $\mu(E)$ in AUTOBK, the spectral separation between μ_0 and χ is valid.

The spline coefficients at each knot are determined by optimizing the Fourier components of $\chi(k)$ in the frequency range between 0 and R_{bkg} . The optimization is performed using a Levenberg–Marquardt non–linear least–squares minimization [61]. The knot coefficients may simply be chosen to minimize the amplitude of the low frequency components of $\chi(k)$. This may not be satisfactory as there often are sources of broadening which cause leakage of the structural signal into the low frequency range. A preferable choice is to optimize the low frequency components of $\chi(k)$ to best fit the low frequency components of a standard $\chi(k)$. Usually a calculation from FEFF is used for the standard, although data can be used as well.

$\mu(E)$ data is often displayed after *pre-edge removal* and *normalization* [62]. The pre–edge removal refers to the process of regressing a line to the data well below the Fermi energy then subtracting this line from all data points. This serves to make the pre–edge region zero and the data above the edge positive definite. A line is then regressed to the data in some energy range well beyond the edge. The *edge step*, $\delta\mu_0$, is the height of this line at E_0 . The fine structure is then

$$\chi(E) = \frac{\mu(E) - \mu_0(E)}{\delta\mu_0} \quad (2.13)$$

Because the $\mu_0(E)$ found by AUTOBK can include experimental effects, normalizing by the edge step as shown is usually preferable to normalizing by the functional form of $\mu_0(E)$. $\chi(E)$ is converted to $\chi(k)$ by Eq. (2.2). Normalizing to a single number introduces an energy dependent attenuation to the data due to the energy dependence of the absorption of the embedded atom. An approximation to this effect for use in the analysis of $\chi(k)$ is given in Sec. B.2.2.

2.3 Fitting EXAFS Data

The computer program FEFF provides fitting standards in the form of the terms in the summation in Eq. (2.10). EXAFS data is analyzed by using FEFF’s calculations of $F_j^{eff}(k)$ and $\phi_j^{eff}(k)$ and parameterizing the other terms in Eq. (2.10). The parameters

are optimized to produce the best fit of the theory to the data. The program used in this thesis to perform this optimization is FEFFIT. [52] FEFFIT uses the same Levenberg–Marquardt minimization [61] as does AUTOBK.

FEFFIT determines a best fit by optimizing the parameters in Eq. (2.10) for each path then summing the paths to produce a function to compare with the data. The Levenberg–Marquardt algorithm works by minimizing a statistical parameter called χ^2 [63]. χ^2 is evaluated using the complex Fourier transforms $\tilde{\chi}(R)$ of the data and of the FEFF calculation.

$$\chi^2 = \frac{N_{idp}}{N} \sum_{i=1}^N \left| \frac{\tilde{\chi}(R_i)_{thy} - \tilde{\chi}(R_i)_{exp}}{\sigma_i} \right|^2 \quad (2.14)$$

χ^2 is evaluated at each grid point i in the space of the Fourier transform. Typically a fast Fourier transform is used which requires input data on a uniform grid in k space, so the grid spacing in R is determined. At each point i the difference between the theory and the data is normalized by the measurement uncertainty σ_i at that point.

Some range Δk in k space is the bounds of the Fourier transform. The summation in Eq. (2.14) is over all points within some range ΔR of the Fourier transform $\tilde{\chi}(R)$. This defines the bandwidth of the EXAFS signal and specifies the number of independent points N_{idp} in the measurement. From Refs. [60] and [64]

$$N_{idp} = \frac{2\Delta k \Delta R}{\pi} + 2 \quad (2.15)$$

The addition of two independent points is explained in Ref. [64]. It is important to note that this addition applies to the entire portion of the data analyzed. If a data range is subdivided into two or more ranges, the addition of two points of information applies to the sum of subranges, *not* to each subrange individually.

The prefactor in Eq. (2.14) thus normalizes the evaluation of χ^2 to the number of independent points in the measurement, independent of the density of the energy grid on which the absorption spectrum was initially measured.

The measurement uncertainty is, in practice, not evaluated at each point in R space. Instead, the uncertainty is assumed to be shot noise in k space which corresponds to white noise in R space. Thus a single number $\bar{\sigma}_r$ is pulled outside the summation in Eq. (2.14). In FEFFIT $\bar{\sigma}_r$ is evaluated by measuring the mean value of the data in the R range from 15 to 25 Å. This range is assumed to be well above any structural contribution in real data. For reasons discussed in Sec. 2.4, $\bar{\sigma}_r$ typically

underestimates the true measurement uncertainty (which includes systematic as well as statistical errors) by about one order of magnitude.

The χ^2 of Eq. (2.14) is minimized by adjusting the various structural and electronic parameters in Eq. (2.10) for each path. Clearly each of these parameters cannot be varied independently due to the bandwidth limitation to the information content evaluated in Eq. (2.15). FEFFIT uses a sophisticated macro language to represent the parameters for each scattering path in terms of some smaller number of fitting parameters. In this way physical constraints are built into the fitting model. In Appendix A I describe in detail how I built physical constraints into my fitting models for PbTiO_3 , BaTiO_3 , and EuTiO_3 using FEFFIT.

To evaluate the differences between different fitting models which may use different numbers of fitting parameters, it is useful to evaluate the *reduced* χ^2 using the number of variables N_{var} actually used in the fit

$$\begin{aligned}\chi_\nu^2 &= \frac{1}{\nu}\chi^2 \\ \nu &= N_{idp} - N_{var}\end{aligned}\tag{2.16}$$

The number ν is call the *degrees of freedom* of a fit. When the measurement uncertainty $\bar{\sigma}_r$ is correctly evaluated, $\chi_\nu^2 \approx 1$ for a good fit [63]. A fitting model for which χ_ν^2 increases by more than a factor $1 + \frac{2\sqrt{2}}{\sqrt{\nu}}$ [63, 65] is considered statistically worse.

From the covariance matrix evaluated by the minimization algorithm, FEFFIT can extract error bars on the variables and correlations between the variables. These numbers are written to one of the output files of FEFFIT and are essential to interpreting the physical validity of the fitting model. The error bars reported by FEFFIT are scaled to the size of the measurement uncertainty by multiplying the diagonal elements of the covariance matrix by the value of χ_ν . Doing so assumes that a fit is a good fit and that the value of $\bar{\sigma}_r$ was underestimated as the random errors in an EXAFS experiment are typically much smaller than the systematic errors. While it may not be true that some particular fit is a good one, not scaling the size of the error bars leads to significant underrepresentation of uncertainties of the fitting parameters.

FEFFIT calculates one more useful statistical parameter, an \mathcal{R} -factor which mea-

sures the percentage misfit of the the theory to the data

$$\mathcal{R} = \frac{\sum_{i=1}^N \left| \tilde{\chi}(R_i)_{thy} - \tilde{\chi}(R_i)_{exp} \right|^2}{\sum_{i=1}^N \left| \tilde{\chi}(R_i)_{exp} \right|^2} \quad (2.17)$$

The \mathcal{R} -factor can be helpful determining whether the reason for a $\chi_\nu^2 > 1$ is the underestimation of $\bar{\sigma}_r$ or simply a poor fit. \mathcal{R} is usually smaller than a few percent for a good fit. As seen in Table 5.4, \mathcal{R} was about $\frac{1}{2}$ percent for fits with $10 < \chi_\nu^2 < 85$.

2.4 Interpreting Reduced Chi-Square

As discussed in Ref. [65], the uncertainty in a good EXAFS measurement is generally dominated by systematic errors. Often the statistical errors of the measurement are small compared to various systematic sources of error. This is almost always true for transmission experiments which are characterized by a large signal-to-noise ratio. χ_ν^2 is normalized by the estimated statistical uncertainty. If the statistical errors dominate, then $\chi_\nu^2 \approx 1$ for a good fit. That χ_ν^2 is, in general, larger than 1 even for fits that looks good upon inspection and give physically reasonable results indicates that systematic errors dominate. We account for this by scaling the error bars on our fitting parameters by a factor of χ_ν . Often the absolute error in a fit is quite small with an \mathcal{R} -factor of less than 1 percent. In a fit with small absolute error but a large χ_ν^2 due to incorrect measurement of $\bar{\sigma}_r$, the measured value of χ_ν^2 provides a means of comparing different fitting models. If the χ_ν^2 's of the two models differ by more than a factor of $1 + \frac{2\sqrt{2}}{\sqrt{\nu}}$, then the model with the smaller χ_ν^2 is significantly better.

Two structural models may be statistically indistinguishable based on evaluation of their χ_ν^2 's, but yield physically distinguishable results. In such a case, one fitting model may be rejected on the basis of a physical argument. An example of this is shown in Ch. 5 in the analysis of the barium K edge EXAFS of BaTiO₃. The temperature dependence of the mean square displacements σ^2 in bond lengths using one structural model in that example is less physically reasonable than that for another structural model. The structural model yielding physically reasonable results is the preferable model.

In a carefully executed EXAFS experiment, the statistical errors are limited by shot noise, thus are quite small given the large count rates available at synchrotron sources. Most sources of systematic error (sample inhomogeneity, detector noise,

beam harmonic content, and others) can be reduced to negligible levels by good experimental practice.

Handling systematic errors is more difficult. Unlike the effect of statistical errors, the effects of systematic errors cannot be reduced by the collection of more data. Also systematic errors are not expected to be normally distributed in the data, thus these errors can introduce a systematic bias into the measurement of physical parameters from the data. The dominant remaining sources of error are the uncertainties of the removal of the background function μ_0 and of the fitting standards.

The effect of the background subtraction can be characterized by performing multiple background subtractions with AUTOBK on the same data, each time changing one or more of the parameters used by AUTOBK to perform the Fourier transform or to optimize the spline in R space. The standard deviation of the χ functions from these background removals can be calculated and added in quadrature to the measurement uncertainty used by FEFFIT to normalize χ_ν^2 . Adding this systematic uncertainty in quadrature to $\bar{\sigma}_r$ treats the systematic error as a random error. The main consequence of treating a systematic in this manner is to incorrectly estimate the uncertainties in the fitting parameters. The uncertainty in the fitting parameters varies as the square root of the degrees of freedom whereas the uncertainty due to systematics is constant. Consequently FEFFIT's estimation of error bars tends to err on the side of being too large.

Evaluating the effect of the uncertainty in the fitting standards is trickier and perhaps impossible. FEFFIT uses a minimization technique that assumes quadratic deviation of χ_ν^2 in all directions in the n -dimensional hyperspace of fitting parameters near the best-fit set of parameters. Implicit in this method is the assumption that the lineshape to which the data is fit is a known lineshape. That is, of course, not true in EXAFS fits. FEFF, the source of fitting standards, employs various approximations (spherical muffin tins, neutral atoms within their Norman radii, some parameterization for exchange and correlation terms in the potential, and others) to compute these fitting standards. Consequently FEFF provides only an approximation to the true lineshape. This introduces error into the fits which is difficult to characterize and which leads to evaluated χ_ν^2 's in excess of 1 even for excellent fits.

In the analysis presented in this thesis, systematic errors are treated as though they are another source of random errors. We thus add the systematic errors in quadrature with the statistical. The main consequence of doing this is to incorrectly estimate the size of the error bars on the physical parameters obtained from the data. Typically the size of the error bars is overestimated by adding systematic error

in quadrature. For example, in Ch. 4 the uncertainties on most of the local structural parameters shown in Figs. 4.6 – 4.9 are considerably larger than the scatter of these values about their average temperature behavior.

That χ^2_ν is typically in excess of 1 is not a reason to doubt EXAFS results. Prudent use of statistical parameters such as χ^2_ν and the \mathcal{R} -factor combined with well constructed fitting models and a good physical intuition make for excellent EXAFS analysis.

Chapter 3

XAFS EXPERIMENTS

XAFS data is not difficult to collect, providing a protocol for sample preparation and data collection is strictly followed. In this chapter I will discuss many of the aspects of this protocol with particular attention to their application to the experiments and samples presented in this thesis.

3.1 Data Collection

Fig. 3.1 shows a schematic of an absorption experiment for both the fluorescence and transmission collection geometries. All of the data presented in this thesis were collected at beamline X11A at the National Synchrotron Light Source (NSLS) at Brookhaven National Laboratory in Upton, NY, USA. The x-rays at X11A are produced by a bending magnet.

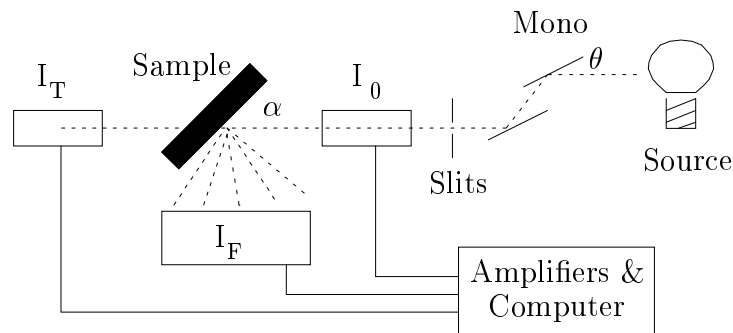


Figure 3.1: Schematic of the XAFS experiment. The setup for both the transmission and fluorescence geometries is depicted.

3.1.1 The Monochromator

X-rays are monochromated with a double crystal, silicon monochromator. For data collected at the titanium K edge 4966 eV and the europium L_{III} edge 6977 eV, silicon

crystals cut along a (111) face were used. For data collected at the barium K edge 37441 eV, (311) crystals were used. Due to the size of the crystals and their placement within the goniometer controlling the monochromator, the (111) crystal has an energy range that extends from about 4 keV to about 25 keV and the (311) crystal has a range of about 7 keV to 41 keV.

The monochromator selects the Bragg angle for the desired photon energy. This angle θ in Fig. 3.1 is the angle between the face of the first crystal and the propagation vector of the incident broad spectrum x-ray beam. The Bragg angle is determined [66] by matching the desired photon wavelength with the planar spacing of the crystal

$$\theta = \sin^{-1} \left(\frac{hc}{2dE_\gamma} \right). \quad (3.1)$$

Here h and c are Planck's constant and the speed of light, d is the planar spacing of the (111) or (311) crystal, and E_γ is the desired photon energy. The energy scan in the XAFS experiment is thus accomplished by rotating the monochromator through the appropriate range of θ . The second crystal follows the first, remaining nearly parallel, to re-diffract the single energy beam in a direction parallel to the broad spectrum beam.

One of the disadvantages of using a double crystal monochromator is that it allows passage of harmonics of the selected energy as those photons will also satisfy the Bragg diffraction condition. This is a serious problem for the data quality, as will be discussed in Sec. 3.1.4. The intensity of the beam diffracted by the second crystal has a Gaussian profile in angle about the optimal angle. This is called the *rocking curve*. The rocking curve becomes narrower in θ for higher harmonics. The best solution for harmonic rejection is to choose a plane for the silicon crystal that rejects certain harmonics. Both the (111) and (311) planes reject the second harmonic but allow the third. Since the rocking curve is considerably wider for the principle frequency than for the third harmonic, it is useful to slightly detune the second crystal by rotating it slightly away from the optimal θ . As the rocking curve is significantly narrower for higher harmonics, detuning enough to reduce the fundamental by a small amount is enough to reject most of the intensity of the third harmonic. For example, at 10 keV with a silicon (111) crystal, detuning such that the intensity of the fundamental is reduced by half reduces the third harmonic by about 10^{-3} [67].

At low energies, the second crystal is detuned to attenuate the intensity of the harmonic by about 20 percent. Due to the narrow rocking curve for the third harmonic, this will reject in excess of 90 percent of the harmonic intensity. It is not

necessary to detune the second crystal for the barium K edge. Its third harmonic $E_3 > 110$ keV is so far above the critical energy that the intensity of those photons is negligibly small.

The second disadvantage of the double crystal monochromator is that the vertical position of the monochromatic beam changes with energy as the crystal angle changes. Typically, the entire table supporting the sample, detectors, and other equipment is moved to track the beam position. In this way, the beam strikes nearly the same spot on the sample at all energies.

3.1.2 The Slits

There are two sets of slits at X11A. The slits depicted in Fig. 3.1 are placed on the optical table and define the size of the beam that strikes the sample. These are called the *table slits*. The other slits define the size of the broad spectrum beam that strikes the first crystal of the monochromator. These are called the *pre-mono slits*.

There are two considerations to choosing the dimensions of the slits, 1) maximizing throughput and 2) maximizing energy resolution. These two considerations are at odds. Throughput is obviously increased by opening the slits to allow more photons to pass through. Due to the angular divergence of the x-ray source and the geometry of the monochromator, there is a spread of energies in the vertical direction, thus energy resolution is lost by opening the vertical slits too wide. It is easy to tell when energy resolution is being compromised by slit size. When two scans through the absorption edge of the sample are taken and the slits are closed by some amount between scans, it will be obvious if resolution was compromised by the original slit size if the features around the edge are noticeably sharper in the scan with narrower vertical slits. The vertical portion of the table slits should be closed until no change in resolution between scans is observed. The slits should then be opened to the widest setting at this fine resolution to allow the most photons through.

At lower energies the most convenient setup is to open the pre-mono slits quite wide (about 2 mm at X11A) and use only the table slits to define energy resolution. At high energies I found that closing the pre-mono slits to about 0.5 mm was necessary to obtain acceptable energy resolution. The angular divergence of the source is a bigger constraint at high energies since $\frac{\partial\theta}{\partial E_\gamma}$ is much smaller at high energies. At the barium K edge, the energy resolution was about 2 eV while at the titanium K and europium L_{III} edges it was about 0.5 eV.

The horizontal dimension of the slits is usually determined by the size of the

sample. Near the center the beam does not change significantly in intensity, quality, or harmonic content across its horizontal dimension, so placement of sample horizontally is not so critical.

The final consideration regarding the slits applied to an experiment in which the polarization of the x-ray beam is used. In the plane of orbit of the storage ring, the photons generated by the bending magnet are linearly polarized. Above and below the plane of orbit, the beam is left and right handedly elliptically polarized. In the single crystal XANES experiments described in Ch. 7. the linearity of the polarization was exploited. Fortunately, the intensity of the beam is highest in the plane of orbit, exactly where the beam is linearly polarized. By moving the table supporting the experiment up and down, the table slits will pass through the plane of orbit. The point of highest throughput as measured by the detector immediately behind the slits is the within the plane of orbit. This should be checked frequently during the course of the experiment, if the polarization is important to the result.

3.1.3 The Ion Chambers

For all of the experiments presented in this thesis, I used ionization chambers as detection devices, thus I will restrict my discussion of x-ray detection to the use of ionization chamber. For the rest of this thesis I will use the shorthand *ion chamber*.

An ion chamber [68,69] is a gas filled box. The x-rays pass through the gas and between the plates of a capacitor inside the box. The gas molecules are ionized by the x-rays and the ions and electrons are collected on the plates of the capacitor. Each photon ionizes many molecules. The resulting current is amplified and converted to a voltage. This voltage is stored on a computer as a measure of the intensity at the detector.

The voltage read by the ion chamber is

$$V = \frac{eE_{\gamma}NG}{E_{eff}}. \quad (3.2)$$

Here e is the electron charge, E_{γ} is the energy of the incident photons, N is the number of photon per second incident on the chamber, G is the amplifier gain of the current-to-voltage converter, and E_{eff} is the effective ionization energy of the gas. For noble gases $E_{eff} \approx 30\text{eV}$. From this, the counting rate on the ion chamber is

determined

$$N \approx \frac{4 \cdot 10^{20} \cdot V}{GE_\gamma}. \quad (3.3)$$

Because of the high intensity of the signal at X11A, special electronics are often not required for the current-to-voltage conversion. Modest amplifier gains are usually sufficient to obtain measurable voltages and the count rates are high enough that an integration times of one or a few seconds usually suffices. For this purpose commercially available converters are usually used. For experiments that involve low count rates and large amplification, low-noise converters [15] created and developed by members of the Stern Research Group have been used.

The main advantage of ion chambers is their ease of use. Following a few simple rules virtually guarantees reliable x-ray detection. It is crucial to choose an appropriate mixture of gases. Noble gases or nitrogen are common choices. Several common atmospheric gases such as oxygen and water vapor are poor choices as they introduce nonlinearities in the counting of the photons. The gases should be chosen such that an appropriate number of photons are absorbed by each chamber. In Fig. 3.1, the ion chamber labeled I_0 measures the intensity of the beam incident upon the sample. Clearly the I_0 chamber should not be so absorbing that too few photons actually strike the sample. For the experiments described in this thesis, about ten percent of the photons are absorbed in the I_0 chamber,

$$\frac{I_{\text{passing}}}{I_{\text{incident}}} \approx 0.9 = e^{-x\mu_{\text{total}}} \quad (3.4)$$

Here x is the length of the chamber and μ_{total} is the absorption of the mixture of gases. The absorption coefficients μ of the gases are tabulated [70] as functions of energy. These gases may be sealed inside the ion chamber or flowed slowly through it. X11A provides a flow meter connected to tanks of helium, nitrogen, and argon for this purpose. When using more expensive gases such as krypton, the chambers are usually sealed.

The chambers labeled I_T and I_F are used in the transmission and fluorescence geometries. It is desirable to choose gases appropriate to detecting all of the photons incident upon these chambers. Choosing gases such that $x\mu \approx 3$ in Eq. (3.4) is a good choice. This absorbs 95 percent of the incident photons. Using a thicker mixture of gases is a poor idea. The fringing fields near the ends of the capacitors within the ion chambers will not follow Eq. (3.2). If the mixture of gases is overly thick, a large

fraction of the photons will be counted within the fringing field and the data will be contaminated.

The final consideration for ion chambers is the voltage applied to the capacitor plates. The voltage–current curve [68] for an ion chamber has a broad plateau at some voltage range. The voltage on the chamber should be chosen within this plateau so that the current collected on the capacitor is insensitive to fluctuations in applied voltage.

3.1.4 Collection Geometries

The Transmission Geometry

The transmission geometry uses the ion chamber labeled I_T in Fig: 3.1. In this geometry the beam passes through the sample and the attenuation of the beam by the sample is directly measured. The attenuation is

$$I_T = I_0 e^{-x\mu(E)}. \quad (3.5)$$

$\mu(E)$ is the energy dependent absorption of the sample. x is the width of the sample. The absorption coefficient is then obtained, within an overall scaling factor, from the voltages on the ion chambers by

$$x\mu(E) = \ln \left(\frac{I_0}{I_T} \right) \quad (3.6)$$

Transmission experiments are the easiest sort of XAFS experiment. If a sample can be prepared that is appropriate for transmission, it is advantageous to do so. There are several criteria for the appropriateness of the transmission geometry and concerns for proper sample preparation.

A transmission experiment is optimized for counting statistics when the sample thickness x is chosen such that $x\mu \approx 2.6$ [53] above the absorption edge. However, to minimize systematic error in the data due to sample thickness [71], $x\Delta\mu$, the change in absorption across the edge, should be $\lesssim 1$. Clearly both these criteria cannot always be satisfied. Of these two criteria, the one resulting in the thinner sample is chosen. Transmission is not appropriate for a very dilute sample. When less than about 3 percent of the total absorption in the sample is from the resonant element, the signal to noise ratio determined from counting statistics for a fluorescence experiment is superior. None of the experiments in this thesis fell into that category.

There may be other reasons why a fluorescence experiment might be preferable to transmission. If, for some reason, a sample cannot be prepared that is thin enough to meet the thickness criteria of the preceding paragraph, then fluorescence is required. The single crystal XANES data shown in Ch. 7 are examples of this. I did not have access to sufficiently thin single crystals, thus I opted to take the data in fluorescence.

The sample prepared for transmission must be homogeneous. There must be heterogeneities neither due to inconsistent thickness of the sample (as in a metal film rolled into a wedge shape) nor due to gaps through which the x-rays pass without striking the sample. This effect has been shown on powdered samples for which the particle size was chosen to be large compared to the length x required for a proper sample [72]. As the powder size was increased, that data suffered a significant attenuation of amplitude due to improper cancellation in Eq. (3.5). Sample inhomogeneity is a particularly severe problem when the beam possesses significant harmonic content.

The Fluorescence Geometry

The fluorescence geometry uses the ion chamber labeled I_F in Fig: 3.1. In this geometry the beam strikes the face of the sample. Secondary photons from the refilling of the core-hole fluoresce over the entire solid angle. The I_F chamber subtends some portion of the solid angle. In the case where the sample is very thick compared to its absorption length and the incident angle of the beam (α in Fig. 3.1) is equal to the exit angle (the angle between the sample surface and the straight line from the sample to the detector), the intensity of photons measured at I_F [53] is

$$I_F = \frac{I_0 \beta(E) \mu_c(E)}{\mu'(E_F) + \mu_b(E) + \mu_c(E)} \quad (3.7)$$

$\mu_c(E)$ is the energy dependent absorption of the resonant atom, i.e. the signal measured in the EXAFS experiment. $\mu_b(E)$ is the absorption of all other atoms in the material and of the electrons in the central atom that are not the excited electron. $\mu'(E_F)$ is the total absorption of the material at the fluorescence energy. The sum in the denominator is the term that accounts for the penetration depth of the x-rays into the sample. The factor β includes all other factors affecting the measurement, such as the solid angle subtended by the detector, the fluorescence efficiency of the

absorbing atom, and the detector gains. In the limit where $\mu'(E_F) + \mu_b(E) \gg \mu_c(E)$

$$I_F = I_0(E)\beta(E)\mu_c(E) \quad (3.8)$$

$$\mu(E) \propto \left(\frac{I_F}{I_0}\right) \quad (3.9)$$

Fluorescence measurements are the best option for very dilute samples or samples that cannot be prepared sufficiently thin for transmission. Sample homogeneity is critical to minimize the systematic error in the data due to spatial inhomogeneities in the incident beam.

To improve the signal-to-noise of the fluorescence experiment, it is useful to prevent Compton scattered radiation from entering the I_F chamber [73]. Soller slits which focus on the line on the sample struck by the x-ray beam are used to prevent radiation scattered by air and other sources from entering the chamber. Filters made from materials with absorption edges between the fluorescence energy of the measurement and the energy of the Compton scattered radiation are used to preferentially pass the photons in the measurement. Unfortunately the only elements with absorption edge at energies suitable for a filter for a titanium K edge experiment are iodine and krypton. L edge filters are less efficient than K edge filters and both of these elements are an inconvenient for making filters. The fluorescence data in this thesis were collected with Soller slits but without filters.

There are two important experimental effects that must be considered in the analysis of fluorescence data. The first is the energy dependence of the detectors. Since the the fluorescence experiment measures the secondary photon, the photons incident upon I_F are always of the same energy. The photons incident upon I_0 are, of course, of variable energy. Thus the energy response of the contents of the I_0 chamber enters into Eq. (3.7) and is neglected in Eq. (3.9). In the EXAFS region, this introduces a k^2 dependent attenuation of the signal. Given the contents of the I_0 chamber as input, an additive correction to the measured σ^2 's in EXAFS analysis can be approximated. This is called the *I0 correction* and is discussed in Sec. B.2.3.

The other experimental effect is the *self-absorption correction* and is due to the extent to which $\mu'(E_F) + \mu_b(E) \gg \mu_c(E)$ is a bad approximation in Eq. (3.8). This can be a very serious effect with large constant and k^2 dependent attenuation of the data. In the limit where the material is very concentrated, say in a metal foil, $\mu'(E_F) + \mu_b(E) \ll \mu_c(E)$. Then $\mu_c(E)$ cancels and almost no fine structure is measured! An approximation to this correction is discussed in more detail in Sec. B.2.4.

3.1.5 *Measurements at Low and High Temperature*

The ferroelectric and structural phase transitions studied in this thesis are induced by temperature. Consequently I measured XAFS as a function of temperature. For both low and high temperature measurements, a vacuum is pulled on the sample with a roughing pump. This produces a vacuum at the level of 10's of millitorr. The low temperature apparatus cryopumps to a level of about 10 mT below 77 K. The roughing vacuum is sufficient for high temperature work, although the vacuum shroud must be cooled with blown air to prevent the failure of the Kapton windows due to overheating.

At temperatures below room temperature, a Displex cryostat was used. A Displex is a two stage helium compressor with a copper cold finger. The cold finger is wrapped with a resistive heating element and is in contact with a temperature sensing diode. Using the heating element and diode, a commercial temperature controller can control the temperature at the cold finger between 10 K and 300 K with a stability of about ± 1 K. The sample holder is a copper box with slots cut in it for the x-rays to pass through. The slots are covered with Kapton sheet and the box is closed with an indium seal. Helium is allowed to diffuse into the sample holder. With the helium still in the sample holder, the sample holder is mounted onto the cold finger and plunged into liquid nitrogen. The Displex is turned on and the entire assembly is placed under vacuum. This procedure reduces the time required to cool the sample to 10 K. By quickly cooling the Kapton windows of the sample holder, the outward diffusion of the helium is slowed. The helium sealed within the sample cell serves as a heat exchange between the sample and the copper sample holder, thus ensuring good thermal contact between the sample and the cold finger.

For measurements at elevated temperatures, I used a furnace designed by members of the Stern Research Group. Some of the data were obtained using an old design which was plagued by electrical problems and by the short life span of its heating elements. To correct these problems I designed a new furnace, which was built by Larry Stark of the University of Washington Tool Making Shop. I will only describe the new furnace, although the two designs are conceptually identical. Both use high-power resistive heaters to heat a large copper block. The samples are then pressed against the copper block for thermal contact.

A schematic of the new furnace is shown in Fig. 3.2 and a close up of the main body is shown in Fig. 3.3. The main body is a copper block. Cut into the face of the block are four transmission slots. The samples are placed in front of these slots to

allow passage of x-rays for a transmission experiment. The furnace can also be used for fluorescence measurements. Drilled into the body of the copper block, as indicated by the dashed lines in Fig. 3.3, are two holes for housing resistive heating elements. I chose Watlow Firerod Cartridge heaters which use nickel–chromium resistive wire surrounded by magnesium oxide insulation. This assembly is sheathed with Incoloy, which is Watlow’s trademark name for an oxidation and corrosion resistant nickel alloy. The heaters are rated at 500 W at 120 V and can operate at temperatures in excess of 1100 K. These heaters exceed the power requirements of the furnace for operation at 1100 K. A Variac transformer is used to step down line voltage, thus derating the power output of the heaters. Derating the power output lengthens the lifespan of the heaters.

The Firerod cartridges have convenient electrical leads. They exit the body of the cartridge at a right angle, which is convenient for the geometry of the furnace. The leads are well insulated electrically and long enough to leave the volume enclosed by the radiation shielding covering the body of the furnace. This allows for electrical contact to the leads in a place that is well removed from the hottest part of the furnace. The radiation shield is an aluminum can which is bolted onto the circular mount shown in Fig. 3.2. The can has holes cut into it to allow passage of the x-rays. This is covered with thin aluminum foil to complete the radiation shielding.¹

Cut into the front of the main body of the furnace are two grooves for housing thermocouples, one on either side of the transmission slots. These are shown in Fig. 3.3 with solid lines. I use K-type thermocouple in a flexible magnesium oxide and inconel sheath. The grooves are cut to the dimensions of the sheath. It is thus easy to slide the thermocouple junction up and down along the face of the furnace allowing temperature measurement at selected spots close to the samples. One of the two thermocouples is used to control the temperature. the other is used as an independent measure of temperature and may be placed a distance away from the control thermocouple to allow measurement of temperature gradients. The thermocouples are pressed against the main body by a face plate, which also is used to hold the samples in place.

The cooling tube shown in Fig. 3.2 is pressed against the back side of the furnace by another face plate. This tube is normally evacuated, but may be used for gas flow

¹ At low energies such as the titanium *K* edge, it is necessary to not place even the thinnest aluminum foil in the path of the beam. The aluminum is sufficiently absorbing at low energy that any inhomogeneities in the aluminum will introduce systematic error to the data.

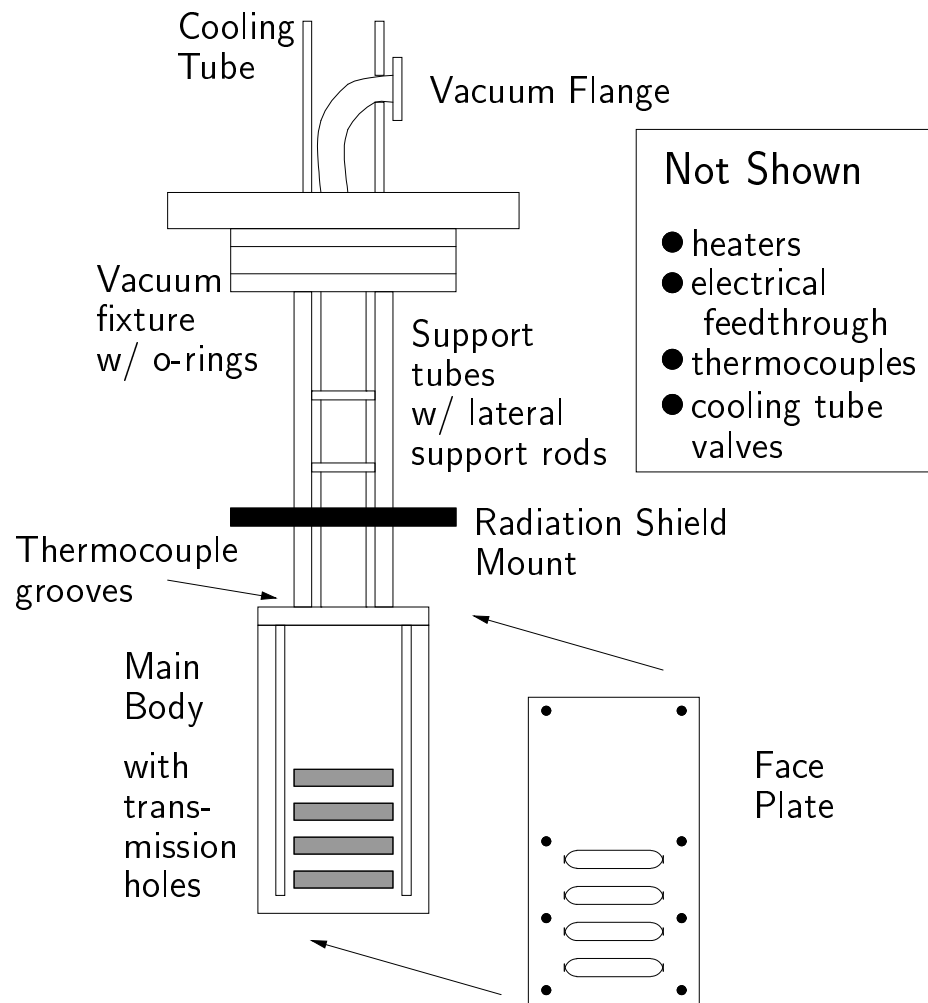


Figure 3.2: Full schematic of the transmission XAFS furnace. This is not drawn to scale in the vertical dimension and several parts are left off for clarity. The arrows from the face plate indicate that it is bolted into place on the main body.

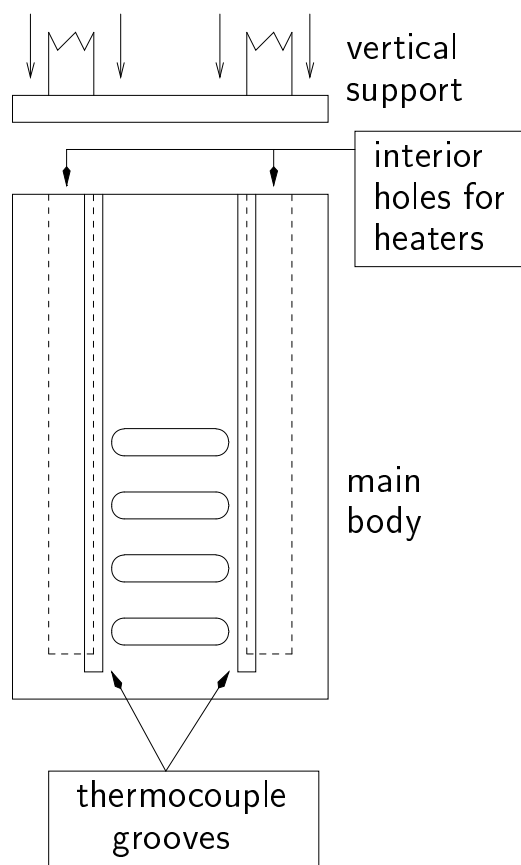


Figure 3.3: Schematic of the main body of the transmission XAFS furnace showing the transmission slots, the thermocouple grooves, and the housings for the Firerod cartridge heaters.

to expedite the cooling of the furnace after operation at high temperature.

The furnace is designed to hang within a vacuum shroud. The fixture that nests into the top of the vacuum shroud with o-rings is of the same dimensions as that used by the Displex, thus the same vacuum shroud may be used for both low and high temperature measurements. Hanging from the vacuum fixture are two stainless steel tubes. These tubes are welded to a stainless block, which is then screwed onto the top of the main body after the heaters are in place, as depicted by the four downward pointing arrows in Fig. 3.3. Stainless tubing is a good choice for this purpose due to its low heat conductivity. The tubes each have a bleed hole and are evacuated during operation.

One face plate presses the copper cooling tube against the back of the furnace for good thermal transfer to the flowing gas. One or more plates are used on the front to press the thermocouples against the furnace and to hold samples in place. The face plates are cut from sterling silver to reduce the emissivity of the furnace. Sheets of graphoil are placed between the silver plates and the main body². The sterling silver remains shiny even in the rough vacuum used in these experiments.

The fixture which nests into the vacuum shroud was designed for ease of use. It includes a four pair electrical feedthrough for the heaters and thermocouples, a quick-connect vacuum flange, and a gas flow system with three easy-to-use Nupro plug valves. The feedthrough and plug valves are not shown in Fig. 3.2.

The furnace is easily broken down into its constituent pieces. The main body is bolted to the support tubes and all of the plumbing fixtures use Swage-lock connections. This is useful for maintenance chores such as replacing broken heaters and it proved useful for recovery from the accident described in footnote 2.

3.2 Sample Preparation

In this section I will discuss the preparation of the samples actually used in this thesis with discussion of why the methods used yielded high quality data.

² The necessity of this was learned the hard way. It turns out the diffusion rate between the copper and silver is quite high at elevated temperature. The melting temperature of eutectic copper-silver with a few percent of nickel (from the sterling silver) thrown in is about 960 K. The first time the furnace was used, a significant portion of the main body and the three cover plates in use melted. The graphoil prevents this diffusion. I now have an interesting molten copper-silver paperweight on my desk.

3.2.1 Powder Samples for Transmission

Thick Samples

Given a source of material of sufficient purity for the intended experiment, there are two major considerations for the preparation of a sample for transmission EXAFS. The sample must be homogeneous and it must be of a form suitable for the experimental conditions. Here I describe the preparation of BaTiO₃ samples for the measurement of the barium *K* edge³.

I started with BaTiO₃ obtained from Aldrich, item #33,884-2. This powder is of 99.9 percent purity and the average particle size of the powder is less than 2 μm. The small size of the particles is an advantage for producing a homogeneous sample. Using tables [70] of x-ray absorption coefficients, I estimated as described in Appendix B.2. that an absorption length, the thickness such that $x\mu \approx 1$ in Eq. (3.5), just above the barium edge in BaTiO₃ is 95 μm. With particles that are much smaller than the absorption length of the sample, it is easy to make a homogeneous sample.

I wanted my sample to be strong enough that I could handle it with my fingers. It also needed to handle thermal cycling between 10 K and as high as 1000 K. To accomplish this, I mixed an appropriate amount of BaTiO₃ with enough fine graphite powder to make a pellet about 500 μm thick when cold pressed in a die of areal dimension 1.5 cm × 0.5 cm. This graphite pellet is strong enough to manipulate by hand and can withstand both high and low temperature. Graphite is a good thermal conductor thus assuring uniformity of temperature at all points in the sample. That graphite is a decent electrical conductor is yet another advantage of this method of sample preparation. The particles of BaTiO₃, and of the other materials studied, carry a surface charge that causes them to agglomerate into clusters that are large compared to the absorption length. By mixing the BaTiO₃ with the graphite carefully and for a long time, the BaTiO₃ becomes dispersed evenly throughout the volume of graphite. The breaking of the weak electrostatic attractions holding the agglomerates together is aided by the conductivity of the graphite. Since the BaTiO₃ powder is light yellow, it is easy to see these agglomerates in contrast to the black of the graphite. As the BaTiO₃ disperses within the graphite and the agglomerates disappear, it becomes increasingly difficult to see the sample within the graphite. I generally continued

³ I prepared samples for the lead *L_{III}* edge of PbTiO₃ using the method described in this section. The results of those measurements are described in Refs. [18] and [19] and were the topic of Noam Sicron's master's thesis at The Hebrew University. I will make reference to that work in Ch. 4, but will not describe it in detail.

mixing for some time after no longer observing the sample by eye.

Thin Samples

For the titanium K edge samples of PbTiO_3 , BaTiO_3 , EuTiO_3 and the europium L_{III} edge samples of EuTiO_3 I had similar sample preparation concerns as those described above. Because these absorption edges are at much lower energy than the barium K edge I was not able to use as much graphite. Around 5 keV one absorption length of graphite is about $240 \mu\text{m}$. Since I did not want to lose too much intensity due to the absorption of the filler material, I chose to make $100 \mu\text{m}$ thick pellets. A pellet this thin is quite fragile and difficult to handle. To address this concern, I developed a method of reinforcing the thin pellet with sheets of Kapton.

Kapton is a commercially available plastic manufactured by DuPont. I obtained a quantity of $8 \mu\text{m}$ thick Kapton sheet. Kapton is a common material for x-ray applications as it has no sulfur or other heavy elements in it. It has a high tensile strength and it decomposes at an extremely high temperature. In one test, I heated a piece of Kapton to $\sim 825 \text{K}$ in atmosphere. It turned from its normal orange color to a dull black, but it retained its shape and much of its tensile strength. Its tensile strength and heat resistance made it an ideal choice for reinforcing my thin samples.

Material for the PbTiO_3 and EuTiO_3 experiments was provided to me by Fatih Dogan of the University of Washington Department of Material Science and Engineering. These were prepared from an aqueous solution of nitrates of titanium and either lead or europium. A molecular mixture of titanium and lead or europium was coprecipitated from the solution by alteration of pH with ammonium. The mixtures were freeze dried then calcined in air for several hours at 750°C . The PbTiO_3 was prepared slightly lead rich to accommodate the high vapor pressure of the lead. The EuTiO_3 was further reduced in a hydrogen atmosphere from its initial $\text{Eu}_2\text{Ti}_2\text{O}_7$ form. Both materials were found to agree with established powder x-ray diffraction patterns for those materials. The particles were checked by optical and electron microscope and were found to have an average size less than $1 \mu\text{m}$.

An absorption length at the low energy edges in these three material is $< 5 \mu\text{m}$. This is not very large with respect to the particle size, so it is critical that the powders be well dispersed within the graphite. I placed an appropriate quantity of the powder mixture between two pieces of the thin Kapton and dry pressed this "sandwich." Upon removal from the die, the edges of the sandwiches tend to fray and some material is lost from the edges, but a large useful region in the middle of

the sample usually remains. By moving the sample relative to the incident x-ray beam and observing the signal in the I_T chamber, a uniform region of the sample can be found. Since the Kapton has sufficient heat resistance, samples prepared in this manner are suitable for high temperature measurements.

3.2.2 Single Crystal Samples for Fluorescence

PbTiO₃

My PbTiO₃ single crystal [74] is an irregularly shaped wafer about 300 μm thick. It was examined under crossed polarizers and at 200x magnification and a mostly single domain region of approximate dimensions 700 μm \times 700 μm was found. The crystal was placed behind a copper mask exposing the single domain region to the 500 μm \times 500 μm beam used in the experiment. The content of 90° domains in the illuminated region was less than 5 percent. As the penetration depth into the sample was several microns, the measurement was dominated by the bulk, and surface effects were negligible.

The single crystal XANES data were taken in the fluorescence geometry. The sample was oriented such that the region around the absorption edge showed no evidence of Bragg peaks, which would give spurious structure to the XANES signals. As the energy of the x-rays and the orientation of the sample change, different peaks diffract into the solid angle subtended by the I_F detector. I monitored each scan to verify that there was no evidence of contamination by Bragg peaks. Whenever Bragg peaks appeared in the data, perhaps due to the thermal expansion of the sample holder, I rotated the sample by a fraction of a degree and repeated the scan. Usually this small adjustment was sufficient to remove Bragg peaks from the XANES region of the data.

The crystallographic \hat{c} axis was parallel to the surface of the crystal facing the beam. I could therefore orient the \hat{c} axis perpendicularly to the x-ray polarization vector $\hat{\epsilon}$, which is transverse to the direction of propagation of the beam. I could not, however, orient the sample with \hat{c} parallel to $\hat{\epsilon}$. Instead we measured the spectrum with the samples in three orientation with three different values of $\alpha = \cos^{-1}(\hat{\epsilon} \cdot \hat{c})$ as depicted in Fig. 3.1. The sample was measured at approximately $\alpha \in \{17^\circ, 30^\circ, 45^\circ\}$. We left the sample in its final position, about 45°, for the high temperature measurements. To extract $\mu_c(E)$, the portion of the signal due to $\hat{\epsilon} \parallel \hat{c}$, the exact value of the final α was required.

Using the measurement of the signal due to $\hat{\epsilon} \parallel \hat{a}$, $\mu_a(E)$, and the three initial

values of α , I extracted a trial function for μ_c from each of the three orientations. I averaged these three trial functions, then used the average μ_c and μ_a as fitting functions to determine the best fit values for the three α 's. I then used these three new values for the α 's to determine a new trial μ_c . I iterated this process until both the trial function and the values of α stopped changing. In this way I determined that $\alpha = 50.6(6)^\circ$ for all of the high temperature measurements. Given this value of α , I extracted μ_c from each of the high temperature data sets by

$$\mu_c(E) = \frac{\mu_\alpha(E) - \mu_a(E) \sin^2(\alpha)}{\cos^2(\alpha)} \quad (3.10)$$

To test the success of this method, I compare the polycrystalline PbTiO_3 data at three temperatures to the weighted sum $\frac{1}{3}(\mu_c + 2\mu_a)$ in Fig. 3.4. The agreement is quite good. The small differences in area indicate a source of systematic uncertainty in the analysis of the single crystal data in Sec. 7.4.4.

As the sample heated up and the sample holder equilibrated at each temperature, Bragg peaks occasionally wandered into the edge region of the data. The sorts of adjustments necessary to remove them were about the same size as the uncertainty in α .

BaTiO₃

From a large single crystal [75] a piece of dimensions 4 mm \times 2 mm \times 1.5 mm was cut [76]. This piece was etched [77] in phosphoric acid at 160° C for about an hour to release surface strain, and one of the 4 mm \times 2 mm faces was polished using fine aluminum oxide grit. The crystal was poled under a 1 kV/cm electric field, thus producing a large single crystal with a surface mostly free of 90° domains. By examining the BaTiO_3 sample under crossed polarizers and at 200x magnification, we found that the polished surface and the bulk of the crystal were a single domain. To assure that the surface of the crystal maintained the same polarization as the bulk, the sample was kept under a 600 V/cm electric field during both storage and data collection. The polished surface was used for data collection. This additional care in sample preparation over that observed for the PbTiO_3 sample seemed warranted due to the softness of the BaTiO_3 domain structure. Any small inconsistencies of the preparation method should manifest at the surface. Since the penetration depth of the x-rays at the titanium K edge energy 4966 eV is several microns, the XANES measurement is dominated by the bulk and any small 90° or 180° domains remaining

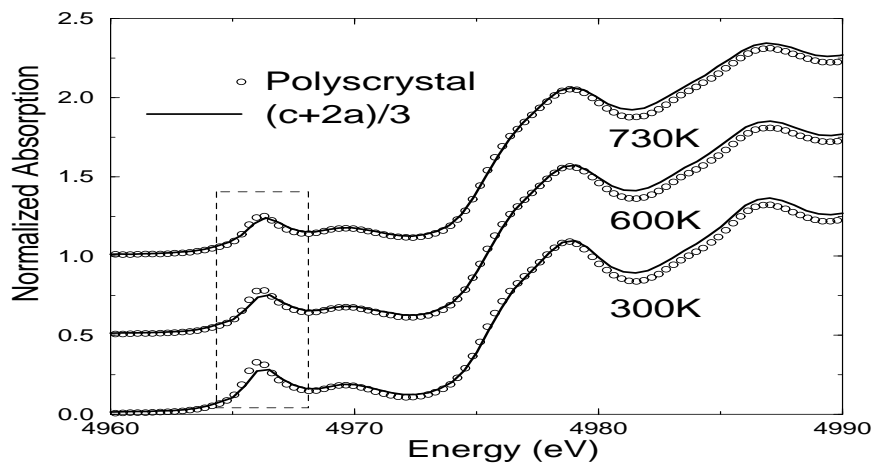


Figure 3.4: Comparison of the polycrystalline and PbTiO_3 data and the weighted sum of the single crystal data in the XANES region. The single crystal data is the sum of $\frac{1}{3}\mu_c$ and $\frac{2}{3}\mu_a$. The single crystal data was actually obtained at 300, 568, and 707 K as described in Sec. 7.4.4. The close agreement of the spectra shows the success of the method of separating μ_c from μ_a . The peak in the dashed box is the subject of Ch. 7.

on the surface would have negligible impact on the measurement.

We did not have the temperature apparatus available to control the direction of poling at other than room temperature, so no temperature dependent XANES on single crystal BaTiO₃ is presented in this thesis. Since the sample was not inside of the furnace or the Displex, it was a simple matter to align it by eye to $\alpha = 45(3)^\circ$. The spectra with $\hat{\epsilon}$ parallel to the aa plane were measured directly. The spectra for $\hat{\epsilon} \parallel \hat{c}$ were found by using Eq. (3.10).

Chapter 4

EXAFS MEASUREMENTS ON PbTiO_3

In light of the findings that BaTiO_3 and KNbO_3 are very much more complicated in their dynamic behavior than was envisaged in the original concept of the displacement ferroelectric, it is particularly interesting to discover that the ferroelectric perovskite PbTiO_3 behaves more closely in the expected manner. In fact it appears to be a textbook example of a displacive ferroelectric transition.

M.E. Lines and A.M. Glass
in Ref. [78], p. 248

4.1 *The Phase Transition of PbTiO_3*

The recent discovery of order–disorder behavior in several oxide perovskites which were thought to be of the displacive type, including $\text{KTa}_{0.91}\text{Nb}_{0.09}\text{O}_3$ [13–15], NaTaO_3 [16], $\text{Na}_{0.82}\text{K}_{0.18}\text{TaO}_3$ [16] and PbZrO_3 [17], motivated the investigation of the local structure of PbTiO_3 , the *textbook* example of a displacive ferroelectric. In this chapter I present EXAFS measurements which demonstrate that PbTiO_3 also has an essential order–disorder component in its ferroelectric to paraelectric transition. Detailed understanding of the material is important not only because it is a well studied example of a ferroelectric, but also because of its considerable practical interest. It is the end member of solid solutions with PbZrO_3 , BaTiO_3 , SrTiO_3 , and others having applications as electrochemical transducers, electromechanical transducers, dielectric devices, and pyroelectric devices.

In its low temperature phase. PbTiO_3 is of tetragonal symmetry and is ferroelectric. At 763 K it undergoes a transition to a cubic and paraelectric state. PbTiO_3 has the soft mode [2] and large dielectric coefficient [6] characteristic of a displacive ferroelectric. Its crystallographic structure shows a clear transition [3, 79–81] from tetragonal to cubic symmetry at 763 K which is weakly first order. The temperature dependence of its Raman spectrum [82] shows the transition from tetragonal to cubic symmetry. This soft mode has been investigated as a function of temperature

[2, 82] and pressure [83]. The soft mode frequency is underdamped and decreases as the transition temperature is approached from above. This soft mode frequency, however, never reaches 0, instead it saturates at 55 cm^{-1} [82].

Table 4.1: The structures of the phases of PbTiO_3 and their transition temperatures. The data in this table is from Ref. [84].

tetragonal (P 4 m m)	\implies 763 K	cubic (P m 3 m)
-------------------------	---------------------	--------------------

In recent years considerable evidence has appeared pointing to the possibility of an order–disorder component to the structure of PbTiO_3 through its phase transition. Near the transition temperature, a large central peak is observed in the Raman spectrum [85, 86]. Its presence, along with a soft mode frequency that does not vanish at the phase transition, is evidence of a disordering process on both sides of the phase transition. The same authors point out that the dielectric constant is larger than that predicted by the Lydane–Sachs–Teller relation for a displacive transition, indicating the presence of a further mechanism in the phase transition. Over the years a variety of techniques have shown further evidence for order–disorder behavior in PbTiO_3 , including refractive index measurements [87], Perturbed Angular Correlation Spectroscopy [88, 89], and single–crystal neutron diffraction [90]. In the neutron diffraction study, the authors fit their diffraction data with a model allowing for disordering of the lead atoms among six sites displaced along the Cartesian directions from the average lead position. However the authors state that their measurement “indicates the possibility of Ti also being disordered above T_c ” but that “multi–site disorder cannot be completely distinguished from thermal anharmonicity” in their measurements.

EXAFS is an ideal tool for investigating the phase transition in PbTiO_3 . EXAFS possesses considerably higher spatial resolution [91] than diffraction in measurements of local structure. By examining the local structure of PbTiO_3 with EXAFS, I can examine the local structure through the phase transition for the possibility of order–disorder behavior.

Investigation of the temperature dependence of the local structure in PbTiO_3 seems particularly important in light of recent attempts [92–95] to compute its structure and phase transitions from first principles. Such work requires detailed knowl-

edge of the true ground state structure of a material as well as its local structure in all of its crystallographic phases.

One recent measurement [96] of the lattice parameters using x-ray and optical techniques suggested the presence of tetragonal to orthorhombic transition at about 183 K with an $\frac{a}{b}$ ratio of less than 1.0002. Subsequent attempts to reproduce this result have met with mixed success and there remains some debate in the literature about the validity of this third structural phase. The size of the splitting reported in that study is quite small and is below the resolution of EXAFS. One of the long standing puzzles about PbTiO_3 and BaTiO_3 is why BaTiO_3 undergoes changes of symmetry with raising temperature from rhombohedral to orthorhombic to tetragonal to cubic, while PbTiO_3 only undergoes the tetragonal to cubic change of symmetry. In this chapter and in Ch. 5, I will show that the reason is due to different local distortions in the two materials. BaTiO_3 possesses a rhombohedral local distortion while PbTiO_3 possesses a tetragonal local distortion. The possibility of a low temperature orthorhombic phase may indicate the presence of an eight site disordering mechanism in PbTiO_3 . The XANES measurements presented and discussed in Sec. 7.3 preclude the possibility of a rhombohedral local distortion in PbTiO_3 , thus I will not consider this possibility in the EXAFS analysis presented here.

I wish to make one final note about the literature on the crystal structure of PbTiO_3 . In the paper by Kuprianov et al. [97], the authors observe a stronger temperature dependence of the titanium displacement, δ_{Ti} in Table 4.4, then do the authors of Refs. [3, 84, 90]. Kuprianov et al. fix the values of δ_{O_1} and δ_{O_2} to be the same in their refinements. Because of this artificial constraint in their refinement, I choose not to use their results for comparison to my EXAFS results.

4.2 PbTiO_3 EXAFS Measurements

I prepared samples for titanium K edge measurements in the manner described in Sec. 3.2. Data were collected in transmission at 300, 450, 600, 700, 730, and 800 K. Because of severe electrical problems with the furnace used at that experimental run at NSLS, only one data point in the cubic phase was collected.¹ For two publications [18, 19] on PbTiO_3 , data taken in fluorescence on a sintered pellet of PbTiO_3 was analyzed. For those papers, I only analyzed the first shell signal. In this chapter I present a more complete analysis of the data including multiple scattering paths

¹ It was the experience on this run that motivated designing the furnace described in Sec. 3.1.5.

out to the fourth shell at low temperatures and the third shell at elevated temperatures. I use the fluorescence data at 10, 300², 790, 850, and 900 K to supplement the temperature points obtained in transmission. Although the two data sets show excellent systematic agreement for fitting parameters affecting the phase in the EXAFS equation Eq. (2.10), including those effecting bond lengths, there is considerable distortion to the amplitudes of the fluorescence data. The effect of this distortion on my measurements will be discussed below. Still, consideration of the fluorescence data allows me to study the temperature dependence of the local structure in a broad temperature range between 10 K and 900 K. An example spectrum at 300 K is shown in Fig. 4.1.

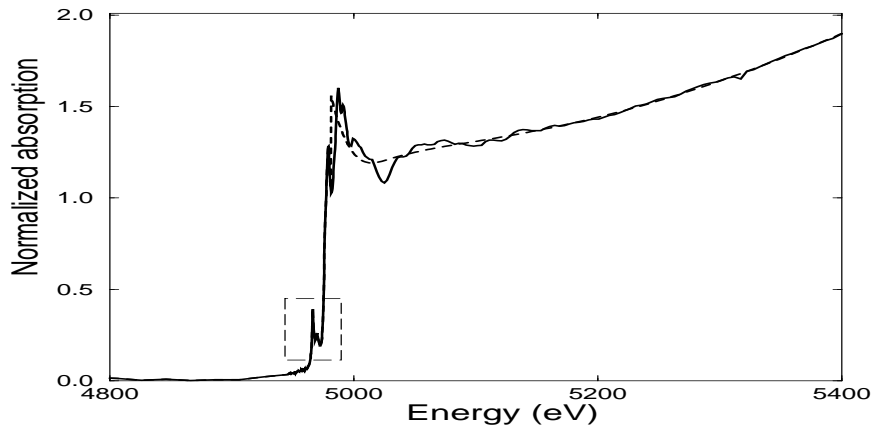


Figure 4.1: Titanium K edge absorption spectrum in PbTiO_3 (solid line) and the background function found by AUTOBK [54] (dashed line). The region in the box is the near edge feature discussed in Ch. 7.

Background subtractions were performed with AUTOBK using the technique described in Sec. 2.2. The isolated $\chi(k)$ are shown in Fig. 4.2 at various temperatures. The background removal parameters used in AUTOBK to produce the $\chi(k)$ spectra are given in Table 4.2.

To test the order-disorder model with these data, I created theoretical fitting standards using FEFF6 and the tetragonal crystal structure [3] of PbTiO_3 at 300 K.

² In Figs. 4.6 – 4.9, the fluorescence result at 300 K is plotted at 290 K for clarity.

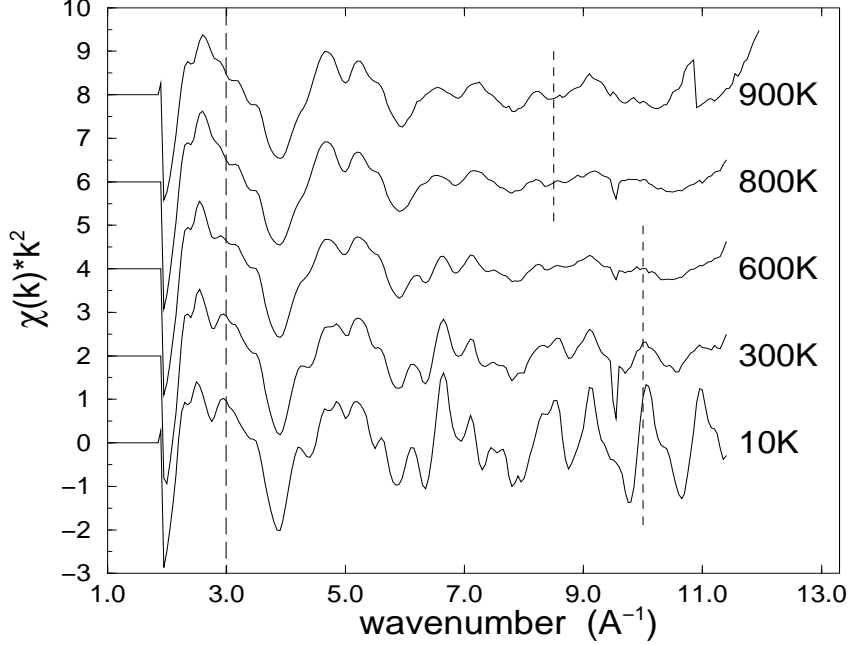


Figure 4.2: The $\chi(k)$ spectra for PbTiO_3 at several temperatures. The phase transition is at 763 K. The data are the average of two or three scans taken at each temperature and were weighted by k^2 . The dashed lines indicate the boundaries of the data range used in the Fourier transforms for the fits. The glitch at about 9.3 \AA^{-1} in some data sets was simply ignored as it is narrow and contributed systematic noise only at high frequency.

Table 4.2: Background removal parameters used in AUTOBK for the PbTiO_3 data. The value of E_0 was fixed in each of the background removals. This is the energy of the peak inside the dashed box in Fig. 4.1. $[0 \rightarrow R_{bkg}]$ is the region over which the non-structural Fourier components are optimized in the background removal. $[R_{bkg} \rightarrow R_{1st}]$ is the data range over which the theory is scaled in the optimization. The default values in AUTOBK for the k -weight (1) and Hanning window sill widths (0) were used.

edge	E_0	k_{min}	k_{max}	R_{bkg}	R_{1st}
Ti K	4966.0	2	end of data	1	2

The contributions from these paths as calculated by FEFF6 were varied according to Eq. (2.10). The values for N were set as indicated by the rhombohedral local symmetry as shown in Table 4.3. To determine the path lengths R of Eq. (2.10), I used the five structure parameters shown in Table 4.4 as possible fitting variables and from these determined R for each path. This fitting model is sufficiently robust to test the differences between the tetragonal and cubic local structures. If δ_{Ti} , δ_{O_1} , and δ_{O_2} relax to zero and the axis lengths become equal then the cubic local structure is obtained. The remaining fitting parameters considered were σ^2 for each of the single scattering (SS) paths, phase corrections parameterized as E_0 variations for each species of backscattering atom, and an amplitude correction for the titanium backscatterers. To reduce the number of fitting parameters, I used the values for the Einstein temperatures of the short and long titanium–lead bonds found in Ref. [18]. These are 227(20) K and 204(20) K respectively. The parameters for all multiple scattering (MS) paths considered in the fits were determined from this set of fitting variables without introducing new parameters. The fitting ranges, information content, and statistical parameters of these fits are shown in Table 4.5. The range in R space included SS and MS paths out to the fourth coordination shell for the lower temperatures and the third shell at higher temperatures. At the distance of the third shell titanium atoms are several double and triple scattering paths which contribute strongly to the EXAFS and which involve the first shell oxygens and the third shell titanium atoms. These were the only MS paths considered in the fits. The σ^2 's for these MS paths were set as described in Sec. A.1.1.

Table 4.3: Multiplicities and lengths of the various near neighbor bond lengths in PbTiO_3 for the local symmetries of the tetragonal and cubic phases as predicted by the displacive model. In the order–disorder model the tetragonal local structure persists in all phases. All distances are in Ångstroms and were determined from the crystallographic data in Ref. [84] at 300 K and 765 K.

local symmetry	Ti–O	Ti–Pb	Ti–Ti
tetragonal	1×1.767	4×3.361	4×3.902
	4×1.980	4×3.556	2×4.156
	1×2.389		
cubic	6×1.985	8×3.438	6×3.970

Table 4.4: Structural fitting parameters used in the fits to the titanium K edge data using the tetragonal local structure. The initial values [3] are for the 300 K crystal structure. The length of the c axis was determined from the length of a by forcing the volume of the unit cell to remain constant. The value of δ_{O_2} was fixed as indicated in the text.

param.		description	initial value
a	measured	the a and b lattice constant	3.905 Å
c	set	the c lattice constant	4.156 Å
δ_{Ti}	measured	the tetragonal displacement of the titanium atom	0.0390
δ_{O_1}	measured	the tetragonal displacement of the axial oxygen atom	0.1138
δ_{O_2}	set	the tetragonal displacement of the planar oxygen atom	0.1169

The structural parameters shown in Table 4.4 were used as fitting parameters in my analysis using FEFFIT. I used the symmetries of the tetragonal structure to compute path lengths for use in Eq. (2.10). The input files for FEFFIT that I used to relate the structural parameters to the path lengths were quite complicated and are discussed in detail in Sec. A.1. The significant contributions from MS paths overlapped the titanium third shell SS paths. Due to the tetragonal distortions, the MS paths through the planar oxygen atoms deviate from collinearity by 9.41° in the low temperature crystallographic structure. The effect of changing this angle was included in the fits by the method described in Sec. A.1.2.

Fits to the data at several temperatures using the tetragonal model are shown in Figs. 4.3 – 4.5. This fitting model gave good agreement to the data throughout the temperature range with physically consistent results for the fitting parameters.

I show in Ch. 6 from my analysis of EuTiO_3 , a structurally simple material, that $S_0^2 = 0.95(0.15)$ for the titanium K edge. S_0^2 is a chemically transferable quantity, thus I used this value in my fits to the PbTiO_3 data. This is somewhat larger than the value I found fitting only the first shell of the fluorescence PbTiO_3 data in Refs. [18] and [19].

The temperature dependence of the unit cell lengths as measured by x-ray diffrac-

Table 4.5: Fourier transform ranges (Δk), fitting ranges (ΔR), number of independent points (N_I), the number of parameters used in the fits (P), number of degrees of freedom (ν), the measurement uncertainty in R -space ($\bar{\sigma}_r$), reduced chi-square (χ_ν^2), and \mathcal{R} -factor (fractional misfit) for the fits to the rhombohedral structure for BaTiO₃. The 8 free variables in these fits were δ_a , δ_{O_1} , δ_{Ti} , σ^2 for the titanium–oxygen, titanium–titanium, and titanium–4th shell oxygen paths, and an E_0 for the oxygen and titanium backscatterers. The other E_0 's was set as described in the text. $\chi(k)$ was weighted by k^2 for all Fourier transforms. The measurement uncertainty is obtained by FEFFIT as described in Sec. 2.3. The large value of σ at 450 K accounts for the small χ_ν^2 but large \mathcal{R} -factor at that temperature.

temp.	Δk	ΔR	N_I	P	ν	$\bar{\sigma}_r$	χ_ν^2	\mathcal{R}
10 K	[3,10]	[1.1,4.2]	15.7	8	7.7	0.0088	42.9	0.0043
290 K	[3,10]	[1.1,4.2]	15.7	8	7.7	0.0078	71.7	0.0127
300 K	[3,10]	[1.1,4.2]	15.7	8	7.7	0.0247	5.0	0.0073
450 K	[3,10]	[1.1,4.2]	15.7	8	7.7	0.0439	5.0	0.0222
600 K	[3,10]	[1.1,4.2]	15.7	8	7.7	0.0120	9.0	0.0042
700 K	[3,8.5]	[1.1,4.2]	12.7	8	4.7	0.0029	154.9	0.0038
730 K	[3,8.5]	[1.1,4.2]	12.7	8	4.7	0.0029	170.5	0.0041
790 K	[3,8.5]	[1.1,4.2]	12.7	8	4.7	0.0056	158.1	0.0235
800 K	[3,8.5]	[1.1,4.2]	12.7	8	4.7	0.0034	163.0	0.0071
850 K	[3,8.5]	[1.1,4.2]	12.7	8	4.7	0.0037	121.3	0.0055
900 K	[3,8.5]	[1.1,4.2]	12.7	8	4.7	0.0042	132.3	0.0048

tion is shown in Fig. 4.6. The central line in the figure is the cube root of the volume of the unit cell. Within about 0.5 percent, the volume of the unit cell does not change within the ferroelectric phase, while it apparently has a discontinuity at the phase transition. The size of this variation on the axis lengths is near the limit of my ability to resolve changes in bond length. I can thus reduce the number of parameters in my fits by one by taking the volume of the unit cell to be a constant. Thus I allow the length of the a axis to change and determine the length of the c axis from that and the constant volume, taken to be 63.375 \AA^3 from the values of a and c used in the FEFF calculation. How this is done in FEFFIT is shown in Fig. A.2. This introduces an error in the determination of the phase of the same order as the level of uncertainty reported by FEFFIT in determining the bond and axis lengths and is much smaller than the differences between the tetragonal and cubic local structures.

As indicated in Table 4.4, the value of δ_{O_2} was fixed in the fits presented here. In an initial round of fits, I allowed this parameter to vary. In those fits the temperature dependence was such that the values of δ_{O_2} and δ_{Ti} became close in value at elevated temperature. From this result I concluded that the titanium atom relaxed into the plane of the O_2 oxygen atoms above the crystallographic phase transition. I then used the structural parameters obtained by these fits in which δ_{O_2} was allowed to vary as the input to a calculation of the XANES spectrum at 900 K using the computer program discussed in Chs. 8 and 9. As I show in detail in Sec. 7.4, the calculation using this structure was unsatisfactory. The XANES data clearly show that the titanium atom does not reside in the plane of the O_2 atoms even at the highest temperatures. To place the constraint on my EXAFS fits that the titanium atom should not reside in the O_2 plane, I fixed δ_{O_2} to its low temperature value. The values for χ^2_D obtained in the presence of this constraint are consistently smaller than those from the fits in which δ_{O_2} was allowed to vary. Furthermore, as shown in Sec. 7.4, the results of the XANES calculation were more consistent with the measured spectrum at 900 K.

As mentioned above, the σ^2 's of the two titanium–lead bonds were determined from the Einstein temperatures reported in Ref. [18]. The other oxygen and titanium bond lengths were each assigned σ^2 's which were varied in the fits. Each backscatterer was also assigned a phase correction in the form of an E_0 . These six parameters as well as the three structural parameters indicated as “measured” in Table 4.4 were the fitting parameters considered in the problem. An amplitude correction to the titanium backscatterer was not necessary in this case.

The E_0 corrections are non–structural fitting parameters which are required to correct for inaccuracies in the FEFF calculation. Due to the approximations used by

FEFF, particularly the use of neutral atomic spheres in the overlapped potential and the use of spherically symmetric scattering potentials, significant error in amplitude and phase of the fitting standards may be introduced. These errors will be particularly large for materials with large anisotropy or with significant transfer of charge between atoms. PbTiO_3 is an example both of an anisotropic material and of a material with significant charge transfer. As shown in Ref. [98], corrections of this sort are essential for accurately measuring the temperature dependence of structural parameters in materials effected by anisotropy and/or charge transfer.

Taken together this set of nine fitting variables was rather ill-constrained. When all the fitting parameters were allowed to float, there was large scatter in the E_0 values for lead and titanium and the difference between the oxygen and lead E_0 's is unphysically large. Assuming that, for the titanium E_0 , this was scatter around the value needed to correctly account for the errors introduced into the FEFF calculation, I used the mean of the measured values as shown in Table 4.6. The large standard deviations are due mostly to one or two outliers. Fixing this parameter yielded physically consistent results for the structural parameters. Of course, fixing these parameters in any way introduces a source of systematic error into the fits. Most of the uncertainty in the structural fitting parameters is due to their correlation with the phase corrections. By changing the set values of the phase corrections for the lead and titanium backscatterers by several volts, I can systematically raise or lower the values of the structural parameters in the fit within their error bars. Since fixing these phase corrections to slightly different values does not qualitatively change the results and changes them quantitatively only within their error bars, I feel justified in setting them to the values shown in Table 4.6.

Table 4.6: E_0 corrections in the PbTiO_3 fits. The values are the averages of the best fit values for these two parameters at each temperature and the uncertainties are the standard deviations. E_0 for the oxygen backscatterers was a variable parameter in the fit. Note that the scatter in the titanium and lead E_0 's is quite large.

Oxygen	Lead	Titanium
10.1(1.0) eV	-14.5(6.0) eV	7.4(4.1) eV

In Ref. [98], a simple argument is used to relate a relative shift in E_0 of 5 eV to the transfer of one full electron between two atoms. The results shown in Table 4.6

suggest the transfer of about 4 electrons from the titanium to the lead atoms. While PbTiO_3 is known to be highly polarizable and that there must be significant overlap of lead $6s$ electrons with titanium $3d$ electrons [92], the transfer of 4 electrons is unreasonable. Thus I hesitate to ascribe physical meaning to these large values of E_0 . However, I needed this correction to obtain good fits and reasonable temperature behavior for the structural parameters.

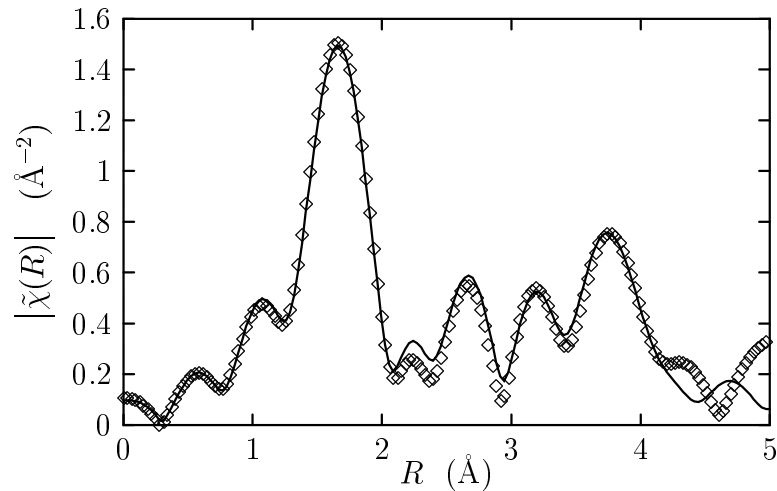


Figure 4.3: Fit to the Ti K edge data in PbTiO_3 at 10 K. The magnitude of the complex Fourier transform of $\chi(k)$ is shown. The diamonds (\diamond) are the data and the line is the fit.

The results for the three structural fitting parameters are shown in Table 4.7. The a axis increases somewhat with temperature. The displacement of the titanium atom δ_{Ti} is essentially constant with temperature. The displacement of the axial oxygen δ_{O_1} decreases with temperature.

The effects of these parameters are shown in the temperature dependence of various structural features of PbTiO_3 in Figs. 4.6 – 4.9. In all these figures, the significant differences between the local structure measured by EXAFS and the average structure measured by diffraction are evident. There is a displacive component to the temperature behavior of the local structure. Near the phase transition temperature, an order–disorder mechanism begins to dominate the local structure as the split in the lengths of cell axes persists into the high temperature phase.

Fig. 4.6 shows the temperature dependence of the unit cell axes. In the tetragonal

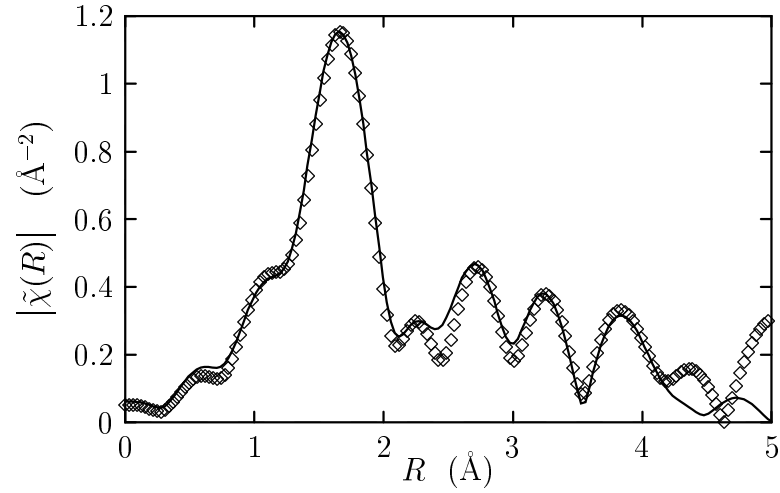


Figure 4.4: Fit to the Ti K edge data in PbTiO_3 at 300 K. The magnitude of the complex Fourier transform of $\chi(k)$ is shown. The diamonds (\diamond) are the data and the line is the fit.

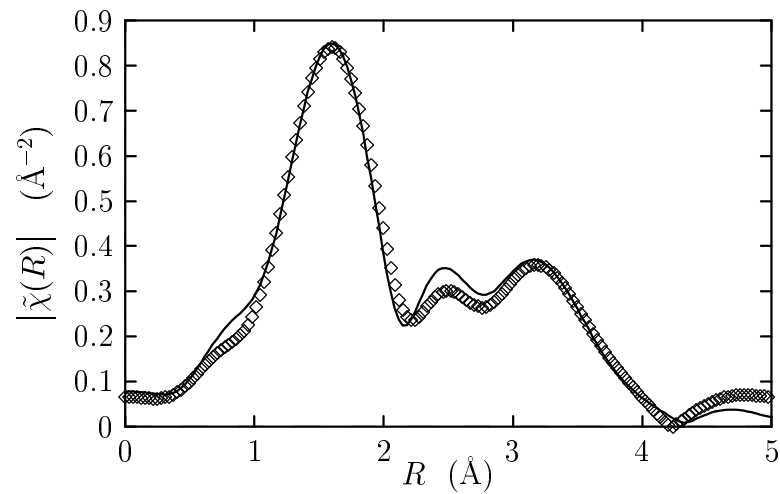


Figure 4.5: Fit to the Ti K edge data in PbTiO_3 at 850 K. The magnitude of the complex Fourier transform of $\chi(k)$ is shown. The diamonds (\diamond) are the data and the line is the fit.

phase, the measurement of the local axis lengths show less temperature dependence than the diffraction measurement and no discontinuity at T_c . This shows that the tetragonal distortion in the local structure persists into the high temperature phase. This can be explained by an order–disorder mechanism. As T_c is approached from below, the direction of the tetragonal distortion begins to disorder. At T_c , long range correlations are lost. Below T_c some number of the local distortions are rotated by 90° , resulting in average unit cell axes which are shorter than those of the local structure. In the high temperature phase the local distortions are fully disordered and the average structure is cubic.

Not only does the tetragonal local distortion persist into the high temperature phase, so do the distortions of the oxygen octahedron. As shown in Table 4.7 each of δ_{Ti} and δ_{O_1} persist into the high temperature phase outside of their uncertainties. The result is that the split in titanium–oxygen and titanium–lead bond lengths also persist into that phase. These splittings are shown in Figs. 4.7 and 4.8.

The displacement of the titanium atom from the midpoint of the axial oxygens is shown in Fig. 4.9. This distortion parameter is computed by

$$d = \frac{r_{long} - r_{short}}{2} \quad (4.1)$$

where r_{long} and r_{short} are the long and short bonds in Fig. 4.7. d is affected by the temperature dependence of both δ_{O_1} and δ_a . d will be used in the interpretation of the PbTiO_3 XANES data in Ch. 7.

This interpretation of the data is consistent with the previous results on PbTiO_3 [18, 19]. Values of structural parameters common between this analysis and the analysis of the lead edge, such as the titanium–lead bond lengths as shown in Fig. 4.8, are consistent within their uncertainties.

As I stated previously, the fluorescence data that I used to supplement the data taken in transmission was distorted in amplitude. The distortion is odd. Using the same S_0^2 as for the transmission data and a self–absorption correction of 1.087 obtained as described in Sec. B.2.4, I obtain values for σ^2 for the titanium–oxygen and titanium–titanium bonds that are systematically too small. By fitting an Einstein temperature to the σ^2 's of these two bonds using only the transmission data, I obtain 582(20) K for the titanium–oxygen bond and 285(5) K for the titanium–titanium bond. For the fluorescence data I obtain values of σ^2 which are consistently $3\text{--}5 \times 10^{-3} \text{ \AA}^2$ smaller than those calculated from the Einstein temperatures. I conclude that I am incorrectly estimating the self–absorption correction or that there is some

other source of systematic error in the fluorescence data. That the measurements of terms affecting the phase (i.e. δR and E_0 terms) in the fluorescence data are consistent with similar measurements at similar temperatures in the transmission data suggests that the distortion to the data is restricted to the amplitude and that I may trust the fluorescence data points in Figs. 4.6 – 4.9 as those figures plot quantities which depend upon the phase of the data.

Table 4.7: Temperature dependence of the structural fitting parameters in the PbTiO_3 fits using the tetragonal local structure.

temp.	δ_a	δ_{O_1}	δ_{Ti}
initial	0.0	0.1138	0.0390
10	0.003(3)	0.130(3)	0.046(1)
300	0.009(3)	0.134(5)	0.052(3)
450	0.013(6)	0.132(12)	0.056(8)
600	0.016(3)	0.134(5)	0.054(4)
700	0.020(8)	0.118(9)	0.052(7)
730	0.022(9)	0.116(10)	0.051(8)
790	0.021(14)	0.110(19)	0.042(14)
800	0.026(10)	0.120(15)	0.054(13)
850	0.029(8)	0.115(11)	0.046(9)
900	0.028(9)	0.108(12)	0.046(11)

The success of the tetragonal fitting model at all temperatures is compelling evidence that PbTiO_3 behaves according to an order–disorder model. To confirm that the cubic local structure is inconsistent with the data above T_c , I use the method described in Sec. A.3 to model the cubic local structure. I fit the 800 K transmission data and 790, 850, and 900 K fluorescence data using $S_0^2 = 0.9$ and allowed eight variables in the fits. These were a lattice expansion coefficient, an E_0 shift for each of three atom types, and σ^2 for each of the first four coordination shells.

Fixing the lattice constant to 3.974 Å, the value given by the crystallography [90], yields the fit shown in Fig. 4.10 for the 850 K data. This is a significantly worse fit. The first shell is substantially broader and $\chi_\nu^2 = 511.6$ which is considerably larger than the χ_ν^2 reported in Table 4.5 for the tetragonal local structure at that temperature. Also the value of σ^2 for the titanium–oxygen bond is 0.061(36) Å² at 850 K as compared to the value of 0.011 Å² obtained at that temperature from the

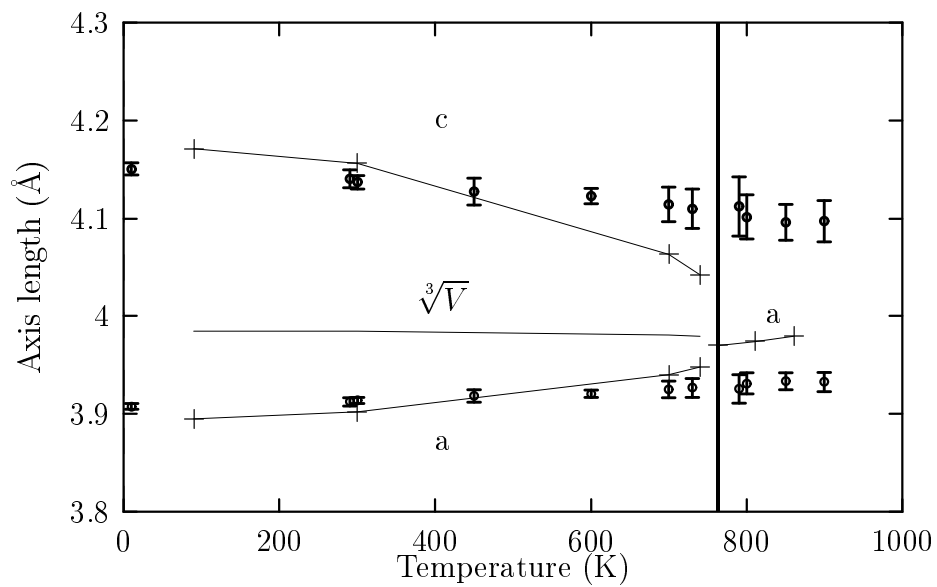


Figure 4.6: Axis lengths for PbTiO_3 as measured by x-ray diffraction (+) [90] and by EXAFS (\circ). The lowest temperature diffraction data point is taken from Ref. [3]. The middle line is the cube root of the volume as measured by the diffraction data. The line in the diffraction data is a guide to the eye. The vertical line indicates the transition temperature 763 K.

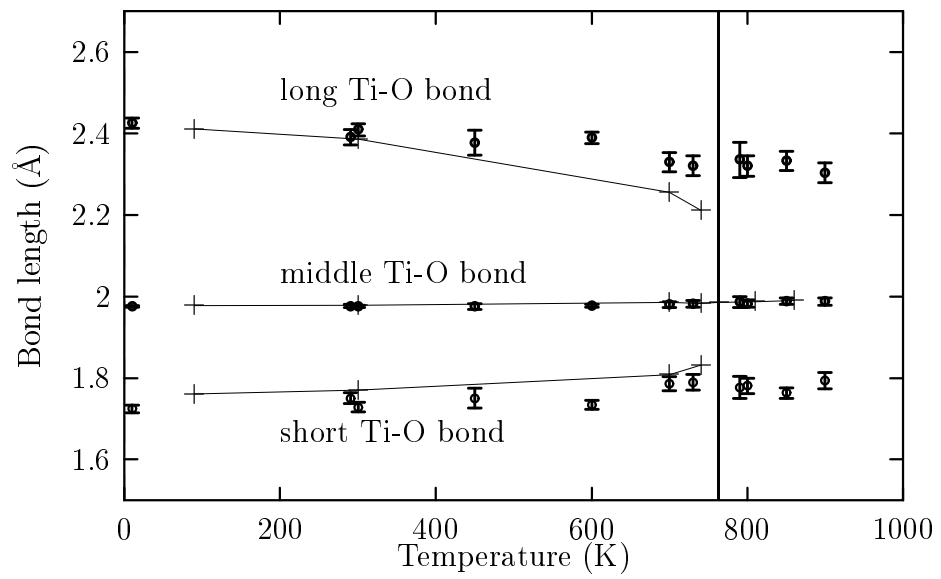


Figure 4.7: Titanium–oxygen bond lengths for PbTiO_3 as measured by x–ray diffraction (+) [90] and by EXAFS (o). The lowest temperature diffraction data point is taken from Ref. [3]. The line in the diffraction data is a guide to the eye. The vertical line indicates the transition temperature 763 K.

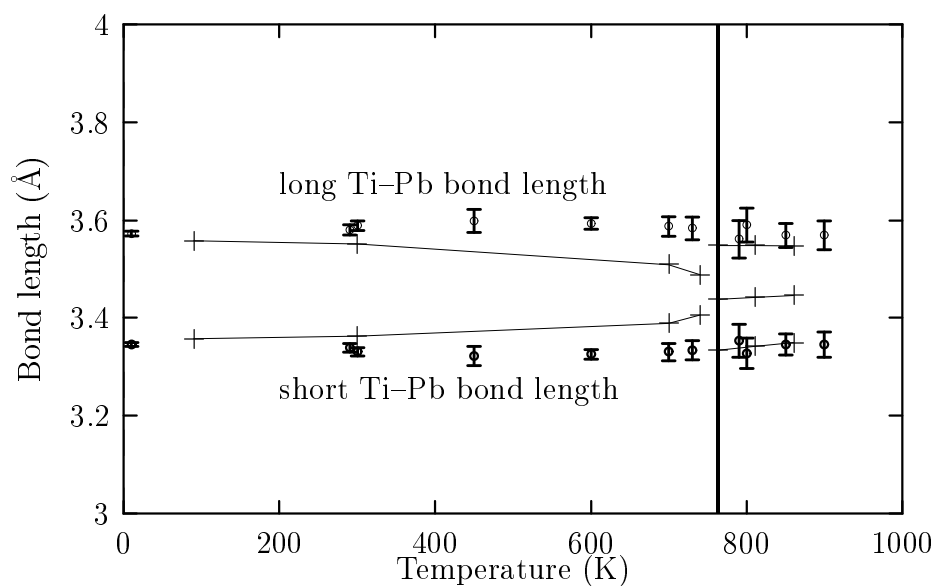


Figure 4.8: Titanium–lead bond lengths for PbTiO_3 as measured by x–ray diffraction (+) [90] and by EXAFS (\circ). The lowest temperature diffraction data point is taken from Ref. [3]. The line in the diffraction data is a guide to the eye. The additional lines in the cubic phase are the largest and smallest possible titanium–lead bond lengths given the lead distortion used in the fitting model in Ref. [90]. The vertical line indicates the transition temperature 763 K.

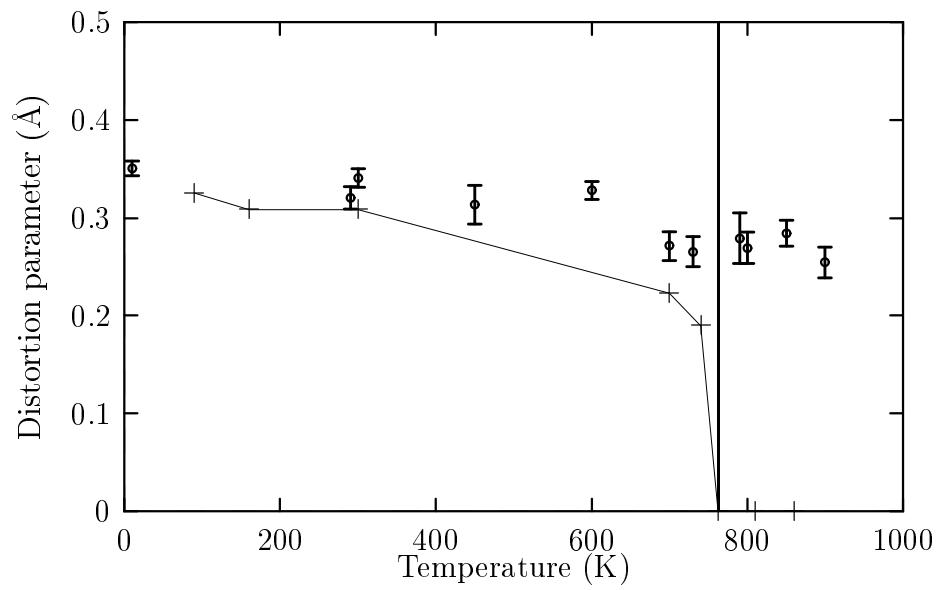


Figure 4.9: Distortion parameter d from Eq. (4.1) in PbTiO_3 as measured by x-ray diffraction (+) [90] and by EXAFS (o). The lowest temperature diffraction data point is taken from Ref. [3]. The line in the diffraction data is a guide to the eye. The vertical line indicates the transition temperature 763 K.

measured einstein temperature using the tetragonal model. This enhanced value is needed in the cubic model fit to compensate for the lack of structural disorder introduced by the cubic fitting model. Using the formulas of Ref. [51] to compute the structural contribution to the titanium–oxygen σ^2 using the low temperature crystallographic structure yields a value of 0.029 \AA^2 . This sharp rise in σ^2 using the cubic fitting model is further evidence that the cubic model is inadequate.

Allowing the lattice expansion coefficient to vary in the cubic model fits improves the fits but gives a best–fit lattice constant $3.922(41) \text{ \AA}$ which is too small compared to diffraction measurements[90]. Thus I am forced to reject the possibility of a transition into a phase of local cubic symmetry. I conclude that the local structure in PbTiO_3 is dominated by an order–disorder mechanism.

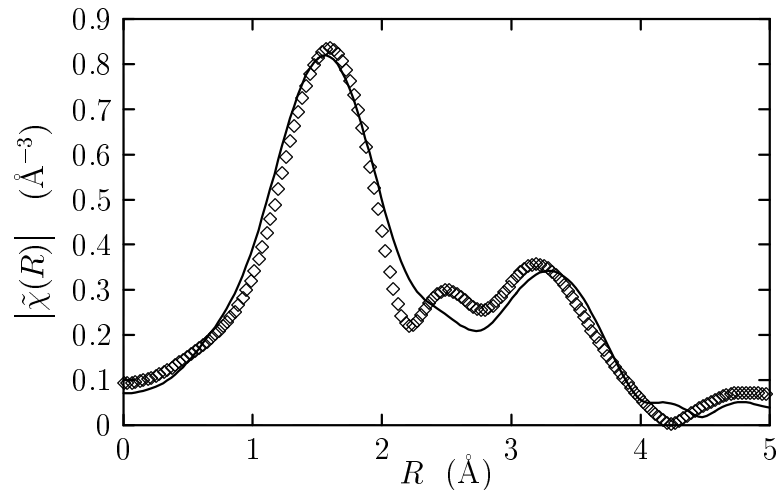


Figure 4.10: Fit to the Ti K edge data in PbTiO_3 at 850 K using the cubic fitting model. The magnitude of the complex Fourier transform of $\chi(k)$ is shown. The diamonds (\diamond) are the data and the line is the fit. Note the broadening of the first peak due to neglecting the structural disorder.

Chapter 5

EXAFS MEASUREMENTS ON BaTiO_3

In Ch. 4 I showed that the local distortion of the titanium atom in PbTiO_3 is in a tetragonal direction and that this distortion persists into the cubic phase. From this local structural information, I determined that the mechanism of the tetragonal to cubic phase transition has both order–disorder and displacive components. I now turn to a second ferroelectric perovskite, BaTiO_3 .

5.1 The Phase Transitions of BaTiO_3

Because BaTiO_3 has a relatively simple crystal structure and a rich ferroelectric and structural phase diagram, it has been one of the most exhaustively studied ferroelectric materials since its discovery as a ferroelectric in 1946 [99]. Despite years of experimental and theoretical attention, the question of whether the phase transitions of BaTiO_3 are predominantly of the displacive or order–disorder type remains open. In this chapter, I present Extended X-ray Absorption Fine Structure (EXAFS) data showing that the phase transitions of BaTiO_3 are predominantly of the order–disorder type.

Because of its high Curie–Weiss constant and zone–centered soft mode [5], BaTiO_3 has long been considered an example of a material whose structural transitions are of the displacive type. In low temperature phases of a displacive crystal some or all of the constituent atoms are displaced from sites of point centrosymmetry. These displacements are of the same symmetry as the macroscopic order parameter. In the case of BaTiO_3 , the ferroelectric phase transitions involve rotations of the macroscopic polarization. In the lowest temperature, rhombohedral phase the polarization is parallel to a $\langle 111 \rangle$ crystal axis. Upon heating BaTiO_3 undergoes transitions to orthorhombic, tetragonal, and finally cubic phases, wherein the macroscopic polarization aligns parallel to a orthorhombic $\langle 011 \rangle$ axis then to a tetragonal $\langle 001 \rangle$ axis before vanishing in the cubic phase. These transitions are summarized in Table 5.1.

In Cochran’s [5] displacive model, the atomic displacements are driven by softening of the appropriate phonon modes as the transition temperature is approached

Table 5.1: The structures of the different phases of BaTiO₃ and their transition temperatures. The data in this table is from Ref. [4].

rhombohedral (R 3 m)	⇒ 183 K	orthorhombic (A m m 2)	⇒ 278 K	tetragonal (P 4 m m)	⇒ 393 K	cubic (P m 3 m)
-------------------------	------------	---------------------------	------------	-------------------------	------------	--------------------

from above. The mode becomes unstable as its frequency goes through zero, producing the displacement of the lower temperature and lower symmetry phase. This model qualitatively explains the structural and ferroelectric phase transitions, the Raman spectrum [1], and much of the thermodynamics of the BaTiO₃ system. The soft mode frequency, however, does not vanish at the phase transition temperature, indicating a fundamental shortcoming of this purely displacive model.

In 1968, Comes *et al.* [100, 101] published photographs of diffuse scattering sheets between the Bragg peaks in three of the four phases of KNbO₃, which is isostructural to BaTiO₃ and undergoes the same sequence of phase transitions. These sheets could not be explained by Cochran's displacive model. They showed that qualitative agreement with their observations could be obtained by application of an order-disorder model first proposed for BaTiO₃ two years earlier by Bersuker [102]. In Refs. [100] and [101], Comes *et al.* state that they interpret their measurements of BaTiO₃ with this same order-disorder mechanism.

An order-disorder crystal is characterized by local atomic configurations which do not necessarily share symmetry elements with the macroscopic order parameter. From calculations of the local adiabatic potential, Bersuker suggested that the titanium atom sits in one of eight potential minima which are displaced from the cell center in the eight $\langle 111 \rangle$ directions, as shown in Refs. [100] and [102]. In the lowest temperature phase, there is long range correlation in all three Cartesian directions between titanium atoms in adjacent unit cells. Thus, in the rhombohedral phase, all the titanium atoms are displaced in the same $\langle 111 \rangle$ direction. At each of the three phase transition temperatures, correlation is lost in one of the three directions. This results in a disordering of the titanium atoms among the $\langle 111 \rangle$ directions. In the orthorhombic phase, the titanium atoms occupy one of two $\langle 111 \rangle$ positions such that the displacements from cell to cell are correlated over long range in two Cartesian directions and uncorrelated in the third. At the transition to the tetragonal phase, the correlations are lost in a second direction, thus four of the $\langle 111 \rangle$ positions are

equally occupied by the titanium atoms. Finally in the cubic phase, correlations in the remaining direction vanish and all eight $\langle 111 \rangle$ sites are randomly occupied.

In all phases the local displacements are rhombohedral and these rhombohedral displacements disorder such that their average over long length scales gives the observed crystallographic structure. Whenever disorder is present, the symmetry of the macroscopic order parameter, in this case the polarization, may be different from the symmetry of the local displacements. The Bragg peaks observed in the experiment by Comes *et al.* arise from the average structure and the diffuse scattering between the peaks indicate that disorder is present. Comes *et al.* interpreted the existence of the planes of diffuse scattering to indicate that the local rhombohedral displacements of the titanium atoms have long correlation lengths in directions perpendicular to the planes.

This order–disorder model is not unique in providing qualitative agreement with the diffuse sheets measured by Comes *et al.* In 1969 Hüller [103] showed that a displacive model allowing for correlated motions of the titanium atoms also gave qualitative agreement with the observed sheets. As Hüller pointed out in his paper, a direct test of these competing models was lacking at the time. This chapter, along with Ch. 7, provides this direct test.

Performing a direct test of the local atomic configurations in the various phases of BaTiO_3 is the topic of this chapter. Although the model of soft phonon modes and displacive structural transitions has enjoyed success qualitatively explaining many of the macroscopic and thermodynamic properties of BaTiO_3 , there are quantitative discrepancies and a number of measurements in the literature which are not well explained by a displacive model. These include measurements of infrared reflectivity [7], cubic phase x–ray diffraction [8], electron spin resonance [9], and impulsive stimulated Raman scattering [10, 11]. Furthermore, knowing the true local atomic configurations in BaTiO_3 throughout its various phases would be crucial to a successful theory of the microscopic mechanism of phase transitions in this material. Recent first principles calculation [104] of the ground state structure and phase transitions of BaTiO_3 have found further evidence of the order–disorder nature of its phase transitions. These calculations require atomic configurations as their initial input parameters. The details of the interactions within the crystal can only be properly understood with knowledge of the true microscopic structure. Recent XAFS measurements on a variety of perovskite ferroelectrics and antiferroelectrics including KNbO_3 [12], $\text{KTa}_{0.91}\text{Nb}_{0.09}\text{O}_3$ [13–15], NaTaO_3 [16], $\text{Na}_{0.82}\text{K}_{0.18}\text{TaO}_3$ [16], PbTiO_3 [18, 19], and PbZrO_3 [17] have shown order–disorder character in phase transitions originally believed to be of the

displacive type. The connection between the off-center displacements of the disordered structure and the softening of the transverse optical phonon modes has been successfully explained [105] for PbTiO_3 and KNbO_3 .

5.2 BaTiO_3 EXAFS Measurements

It is my wish to repeat this analysis for BaTiO_3 , but there is an experimental difficulty with BaTiO_3 that is not present with PbTiO_3 . As discussed in Sec. 2.3, the range of data available imposes a natural bandwidth limiting the information content of the EXAFS signal. The excitation energy of the titanium K edge is at 4966 eV and the energy of the barium L_{III} edge is at 5247 eV. This spectrum is shown in Fig. 5.1. The energy range between the edge steps corresponds to $k = 8.2 \text{ \AA}$. Because of the large systematic uncertainties in the determination of the background function μ_0 at low photoelectron wave number for transition metal oxides, the useful data range is quite small, $\Delta k \approx 5.0 \text{ \AA}$. In Ch. 4, I fit my PbTiO_3 data between 1.1 and 4.2 \AA . With $\Delta k = 5.0 \text{ \AA}$, this R range of $\Delta R = 3.1 \text{ \AA}$ corresponds to $N_I \simeq 9.9$. While I used eight parameters for the final fits to the PbTiO_3 data, I needed to consider as many as fourteen parameters. The data range is thus inadequate to properly define the structure. By corefining these data with the barium K edge data, six of the fourteen parameters variables could be used commonly in the two data sets. Although a corefinement formally removes the information content restriction, I found that most of these variables were very closely coupled with the background function μ_0 and could not be determined in a statistically significant manner. Consequently I used only the barium K edge EXAFS for this work.

I measured the barium K edge EXAFS on powdered samples at 9 temperatures between 35 K and 750 K, a range spanning all four phases. An example of the absorption data is shown in Fig. 5.2.

Background subtractions were performed with AUTOBK using the technique described in Sec. 2.2. The isolated $\chi(k)$ are shown in Fig. 5.3 at various temperatures. The background removal parameters used in AUTOBK to produce the $\chi(k)$ spectra are given in Table 5.2.

To test the order-disorder model with these data, I created theoretical fitting standards using FEFF6 and the rhombohedral crystal structure [4] of BaTiO_3 at 40 K. The contributions from these paths as calculated by FEFF6 were varied according to Eq. (2.10). The values for N were set as indicated by the rhombohedral local symmetry as shown in Table 5.3. To determine the path lengths R of Eq. (2.10), I used

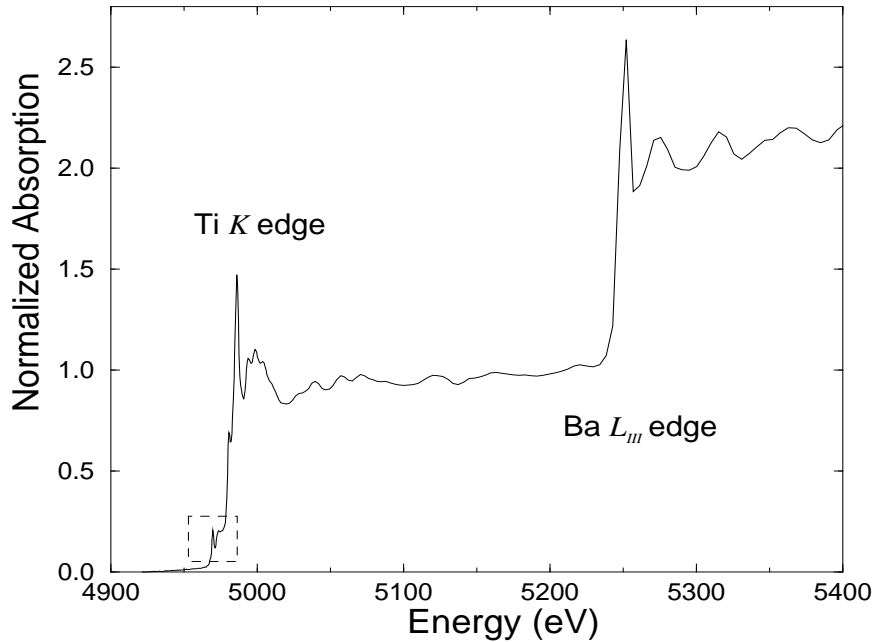


Figure 5.1: The XAFS spectrum of BaTiO_3 in an energy range spanning the titanium K edge at 4966 eV and the barium L_{III} edge at 5247 eV. The XANES feature discussed in Ch. 7 is shown in the dashed box.

Table 5.2: Background removal parameters used in AUTOBK for the BaTiO_3 data. The value of E_0 was fixed in each of the background removals. This value corresponds to the x-axes of Fig. 5.2. $[0 \rightarrow r_{\text{bkg}}]$ is the region over which the non-structural Fourier components are optimized in the background removal. $[r_{\text{bkg}} \rightarrow r_{1\text{st}}]$ is the data range in which the overall scaling factor for the theory is chosen for optimizing the low frequency components of the signal. The default values in AUTOBK for the k -weight (1) and Hanning window sills (0) were used.

edge	E_0	k_{min}	k_{max}	k -weight	r_{bkg}	$r_{1\text{st}}$
Ba K	37441.0	2	end of data	2	1.5	2.5

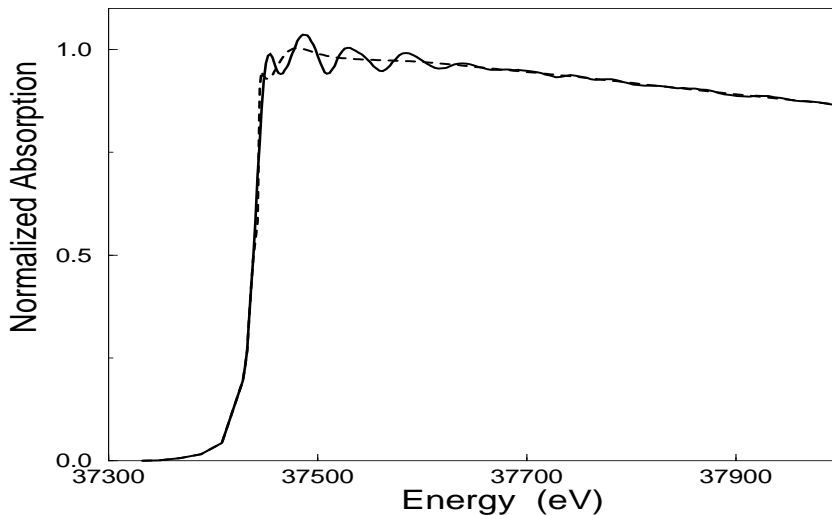


Figure 5.2: Barium K edge absorption spectrum in BaTiO_3 .

the five structure parameters shown in Table 5.5 as possible fitting variables and from these determined R for each path. Using these five structural parameters as fitting parameters, this fitting model allows, as a limiting case, the possibility of finding the cubic, centrosymmetric local structure. The remaining fitting parameters considered were σ^2 for each of the single scattering (SS) paths, phase corrections parameterized as E_0 variations for each species of backscattering atom, and an amplitude correction for the titanium backscatterers. The parameters for all multiple scattering (MS) paths considered in the fits were determined from this set of fitting variables without introducing new variables. For the fits shown in Figs. 5.4 – 5.7, ten free parameters were used. The fitting ranges, information content, and statistical parameters of these fits are shown in Table 5.4. In all cases, the number of parameters varied was smaller than the information content of the analyzed portion of the signal. The range in R space included SS out to the fifth coordination shell and MS paths at the distance of the fifth shell. The only significant MS paths were double and triple scattering among barium and oxygen atoms along the face diagonal of the unit cell.

A thorough explanation of how the five structural parameters were used in FEFFIT to constrain the fits is given in Sec. A.2. The fits shown in Figs. 5.4 to 5.7 consider

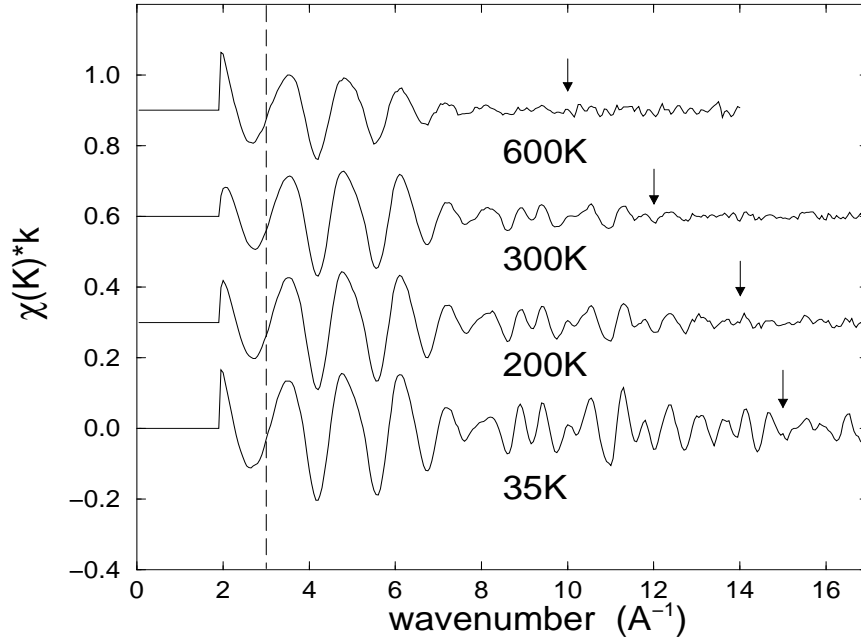


Figure 5.3: The $\chi(k)$ spectra for BaTiO_3 at several temperatures. One data set from each of the four crystallographic phases is shown. The data are the average of two or three scans taken at each temperature. The dashed line is the lower bound of the data range used in the fits and the arrows indicate the upper bound.

five coordination shells. There are several nearly collinear MS paths at the distance of the 5th shell. The buckling angle in these paths was less than 4°. Due to this small angle and the long path length, changes in this angle were difficult to resolve, particularly at high temperature, and did not contribute significantly to my ability to distinguish between the different local structural discussed below. The method of measuring buckling angle is discussed in detail in Sec. A.1.2 and was used in these fits.

Fits to the data at several temperatures using the rhombohedral local structure are shown in Figs. 5.4 to 5.7. I found good agreement to the data using the rhombohedral model at all temperatures. In Ref. [98], S_0^2 for barium was found to be 1.00(5) and so was set to 1 for these fits. The phase corrections [50] for the three types of

Table 5.3: Multiplicities and lengths of the various near neighbor bond lengths in BaTiO_3 for the various local symmetries predicted by the displacive model. In the order-disorder model the rhombohedral local structure persists in all phases. All distances are in Ångstroms and were determined from the crystallographic data in Ref. [4] at 40 K, 250 K, 300 K for the three low temperature phases. The cubic distances assume the perovskite structure with $a = 4.016$ Å.

local symmetry	Ba-O	Ba-Ti	Ba-Ba and Ti-Ti	Ti-O
rhombohedral	3×2.786	1×3.370	6×4.003	3×1.827 3×2.141
	6×2.828	3×3.430		
	3×2.886	3×3.501 1×3.583		
orthorhombic	1×2.793	2×3.416 4×3.468 2×3.532	2×3.986 4×4.018	2×1.875 2×1.997 2×2.146
	4×2.808			
	2×2.837			
	4×2.854 1×2.897			
tetragonal	4×2.808	4×3.417 4×3.522	4×3.991 2×4.035	1×1.829 4×2.000 1×2.206
	4×2.824			
	4×2.868			
cubic	12×2.839	8×3.478	6×4.016	6×2.008

Table 5.4: Fourier transform ranges (Δk), fitting ranges (ΔR), number of independent points (N_I), the number of parameters used in the fits (P), number of degrees of freedom (ν), the measurement uncertainty in R -space ($\bar{\sigma}_r$), reduced chi-square (χ_ν^2), and \mathcal{R} -factor (fractional misfit) for the fits to the rhombohedral structure for BaTiO₃. The ten free variables in these fits were 3 phase corrections, 5 σ^2 's, the lattice constant a , and δ_{O_x} . $\chi(k)$ was weighted by k for all Fourier transforms.

temperature	Δk	ΔR	N_I	P	ν	$\bar{\sigma}_r$	χ_ν^2	\mathcal{R}
35 K	[3,15]	[1.6,5.7]	32.0	10	22.0	0.0009	84.8	0.0088
150 K	[3,15]	[1.6,5.7]	32.0	10	22.0	0.0008	74.1	0.0062
200 K	[3,14]	[1.6,5.7]	29.5	10	19.5	0.0010	41.8	0.0056
250 K	[3,13]	[1.6,5.7]	27.0	10	17.0	0.0009	48.5	0.0049
300 K	[3,12]	[1.6,5.7]	24.5	10	14.5	0.0007	72.3	0.0045
350 K	[3,12]	[1.6,5.7]	24.5	10	14.5	0.0011	22.7	0.0057
450 K	[3,10]	[1.6,5.7]	19.5	10	9.5	0.0008	12.6	0.0009
600 K	[3,10]	[1.6,5.5]	18.4	10	8.4	0.0007	15.4	0.0008
750 K	[3,10]	[1.6,5.5]	18.4	10	8.4	0.0008	11.2	0.0025

Table 5.5: Fitting parameters used in the fits of the barium K edge data to the rhombohedral local structure. The initial values [4] are for the 40 K crystal structure. Three of these parameters had little impact on the quality of our fits and were consistent with their initial values at all temperatures. For the results in Table 5.4 these values were fixed to their initial values.

param.		description	initial value
a	measured	the rhombohedral lattice constant	4.0035 Å
α	set	the rhombohedral angle	89.84°
δ_{Ti}	set	the rhombohedral displacement of the titanium atom	-0.015
δ_{O_x}	measured	the displacement of the oxygen atom in the \hat{x} and \hat{y} directions	0.009
δ_{O_z}	set	the displacement of the oxygen atom in the \hat{z} direction	0.018

backscatterers were expressed as shifts of E_0 and were found to be $-2.18(70)$ eV for oxygen, $-3.89(87)$ eV for titanium, and $-2.75(1.54)$ eV for barium relative to the nominal value of 37441 eV. The measured σ^2 's were fit with the Einstein temperatures [53] shown in Table 5.6. The lattice constant a showed a thermal expansion from $4.001(1)$ Å to $4.041(9)$ Å between 35 K and 750 K. The parameter δ_{O_x} varied smoothly from $0.015(6)$ to $0.027(4)$ in that temperature range. The other three structural parameters in Table 5.5 showed no change from their initial values outside of their uncertainties and so were fixed to their 40 K values.

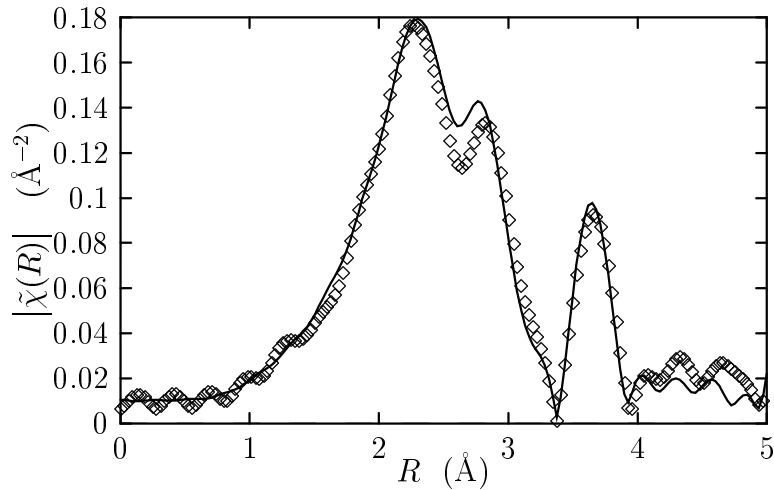


Figure 5.4: Fit to the Ba K edge data in BaTiO_3 at 35 K. The magnitude of the complex Fourier transform of $\chi(k)$ is shown. The diamonds (\diamond) are the data and the line is the fit.

Although the success of the rhombohedral structural model is good evidence to support an order–disorder model in BaTiO_3 , it is not compelling by itself. I repeated the analytical approach described above on the data in the orthorhombic, tetragonal, and cubic phases. In each of these phase, I used the average structure as the fitting model and created fitting standards with FEFF6 using these average structures. I used the multiplicities N given in Table 5.3 and varied R for each path according to the values of the structural parameters appropriate to the orthorhombic, tetragonal, and cubic phases. In Table 5.7 I compare the reduced chi–squares χ^2_ν for the orthorhombic, tetragonal, and cubic models with the χ^2_ν from the rhombohedral fitting model. As discussed in Sec. 2.4, the uncertainty in a good EXAFS measurement is

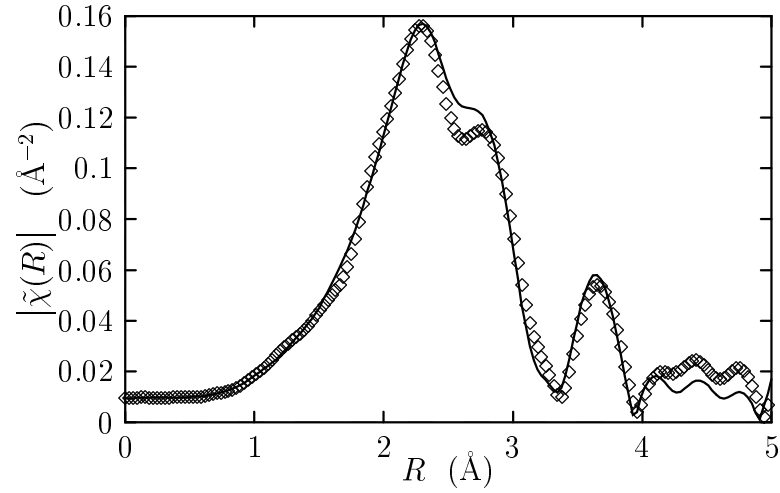


Figure 5.5: Fit to the Ba K edge data in BaTiO_3 at 200 K. The magnitude of the complex Fourier transform of $\chi(k)$ is shown. The diamonds (\diamond) are the data and the line is the fit.

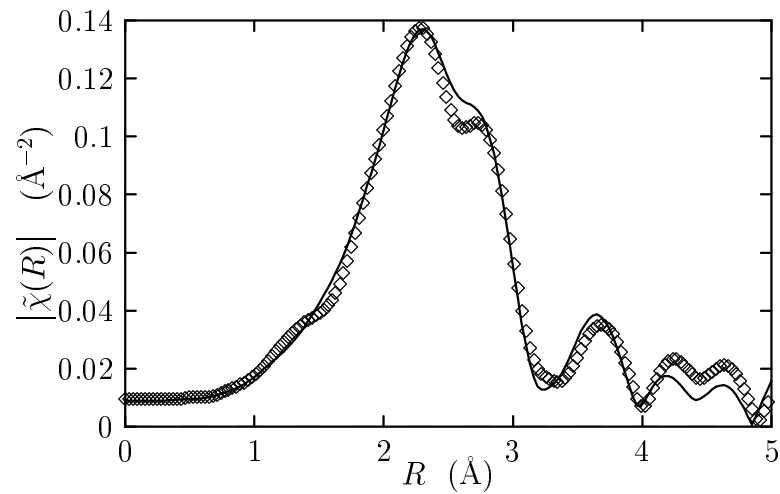


Figure 5.6: Fit to the Ba K edge data in BaTiO_3 at 300 K. The magnitude of the complex Fourier transform of $\chi(k)$ is shown. The diamonds (\diamond) are the data and the line is the fit.

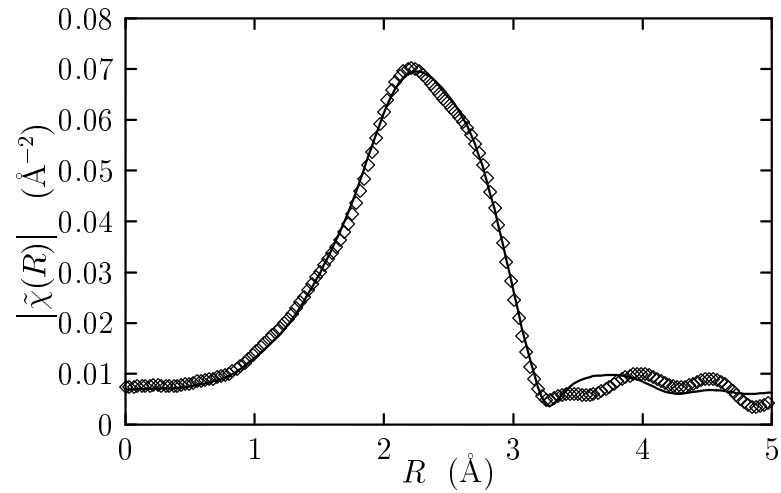


Figure 5.7: Fit to the Ba K edge data in BaTiO_3 at 750 K. The magnitude of the complex Fourier transform of $\chi(k)$ is shown. The diamonds (\diamond) are the data and the line is the fit.

Table 5.6: Einstein temperatures for the five single scattering paths considered in the barium K edge fits to the rhombohedral model.

SS path	Θ_E
1 st shell O \longleftrightarrow	630(99) K
2 nd shell Ti \longleftrightarrow	267(5) K
3 rd shell Ba \longleftrightarrow	161(4) K
4 th shell O \longleftrightarrow	449(80) K
5 th shell Ba \longleftrightarrow	152(6) K

generally dominated by systematic errors. The statistical errors of the measurement are small compared to the uncertainty of the fitting standards and of the removal of the background function μ_0 . In evaluating χ_ν^2 , I normalize by the estimated statistical uncertainty and would get $\chi_\nu^2 \approx 1$ if the statistical errors were dominant. That χ_ν^2 is, in general, larger than 1 even for fits that look good upon inspection and give physically reasonable results indicates that systematic errors dominate. I account for this by scaling the error bars on our fitting parameters by a factor of χ_ν . Note that the absolute error in these fits is quite small as the \mathcal{R} -factors shown in Table 5.4 are less than 1 percent. The measured values of χ_ν^2 provide a means to compare different fitting models. As discussed in Sec. 2.3, if the χ_ν^2 's of the two models differ by more than a factor of $1 + \frac{2\sqrt{2}}{\sqrt{\nu}}$, the model with the smaller χ_ν^2 is significantly better. As shown in Table 5.7, there is no preference for the rhombohedral model by this criterion.

Table 5.7: Comparing the reduced chi-square for the rhombohedral model with those of the average structural models in the orthorhombic, tetragonal, and cubic phases.

phase	structural model			
		χ_ν^2 (rhomb.)	χ_ν^2 (ortho.)	χ_ν^2 (cubic)
orthorhombic	200 K	41.8	32.6	
	250 K	48.5	47.9	
tetragonal	300 K	72.3		71.1
	350 K	22.7		22.3
cubic	450 K	12.6		12.2
	600 K	15.4		10.4
	750 K	11.2		10.8

To distinguish the structural models, I rely on physical arguments. In the fits to the tetragonal and cubic phase data using the tetragonal or cubic local symmetry as the fitting model, I found that σ^2 's obtained from the minimizations were consistently larger than those found using the rhombohedral local symmetry. These values are shown in Table 5.8 for the σ^2 's of the barium-titanium bonds. These larger σ^2 's can be understood in two ways. They can result from a softening of the effective spring constant connecting the atoms. This seems unphysical. As shown in Table 5.3, the barium-titanium bond lengths change by at most 3 percent, but the change in σ^2 is much larger. A softening of the spring constant would result in a faster increase of σ^2

with raising temperature. The results shown in Table 5.8 show discontinuities at each of the phase transitions when the average structure fitting models are used, but the rate of change of σ^2 with increasing temperature is the same regardless of which structural model is used. A softening of the effective spring constant is inconsistent with the measurements. In fact, the temperature dependence of σ^2 assuming a rhombohedral local structure gives a temperature dependence consistent with a force constant which fits the single Einstein temperature given in Table 5.6. The latter explanation is more physically reasonable. The fit using the cubic local symmetry requires a larger σ^2 to compensate for the static disorder of the true rhombohedral local symmetry. The rhombohedral fitting model has an inherent amount of static disorder due to the set of barium–titanium path lengths used to create the fitting standards. Using the R 's and N 's shown in Table 5.3 and the static cumulant formulas of Ref. [51], the rhombohedral model has a built-in static disorder of 0.0038 \AA^2 . The cubic model has no static disorder, thus requires an enhanced σ^2 to compensate for its neglect. The orthorhombic and tetragonal models have built-in static disorders of 0.0017 \AA^2 and 0.0028 \AA^2 respectively. The σ^2 's shown in Table 5.8 for the orthorhombic, tetragonal, and cubic phases are systematically larger than for the rhombohedral model. In each case, within their uncertainties, these σ^2 's are those of the rhombohedral model plus a static component to correct for neglecting the contribution of the rhombohedral disorder.

Table 5.8: σ^2 s of the barium–titanium distance in the high temperature cubic phase as measured using the rhombohedral and cubic local symmetries. The values for the rhombohedral model come from the Einstein temperature shown in Table 5.6. All numbers have units of \AA^2 .

phase	structural model				
		rhombohedral	orthorhombic	tetragonal	cubic
orthorhombic	200 K	0.0038(4)	0.0070(3)		
	250 K	0.0046(5)	0.0077(4)		
tetragonal	300 K	0.0055(7)		0.0075(10)	
	350 K	0.0064(8)		0.0085(12)	
cubic	450 K	0.0083(10)			0.0137(10)
	600 K	0.0111(12)			0.0175(10)
	750 K	0.0140(11)			0.0170(14)

The physical behavior of the σ^2 's in the rhombohedral fitting model is a strong argument in favor of the order–disorder model over the displacive model in BaTiO₃. However, the distinction between the displacive and order–disorder models on the basis of our barium *K* edge EXAFS data may not be fully compelling. This ambiguity will be resolved by consideration of the titanium *K* edge XANES spectra presented in Ch. 7.

Chapter 6

EXAFS MEASUREMENTS ON EuTiO_3

Now I turn my attention to a third titanate perovskite, EuTiO_3 . Unlike PbTiO_3 and BaTiO_3 , the local structure of EuTiO_3 retains its crystallographic centrosymmetry at all temperatures, showing no evidence of structural or electric phase transitions. It is an antiferromagnet at very low temperature [106, 107], but shows not ferro- or antiferroelectric behavior.

I have two interests in studying EuTiO_3 . In the previous two chapters I have demonstrated the persistence of local distortions into the crystallographically cubic phases of PbTiO_3 and BaTiO_3 . It adds weight to the argument to show an example of successful analysis on a structure with centrosymmetry. In Ch. 7 it is necessary to distinguish the structural contribution of the near-edge structures of PbTiO_3 and BaTiO_3 from the thermal contribution. The main result of the analysis presented in this chapter is the mean square displacement σ^2 of the titanium–oxygen bond. At the end of this chapter I derive a relationship between this measured σ^2 and the thermal contribution to the near-edge structure of titanium perovskites.

6.1 EuTiO_3 EXAFS Measurements

Data was collected at both the titanium K and europium L_{III} edges at 15 K, 128 K, 300 K. Samples of these spectra are shown in Fig. 6.1. The titanium edge data were affected by systematic noise beyond 15.5 \AA^{-1} . The useful data range at the europium L_{III} edge was limited by the presence of the L_{II} edge to about 12.5 \AA^{-1} .

Background subtractions were performed using AUTOBK using the technique described in Sec. 2.2. The isolated $\chi(k)$ is shown in Figs. 6.2 and 6.3 for the two edges at various temperatures. The background removal parameters used in AUTOBK to produce the $\chi(k)$ spectra are given in Table 6.1.

To fit the data, I used FEFF6 to generate a set of fitting standards based on the perovskite structure and a lattice constant of 3.923 \AA , which is about 0.02 \AA larger than that given in Ref. [108]. At the europium edge, I considered SS paths out the fourth coordination shell. At the titanium edge I considered SS paths out to the

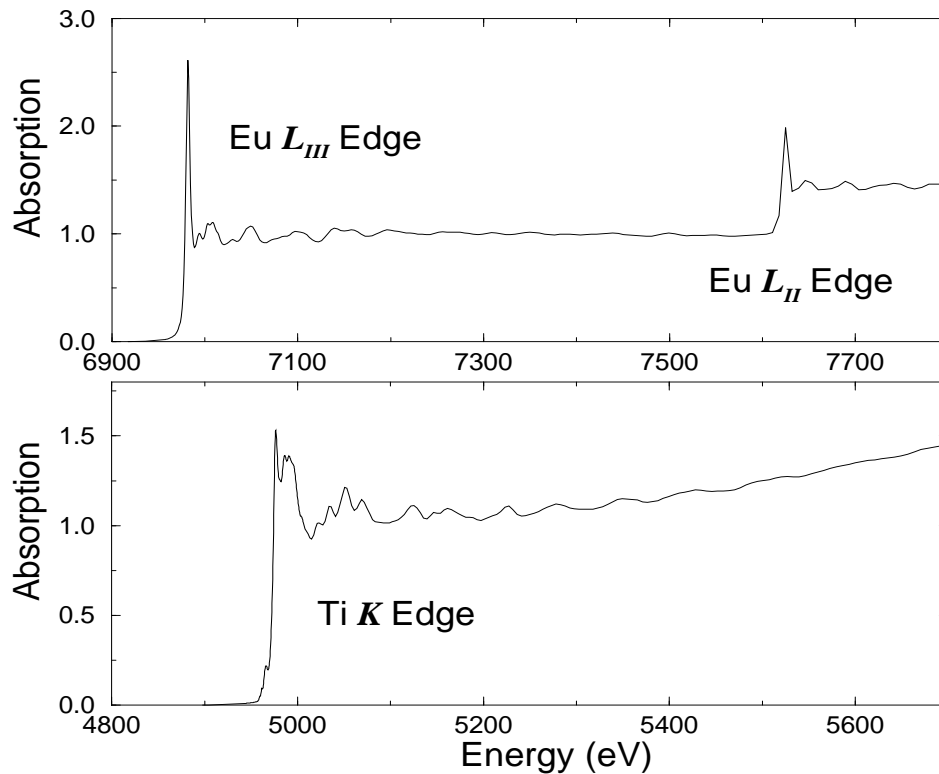


Figure 6.1: The absorption edges of EuTiO_3 at 15K. The titanium K edge is at 4966 eV, the europium L_{III} edge is at 6977 eV, and the europium L_{II} edge is at 7617 eV.

Table 6.1: Background removal parameters used in AUTOBK for the EuTiO_3 data. The value of E_0 was fixed in each of the background removals. These values correspond to the energy axes of Fig. 6.1. $[0 \rightarrow R_{bkg}]$ is the region over which the non-structural Fourier components are optimized in the background removal. $[R_{bkg} \rightarrow R_{1st}]$ is the data range over which the theory is scaled in the optimization. The data range over which the background was removed, $[k_{min} \rightarrow k_{min}]$ was limited in the europium data by the onset of the europium L_{II} edge.

edge	E_0	k_{min}	k_{max}	k -weight	R_{bkg}	R_{1st}
Ti K	4971.2	0.85	end of data	1	0.98	2.14
Eu L_{III}	6978.0	1.55	12.6	1	0.98	2.95

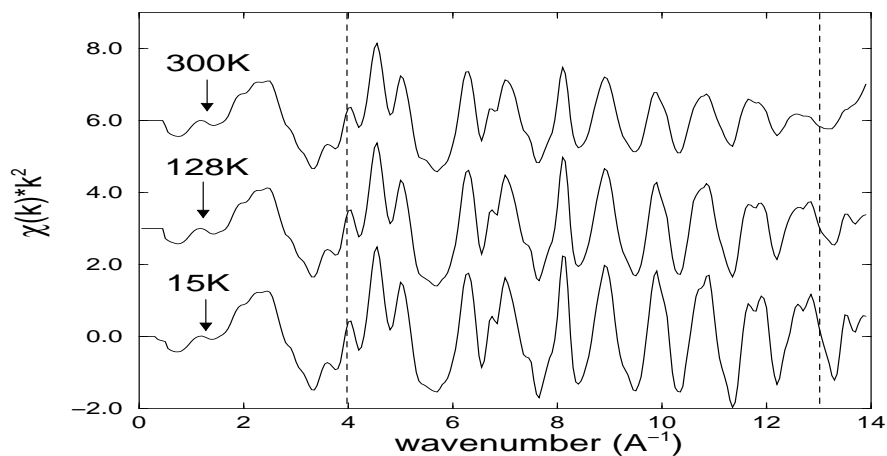


Figure 6.2: The temperature dependence of $\chi(k)$ for the titanium K edge of EuTiO_3 . The boundaries of the Fourier transform used in the fits are shown by the dashed lines.

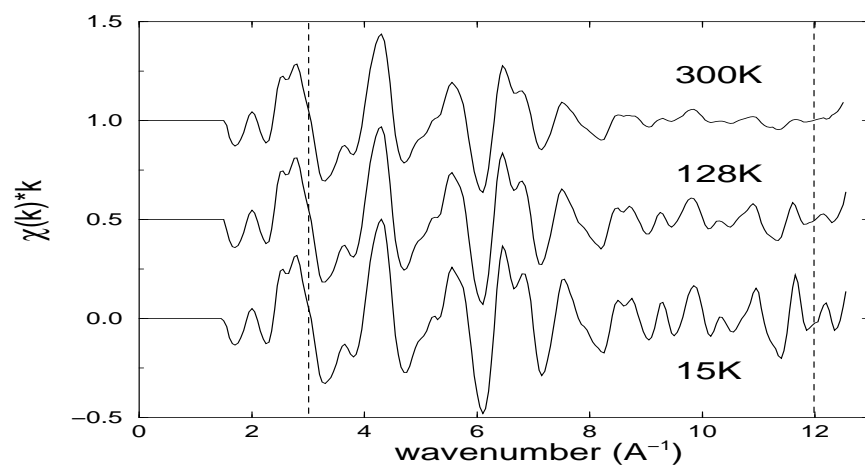


Figure 6.3: The temperature dependence of $\chi(k)$ for the europium L_{III} edge of EuTiO_3 . The boundaries of the Fourier transform used in the fits are shown by the dashed lines.

fourth shell and the collinear double and triple scattering paths involving the first shell oxygen atoms and the third shell titanium atoms. These MS paths were at the same distance as the third shell titanium atoms and were the only significant MS paths.

The cubic perovskite structure was the basis of my fitting model. I used an isotropic expansion factor as described in Sec. A.3 to parameterized the bond lengths. I assigned a σ^2 to each near-neighbor bond length and a phase correction in the form of an E_0 shift for each species of backscatterer. I parameterized σ^2 and the phase correction for each multiple scattering path considered in the manner described in Sec. A.1.1. For the europium edge fits it was necessary to introduce an amplitude correction to the titanium backscattering in the form of a correction to the photoelectron mean free path for that scattering path. At each temperature the data from the two edges were refined simultaneously. As the lattice expansion constant and σ^2 for the titanium–europium bond are common parameters between the two data sets, corefinement allows tighter constraints to be placed on the parameter set.

Table 6.2 shows the transform and fitting ranges used in the fits to the europium and titanium edge data along with the various statistical parameters of the co-refined fits. See Sec. 2.3 for a discussion of the statistical parameters. Example fits are shown in Figs. 6.5 – 6.8

Table 6.2: The upper table shows Fourier transform and fitting ranges used for the titanium and europium edges in EuTiO_3 , as well as the information content of each signal. The lower table shows results for the corefinements at each temperature, including the total number of independent points N_I in the corefinement, the number of parameters varied in the final fits P , the number of degrees of freedom ν , the measurement uncertainty in R -space ($\bar{\sigma}_r$) for each absorber, the reduced chi-square χ_ν^2 , and the \mathcal{R} -factor.

edge	k -range	k -weight	R -range	N_I
Ti	[4.0-13.0]	2	[1.2-4.0]	17.47
Eu	[3.0-12.0]	1	[1.8-4.0]	13.95

temp.	N_I	P	ν	$\bar{\sigma}_r$ (Ti)	$\bar{\sigma}_r$ (Eu)	χ_ν^2	\mathcal{R}
15 K	31.42	16	15.42	0.0129	0.0014	90.05	0.0092
128 K	31.42	16	15.42	0.0079	0.0012	111.91	0.0043
300 K	31.42	16	15.42	0.0056	0.0009	158.91	0.0055

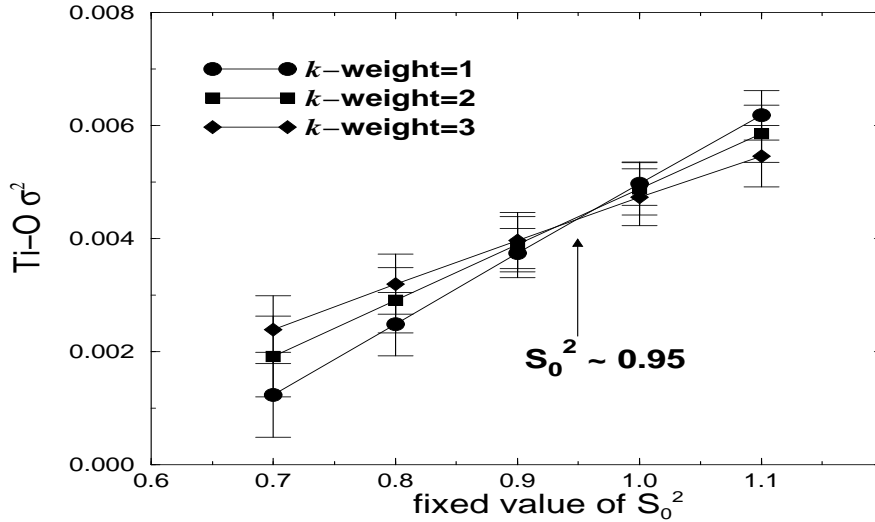


Figure 6.4: Determination of S_0^2 for the K edge of titanium in EuTiO_3 . The correlation between S_0^2 and σ^2 for the titanium-oxygen bond is mostly broken by sequentially fixing S_0^2 and performing the fits using different k weights. This method works well since the first shell signal is well isolated in the Fourier transform of the titanium $\chi(k)$ in EuTiO_3 . The three lines form a small triangle around $S_0^2 \approx 0.95$.

For the titanium atom, S_0^2 was determined by setting it to a sequence of values between 0.7 and 1.1 and varying the remainder of the parameters in the problem. For each value of S_0^2 , the titanium data were fit with k weighting of 1, 2, and 3. Because S_0^2 is highly correlated with the σ^2 's used in the problem and because σ^2 is multiplied by k^2 in the EXAFS equation Eq. (2.10), the best fit values of the σ^2 's vary with different k weights. In Fig. 6.4, I show the variation of the best-fit value of σ^2 for the first neighbor titanium-oxygen bond. Since any measurement of the fitting parameters should find the same S_0^2 , the true value of S_0^2 for these data must be at the intersection of the lines for the three k weights. In Fig. 6.4 the three lines nearly intersect, forming a small triangle around $S_0^2 \approx 0.95$. This value is used in subsequent fits. I approximate the uncertainty in this value by the extent to which the error bars on the best-fit values of σ^2 for k weight of 1 and 3 overlap. Thus $S_0^2 = 0.95(15)$.

This method of determining S_0^2 works by forcibly removing the correlation between S_0^2 and other parameters that effect the amplitude of χ in Eq. (2.10). For the first

shell peak in the transform of the titanium edge $\chi(k)$, only S_0^2 and the σ^2 for the first shell bond significantly effect the amplitude. Thus the correlation between the two is mostly broken by sequentially fixing S_0^2 in the manner described above. This same method did not work for the europium edge. For that edge, the first shell is not well isolated from other shells. Thus fixing S_0^2 does not sufficiently break correlations among the amplitude factors. When this method was attempted using the best-fit σ^2 's for the europium–oxygen and europium–titanium bonds, S_0^2 values of about 1.5 and 1.15 were found respectively. Neither of these are physically reasonable values. For the titanium edge, the first shell is well isolated from higher shells, thus the method worked well. I therefore allowed S_0^2 for the europium atom to float in subsequent fits.

Table 6.3: Fitting parameters for EuTiO_3 . Parameters used to modify $\chi(k)$ for either edge are indicated in the first column. The common parameters between the two edges are also indicated. Best-fit values for the σ^2 's are given as Einstein temperatures fit to the σ^2 's measured at each temperature. Offsets values of σ^2 's are given for those bonds which required one.

edge	parameter	description	best-fit value
Ti	E_0 (O)	δE_0 for O scatterer	$-1.81(1.11)$ eV
Ti	E_0 (Eu)	δE_0 for Eu scatterer	$-2.87(1.61)$ eV
Ti	E_0 (Ti)	δE_0 for Ti scatterer	$5.57(1.84)$ eV
Ti	σ^2 (Ti–O)	MSD for Ti–O bond	$451(26)$ K
Ti	σ^2 (Ti–Ti)	MSD for Ti–Ti bond	$329(26)$ K + $0.0016(5)$ Å ²
Eu	S_0^2	Amplitude reduction factor	$1.10(11)$
Eu	E_0 (O)	δE_0 for O scatterer	$4.57(62)$ eV
Eu	E_0 (Ti)	δE_0 for Ti scatterer	$4.79(67)$ eV
Eu	E_0 (Eu)	δE_0 for Eu scatterer	$4.27(1.24)$ eV
Eu	σ^2 (Eu–O)	MSD for Eu–O bond	$0.0135(21)$ Å ²
Eu	σ^2 (Eu–Eu)	MSD for Eu–Eu bond	$158(7)$ K
Eu	λ (Ti)	δE_i for Ti scatterer	$-1.03(47)$ eV
both	η	lattice expansion coefficient	$6.7(2.4) \cdot 10^{-5}$ Å/K
both	σ^2 (Eu–Ti)	MSD for Eu–Ti bond	$290(24)$ K + $0.0013(5)$ Å ²

Fourteen of the sixteen variables used in the fits to EuTiO_3 along with their best-fit values are shown in Table 6.3. These include δE_0 corrections for each of

the first three shells and mean square displacements (MSD) σ^2 for each of the first three bonds around both the titanium and europium atoms. Also used were an S_0^2 for the europium atom, a lattice expansion constant η , and an amplitude correction for the titanium backscatterers around the europium atoms. These were applied to the various SS and MS paths as described in Secs. A.1.1 and A.3. These variables were used to fit both edges simultaneously at each temperature. I also included the fourth shell oxygen atoms in both parts of the fits, but the σ^2 for these paths were not well determined in these fits.

In Table 6.3, the values for the σ^2 are given as Einstein temperatures which were fit to the results for the σ^2 's at each temperature. For two bonds the σ^2 's required a small offset to follow the behavior of an Einstein model. The σ^2 for the europium–oxygen bond did not change with temperature outside of its error bars, so no Einstein temperature is reported for that bond in Table 6.3.

S_0^2 for the europium atom is rather large, but consistent with 1.0 within its error bar. The lattice constant increased linearly from 3.920(5) Å at 15 K to 3.940(7) Å at 300 K. These values are about 1 percent larger than the lattice constant given in Ref. [108].

From these data I obtained a good measurement of σ^2 for the titanium–oxygen bond, which was my stated goal in analyzing these data. There are, however, several systematic problems in this analysis. The best–fit lattice constant as measured by EXAFS is 0.5% larger than that measured by diffraction. Also the temperature dependence of three of the σ^2 fail to follow properly and Einstein behavior. This may indicate the presence of static local disorder which was not included in my fitting model. I will not address these systematic problems with the EuTiO₃ fitting model in this thesis as they do not effect the quantitative result on the titanium–oxygen σ^2 , which was the important result of this chapter.

6.2 Thermal Distortion Parameter

In Ch. 7 I use the Einstein temperature of the titanium–oxygen bond to interpret the near–edge structure of the EuTiO₃ titanium *K* edge XANES spectrum. As discussed in Sec. 7.1, there is a peak in the near–edge spectra of transition metal oxides that is a fingerprint that the transition metal atom is located in a site that lacks point centrosymmetry. From a simple perturbation theory argument, I show that there is a simple relationship between the magnitude of the distortion away from point centrosymmetry and the area of the fingerprint peak in the near–edge spectrum. If \vec{d}

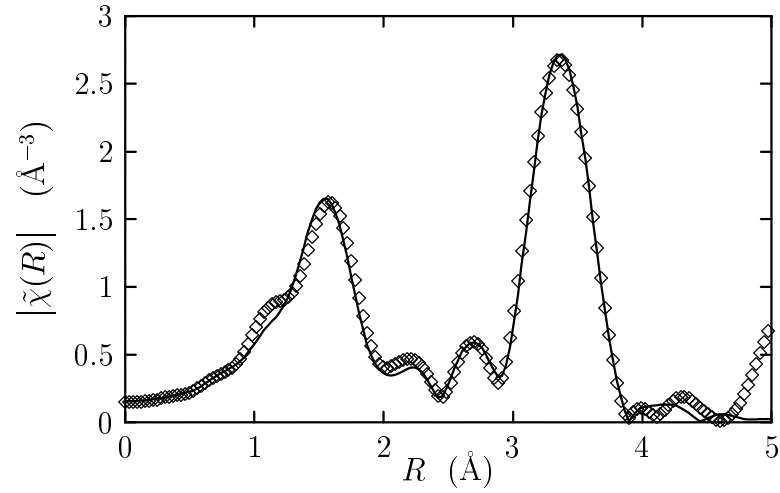


Figure 6.5: Fit to the titanium K edge data in EuTiO_3 at 15 K. The magnitude of the complex Fourier transform of $\chi(k)$ is shown. The diamonds (\diamond) are the data and the line is the fit.

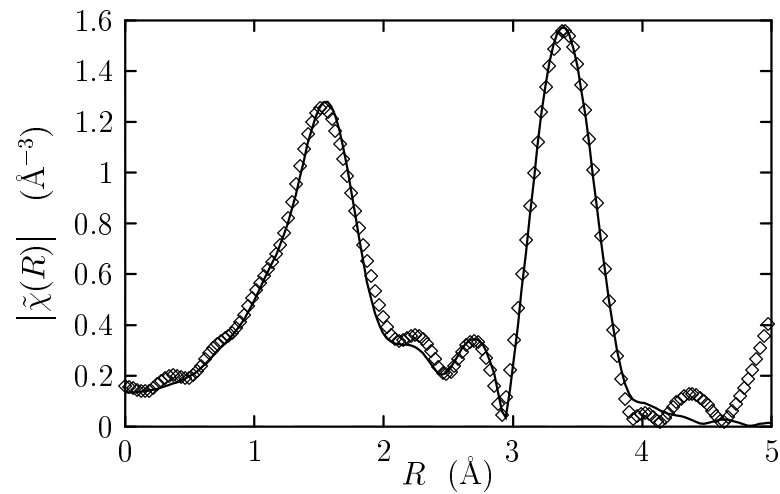


Figure 6.6: Fit to the titanium K edge data in EuTiO_3 at 300 K. The magnitude of the complex Fourier transform of $\chi(k)$ is shown. The diamonds (\diamond) are the data and the line is the fit.

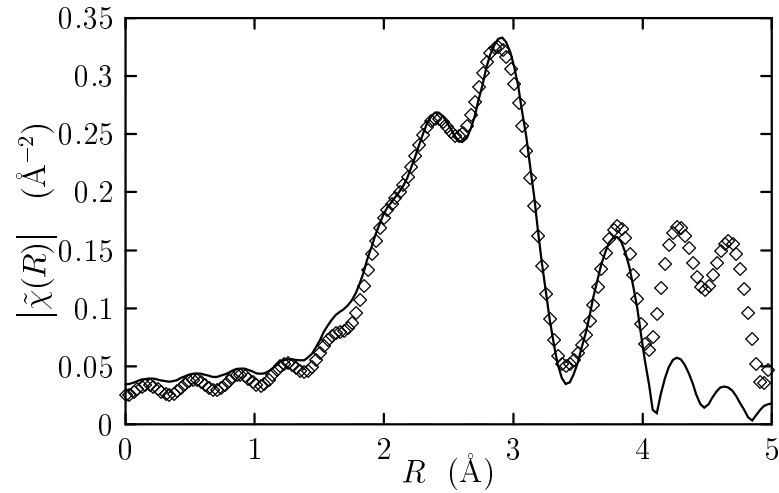


Figure 6.7: Fit to the europium L_{III} edge data in EuTiO_3 at 15 K. The magnitude of the complex Fourier transform of $\chi(k)$ is shown. The diamonds (\diamond) are the data and the line is the fit.

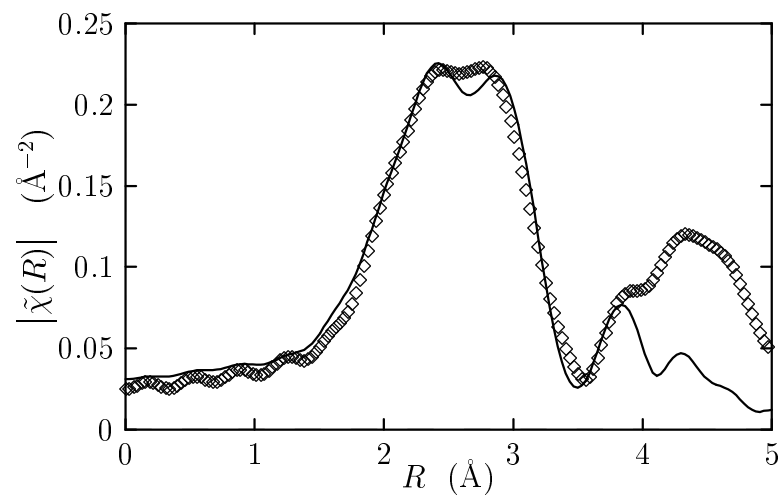


Figure 6.8: Fit to the europium L_{III} edge data in EuTiO_3 at 300 K. The magnitude of the complex Fourier transform of $\chi(k)$ is shown. The diamonds (\diamond) are the data and the line is the fit.

is a parameter describing the displacement of the titanium atoms from the midpoint of the oxygen octahedron, then

$$\mathcal{A} \propto \langle (\hat{\epsilon} \cdot \hat{d})^2 \rangle \quad (6.1)$$

which, for a sample which is randomly oriented with respect to the x-ray beam, is

$$\mathcal{A} \propto \frac{|d|^2}{3}. \quad (6.2)$$

Consider a line in one dimension of equally spaced atoms of alternating species. If the distortion is the displacement of one of the species from its nominal location, then $\vec{\delta}$ is the displacement of that species from the midpoint between its neighboring atoms,

$$\delta = \frac{(r_2 - r_1)}{2} \quad (6.3)$$

where $r_{1(2)}$ is the distance from the displaced atom to its nearer (further) neighbor. In the case of a titanium perovskite, the r 's represent titanium–oxygen bonds along each of the Cartesian axes.

Eq. (6.3) holds for each of the three Cartesian directions, so I define a thermal distortion parameter $d_t = \sqrt{3}\delta$. In the absence of a static displacement and of thermal motion, the area of the peak \mathcal{A} observed in the XANES spectrum is expected to be zero. At finite temperature, a small pre-edge peak is still expected due to the thermal mean squared variation of the two metal–oxygen bonds. Taking a snapshot of the three atoms along one of the Cartesian directions, $|r_2 - r_1| > 0$ at any instant due to this thermal motion. Thus an area $\mathcal{A}_t \propto d_t^2$ will be measured.

To start, consider a split in distances $\zeta = r_2 - r_1$. Each of the r_i are $r_0 - \Delta_i$ where Δ_i is some instantaneous deviation from r_0 due to thermal motion. So $\zeta = \Delta_2 - \Delta_1$ and the thermal average of its square is $\langle \zeta^2 \rangle = \langle (\Delta_2 - \Delta_1)^2 \rangle$.

The distribution of Δ_i is a Gaussian of half width equal to the measured σ^2 . Normalized to unit area, this distribution function is

$$\mathcal{P}_{\Delta_i} = \sqrt{\frac{1}{2\sigma^2\pi}} e^{-\Delta_i^2/2\sigma^2} \quad (6.4)$$

Integrating over this distribution,

$$\begin{aligned} \langle \zeta^2 \rangle &= \int_{-\infty}^{\infty} (\Delta_2 - \Delta_1)^2 \cdot \mathcal{P}_{\Delta_1} d\Delta_1 \cdot \mathcal{P}_{\Delta_2} d\Delta_2 \\ &= \left(\sqrt{\frac{1}{2\sigma^2\pi}} \right)^2 \int_{-\infty}^{\infty} [\Delta_1^2 + \Delta_2^2 - 2\Delta_1\Delta_2] \cdot e^{-\Delta_1^2/2\sigma^2} d\Delta_1 \cdot e^{-\Delta_2^2/2\sigma^2} d\Delta_2 \end{aligned} \quad (6.5)$$

The cross product term in this integral is 0 by symmetry. The other two integrals are the same and are easily solved. The thermal mean square of the split in distances is

$$\langle \zeta^2 \rangle = 2\sigma^2 \quad (6.6)$$

This result is obtained in each dimension, so, from Eq. (6.3),

$$d_t^2 = 3 \left\langle \left(\frac{\zeta}{2} \right)^2 \right\rangle = \frac{3\sigma^2}{2}. \quad (6.7)$$

$$d_t = \sqrt{\frac{3\sigma^2}{2}}. \quad (6.8)$$

Even a centrosymmetric perovskite such as EuTiO_3 has a small peak just above the Fermi energy of a size proportional to d_t^2 . This can be seen in the data in Fig. 7.9. In my analysis of the Ti K edge data on EuTiO_3 , I assumed that the titanium atom did lie in a centrosymmetric site, thus the Ti–O bond length and σ^2 was the same in all six directions. This discussion could easily be generalized to consider different bond lengths and σ^2 's.

Table 6.4: Thermal distortion parameter in EuTiO_3 for an Einstein temperature $\theta = 451$ K for the titanium–oxygen bond.

temp.	σ^2 (\AA^2)	d_t (\AA)
15 K	0.00448	0.082
128 K	0.00477	0.085
300 K	0.00705	0.103
500 K	0.01061	0.126

Chapter 7

XANES MEASUREMENTS ON BaTiO₃, PbTiO₃, AND EuTiO₃

In the titanium K edge spectra of PbTiO₃ and BaTiO₃ shown in Figs. 4.1 and 5.1, a prominent feature in the near edge region of these materials is seen. In this chapter I examine the dependence of this feature on the local structures about the titanium atoms in PbTiO₃, BaTiO₃, and EuTiO₃. Careful consideration of the XANES spectrum in these material complements the structural information available from analysis of the EXAFS. In the case of BaTiO₃, the XANES spectrum offers crucial information for resolving its local structure.

7.1 Symmetry and the XANES Spectrum

At the titanium K edge, a $1s$ electron having initial angular momentum $l = 0$ is excited. Because dipole transitions dominate in $\mu(E)$ the final state of the photoelectron will be of angular momentum $l = 1$ due to the dipole final state selection rule. The interaction between the photoelectron excited by the polarized radiation and a single crystal is illustrated in Fig. 7.1. The directional sense of the excited $l = 1$ photoelectron is determined by the direction of polarization of the incoming photons. As the photoelectron has no amplitude in directions perpendicular to the direction of polarization, $\mu(E)$ will contain no information concerning the local environment about the titanium atom perpendicular to the polarization. Thus an experiment on a single crystal sample can resolve the directional dependence of the local structure, while an experiment on a polycrystalline sample averages over all directions.

Titanium and other transition metals possess a large density of unfilled d states just above the Fermi energy. Ordinarily, this d density is not accessible to the XAFS experiment on a K edge due to the dipole selection rule, which requires that the difference in angular momentum of the initial and final states be 1. It is well known from molecular orbital theory [109] that mixing of the transition metal d states with states of p character from the surrounding atoms can occur in the presence of an asymmetric Hamiltonian, such as that for a material which lacks inversion symmetry

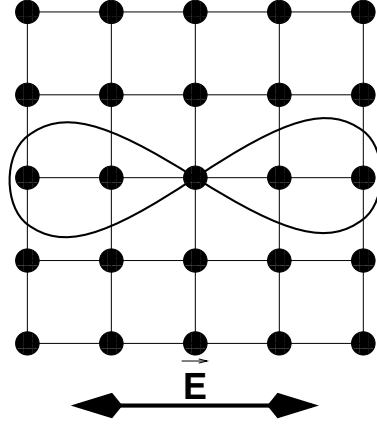


Figure 7.1: Schematic of the interaction between the $l = 1$ photoelectron and a square lattice.

about the transition metal site. Materials in which the transition metal does not reside on a site of point centrosymmetry characteristically display a peak in their XANES spectra above the Fermi energy but before the steeply rising part of the edge. This is shown in, for example, Refs. [110] and [111] and in numerous other examples of transition metal oxide XANES studies in the literature. It is the same feature shown in the dashed boxes in Figs. 4.1 and 5.1. This peak is much diminished in transition metal oxides of point centrosymmetric local structure, as seen in the EuTiO_3 data in Fig. 6.1.

Assuming that the displacement d of the titanium atom from the site of point centrosymmetry is a small perturbation to the crystal Hamiltonian, perturbation theory can be applied to the problem. The effect of the displacement must be of even parity, thus the area of the peak can be related to the displacement in three dimensions by

$$\mathcal{A} = \gamma \langle (\hat{\mathbf{e}} \cdot \vec{d})^2 \rangle. \quad (7.1)$$

Here $\hat{\mathbf{e}}$ is the polarization vector of the incident x-ray beam and the angle brackets represent an ensemble average, possibly over orientations of $\hat{\mathbf{e}}$ relative to \vec{d} and γ is a proportionality constant. In this chapter I will determine γ for PbTiO_3 , BaTiO_3 , and EuTiO_3 . For a polycrystalline sample the ensemble average over orientations of

the crystal domains relative to $\hat{\mathbf{e}}$ leads to a factor of $\frac{1}{3}$, i.e. $\mathcal{A} = \gamma \frac{|d|^2}{3}$. In the case of a polarized, single crystal experiment, the area \mathcal{A} will be sensitive to the direction of \vec{d} . In the most general case, this expression for \mathcal{A} is too simplistic. For a crystal of arbitrary symmetry, a tensor of fourth rank would relate $\hat{\mathbf{e}}$ and \vec{d} to \mathcal{A} [112].

7.2 Measuring the Area of the Near Edge Peak

To interpret the near-edge peak associated with the displacement of the titanium atom from centrosymmetry in terms of the local structure using Eq. 7.1, it is necessary to measure its area. In this section, I will describe the method I developed for doing so.

To measure XANES peak areas, I wrote a program called PHIT¹. I wanted a tool of sufficient generality to tackle this problem with flexibility and also to solve several related problems in the interpretation of XAFS and other data. The purpose of PHIT is to fit an arbitrarily parameterized sum of lineshapes to arbitrary real valued data. For use with XANES data, I fit an arctangent or similar function along with one or more peaked lineshapes to the data. The parameters describing the lineshapes can be used as the fitting parameters. PHIT is sufficiently general to solve other problems as well. I used PHIT throughout Chs. 4 – 6 to fit Einstein temperatures to measured values of σ^2 . PHIT has even been used to fit lattice parameters to powder diffraction data [113] and other problems.

The input structure to PHIT is very similar to that of FEFFIT. The user specifies a group of `set` and `guess` variables in the same manner as in FEFFIT². A set of lineshapes is specified and parameterized in terms of the `set` and `guess` values. The same Levenberg–Marquardt [61] algorithm used in FEFFIT is used in PHIT. Statistical analysis is performed by PHIT, including computation of error bars on the fitting parameters and of correlations between the parameters.

It is common in the literature to fit lineshapes to XANES spectra and to interpret energy positions and line widths in terms of molecular orbitals. I find these interpretations ambiguous. My purpose in fitting lineshapes to the spectra shown in this chapter is to develop a numerical representation of the edge structure and to isolate the portions of the spectra that show temperature dependence from those parts that

¹ I usually pronounce this “pee-hit” to disguise the fact that this is a really dumb name for a computer program.

² See Appendix A or the FEFFIT document [52] for the details of using FEFFIT.

are essentially constant with temperature. In all these data it is a good approximation to leave most of the lineshapes constant in temperature within the limited energy range that I consider and to measure the variation of the lineshape used to describe the peak that arises from the off-center displacement of the titanium atom.

An example of fitting a set of lineshape to XANES data is shown in Fig. 7.2. These data are the titanium K edge of polycrystalline BaTiO_3 at 80 K. The fit uses three lineshapes. Since I don't wish to ascribe any physical significance to any of these lineshapes, I am free to choose lineshapes that provide a faithful numerical representation of the data. In Fig. 7.2, I used two Lorentzians for the two peaks. The background portion of the fit is an arctangent function with an energy dependent prefactor. In the fits to the data at varying temperatures, the parameters for the higher energy peak and for the background were held constant and only the height of the lower energy peak function was varied.

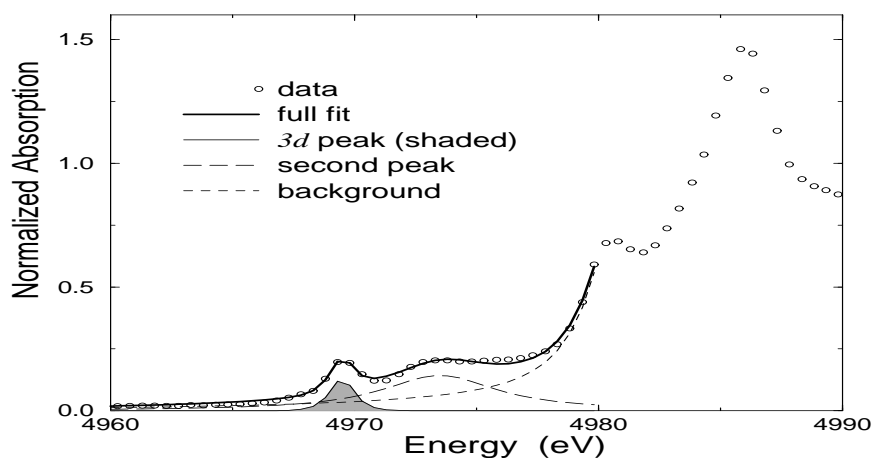


Figure 7.2: Example use of PHIT to obtain a numerical representation of the titanium XANES spectrum of polycrystalline BaTiO_3 at 80 K. The area of the shaded region is measured to obtain the temperature dependence of the peak that arises from the displacement of the titanium atom.

7.3 The Temperature and Polarization Dependence of the XANES Spectra of BaTiO₃

In Ch. 5 I analyzed the EXAFS spectra of BaTiO₃ as a function of temperature through the various phase transitions. From the behavior of the σ^2 of the barium–titanium bond I argued that the order–disorder model provides a more suitable explanation of the local structure than does the displacive model. Since fits using average structure predicted by the displacive model are as satisfying by statistical criteria as are fits using the rhombohedral local structure predicted by the order–disorder model, it is necessary to examine the XANES spectra of polycrystalline and single crystal BaTiO₃ samples. The temperature dependence of the XANES spectrum in a polycrystalline sample is shown in Fig. 7.3. Room temperature single crystal data obtained as described in Sec. 3.2.2 are shown for BaTiO₃ in Fig. 7.4 and, for comparison, for PbTiO₃ in Fig. 7.5.

Examining the polycrystalline data shown in Fig. 7.3 with Eq. 7.1, it follows that the titanium atom sits in a non-centrosymmetric site in BaTiO₃, as there is a distinctive peak in the spectra at each temperature. However information about the direction of \vec{d} is not available in polycrystalline data. To determine the direction of \vec{d} , I examine the single crystal, single domain spectra of BaTiO₃ and PbTiO₃ shown in Figs. 7.4 and 7.5. There is a significant difference in the oriented spectra of PbTiO₃ but only a small difference in the oriented spectra of BaTiO₃. As discussed in the following paragraphs, the PbTiO₃ data indicate a tetragonal titanium distortion, i.e. \vec{d} is along a $\langle 001 \rangle$ axis, while the BaTiO₃ data indicate a nearly rhombohedral displacement, i.e. \vec{d} approximately along a $\langle 111 \rangle$ axis.

To understand why the BaTiO₃ and PbTiO₃ XANES data indicate these directions for the titanium distortions, consider the local environments about the titanium atom predicted by the displacive and eight–site models. They are depicted in the cartoon shown in Fig. 7.6. Fig. 7.6a shows the tetragonal titanium distortion predicted by the displacive model for a crystallographically tetragonal phase. The titanium atom, depicted by the head of the arrow, is displaced in the $\langle 001 \rangle$ direction. The entire crystal is tetragonally distorted and the macroscopic polarization points along a tetragonal axis. If the polarization vector of the x–rays is parallel to the crystallographic c axis, thus parallel to \vec{d} , the area \mathcal{A} under the peak will be large. If the polarization is perpendicular to \vec{d} , then $\hat{\epsilon} \cdot \vec{d} = 0$ and \mathcal{A} will vanish. This picture is consistent with the PbTiO₃ data but not with the BaTiO₃ data. As shown in Ch. 4 and in Refs. [18] and [19] the local structure of PbTiO₃ is tetragonal at

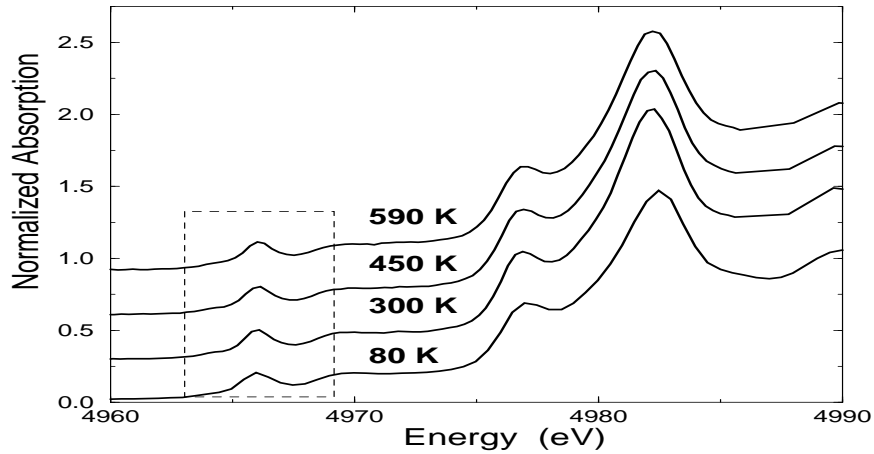


Figure 7.3: The titanium *K* edge XANES spectrum of polycrystalline BaTiO₃ at several temperatures. 80 K is in the rhombohedral phase, 300 K is in the tetragonal phase, the remaining two temperatures are in the cubic phase. The peak discussed in this chapter is shown within the dashed box.

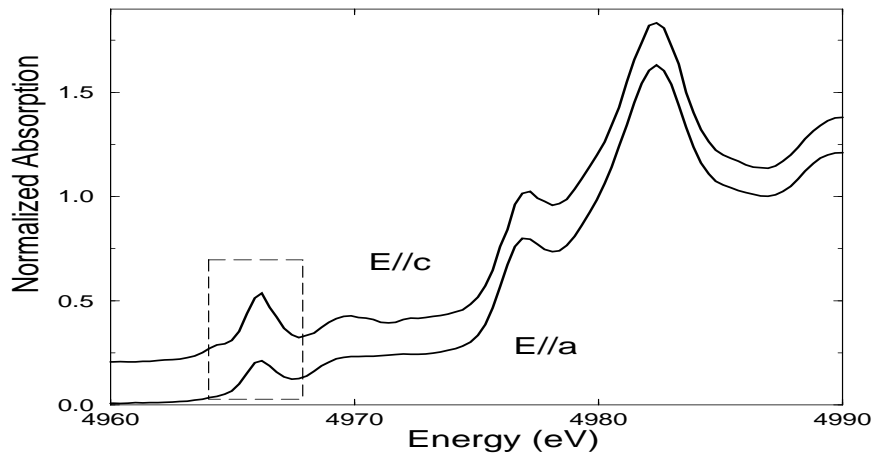


Figure 7.4: Titanium *K* edge XANES of single domain, single crystal BaTiO₃ with the x-ray polarization parallel (top) and perpendicular (bottom) to the crystallographic *c*-axis. See Sec. 3.2.2 for a discussion of isolating the spectrum for $\hat{\epsilon} \parallel \hat{c}$.

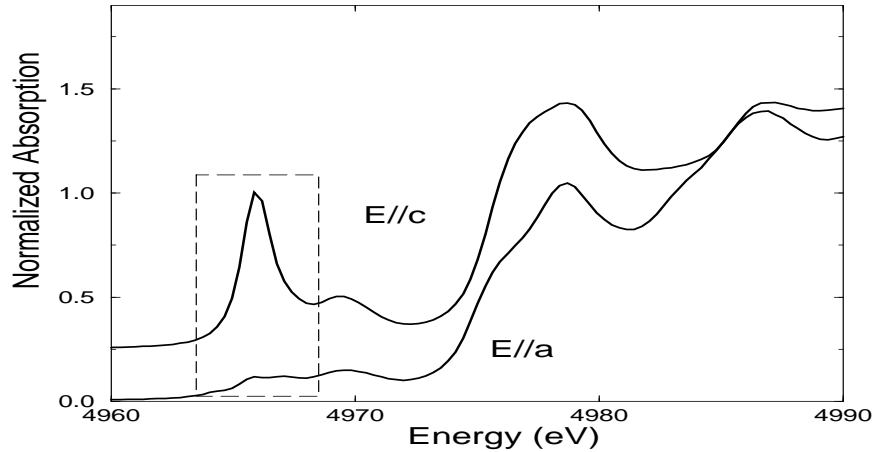


Figure 7.5: Titanium K edge XANES of single domain, single crystal PbTiO_3 with the x-ray polarization parallel (top) and perpendicular (bottom) to the crystallographic c -axis. See Sec. 3.2.2 for a discussion of isolating the spectrum for $\hat{\epsilon} \parallel \hat{c}$.

room temperature. A local tetragonal distortion of the titanium atom in BaTiO_3 would be inconsistent with its XANES spectra, as the peak does not vanish when the polarization is perpendicular to the c axis.

Fig. 7.6b shows a two-dimensional “four-site” schematic of the eight-site model for a crystallographically tetragonal phase. In this model, the titanium atom is always displaced towards the corner of the unit cell. In three dimensions this displacement is in a $\langle 111 \rangle$, or rhombohedral, direction. In this phase, the titanium displacement is randomly distributed among those directions with a positive component along the c -axis. In each unit cell, the local distortion and the local dipole point in a rhombohedral direction. When these vectors are averaged over the entire crystal, the observed displacement and macroscopic polarization point in a tetragonal direction.

XAFS, however, is sensitive only to the local structure. When the polarization of the x-rays is parallel to the crystallographic c -axis in Fig. 7.6b, $\hat{\epsilon}$ and \vec{d} form a 45° angle. When the polarization is perpendicular to the crystallographic c -axis, $\hat{\epsilon}$ and \vec{d} again form a 45° angle. In both orientations $\cos^{-1}(\hat{\epsilon} \cdot \hat{d}) = 45^\circ$, thus $\mathcal{A}_{\parallel} = \mathcal{A}_{\perp}$. This is close to the behavior of the data in Fig. 7.4. These spectra demonstrate that the order-disorder model describes the tetragonal phase of BaTiO_3 .

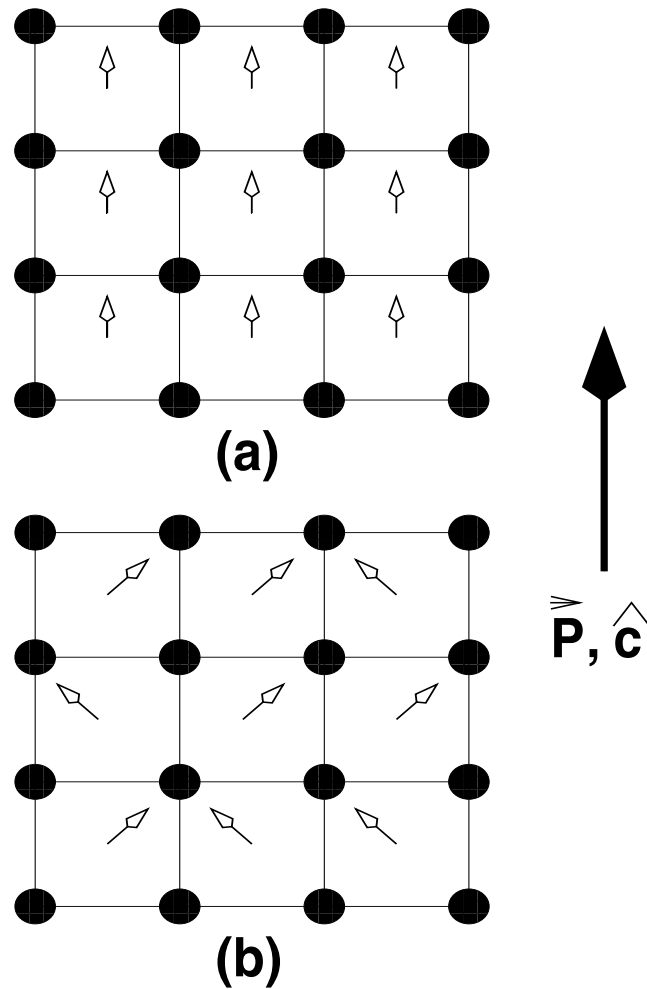


Figure 7.6: Cartoon representing the local structures of tetragonal BaTiO₃ in the displacive (a) and order-disorder (b) models. The macroscopic polarization \hat{P} is in the \hat{c} direction. The large arrow between the panel indicates the direction of the macroscopic polarization and the c -axis of the crystal. The shaded circles represent the barium atoms, the heads of the arrows represent the titanium atoms, and the oxygen atoms have been left out.

In the range of temperatures shown in Fig. 7.3, the area under the peaks changes from 0.20(3) eV to 0.15(2) eV. By Eq. 7.1, the magnitude of \vec{d} decreases by only about 13 percent from its value of 0.23(5) Å as measured from our 35 K EXAFS data. In this temperature range, the thermal root mean square displacement of the titanium atom from its site near the center of the oxygen octahedron given the values of σ^2 for the titanium–oxygen bond are much too small to account for the size of the peak [114]. Since the local distortion persists well into the cubic phase, these data, like the polarization dependent data in Fig. 7.4, cannot be explained by the displacive model. Together with the barium EXAFS results, these XANES spectra demonstrate that the local displacement of the titanium atom in BaTiO₃ is approximately in a rhombohedral direction at all temperatures and that an order-disorder model explains the dominant behavior of the local structure throughout its the phase transitions. The small displacive component of \vec{d} is smoothly varying through the various phase transitions and $|\vec{d}| > 0$ at all temperatures.

There is one more piece of information about the local structure of BaTiO₃ contained in Fig. 7.4. The peaks in the parallel and perpendicular orientations are of similar area, but not quite the same. The areas under these peaks are $\mathcal{A}_{\parallel} = 0.39(04)$ eV and $\mathcal{A}_{\perp} = 0.17(02)$ eV. Applying Eq. 7.1 to these areas, I find them consistent with \vec{d} lying 11.7(1.1)° towards the c axis away from the $\langle 111 \rangle$ axis. This is a believable result for the tetragonal phase. The presence of a macroscopic polarization reasonably could bias the locations of the minima in the local potential surface slightly away from the $\langle 111 \rangle$ axes in the direction of the macroscopic polarization. Our measurements show a slightly altered case of the eight–site model wherein the strain introduced by the macroscopic polarization is accommodated by the appropriate displacements of the adiabatic minima away from the $\langle 111 \rangle$ axes. Although this sort of fine detail about the local structure is not resolved with statistical significance using the barium K edge EXAFS data alone, adding the single domain XANES results requires a modified eight–site model to completely explain our XAFS data.

As mentioned in Sec. 4.1, a recent diffraction measurement [96] of PbTiO₃ at low temperature suggested the possibility of a low temperature orthorhombic phase. This suggests the possibility of an eight–site disorder model in PbTiO₃. The spectra shown in shown in Fig. 7.5 precludes this possibility. The local displacement of the titanium atom is clearly tetragonal at 300 K. For an eight–site model to explain the low temperature orthorhombic phase, a *different* local environment about the titanium site would be required at low temperature. In light of the results of this thesis, that seems unlikely. If a low temperature orthorhombic phase in fact exists in

PbTiO₃, I would hypothesize that the titanium displacement must be in a pseudo-tetragonal direction. The $\frac{a}{b}$ ratio reported in Ref. [96] is only about 1.00015 at 75 K. This is smaller than a typical uncertainty in bond length measurement in an EXAFS experiment. The presence of this additional phase cannot be resolved unambiguously in an EXAFS measurement. For comparison, recall that the $\frac{c}{a}$ ratio in PbTiO₃ is 1.065 at room temperature.

7.4 Relating the 3d Peak to the Local Distortion in PbTiO₃, BaTiO₃, and EuTiO₃

As discussed in Sec. 7.1, the peak just above the Fermi energy in the titanium perovskites is due to the overlap of the titanium d states with the oxygen p states. For a polycrystalline sample, the simple perturbation argument of Eq. (7.1) relates the area of the peak to the square of the magnitude of the displacement of the titanium atom from the center of the oxygen octahedron. In the simplest case, the A cation would not contribute to the area of the peak and a common constant of proportionality between \mathcal{A} and d^2 would be observed in all titanium–oxygen octahedrons. In this section I measure that proportionality constant for each of PbTiO₃, BaTiO₃, and EuTiO₃.

7.4.1 Polycrystalline PbTiO₃

The XANES spectrum of polycrystalline PbTiO₃ is shown in Fig. 7.7 at various temperatures spanning the phase transition temperature at 763 K. I measured the areas under these peaks using the method described in Sec. 7.2. These areas are plotted in Fig. 7.8. Note that the peak area diminishes as the phase transition temperature is approached from below, consistent with a small displacive component of the behavior of the local distortion. There is a discontinuity in the area slightly above³ T_c . This behavior is consistent with the weak first order behavior of the macroscopic order parameter. The area remains large above T_c , indicating that the local distortions

³ To avoid distortion of the data due to inhomogeneity in the thickness of radiation shield covering the furnace, holes were cut in the radiation shield to allow the unobstructed passage of the incoming and fluoresced photons. These large holes produce a temperature gradient in the furnace such that the surface of the furnace is cooler than its center. The samples must be at the surface and exposed to the incident x-rays, while the thermocouple was shielded by metallic pieces of the furnace. Consequently the sample was cooler than the thermocouple. Examining Fig. 7.8, it appears that the sample was about 15 K cooler at T_c , as the discontinuity just above T_c probably represents the true phase transition temperature.

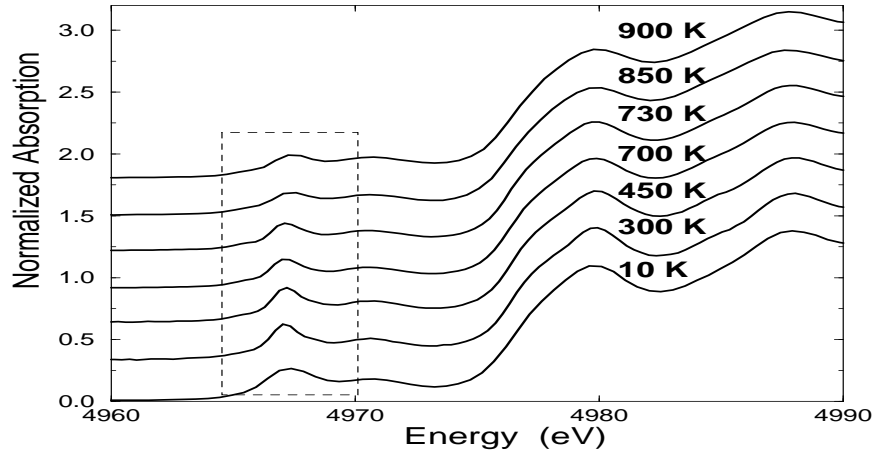


Figure 7.7: The Titanium K edge XANES spectrum of PbTiO_3 at several temperatures in the tetragonal and cubic phases. The peak discussed in this chapter is shown within the dashed box.

persist well into the high temperature phase and requiring that they be disordered to produce the cubic crystallographic phase. The dominant contribution to the error bars in Fig. 7.8 is systematic and is due to the uncertainties in the temperature independent parameters used to describe the portions of the edge structure to either side of the peak at 4966 eV as described in Sec. 7.2. These systematic uncertainties are independent of temperature and will not effect the temperature dependence of the area shown in Fig. 7.8. The statistical uncertainty of these area measurements is apparently quite small, as the scatter in the points around 740 K is much smaller than the error bars dominated by systematic uncertainties

The distortion parameter d obtained from analysis of the PbTiO_3 EXAFS is defined in Eq. (4.1) and plotted as a function of temperature in Fig. 4.9. Using these values for d and the area shown in Fig. 7.8, the constant of proportionality γ for PbTiO_3 is $12.3(1.4) \frac{\text{eV}}{\text{\AA}^2}$. Alternately, the crystallography measurement on PbTiO_3 [90] gives a titanium distortion parameter of 0.308 \AA at 300 K. Using this and the peak area at 300 K gives $\gamma = 14.2(8) \frac{\text{eV}}{\text{\AA}^2}$. The temperature dependence of the distortion parameter calculated from the peak areas and this proportionality is shown by the crosses in Fig. 7.8 and compared to the distortion parameter obtained from

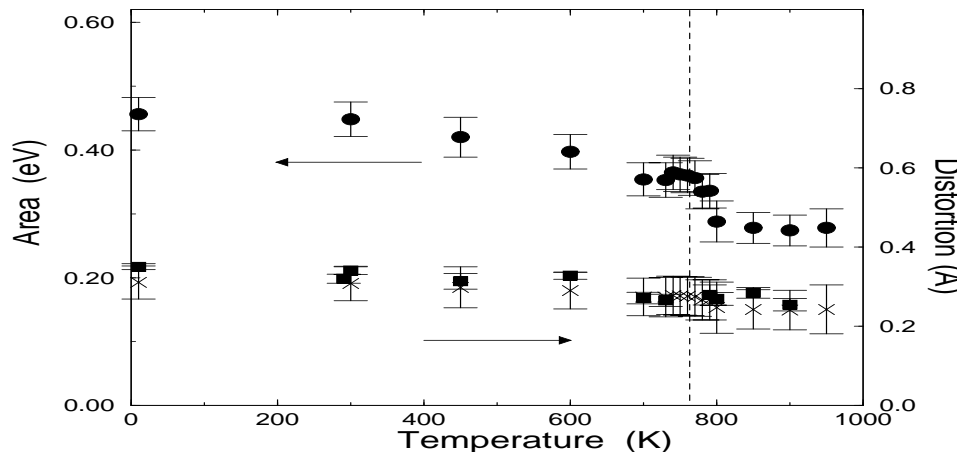


Figure 7.8: Areas (\bullet) under the near edge $3d$ peaks in the titanium K edges of PbTiO_3 as a function of temperature. Also plotted are the are the distortion parameters measured from the EXAFS (\blacksquare) and shown in Fig. 4.9 compared with the distortion parameter extracted from the areas (\times) as described in the text.

the EXAFS, which are shown in both Figs. 4.9 and 7.8. These two measurements of the distortion parameter show excellent agreement within their uncertainties. Note that the area of the $3d$ peak, with its d^2 dependence, provides a much more accurate measurement of the temperature dependence of the local distortion than does the EXAFS. As seen in Fig. 7.8, the discontinuity at T_c is within the error bars in the plot of distortion, but is clearly evident in the plot of areas.

7.4.2 Polycrystalline BaTiO_3 and EuTiO_3

BaTiO_3

As indicated in Table 5.5, the fits to the barium edge data were insensitive to the rhombohedral distortion of the titanium atom, thus I could not accurately measure the temperature dependence of the displacement of the titanium atom from the center of the oxygen octahedron with my barium edge data. With the parameters set as indicated in Table 5.5, I measured the distortion parameter to be $0.23(1) \text{ \AA}$ at all temperatures. I then measured the areas of the peaks shown in Fig. 7.3 using the

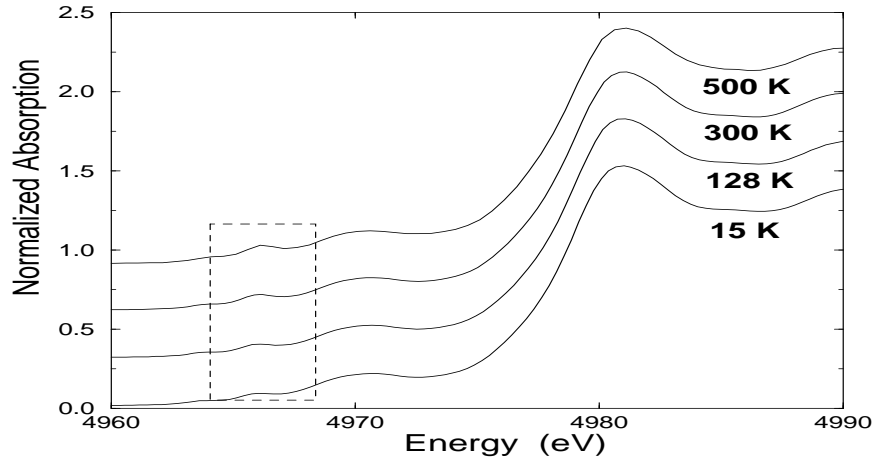


Figure 7.9: The titanium K edge XANES spectrum of EuTiO_3 at several temperatures. The peak discussed in this chapter is shown within the dashed box.

method described in Sec. 7.2. With these values obtained from the XAFS spectra, I obtain $\gamma = 11.1(1.6) \frac{\text{eV}}{\text{\AA}^2}$. Alternately using the 70 K crystallography data from Ref. [4] gives a displacement of 0.229 \AA for the titanium atom and $\gamma = 11.2(1.7) \frac{\text{eV}}{\text{\AA}^2}$.

EuTiO₃

The $3d$ peaks in the EuTiO_3 data shown in Fig. 7.9 are quite small. Small areas are difficult to measure by the technique of Sec. 7.2 since the systematic uncertainties of the technique are similar in size to the area. Instead, I evaluated difference spectra in the near edge region between the 15 K data and the data at each of the higher temperatures. I then measured the area between 4965 and 4968 eV using a simple trapezoid integration. The results are given in Table 7.1. Using the thermal distortion parameters from Table 6.4, I obtain a proportionality constant of $\gamma = 13.6(2.8) \frac{\text{eV}}{\text{\AA}^2}$.

7.4.3 Summary of Polycrystalline Results and Comparison with XANES Calculations

Table 7.2 summarizes my measurements of the proportionality constant relating the $3d$ peak area and the titanium displacement in PbTiO_3 , BaTiO_3 , and EuTiO_3 . These

Table 7.1: Areas of the $3d$ peaks in EuTiO_3 . These are the areas of the difference spectra between the 15 K data and the higher temperature data, thus there is no area for the 15 K data. The variation in peak areas in the data is typically about 5% between scans at the same temperature.

temperature	area
15 K	—
128 K	0.031 eV
300 K	0.057 eV
500 K	0.089 eV

numbers are in reasonably good agreement with one another. From these results I hypothesize that the proportionality constant γ is insensitive to the species of the A cation in these three titanium oxide perovskites. Averaging over the values given in Table 7.2 gives $\gamma = 12.5(1.4) \frac{\text{eV}}{\text{\AA}^2}$.

Although the agreement in the measurement of γ is fairly good, the γ 's obtained using the crystallographic value of d for PbTiO_3 and BaTiO_3 disagree with one other outside their error bars. There is some missing physics in the simple argument presented in Eq. (7.1). In the molecular orbital picture, the peak is due to the overlap of the titanium $3d$ states with the surrounding oxygen $2p$ states. The amount of hybridization depends not only on the size of the distortion of the titanium atom from a site of point centrosymmetry, but also on the proximity of the ions. If the ions are farther apart, then the spatial overlap of the electron wave functions will be smaller. I suggest that the large value of $\gamma = 14.2(0.8) \frac{\text{eV}}{\text{\AA}^2}$ for PbTiO_3 is due to enhancement of the hybridization due to the short titanium–axial oxygen bond length. The parameterization of the effect of the bond length is unclear at this time.

In Chs. 8 and 9 I describe a newly developed *ab initio* XANES code which I use to calculate the effect on the XANES of the displacement of the titanium atom from its centrosymmetric site in EuTiO_3 . These calculations are shown in Fig. 7.10. The solid line is a calculation using the cubic perovskite structure. This shows good agreement in the region of the $3d$ peak, although the calculation fails to resolve the next peak at about 4970 eV. For the other two calculations, I introduced tetragonal distortions of the titanium and oxygen atoms like those found in PbTiO_3 while retaining the cubic axis lengths. As the size of the displacement of the titanium atom used in the calculation grows, the size of the calculated $3d$ peak grows.

Table 7.2: Proportionality constants between \mathcal{A} and d^2 for PbTiO_3 , BaTiO_3 , and EuTiO_3 . The first three columns use the distortion parameter d determined from the EXAFS results presented in Chs. 4 – 6. The last two columns use d determined from low temperature diffraction measurements on PbTiO_3 [90] and BaTiO_3 [4]. The units are $\frac{\text{eV}}{\text{\AA}^2}$.

using d from EXAFS			using d from cryst.	
PbTiO_3	BaTiO_3	EuTiO_3	PbTiO_3	BaTiO_3
12.3(1.4)	11.1(1.6)	13.6(2.8)	14.2(0.8)	11.2(1.7)

I measured the areas of the peaks in these calculations by subtracting the calculation on the undistorted structure from the calculations on the distorted structures and measuring the areas of the difference spectra between 4963 and 4970 eV. Using the distortion parameter defined by Eq. (4.1), I obtain a constant of proportionality of $18.0(0.3) \frac{\text{eV}}{\text{\AA}^2}$. For comparison, a similar calculation to Fig. 7.10 is shown for PbTiO_3 in Fig. 9.11. I measured the constant of proportionality for the PbTiO_3 calculation in the same manner as for the EuTiO_3 calculation and obtained $15.8(0.6) \frac{\text{eV}}{\text{\AA}^2}$. The calculated proportionality constant is systematically larger than the experimental number, but the area shows the same dependence on the square of the displacement parameter.

7.4.4 *PbTiO₃ Single Crystal Data*

In this section I interpret single crystal PbTiO_3 titanium K edge XANES measurements within the context of the order–disorder model discussed in Ch. 4. There are, unfortunately, significant systematic problems with the data in this section. I collected single crystal PbTiO_3 data on two occasions, April and November of 1995, and both data sets are affected by experimental problems. The first attempt at collecting the data was plagued by difficulties with the temperature controlling apparatus, while the second data set shows systematic distortions to the data on a scale larger than the effect that I intend to measure. Consequently, I have discarded the second data set. After describing the problems with the temperature controller in the first data set and how I have accounted for them, I will interpret these data.

The major problem in the April 1995 data set was that a J–type thermocouple was used as a temperature sensor while the temperature controller used in the course

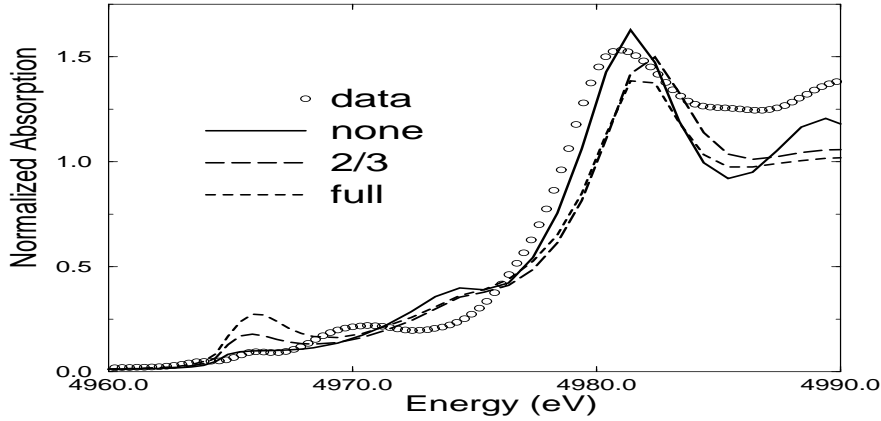


Figure 7.10: Comparison of data and calculation of the titanium K near edge structure in EuTiO_3 . The data is transmission XAFS. The solid line is the XANES calculation using the cubic perovskite structure from Ref. [108]. The short dashed line is a calculation on this same structure, but with tetragonal fractional distortions of the oxygen and titanium atoms from sites of centrosymmetry in the unit cell equal to those in PbTiO_3 as given in Table 4.4. The long dashed line is a calculation with those distortions reduced by $\frac{1}{3}$. The cell axis lengths are the same in all three calculations.

of the experiment was calibrated for K-type thermocouples. Consequently, the temperature readings for this part of the single crystal data set are incorrect. For both orientations, I intended to take data at 300, 400, 500, 600, and 700 K, however the temperatures above room temperature were systematically higher than anticipated. By consulting tables of voltages for the two types of thermocouple, I was able to approximate the true temperature on the sample at the time of the measurement. The temperatures for these data in the ferroelectric phase are 300, 431, 568, 707, and 830 K. This last temperature is in the paraelectric phase. Other than the ambiguity about temperature, this data set seems to be of good quality and is used throughout this section. I guess that the uncertainty in temperature measurement in the data presented in this section is less than 20 K. Clearly this situation is unsatisfactory. The best course is to remeasure the single crystal data so that the results of this section can be verified.

Measuring disorder using the peak areas

Shown in Figs. 7.11 and 7.12 are the temperature dependences of the single crystal PbTiO_3 data with $\hat{\epsilon} \parallel c$ and $\hat{\epsilon} \perp c$. Note that the magnitude of the $\hat{\epsilon} \parallel c$ peak in the box in Fig. 7.11 diminishes with increasing temperature while the $\hat{\epsilon} \perp c$ peak in the box in Fig. 7.12 increases with increasing temperature. In Fig. 7.11, the peak becomes much smaller in the high temperature phase as the local distortions become disordered.

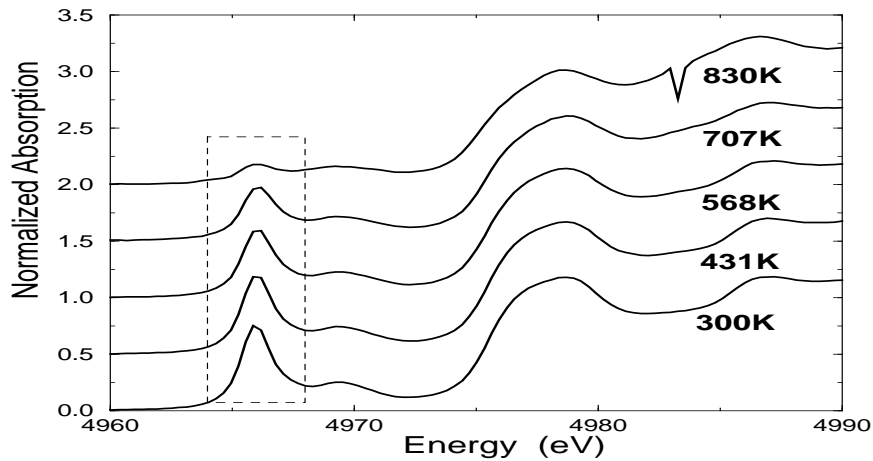


Figure 7.11: The titanium K edge XANES spectrum of PbTiO_3 with $\hat{\epsilon} \parallel c$ at several temperatures in the tetragonal phase and one temperature in the cubic phase.

In a displacive model for the temperature dependence of the PbTiO_3 local structure the size of the peak in the c polarized data would shrink proportionately to the titanium displacement, which would be relaxing with temperature into a centrosymmetric position. The titanium displacement as measured by x-ray diffraction is shown by the crosses in Fig. 4.9. Above T_c the titanium atom would relax completely to a site of point centrosymmetry and the peak would vanish. The a polarized peak would grow only slightly due to the increasing thermal distortion parameter. The Einstein temperature for the titanium–oxygen bond in PbTiO_3 is given in Ch. 4 as 582(20) K.

In an order–disorder model, the behavior of the c peak with temperature would be similar to its behavior by the displacive model. The disordering of the local

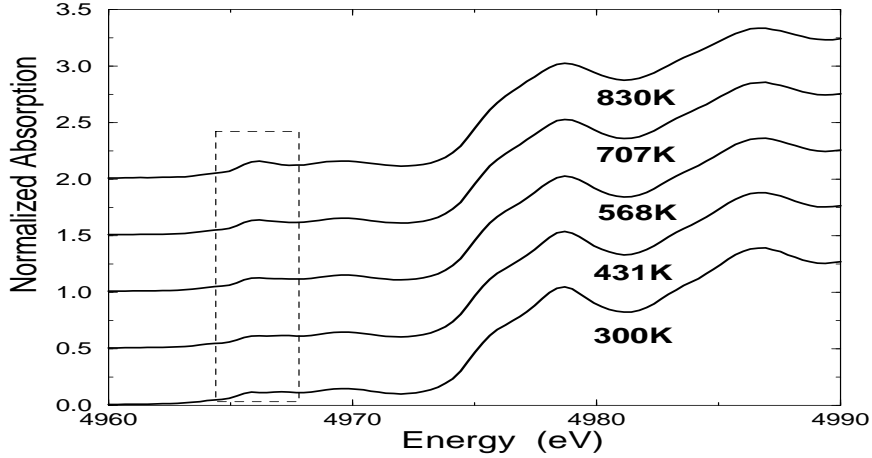


Figure 7.12: The titanium K edge XANES spectrum of PbTiO_3 with $\hat{\epsilon} \perp c$ at several temperatures in the tetragonal phase and one temperature in the cubic phase.

displacements and local elongations of the c -axis result in 90° rotations of the local structure. Thus some fraction of the local displacements that were aligned parallel to $\hat{\epsilon}$ at lower temperature rotate away from that direction. The c peak thus diminishes. Similarly, the a peak grows due to some number of local displacements rotating to an orientation parallel to $\hat{\epsilon}$. The main difference in the temperature dependence of the XANES between the two models is that the a -axis grows faster under the order-disorder model.

Assuming the order-disorder model, the fraction of local unit cells rotated away from the nominal polarization can be determined from the temperature dependence of the peak areas. If x is the fraction of local cells rotated

$$\mathcal{A}_c(T) = (1 - x)\mathcal{A}_c(0) \frac{d_T^2}{d_0^2} \quad (7.2)$$

$$x = 1 - \frac{d_0^2}{d_T^2} \frac{\mathcal{A}_c(T)}{\mathcal{A}_c(0)} \quad (7.3)$$

where $\mathcal{A}(T)$ is the area at temperature T and $\mathcal{A}(0)$ is the area at zero temperature. To accurately measure the fraction of cells rotated away from this orientation, the measurements of the areas must be scaled by the by the size of the titanium displace-

ments at low and high temperature. For this I use the displacements obtained from the polycrystalline peak areas shown in Fig. 7.8.

Similar expressions can be constructed for the temperature dependence of the a peaks

$$\mathcal{A}_a(T) = \frac{x}{2} \mathcal{A}_c(0) * \frac{d_T^2}{d_0^2} \quad (7.4)$$

$$x = 2 \frac{d_0^2}{d_T^2} \frac{\mathcal{A}_a(T)}{\mathcal{A}_c(0)} \quad (7.5)$$

The factor of two in the a peak equations arises from the equivalence of the a and b axes. When a local unit cell rotates away from the macroscopic \hat{c} direction, it will end up in one of the two equivalent a directions. In my experiment, one of these directions was parallel to the incoming x-ray polarization and one was perpendicular. Note that, in these equations, I assume that the contribution to the a -axis peak due to the σ^2 of the titanium-oxygen bond is small as the Einstein temperature was measured to be 582(2) K.

To measure the area of these peaks, I made two assumptions, both of which seem reasonable in light of the EXAFS results on PbTiO₃ in Ch. 4. The first is that the disordering is negligibly small at room temperature so that the area of the c -axis peak at 300 K is the same as at 0 K. The second is that the a -oriented peak measured at 300 K is a good measure of the signal in the $3d$ region of the spectrum in the absence of distortion. Using these assumptions, I made the difference spectra shown in Fig. 7.13 by subtracting the 300 K a -axis data from each of the other oriented, single domain spectra. I used a trapezoid integration to obtain the area under $\hat{\epsilon} \parallel \hat{a}$ difference spectra. The temperature dependent part of the $\hat{\epsilon} \parallel \hat{c}$ difference spectra is the peak centered at 4966 eV. I measured the area under this using the method presented in Sec. 7.2.

Upon examination of the contents of Table 7.3, it is clear that single crystal peak areas are not consistent with the interpretation of the local structure presented elsewhere in this thesis. In fact, these measurements are not even consistent with one another in the cubic phase. There are several possible sources of error in this presentation.

1. The interpretation of disordered local displacements or its effect on the single crystal data is incorrect.
2. The determination of the temperatures as described at the beginning of this

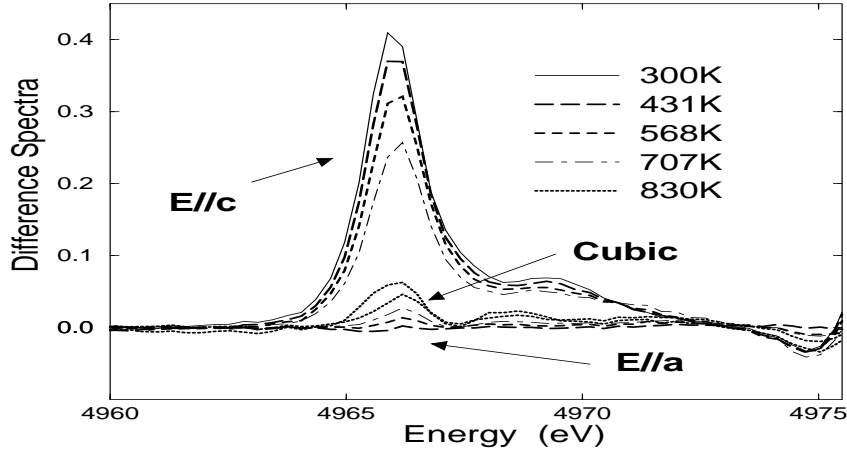


Figure 7.13: Difference spectra for the temperature and polarization dependent, single crystal PbTiO_3 Ti XANES spectra. The a spectrum at 300 K was subtracted from each of the other spectra to create the difference spectra. The dashed vertical lines indicate the region within which the areas in Table 7.3 were measured. The temperatures of the measurements of the a - and c -axis spectra are explained in the text.

Table 7.3: Fractions of rotated cells in PbTiO_3 computed using the the single crystal peak areas and assuming an order-disorder model. The temperatures for the two orientations are given as described in the text. The area are measured from the difference spectra in Fig. 7.13 as described in the text. x_a and x_c are evaluated using Eqs. 7.3 and 7.5. $x = \frac{2}{3}$ is expected in the cubic phase, i.e the three directions are equally occupied.

temp.	a area	x_a	c area	x_c
300 K	0 eV	0	0.704(9) eV	0
431 K	0 eV	0	0.632(10) eV	0.03(10)
568 K	0.011 eV	0.05(1)	0.533(12) eV	0.13(9)
707 K	0.027 eV	0.11(1)	0.403(13) eV	0.21(9)
830 K	0.060 eV	0.28(3)	0.087 eV	0.80(2)

section is incorrect. In fact, the values of x appear to be consistent if the *uncorrected* temperatures are used for x_a .

3. The separation of c -axis contribution from the measured signal as described in Sec. 3.2.2 was incorrect, resulting in an incorrect evaluation of $\mathcal{A}_c(0)$. It is possible to measure these data in a geometry that isolates the c -axis signal and does not require the data processing used in this thesis.

This analysis may benefit from re-collection of the single crystal, single domain data using an appropriate measurement geometry and a reliable temperature sensor. Certainly the assumptions made about the disordering of the local structure, the effect of disordering on the single domain XANES spectra, and the method of analysis must be reevaluated. This remains an open question in my thesis.

Measuring disorder using the axis lengths

The relationships between the average a - and c -axis lengths measured by diffraction and the local axis lengths measured by EXAFS can be written in similar form to Eqs. 7.2 – 7.5. The axis lengths of the crystallographic structure are the weighted average of the local axis lengths where the weights depend on the fraction of local cells rotated due to the disordering. If a_{cr} and c_{cr} are the average axis lengths measured by crystallography and a_{ex} and c_{ex} the local axis lengths measured by EXAFS, then the fraction of unit cells rotated as measured using the c -axis lengths is

$$c_{cr}(T) = (1 - x)c_{ex}(T) + xa_{ex}(T) \quad (7.6)$$

$$x_c = \frac{c_{ex}(T) - c_{cr}(T)}{c_{ex}(T) - a_{ex}(T)} \quad (7.7)$$

and using the a -axis lengths

$$a_{cr}(T) = (1 - \frac{x}{2})a_{ex}(T) + \frac{x}{2}c_{ex}(T) \quad (7.8)$$

$$x_a = \frac{2(a_{cr}(T) - a_{ex}(T))}{c_{ex}(T) - a_{ex}(T)}. \quad (7.9)$$

In the high temperature phase, I expect to find that $x = \frac{2}{3}$, which is the condition of complete disorder, i.e. that each direction is $\frac{1}{3}$ occupied.

A measure of the difference in the lattice lengths can also be expressed in terms

of x

$$\frac{c_{cr}(T) - a_{cr}(T)}{c_{ex}(T) - a_{ex}(T)} = 1 - \frac{3x}{2} \quad (7.10)$$

$$x_{diff} = \frac{2}{3} \left(1 - \frac{c_{cr}(T) - a_{cr}(T)}{c_{ex}(T) - a_{ex}(T)} \right) \quad (7.11)$$

In the high temperature, cubic phase, x in Eq. 7.11 evaluates to $\frac{2}{3}$ regardless of the the local axis lengths.

I use the data displayed in Fig. 4.6 to evaluate Eqs. 7.6 – 7.11. The measurements of the number of local unit cells rotated due to the disordering mechanism are given in Tab. 7.4. In the ferroelectric phase, the various measurements of x agree at each temperature within their uncertainties although the a -axis measurement is systematically smaller than the c -axis measurement. They agree within their error bars with the fractions measured from the peak areas. In the high temperature phase x_c is consistent with $\frac{2}{3}$, the condition of complete randomness, but x_a is not.

The discrepancies between the x_a and x_c in Table 7.4 indicate the level of systematic error in the axis lengths determined from the EXAFS measurements. It is possible that the fitting values in the fits presented in Sec. 4.2 (e.g. the axis lengths and the E_0 's for the various backscatterers) could be further refined with the constraint that x_a and x_c are more closely consistent. I imagine this constraint would change the values found in Sec. 4.2, but would not qualitatively change the results.

Table 7.4: Fractions of rotated cells in PbTiO_3 computed using the the axis lengths and assuming an order–disorder model. The fractions x_c are computed using Eq. (7.7), x_a using Eq. (7.9), and x_{diff} using Eq. (7.11). The last column is the σ^{-2} weighted average of the three previous columns. The data used to evaluate these equations is shown in Fig. 4.6.

temp.	x_c	x_a	x_{diff}	average
450 K	0.000(69)	-0.030(34)	-0.010(52)	-0.013(15)
600 K	0.183(40)	0.099(19)	0.155(22)	0.145(43)
700 K	0.270(99)	0.159(48)	0.233(46)	0.221(56)
730 K	0.372(118)	0.230(56)	0.324(41)	0.309(72)
800 K	0.747(137)	0.506(60)	0.667	0.627(170)
850 K	0.723(154)	0.554(70)	0.667	0.639(120)

Chapter 8

THEORY OF XANES

The literature on x-ray absorption spectroscopy (XAFS) traditionally places the cut-off between the near-edge (XANES) and extended (EXAFS) parts of the spectrum at about 20–40 eV above the Fermi energy. This distinction is somewhat ambiguous. As shown below in Eq. (8.1), the x-ray absorption cross section is related to Fermi's Golden Rule, which is a dipole matrix element that can, in principle, be evaluated at any energy. In that sense, there is no distinction between XANES and EXAFS. High order multiple scattering (MS) contributes strongly to the XANES and much less so to the EXAFS. The path expansion described in Sec. 2.1.2 converges to a good description of the EXAFS in a small number of terms, while a path expansion may require an enormous number of terms or simply fail to converge in the XANES region. Later in this chapter, I will suggest the convergence of the path expansion as an unambiguous criterion for the separation of XANES from EXAFS.

A practical reason for the distinction between XANES and EXAFS is their relative ease of analysis and interpretation. The EXAFS spectrum can usually be interpreted by considering the signal from some small number of scatterers. Usually single scattering and low order multiple scattering suffice to analyze the EXAFS spectrum and interpret it in terms of local atomic structure. As discussed in Ch. 2, EXAFS analysis is a signal processing problem with a well determined bandwidth. Typically an analysis of EXAFS can be parameterized with a number of variables which is small compared to the bandwidth.

Treating the XANES as a bandwidth limited signal and attempting to directly analyze it by the same techniques as those used in EXAFS analysis is not a promising approach. The mean free path λ of the photoelectron is typically a few Ångstroms at energies in the EXAFS region and will attenuate the contributions to the spectrum from very long paths. Even when forward modeling an EXAFS spectrum in energy space, very long paths can be neglected due to the attenuation by λ . In the XANES region, however, λ can be 10's of Ångstroms. Below the energy at which the photoelectron can excite a bulk plasmon, typically a few 10's of eV above the Fermi energy [115], it experiences only intrinsic losses, which are smaller than the loss due

to the plasmon excitation [116]. This results in a very long mean free path. Furthermore, the energy of the photoelectron in the XANES region is not large compared to the variations in the potential, thus high orders of multiple scattering will not be negligible compared to single scattering. Thus the consideration of many atoms and high order multiple scattering is required to understand the XANES. As the XANES extends only a few inverse angstroms in photoelectron wavenumber, the number of fitting parameters required to analyze so many paths would surely exceed the information content of the narrow bandwidth signal. Furthermore, the empirical isolation of the fine structure χ from the absorption spectrum μ using a technique such as that employed by AUTOBK is not reliable in general. Through the steeply rising part of the absorption edge, the spectrum changes too rapidly to be well approximated by a spline or similar functional form.

Despite the complexity of the XANES signal, it contains a wealth of information. As shown in Ch. 7, the XANES spectrum contains information about the local configurational environment about the absorbing atom. The XANES of materials is also examined for electronic information such as chemical valence and charge transfer. The prospect of interpreting the XANES using *ab initio* principles is compelling.

In this chapter, I present a full multiple scattering (FMS) theory of XANES. I will discuss the path expansion used successfully by FEFF to calculate the EXAFS and why it can fail in the XANES region. I will then present a development of the computational method of my FMS code XANES. In the following chapter, I will present results from the XANES code and discuss the interpretation of the XANES spectrum in terms of the FMS approach.

8.1 The Multiple Scattering Path Formalism

FEFF has proven successful as a tool for EXAFS analysis by providing accurate theoretical fitting standards. It uses a quickly calculated, rapidly convergent expansion of the free electron propagator to provide a convenient description of a multiple scattering problem in terms of scattering geometries. These calculations provide the theoretical fitting standards which are parameterized and used in a fit of the sort described in Ch. 2.

The absorption function measured by an XAFS experiment is related to the transition rate of the photoelectron from some initial deep core state, $|i\rangle$, to a final state above the Fermi energy, $|f\rangle$. This transition rate is determined within the one-electron

and dipole approximations by Fermi's Golden Rule [117]:

$$\mu \propto \sum_f |\langle f | \hat{\epsilon} \cdot \mathbf{r} | i \rangle|^2 \delta(\varepsilon_f - \varepsilon_i - \omega). \quad (8.1)$$

In this equation, $\hat{\epsilon} \cdot \mathbf{r}$ is the dipole operator for the incident electromagnetic wave on the system of atoms and electrons. Therefore, μ is a dipole matrix element of the initial core state and the final state restricted to those final states which are accessible by a incident photon of frequency ω . Throughout most of this chapter Hartree atomic units $\hbar = m = e = 1$ will be used.

Consider a flat interstitial potential V_{int} due to a system of ions and electrons in a crystal. The ions in the crystal are scattering sites of potential δV . The Hamiltonian for this system is $H = H_0 + V$. A one-particle Green's function for this Hamiltonian can then be written as $\mathbb{G} = 1/(E - H + i\zeta)$. Using the operator associated with this Green's function, $\sum_f |f\rangle \mathbb{G} \langle f|$, the expression for μ is rewritten

$$\mu \propto -\frac{1}{\pi} \text{Im} \langle i | \hat{\epsilon}^* \cdot \mathbf{r} \mathbb{G}(r, r'; E) \hat{\epsilon} \cdot \mathbf{r}' | i \rangle \Theta(E - E_F). \quad (8.2)$$

where Θ is the broadened Heaviside step function assuring that μ is non-zero only above the Fermi energy, i.e. only for incident photon energies that are large enough to promote the core electron into an unfilled state. This step function is Lorentzian broadened to account for the lifetime of the excited core hole and experimental resolution.

The \mathbb{G} defined above is the full one-electron propagator in the presence of the scattering potential. \mathbb{G} can be expressed in a series by the Dyson equation

$$\mathbb{G} = G^0 + G^0 T G^0. \quad (8.3)$$

G^0 is the free electron propagator, $G^0 = 1/(E - H_0 + i\zeta)$, and $T = V + V \mathbb{G} T$ is the atomic scattering matrix [21, 118]. The full scattering matrix is expressed in terms of the single site scattering matrices \mathbf{t} by

$$T = \mathbf{t} + \mathbf{t} G^0 \mathbf{t} + \mathbf{t} G^0 \mathbf{t} G^0 \mathbf{t} + \dots \quad (8.4)$$

Equation 8.3 is solved using Eq. (8.4) and expanded in a Taylor expansion

$$\mathbb{G} = \mathbf{G}^0 + \mathbf{G}^0 \mathbf{t} \mathbf{G}^0 + \mathbf{G}^0 \mathbf{t} \mathbf{G}^0 \mathbf{t} \mathbf{G}^0 + \dots \quad (8.5)$$

$$= (\mathbf{1} - \mathbf{G}^0)^{-1} \mathbf{G}^0 \quad (8.6)$$

The diagonal elements of first term are 1. Thus if all the elements of \mathbf{t} are zero, i.e. if there are no scatterers, then the free atom dipole matrix element is recovered in Eq. (8.2). \mathbf{G}^0 , the free electron propagator, describes the propagation of an electron from one angular momentum state in one atom to another atom and another angular momentum state and \mathbf{t} describes the scattering from each site. The successive terms are the successive orders of scattering contributing to the dipole matrix element. The second term contains the description of all single scattering events wherein an electron propagates to the scatterer, scatters from it, and propagates back to the first atom. The third term describes all events involving the scattering from two atoms before propagating back to the first atom. Higher order terms have similar interpretations.

FEFF explicitly calculates the terms of Eq. (8.5) for all propagations starting at the central atom, that atom which absorbed the photon and emitted a photoelectron.

$$\mathbb{G} = \mathbf{G}_c + \sum_{i \neq 0} \mathbf{G}_c \mathbf{t}_i \mathbf{G}_c + \sum_{\substack{i, j \neq 0 \\ i \neq j}} \mathbf{G}_c \mathbf{t}_i \mathbf{G}_{i, j}^0 \mathbf{t}_j \mathbf{G}_c \quad (8.7)$$

$$+ \sum_{\substack{i, k \neq 0 \\ i \neq j \\ j \neq k}} \mathbf{G}_c \mathbf{t}_i \mathbf{G}_{i, j}^0 \mathbf{t}_j \mathbf{G}_{j, k}^0 \mathbf{t}_k \mathbf{G}_c + \dots$$

$$\equiv \sum_{\substack{\text{all possible} \\ \text{paths}}} \mathbf{G}^\Gamma \quad (8.8)$$

\mathbf{G}_c is the free electron propagator between the central atom and some neighboring atom and $\mathbf{G}_{i, j}^0$ is the propagator between atoms i and j . The sums are over all possible scattering geometries of each order of scattering. The terms excluded from the sums are those for the propagation of an electron from some atom back to itself. The superscript Γ denotes some scattering path. FEFF determines all possible scattering geometries Γ within some cluster of atoms centered around the absorbing atom [119]. It then computes \mathbf{G}^Γ for each Γ individually.

FEFF determines the contribution of each scattering path to the total $\chi(k)$ of the problem by taking a trace¹ over azimuthal states of $\mathbf{G}_{L_f, L_f}^\Gamma$ for the central atom and

¹ This trace is for the case of a polarization averaged calculation. FEFF6 can also calculate χ for

the final state angular momentum. For a single scattering path, this is [30]

$$\chi^{\text{SS}} = \text{Im} \left(\exp(2i\delta_{l_f}) \frac{1}{2l_f + 1} \sum_m \mathbb{G}_{l_f m, l_f m}^{\text{SS}} \right) \quad (8.9)$$

where l_f is the final state angular momentum, R_0 is the central atom, δ_{l_f} is the central atom phase shift for angular momentum l_f . The contributions to χ due to higher order scattering are computed by similar traces.

8.2 The Full Multiple Scattering Formalism

The large photoelectron mean free path near the absorption edge means that, in the XANES region, the photoelectron probes scattering paths of very long paths lengths, including very high order paths which bounce around the atoms within a relatively small radius of the absorber. As the cluster size grows or as higher orders of multiple scattering are considered, the number of scattering paths required in a path expansion grows exponentially [119]. Although the task of enumerating all of these paths is automated by FEFF and any number of paths can, in principle, be considered, the path expansion may not be formally convergent near the absorption edge². Even a convergent expansion might consume significant resources of time, computer memory, and disk space. In the XANES region, it may be more practical to directly compute \mathbb{G} using Eq. (8.6).

To accomplish this, I encoded the direct calculation of \mathbb{G} into an automated Fortran program, XANES. In this and following section I will present the theory of the FMS method, and its application to computation of XANES spectra and of local electronic densities of state. Elements of FEFF are used to compute \mathbb{G}^0 and \mathbb{T} . Both \mathbb{G}^0 and \mathbb{t} are computed in a real-space basis of angular momentum and atomic position, $|\mathbf{L}\mathbf{R}\rangle$. The shorthand $\mathbf{L} = \{l, m\}$ will be used throughout this chapter.

8.2.1 The Scattering Matrix

A dimensionless scattering matrix is used

$$\mathbf{t}_{\mathbf{L}\mathbf{R}, \mathbf{L}'\mathbf{R}'} = e^{i\delta_l} \sin(\delta_l) \delta(l - l') \delta(\mathbf{R} - \mathbf{R}') \delta(m) \delta(m') \quad (8.10)$$

any path given arbitrary elliptical polarization.

²The criterion for formal convergence of the path expansion will be discussed in Sec. 8.2.3.

This dimensionless \mathbf{t} matrix lacks the factor of $\frac{1}{k}$ usually included in the scattering matrix [47]. The partial wave phase shifts δ_l are computed by FEFF from free atom relativistic Dirac–Fock potentials which are overlapped to form muffin tin spheres. The phase shifts are written to one of the output files of FEFF, `phase.bin`. The details of the potentials and phase shifts calculation are discussed in detail in several references [27, 29, 119, 120]. The Dirac delta functions restrict the \mathbf{t} matrix to its diagonal elements.

The diagonality of the \mathbf{t} matrix is due to an approximation used by FEFF to construct its muffin tin. FEFF uses a spherically symmetric charge density within the muffin tin spheres. Because of this approximation, the scattered photoelectron cannot change angular momentum state. This approximation lends computational efficiency to the code. The product $\mathbf{G}^0\mathbf{t}$ in Eq. (8.6) is made in n^2 time, where n is the dimension of the basis, rather than in n^3 time.

8.2.2 The Free Propagator Matrix

The exact calculation of the outgoing free electron propagator

$$\mathbf{G}^0(\mathbf{r}, \mathbf{r}'; E) = -\frac{e^{ik|\mathbf{r}-\mathbf{r}'|}}{4\pi k|\mathbf{r}-\mathbf{r}'|} \quad (8.11)$$

can be a substantial computational barrier to an FMS calculation as it must be projected onto the angular momentum space of the \mathbf{t} matrix.

\mathbf{G}^0 can be expanded about two fixed sites \mathbf{R} and \mathbf{R}' as

$$\mathbf{G}^0(\mathbf{r}, \mathbf{r}'; E) = \sum_{L,L'} j_L(\mathbf{r}-\mathbf{R}) j_{L'}^*(\mathbf{r}'-\mathbf{R}') \mathbf{G}_{L,L'}^0(\boldsymbol{\rho}). \quad (8.12)$$

The coefficients are products of spherical Bessel's function and spherical harmonics $J_L = i^l j_l(kr) Y_L(\hat{\mathbf{r}})$ and $\rho = p|\mathbf{R}-\mathbf{R}'|$ where p is complex momentum of the photoelectron given in Eq. (2.9).

The Rehr–Albers [30] algorithm is used to compute the coefficients $\mathbf{G}_{L,L'}^0(\boldsymbol{\rho})$. The aim of the Rehr–Albers algorithm is to separate these coefficients into products of radial and angular terms. The radial dependence is expressed as a fast, accurate expansion of z -axis propagators. The remainder of this section is adapted from Ref.

[30] and is included here in enough detail for the reader to reproduce XANES.

$$\mathbf{G}_{L,L'}^0(\boldsymbol{\rho}) = \frac{\exp(i\rho)}{\rho} \sum_{\mu=-l}^l \mathbf{R}_{m\mu}^l(\Omega_{\hat{\rho}}^{-1}) \mathbf{g}_{l,l'}^{|\mu|}(\rho) \mathbf{R}_{\mu m'}^{l'}(\Omega_{\hat{\rho}}). \quad (8.13)$$

The \mathbf{R} are rotation matrices in an angular momentum basis [117, 121] and the $\Omega_{\hat{\rho}}$ represent the Euler angles (α, β, γ) of the rotation of $\hat{\rho}$ onto the \hat{z} axis. Expressed in terms of polar angles, these rotations are $\Omega_{\hat{\rho}} = (0, \theta, \pi - \phi)$ for the forward rotation and $\Omega_{\hat{\rho}}^{-1} = (\phi - \pi, -\theta, 0)$ for the return rotation.

The $\mathbf{g}_{l,l'}^{|\mu|}(\rho)$ are the \hat{z} -axis propagators. These are expanded in terms of special functions

$$\mathbf{g}_{l,l'}^{|\mu|}(\rho) = \sum_{\nu=0}^{\min(l,l'-|\mu|)} \tilde{\gamma}_{\mu\nu}^l(\rho) \gamma_{\nu\mu}^{l'}(\rho). \quad (8.14)$$

The γ -functions are polynomials related to spherical Hankel functions by Eqs. (8.15) and (8.18) below.

Letting $\eta = -i/\rho$, the outgoing spherical Hankel function can be written in terms of another polynomial, c_l :

$$h_l^+(\rho) = -i^{-l-1} \eta e^{1/\eta} c_l(\eta). \quad (8.15)$$

The c_l follow the standard Bessel function recurrence relation:

$$\begin{aligned} c_0(\eta) &= 1 \\ c_1(\eta) &= 1 - \eta \\ c_{(l+1)}(\eta) &= c_{(l-1)}(\eta) - (2l + 1) \cdot \eta \cdot c_l(\eta) \end{aligned} \quad (8.16)$$

Differentiating the recurrence relation in Eq. (8.16) yields the following relations for $c_l^\nu = (\partial^\nu / \partial \eta^\nu) c_l$

$$\begin{aligned} \frac{\partial^\nu}{\partial \eta^\nu} [c_{(l+1)}(\eta)] &= \frac{\partial^\nu}{\partial \eta^\nu} [c_{(l-1)}(\eta) - (2l + 1) \cdot \eta \cdot c_l(\eta)] \\ &\Downarrow \\ c_{l+1}^\nu(\eta) &= c_{l-1}^\nu(\eta) - (2l + 1) \cdot \eta \cdot (c_l^\nu(\eta) + c_l^{\nu-1}(\eta)) \\ c_\nu^\nu(\eta) &= (-1)^\nu \cdot \frac{(2\nu)! \eta^\nu}{2^\nu \nu!} \end{aligned} \quad (8.17)$$

The γ -functions are

$$\begin{aligned}\gamma_{\mu\nu}^l(\rho) &= (-1)^\mu N_{l\mu} \frac{c_l^{\mu+\nu}(\eta)}{(\mu+\nu)!} \eta^{\mu+\nu} \\ \tilde{\gamma}_{\mu\nu}^l(\rho) &= \frac{(2l+1)c_l^\nu(\eta)}{N_{l\mu}\nu!} \eta^\nu\end{aligned}\quad (8.18)$$

where $N_{l\mu}$ are the spherical harmonic normalization factors

$$N_{l\mu} = \left[\frac{(2l+1)(l-\mu)!}{4\pi(l+\mu)!} \right]^{\frac{1}{2}}$$

For small η , $c_l(\eta) \rightarrow \exp(i l(l+1)/2\rho) \cdot (1 + l(l+1)/2\rho^2)^{\frac{1}{2}}$ [30, 43]. At large ρ , the first correction to the asymptotic form of the Hankel function is of the size of $l(l+1)/2\rho$ [117]. When this correction term is small, the $c_l(\eta)$ reduce to plane waves. If we consider that $|p|$ is about 1–3 in the XANES region and that a typical cluster size in a calculation is about 5 Å, then ρ is $\mathcal{O}(10^1)$. Partial wave scattering is important within the “centrifugal barrier”, i.e. for l such that $l_{max} \lesssim kR_{MT}$ where R_{MT} , the muffin tin radius, is 1–2 Å. Thus a typical l_{max} in a xanes calculation is 3. The correction term is not small and plane waves should not be used in the XANES region [43].

With this, Eq. (8.14) is solved. The rotation matrices \mathbf{R} in Eq. (8.13) are energy independent and calculated by an iterative technique [117, 121]. As the rotation matrices are independent of energy, they may be calculated once for all pairs of atoms in the cluster and saved for use at each energy point. Although saving all rotation matrix elements within a large cluster requires significant computer memory, doing provides considerable computational efficiency. Finally, Eqs. (8.13) and (8.10) are used to solve the FMS matrix \mathbb{G} by Eq. (8.6) in the $|\mathbf{LR}\rangle$ basis.

This approach to calculating \mathbb{G} is solved entirely in real space with no assumption of symmetry or periodicity. Unlike band structure based approaches to calculating absorption spectra and electronic densities, this method may be applied equivalently to crystals and non-crystals, including surfaces, biological materials, quasicrystals, amorphous solids and liquids, and others.

The Rehr–Albers technique is stable, accurate, and quickly convergent compared with other techniques of computing \mathbb{G}^0 [122, 123]. This speed is a significant feature of the FMS method presented here. Profiling [124] the execution of my XANES code

reveals that about 16 percent of its execution time is spent evaluating the $\mathbf{g}_{l,l'}^{|\mu|}(\rho)$ terms for a medium sized problem, such as the boron nitride calculations shown in Sec. 9.3. This is only a few percentile fewer than the time spent inverting $(1 - \mathbf{G}^0\mathbf{t})$. As the size of the basis increases, the time spent on the matrix inversion scales faster than the evaluation time of the $\mathbf{g}_{l,l'}^{|\mu|}(\rho)$ terms. For the copper calculation in Sec. 9.1, 8 percent of the two hour execution time was spent calculating the $\mathbf{g}_{l,l'}^{|\mu|}(\rho)$ terms while about 50 percent of the time was spent on matrix inversion. Calculating \mathbf{G}^0 is a significant fraction of the execution time spent on a problem of any size. The speed of the Rehr–Albers algorithm is a significant feature of XANES.

8.2.3 Matrix Algebra

Solving Eq. (8.6) is a problem of matrix inversion. There are several standard techniques for tackling a matrix inversion. In XANES, I use a Lower–Upper (LU) [125] decomposition, a speedy, reliable technique for the decomposition of an arbitrary matrix with no particular internal symmetries, such as triangularity, diagonality, or sparseness. An LU decomposition can, however, provide an unstable solution for a singular or nearly singular matrix. In that case, the answer provided by the LU decomposition can be dominated by numerical error. As an option, XANES can perform the matrix decomposition with a Singular Value Decomposition (SVD) [125]. The SVD is slower than LU and requires more computer memory, but provides a numerically reliable approximate solution for a singular or nearly singular matrix. In practice an LU decomposition of $(1 - \mathbf{G}^0\mathbf{t})$ is usually adequate³. Excellent descriptions of both the LU and SVD techniques can be found in Numerical Recipes [126].

The solution of Eq. (8.6) is the most significant computational bottleneck of the FMS technique. The time necessary to solve Eq. (8.6) scales as n^3 where n is the number of states $|\mathbf{LR}\rangle$ in the problem. The R basis is the number of atoms in the chosen cluster and the L basis spans all angular momentum and azimuthal states of

³ In fact, I have yet to find a case where SVD and LU give different answers. The SVD is necessary in a case where the matrix $(1 - \mathbf{G}^0\mathbf{t})$ is close enough to being either row or column degenerate that computer roundoff error dominates the computation of the decomposition. Even in cases where the convergence criterion of Eq. (8.20) is not met, the decomposition of the $(1 - \mathbf{G}^0\mathbf{t})$ is computationally stable and the LU suffices.

the atoms in the cluster.

$$\begin{aligned}
 N_{\text{states}} &= \sum_i l_{\text{max}}^i (l_{\text{max}}^i + 1) \\
 &\leq N_{\text{atoms}} \times l_{\text{max}} (l_{\text{max}} + 1)
 \end{aligned}
 \tag{8.19}$$

Here l_{max}^i is the maximum angular momentum state to be considered for atom i and l_{max} is the largest angular momentum state considered for any atom in the cluster. It is clearly advantageous to keep the size of the basis as small as possible without discarding any important physics.

The rule that the centrifugal barrier, $l_{\text{max}} \approx pR_{\text{MT}}$, limits the importance of the terms in the angular momentum expansion can be used. Here p is the complex momentum and R_{MT} is the muffin tin radius of the atom. The energy dependence of the centrifugal barrier limits the practical extent of the full multiple scattering approach to a few 10s of eV above the edge. The centrifugal barrier provides a practical, computational barrier between the XANES and EXAFS regions of the XAFS spectrum. l_{max} is less than 4 in an energy range extending to about 25 eV above the Fermi energy. If the basis of the FMS calculation is restricted to $l \leq 3$, then about 25 eV is the energy at which the XANES becomes the EXAFS.

The question of the convergence of the path expansion can be addressed by examination of the matrix $\mathbf{G}^0\mathbf{t}$. There is a theorem of linear algebra [127] which states

<p>If the moduli of the eigenvalues of all eigenvectors of \mathbf{A} are less than 1, then $(\mathbf{1} - \mathbf{A})^{-1}$ is non-singular, and the series</p> $ \mathbf{1} + \mathbf{A} + \mathbf{A}^2 + \mathbf{A}^3 + \dots $ <p style="text-align: right;">(8.20)</p> <p>converges to $(\mathbf{1} - \mathbf{A})^{-1}$.</p>
--

A Schurr factorization [125] is used in XANES to compute the eigenvalues of $\mathbf{G}^0\mathbf{t}$. The applicability of this convergence criterion to the MS XAFS problem is discussed in Ref. [46].

It would be interesting to examine the convergence properties of $(\mathbf{1} - \mathbf{G}^0\mathbf{t})$. The following are still open questions about the FMS matrix:

- Are there classes of materials for which $(\mathbf{1} - \mathbf{G}^0\mathbf{t})$ is or is not convergent throughout the XANES region? Are these classes based on coordination, electronic properties, element composition, or any other common characteristic?

- For materials for which $(1 - \mathbf{G}^0 \mathbf{t})$ is convergent, how many and what kinds of paths are required to reach convergence?
- For materials with convergent $(1 - \mathbf{G}^0 \mathbf{t})$, is it more efficient computationally to use a path expansion or an FMS technique?
- How important is convergence? That is, can a finite path expansion in a material with a non-convergent FMS matrix produce physically meaningful results?

8.2.4 Computing χ and μ

Once Equation 8.6 is calculated, χ_{FMS} , the full multiple scattering fine structure, can be extracted from $\mathbb{G}_{L,L'}(\boldsymbol{\rho}, E)$ in a manner equivalent to Eq. (8.9)

$$\chi_{FMS} = \text{Im} \left(\exp(2i\delta_{l_f}) \frac{1}{2l_f + 1} \left[\sum_m \mathbb{G}_{L,L'}(\boldsymbol{\rho}, E) \right] \right) \times \delta(\mathbf{R} - \mathbf{R}_{central}) \delta(\mathbf{R}' - \mathbf{R}_{central}) \delta(l - l_f) \delta(l' - l_f) \delta(m - m'). \quad (8.21)$$

The Dirac delta functions restrict this trace to the central atom and to the angular momentum of the photoelectron final state l_f . The trace is over $\boldsymbol{\rho} = 0$ terms of the Green's function, as indicated by the delta functions in \mathbf{R} and \mathbf{R}' . The site-projected χ functions used to compute the local densities of state in Sec. 8.2.5 involve similar traces over different sites. I use this notation to underscore the similarity of the χ functions used the calculation of the XANES and of the densities of state.

The polarization dependence of χ_{FMS} is extracted from the l_f submatrix by projecting the submatrix onto the polarization vector expressed in an angular momentum basis. This can be solved for an arbitrary photoelectron final state and for arbitrary ellipticity of the incoming photon⁴. For K edges and linear polarization, the projection of χ onto the polarization vector is

$$\chi_{FMS}(\hat{\boldsymbol{\epsilon}}) \propto \sum_{m,m'} \hat{\boldsymbol{\epsilon}}_{m'}^* \cdot \mathbf{G}_{1m1m'}(\rho) \cdot \hat{\boldsymbol{\epsilon}}_m. \quad (8.22)$$

In a XANES experiment the total absorption $\mu(E)$, is measured. $\mu(E)$ contains both the embedded atom absorption μ_0 [58] and the fine structure $\chi(E)$. It is not, in general, practical to extract $\chi(E)$ from a measurement due to the difficulties of

⁴ One would use Eq. B2 of Ref. [27]. The XANES program currently only calculates linear polarization for $l_f = 1$.

determining the rapidly varying part of the background function in the real data near the absorption edge. Consequently, a calculation of μ_{FMS} is more useful than χ_{FMS} for comparison with experiment.

Eq. (8.13) has a prefactor of $1/\rho$ and two rotation matrices for the angle between $|\mathbf{R} - \mathbf{R}'|$ and \hat{z} . $\mathbf{G}_{L,L'}^0(\boldsymbol{\rho})$ is thus ill-defined for $\mathbf{R} = \mathbf{R}'$. As an aid in computation, the elements of \mathbf{G}^0 which are diagonal in the R basis are set to zero. This has the additional advantage of forcing to zero the contributions to \mathbb{G} which propagate an electron from an atom to the same atom.

The embedded atom background μ_0 is obtained by directly evaluating the dipole matrix element of Eq. (8.1) for the central atom. This is calculated by FEFF at the same time as the partial wave phase shifts δ_l and is saved to a file called `xsect.bin`. The full multiple scattering absorption cross-section μ_{FMS} is computed from μ_0 and Eq. (8.21)

$$\mu_{FMS}(E) = \mu_0(E)(1 + \chi_{FMS}(E)) \quad (8.23)$$

$\mu_0(E)$ is computed by directly evaluating the integral in Eq. (8.1) using the deep core initial state and the final state of the embedded atom, i.e. the neutral atom within the muffin tin potential. This calculation is performed by FEFF and written to one of its output files, `xmu.dat`.

For comparison to experiment, it is useful to allow for adjustments to the Fermi energy and the line broadening of the calculation. FEFF provides an approximation to the Fermi energy and uses tabulated values for core-hole lifetimes γ_{ch} as a broadening term. An experiment might be further broadened by monochromator resolution or electronic effects in the material. The Fermi energy and broadening are included in the calculation by multiplying the spectrum by a function $\Theta(E_F)$ which is zero below E_F and 1 above. This product is then convolved with a Lorentzian \mathcal{L} of a width w . w is the sum of γ_{ch} and an additional broadening chosen to account for experimental effects.

$$\mu_0^C = \mathcal{L}(E, w) \otimes \left[\Theta(E_F)\mu_0(E) \right] \quad (8.24)$$

$$(\mu_0\chi_{FMS})^C = \mathcal{L}(E, w) \otimes \left[\Theta(E_F)\mu_0(E)\chi_{FMS}(E) \right] \quad (8.25)$$

$$\mu_{FMS}^C = \mu_0^C + (\mu_0\chi_{FMS})^C \quad (8.26)$$

8.2.5 Local Electronic Densities of State

The electronic density of state (DOS) matrix is related [22, 23, 118, 128] to the Green's function by

$$\boldsymbol{\varrho} = -\frac{1}{\pi} \text{Im } \mathbb{G} \quad (8.27)$$

We can evaluate the angular momentum projected DOS at each atom centered at \mathbf{R}_i in the cluster

$$\varrho_{l,\mathbf{R}_i}(E) = \int_0^{r_N} d^3(|\mathbf{r} - \mathbf{R}_i|) \text{Tr}_m \left[|R_L(\mathbf{r} - \mathbf{R}_i)|^2 \boldsymbol{\varrho}_{L\mathbf{R}_i, L\mathbf{R}_i}(E) \right] \quad (8.28)$$

The radial integral is performed out to the Norman radius of the atom centered at \mathbf{R} . The Norman radius is the radius of a sphere approximating the volume of the the Wigner–Seitz cell in a crystalline material. The Norman sphere contains a neutral atom. $R_L(\mathbf{r} - \mathbf{R}_i)$ is the radial wave function centered at \mathbf{R}_i . The trace is over all azimuthal states of R_L and of the density matrix. Expressed in this manner, $\varrho_{l,\mathbf{R}}(E)$ is solved analogously to Eq. (8.23).

$$\varrho_{l,\mathbf{R}_i}(E) = \varrho_{l,\mathbf{R}_i}^0(E) (1 + \chi_{l,\mathbf{R}_i}(E)) \quad (8.29)$$

The fine structure projected onto a specific site i and angular momentum ℓ is calculated in a manner analogous to Eq. (8.21)

$$\begin{aligned} \chi_{\ell,i} = \text{Im} \left(\exp(2i\delta_{\ell,i}) \frac{1}{2\ell + 1} \left[\sum_m \mathbb{G}_{L,L'}(\boldsymbol{\rho}, E) \right] \right) \times \\ \delta(\mathbf{R} - \mathbf{R}_i) \delta(\mathbf{R}' - \mathbf{R}_i) \delta(l - \ell) \delta(l' - \ell) \delta(m - m'). \end{aligned} \quad (8.30)$$

The atomic electronic densities for each embedded atom and angular momentum state are computed directly from the atomic wave functions:

$$\varrho_{l,i}^0(E) = \frac{2p \cdot 2(2l + 1)}{\pi} \left| \int_0^{r_N} d^3(|\mathbf{r} - \mathbf{R}_i|) R_l(\mathbf{r} - \mathbf{R}_i, E) \right|^2. \quad (8.31)$$

The integral is over the embedded atom radial function, which matches to an outgoing Hankel function at r_N . The first factor of 2 is for spin degeneracy, the $2(2l + 1)$ is from

the radial average and sum over azimuthal states, and p is the complex momentum.

Eqs. (8.30) and (8.31) are solved and put into Eq. (8.29) for the site and angular momentum projected DOS. The DOS projected onto a site is

$$\varrho_i(E) = \sum_l \varrho_{l,i}(E) \quad (8.32)$$

the total DOS for the cluster is

$$\varrho(E) = \sum_l \sum_i \varrho_{l,i}(E). \quad (8.33)$$

8.2.6 Computing the Fermi Energy and Charge Transfer

The Fermi energy for the cluster of atoms in a calculation can be obtained by integrating ϱ from Eq. (8.33) until all valence electrons N_e are accounted for.

$$\begin{aligned} N_e &= \int^{E_F} \varrho(E) dE \\ &= \sum_l \sum_i \int^{E_F} dE \varrho_{l,i}(E) \end{aligned} \quad (8.34)$$

The lower bound on this integral is the bottom of the valence band. In the muffin tin potential of FEFF7 this is a rather ambiguous concept. The bottom of the valence band is near the level of FEFF's interstice, but usually slightly below. The interstice in FEFF is at the energy of the flat portion of the muffin tin. When FEFF7 constructs its muffin tin, some of the charge gets pushed below the interstice. To work with my XANES code, I modified FEFF7 to continue its calculation of $\varrho_{l,i}^0(E)$ below the interstice.

In XANES the number of valence electrons is taken to be the number of free atom electrons in energy states above the level of the interstice as calculated by FEFF. I modified FEFF to write a file containing enough information to determine the number of valence electrons in the cluster.

The charge and orbital occupancy of a site can be calculated by neglecting one or both of the summations in Eq. (8.34). The evaluation of net charge can also be split into central atom and scattering components by separately evaluating the integrals of $\varrho_{i,\mathbf{R}}^0(E)$ and $\varrho_{l,\mathbf{R}}^0(E)\chi_{l,\mathbf{R}}(E)$. The calculations are shown for boron nitride in Sec.

9.3.

For an open structure such as boron nitride, it may be necessary to consider that some valence charge does not reside within the Norman sphere, which was determined for the free atom. That charge will be accounted for in Eq. (8.29). The effect of the open structure is that the integral of $\chi_{l,\mathbf{R}}(E)$ will be negative below the Fermi energy. The charge removed from the Norman spheres is in the open regions of the structure. For a crystal such as boron nitride, this interstitial volume is calculated by subtracting the volume of the Norman spheres in the unit cell from the volume of the unit cell. Treating the electrons in this open region as a free electron gas yields [129]

$$N_{free} = \frac{V}{3\pi^2} \left(\frac{2m(E_F - E_{int})}{\hbar^2} \right)^{\frac{3}{2}} \quad (8.35)$$

where V is the volume of the open region and m is the electron mass. This value of N is added to the integral of Eq. (8.34) and E_F is found such that $N_{DOS} + N_{free}$ equals the number of valence electrons.

8.2.7 Limitations of the FMS Method

The FMS method is not a magic bullet for understanding absorption problems. It has several limitations.

Limitations of the muffin tin potential

Every approximation used to construct a muffin tin is most severe at low energy. The effects of a non-flat interstice and of neglecting charge transfer will, then, be most apparent in the XANES region of the absorption spectrum. The non-flat interstice can be handled by introducing off-diagonal terms in the \mathbf{t} matrix. This can be quite important for highly anisotropic materials or in materials with strongly directional covalence at the cost of a sizable increase in computation time. The effect of using neutral spheres to construct the muffin tin can be corrected by using the values for charge transfer from Eq. (8.34) to construct a new muffin tin potential. Doing so is the beginning of a self-consistency loop.

Limited energy range

Because the size of the required angular momentum basis increases dramatically at higher energies, the size of the computation basis scales as l_{\max}^2 , and the computation time scales as l_{\max}^6 . Thus there is a practical limit on the energy range of the technique. At energies in the EXAFS region of the spectrum,

the size of \mathbb{G} becomes a computational burden. Fortunately, the path expansion converges in a small number of terms in the EXAFS region.

Finite spatial dimension

Since the number of atoms in the cluster scales as the cube of the radius, large clusters are a computational burden. Limiting the size of cluster neglects the contribution from paths which leave the cluster. Also, care must be taken to avoid surface effects in the construction of the muffin tin. This is easily avoided by constructing the muffin tin with a much larger cluster than is used in the FMS calculation.

Thermal disorder is incorrectly handled

My XANES code currently neglects thermal disorder. Thermal motion within the cluster can be approximated by multiplying each element of \mathbb{G} by an exponential of the mean square displacement about the value of $|\mathbf{R} - \mathbf{R}'|$ for that element. Looking at the expansion of Eq. (8.5), the σ^2 's of each leg will be added. However, consider the following two scattering paths:



The single scattering path is of total path length R and has a thermal mean square displacement σ^2 . The triple scattering path is of length $2R$. It should have a mean square displacement of $4\sigma^2$, but is given one of $2\sigma^2$ by the FMS technique. Other classes of paths are similarly mistreated by FMS. Fortunately, the exponential is a function of p^2 , which is small in the XANES region, so the mistreatment or neglect of the thermal disorder is generally a small effect.

Chapter 9

XANES SIMULATIONS

In this chapter, I discuss applications of the XANES code to real materials. A prominent member [130] of the XAFS community recently stated to an audience at the Ninth International Conference on XAFS that XANES is in a similar state to that of EXAFS at the first XAFS conference 14 years earlier. At that first XAFS conference, formal theories and analytical techniques for interpreting the EXAFS spectrum were in their infancy. Most papers on the topic of EXAFS presented their arguments in a descriptive, hand-waving manner. Today EXAFS is a mature and quantitative spectroscopy, but XANES is still hindered by a lack of rigorous technique. I make no claim in this chapter to provide qualitative formalism for XANES on par with what exists for EXAFS. I am confident, though, that what I present is a step towards that goal. What I present here is the equal of any extant XANES technique in the scientific literature. Here and in my discussion of future goals in Ch. 10, I present tools that I hope will help the development of XANES into a mature spectroscopy.

9.1 Copper

Following in a long tradition of XAFS theorists, I will start with a presentation of a calculation of FCC copper metal. The XANES portion of the copper spectrum is characterized by a famous¹ jog half way up its absorption edge. It has been shown [119, 120] that multiple scattering effects are required to reproduce this effect. With a sufficiently large cluster, the FMS technique should reproduce this feature.

In Fig. 9.1 I present a calculation of the the XANES spectrum in FCC copper using the path expansion of FEFF7. The atoms list for the FEFF input file was created by ATOMS using the FCC structure and an a lattice constant of 3.81. To make the thin solid line I used the exchange model of Hedin and Lundqvist and chose input parameters to FEFF to limit the number of paths considered². to 438 unique

¹ It is very common at XAFS beamlines at synchrotrons to calibrate monochromators by setting the peak of this distinctive feature to the published [131] absorption edge of 8979 eV.

² This was done by setting the length of the longest path considered by the path finder to 8 Å using

scattering paths. The bold solid line uses found 938 unique paths³ out of 151,784 total paths. This picture roughly reproduces Fig. 6.3 Alex Ankudinov's doctoral dissertation [120]. This is a fairly good simulation of the copper near edge and the approach to convergence is seen in the improvement between the 438 and 938 path calculations. To consider a path expansion using a larger value of `RMAX` would require careful use of the `CRITERIA` and `PCRITERIA` keywords of `FEFF`.

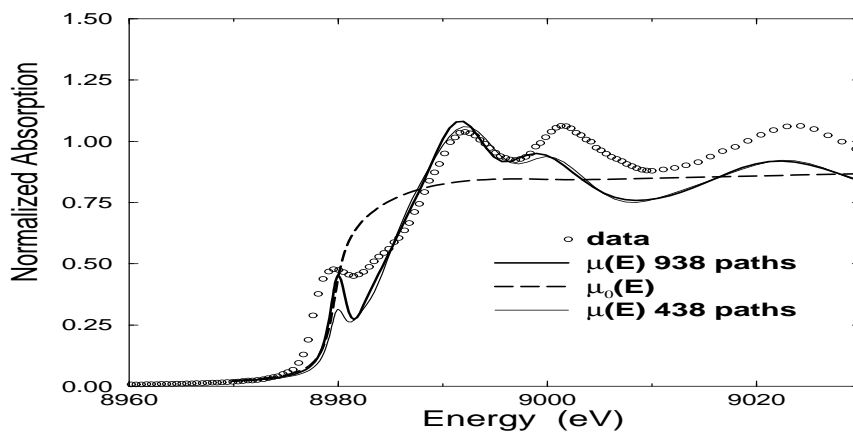


Figure 9.1: Copper K near edge structure in FCC copper as calculated by `FEFF7` using the `XANES` card. The data is transmission XAFS. The this solid line is a calculation using 438 unique paths out to 8 Å and the bold solid line uses 938 paths out to 9 Å. $\mu_0(E)$ is given by Eq. (8.23).

The result of a `XANES` run on FCC copper is shown in Fig. 9.2. The details of the run are shown in Table 9.1. This calculation takes under two hours of CPU time on an Indigo II workstation. We see a substantive improvement in the quality of the simulation out to about 8995 eV. The restriction of the angular momentum basis to $l \leq 2$ in the calculation becomes too severe of an approximation beyond that energy. Before that energy, the simulation is excellent. I conclude that the shortcoming of Fig. 9.1 is the use of a finite number of paths. Apparently scattering paths which include

the `RMAX` keyword and by rejecting paths of tiny amplitude by setting the `CRITERIA` keyword to 0.25 and 0.25 in the `FEFF` input file.

³ By setting `RMAX` to 9.

Table 9.1: Information about each of the XANES runs presented in this chapter. The “structure reference” column contains the crystallographic information used to make the input file for FEFF. The “exchange” column refers to the type of exchange–correlation potential used in FEFF, HL = Hedin–Lundqvist and GS = Ground State. The cluster size refers to the number of atoms within R_{max} from the absorber. The Fermi energy and additional broadening were applied by CORRECT. The Fermi energies refer to the energy axes of the appropriate figures and are not meant to indicate the Fermi energies on an absolute scale.

material	structure reference	exchange	R_{max}	cluster size	shells	angular momentum basis
Cu	[129]	HL	6.0 Å	79	5	Cu: <i>spd</i>
SF ₆	[132]	GS	2.0 Å	7	1	S: <i>spd</i> F: <i>sp</i>
BN	[133]	GS	5.0 Å	87	7	B: <i>sp</i> N: <i>sp</i>
PbTiO ₃	[84]	GS	5.0 Å	45	4	Pb: <i>spdf</i> Ti: <i>spd</i> O: <i>sp</i>

material	Fermi energy	additional broadening	notes
Cu	8978 eV	0	amplitude = 0.9 used in CORRECT
SF ₆	2485.7 eV	0.5 eV	
BN	195 eV	1.3 eV	ION 0 1 used in FEFF 1.385 Å ³ interstitial volume per atom
PbTiO ₃	4964.6 eV	0	300 K tetragonal structure ION 0 1 used in FEFF

atoms a long distance away from the absorber are less important than the high order scattering paths that bounce around inside a cluster of limited radial dimension. The restriction of the path list by half path length excludes high order paths of that sort. The calculation was much improved by expanding the cluster from four shells to five. The four shell calculation showed only a shoulder rather than a peak for the feature half way up the edge. The four shell calculation showed only a shoulder rather than a peak for the feature half way up the edge.

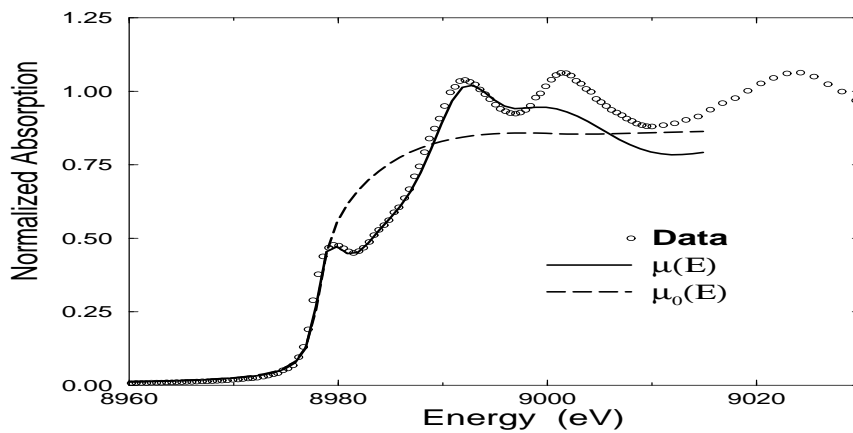


Figure 9.2: Copper K near edge structure in FCC copper. The data is transmission XAFS. $\mu_0(E)$ is given by Eq. (8.23).

The calculation of the Fermi energy as described in Sec. 8.2.6 was not successful in this case. E_{Fermi} was found by XANES to be 8981.4 eV, 3.4 eV higher than the value I used in CORRECT to produce Fig. 9.2.

There are significant differences in the region between about 8978 and 8993 eV in Figs. 9.1 and 9.2. Although, there seems to be a slow approach to convergence in that region between the two path expansion calculations shown in Fig. 9.1, neither path expansion calculation is a good approximation of the FMS calculation. I used Eq. (8.20) to determine the possibility of convergence of the path expansion. Shown in Fig. 9.3 are the largest eigenvalues of $G^0 t$. Starting just above the Fermi energy and extending for about 15 eV is a region in which the largest eigenvalues exceed 1 and, throughout the energy range of the peak in the middle of the edge, 5 to 10 percent of these eigenvalues are greater than 1. The path expansion is formally non-convergent in this region. It is possible that an acceptable path expansion calculation can be

made by consideration of a large number of paths, but that number must greatly exceed the 938 that I used in Fig. 9.1.

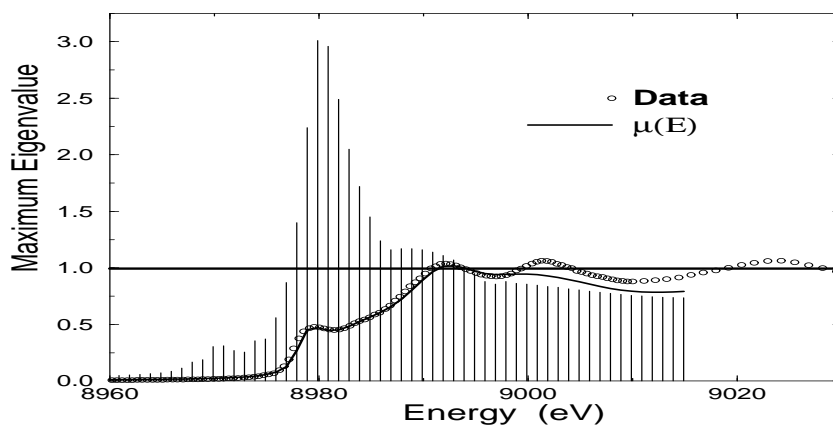


Figure 9.3: Eigenvalues of G^0t for copper computed using a Schurr factorization [125] and compared with the K edge FMS calculation and data. The impulses represent the largest eigenvalue of that matrix. The matrix $(1 - G^0t)^{-1}$ is non-convergent in a path expansion at energy points at which one or more eigenvalues of G^0t exceed 1.

9.2 Sulfur Hexafluoride

The result of the run on SF_6 using the example input files shown in Sec. C.1 is shown in Fig. 9.4A. This is a speedy calculation due to the small cluster size, running in under a minute on my Pentium 133⁴. The code reproduces well the white line and the large peak at 2550 eV. The agreement with the data is superior to a calculation [134] of this same material using the “extended continuum- $X\alpha$ ” method of Natoli, Benfatto, and others. Still there are approximations in this calculation. The XANES code operates within the one electron approximation, thus neglects multi-electron

⁴ The Pentium competes quite well with the Indigo II in terms of speed. However the Indigo II used for this work has six times the RAM of my Pentium. For large problems, my 32 MB Pentium is severely hampered by needing to access swap space continuously. This is actually a wonderful result. Modestly priced personal computers are quite up to the task of these calculations, provided that they are supplied with sufficient memory.

excitations. Some of the spectral features in the data may be explained in this way. Another possible shortcoming of the calculation is how the muffin tin potential is constructed for a molecule. The fluorine muffin tins are unbounded on the outside thus are poorly approximated by spherical muffin tins. One way of handling molecules within a muffin tin scheme is to apply an “outer sphere” potential [134] centered at the geometric center of the molecule to provide an outer bound to the potentials. This additional potential is another scattering site and may add structure to the calculation or slightly shift the peak locations⁵.

Another possible explanation for the missing spectral features in the calculation is suggested upon examination of the site and angular momentum projected DOS functions. The Sulfur d DOS is displayed in Fig. 9.4B. There is a large peak in this band very near in energy to the large peak in the data at about 2507 eV. It is well-known [136] that nominally octahedral hexafluoride compounds such as SF₆ and others are subject to pseudo-Jahn-Teller distortions. Just as the large peak in the titanium perovskite data shown in Ch. 7 arises from the local distortions of titanium-oxygen octahedrons, we may expect some sort of hybridization of sulfur p and d states in SF₆ due to a displacement of the sulfur atom from the center of the fluorine octahedron. Evidence is presented in Ref. [132] for the presence of strong t_{1u} and t_{2g} ⁶ vibrational modes allowing vibronic coupling of states of p and d character. In that reference, the authors speculate on the possibility that the pseudo-Jahn-Teller distortion in SF₆ is quite large.

To test the effect of a Jahn-Teller type distortion on the calculation I altered the FEFF input file shown in Fig. C.1 to include a distortion approximating the symmetry discussed in Ref. [132]. The altered list of atomic coordinates is shown in Fig. 9.5. The result of the calculation on this structure is shown in Fig. 9.6. The configurational distortion does introduce a peak at the energy of the peak in the sulfur d DOS. $X\alpha$ molecular orbital calculation [137] find a vibronically assisted but dipole-forbidden transition at the energy of that peak.

Including the configurational distortion in the calculation certainly does not fix all of the problems with this calculation. There are still significant differences between the data and the calculation, some of which may be due to lacking the many-body

⁵ Modifying FEFF to compute an outer sphere is a relatively simple problem. The partial wave phase shifts from the outer sphere could then be used in the calculation of the FMS matrix.

⁶ See Ref. [136] for some nice diagrams of these two vibrational modes. The t_{1u} mode involves anti-parallel displacements of the sulfur atom with planes of 4 fluorine atoms. The t_{2g} mode is a bending mode involving 4 fluorine atoms in a plane.

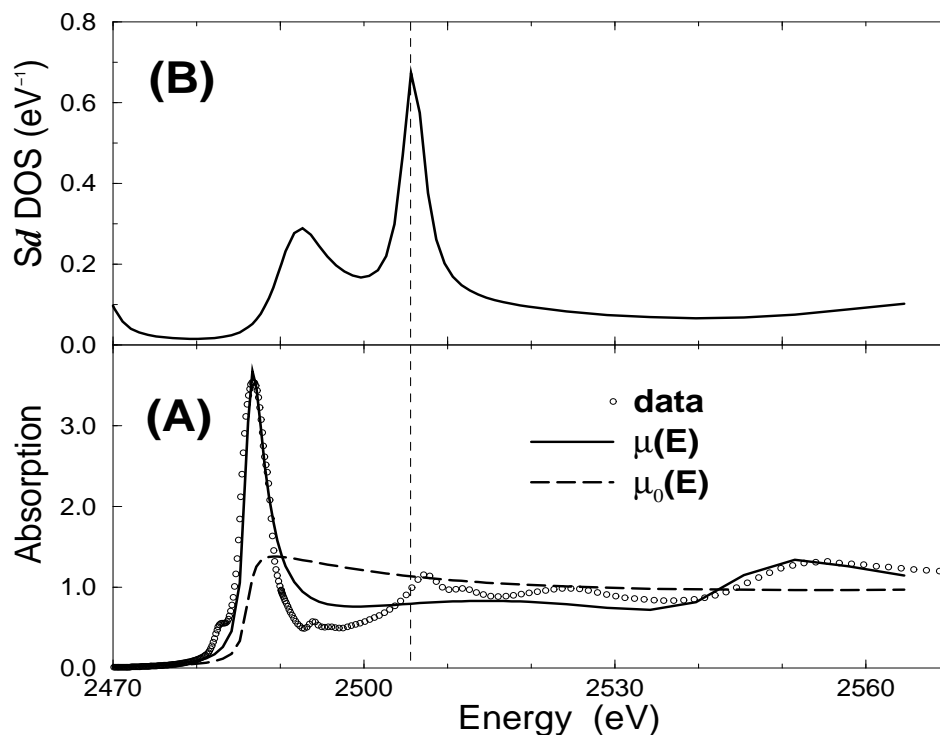


Figure 9.4: (Panel A) Sulfur *K* near edge structure in SF_6 . The data is gas phase transmission XAFS [135]. $\mu_0(E)$ is given by Eq. (8.23). (Panel B) The Sulfur *d* DOS. As discussed in the text, the large peak in the *d* DOS is closely situated in energy to the peak in the data at about 2507 eV. A distortion induced hybridization of sulfur *p* and *d* states can account for that feature in the data. The result of the calculation in the presence of a distortion is shown in Fig. 9.5. The vertical dashed line is a guide to the eye showing the proximity in energy of these features in the data and the sulfur *d* DOS.

```

ATOMS
*  x      y      z      ipot
   0.1    0.1    0.1     0          S absorber
   1.56   0.05   0.05    1          6 F backscatters
   0.05   1.56   0.05    1
   0.05   0.05   1.56    1
  -1.56   0.0    0.0     1
   0.0   -1.56   0.0     1
   0.0    0.0   -1.56    1

```

Figure 9.5: A sample FEFF input file for SF₆ for use with a run of XANES. The approximation of the pseudo-Jahn-Teller distortion is included in this input file.

effects or the outer sphere. Still, this result suggests that the FMS approach can be a useful tool for interpreting the XANES spectrum in structural terms. Additional computer experiments to probe the response of the calculated spectrum to changes in structure will be shown in Sec. 9.4. The utility of the simultaneous calculation of the XANES and the DOS functions is demonstrated in this example.

9.3 Boron Nitride

A calculation on the boron *K* edge of an 87 atom cluster of BN is shown in Fig. 9.7 and compared to electron energy loss near edge structure (ELNES) data. This calculation requires about 11 minutes of CPU time on an Indigo II. Despite the use of spherically symmetric muffin tins and non-self-consistent potentials, I find that this FMS technique is quite sufficient even for a strongly covalent material such as BN.

The site and angular momentum projected densities of state $\varrho_{l,i}(E)$ are shown in Figs. 9.8 and 9.9 by the thick solid lines. The embedded atom density $\varrho_{0l,i}(E)$ from Eq. (8.31) are given by the dashed lines. The $\varrho_{l,i}(E)$ are compared with the same functions calculated by a self-consistent linearized muffin-tin orbital (LMTO) calculation [139], which are the thin solid lines with diamonds (\diamond). The LMTO calculations were broadened by convolution with a Lorentzian of 1 eV half-width. Fig. 9.8 also shows $\varrho_l(E)$ for the ionized central atom, which is calculated in the presence of a core hole.

Using the method of Sec. 8.2.6 for computing the Fermi energy was successful in

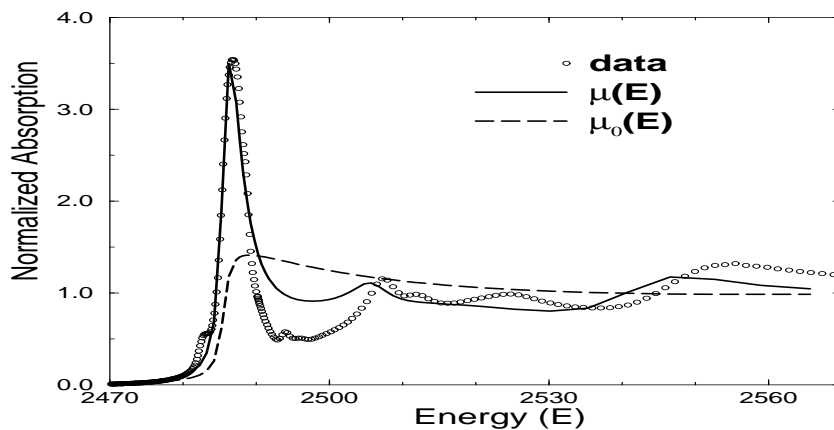


Figure 9.6: Sulfur K near edge structure in SF_6 . The data is gas phase transmission XAFS. [135] The calculation uses an atomic configuration chosen to simulate a Jahn-Teller distortion of the sort suggested in Refs. [136] and [132]. $\mu_0(E)$ is given by Eq. (8.23).

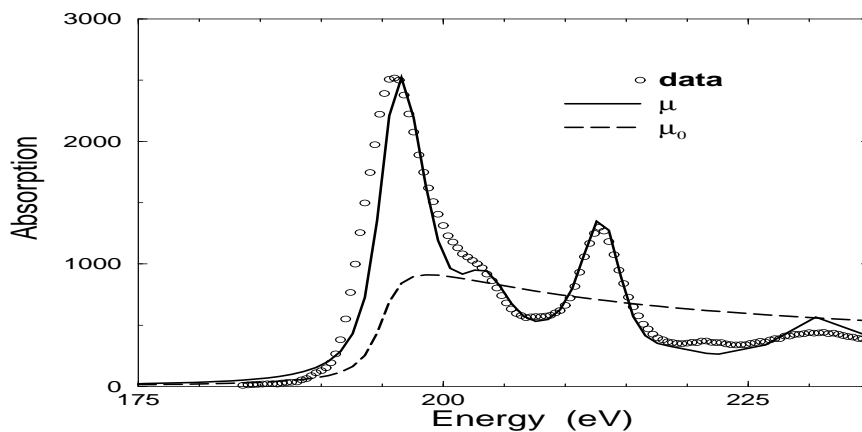


Figure 9.7: Boron K near edge structure in BN . The data is ELNES [138]. Additional broadening as given in Table 9.1 was added to the calculation to compensate for the low energy resolution of the ELNES experiment. $\mu_0(E)$ is given by Eq. (8.23).

this case. From the Norman radii of the atoms computed by FEFF (1.041 Å for B and 1.010 Å for N) and the lattice constant of the cubic unit cell (3.615 Å, 4 formula units per cell), I determined that for each atom in the unit cell of BN, there is 1.385 Å³ not occupied by any atom. This volume is assigned to the interstice and Eq. (8.35) was used. For the calculation of the Fermi energy, interstitial charge was allowed to reside in this volume. With this interstitial charge and the DOS functions of Figs. 9.8 and 9.9, a Fermi energy of 195 eV was found on the energy axis of Fig: 9.7. Using this value in CORRECT produces excellent agreement between calculation and experiment. This value falls within the gap depicted in Figs. 9.8 and 9.9.

The gap is a region where $\chi_{l,i}(E) \approx -1$ such that $q_{l,i} \approx 0$. The calculated DOS functions are broadened by the finite cluster size, the consideration of the core-hole lifetime, and the use of a lossy potential. Consequently, distinct band gaps, Van Hove singularities, and other sharp features are absent from my calculations.

Knowing the Fermi energy, I calculate the net charge n_i on each atom i

$$\begin{aligned} n_i &= \sum_l \int_{-E_F}^{E_F} dE q_{i,l}(E) \\ &= \sum_l \int_{-E_F}^{E_F} dE q_{0,i,l}(E) (1 + \chi_{i,l}(E)) \\ &= n_i^0 + n_i^{sc} \end{aligned} \tag{9.1}$$

These are shown in Table 9.2 for boron and nitrogen. The interstitial charge determined from the interstitial volume is also shown there. The numbers are reasonable, although they suggest a more charged nitrogen atom and less charge boron atom than does the LMTO calculation. Also note that the integer formal valences of ± 1 for B and N do not describe the actual charges found within the Norman spheres.

This computation of charge transfer is the end of the first step in a self-consistency loop. The neutral atoms used in FEFF to compute the muffin tin can be replaced by these charged atom and new potentials can be generated. This procedure could be iterated until some desired level of self-consistency is attained.

Finally note the enhanced DOS of the central boron atom shown in Fig. 9.8. That the integrated area of this function is larger than for the ground state boron atom is due to the use of an ionized central atom in the FEFF calculation. This is an *ad hoc* removal of an electron from the central atom. This was done to enhance the area of the peak near the Fermi energy for improved agreement with the data. It is my hope

that such *ad hoc* additions to the theory would be unnecessary with self-consistent potentials. Also note the shift downward in energy of the DOS of the central boron relative to the ground state atom. This is due to relaxation in the presence of the core hole.

Table 9.2: Charge distribution in the ground state of BN within the Norman spheres. The units on these numbers are electrons per atom. The LMTO results were obtained by summing the areas integrated up to the LMTO Fermi energy under the angular momentum projected DOS functions for each atom. The interstitial charge is computed from Eq. (8.35). n_i^{sc} is the scattering contribution from Eq. (9.1).

	free atom	embedded atom	LMTO	n_i^{sc}
Boron	3	2.53	2.13	-0.77
Nitrogen	5	4.20	4.62	-1.00
interstice	0	0.64	0.63	

9.4 Lead Titanate

As my final example, I will examine XANES calculations on PbTiO_3 . The results of a calculation using the room temperature crystal structure [84] are shown in Fig. 9.10. The 4 shell calculation takes 14 minutes of CPU time on an Indigo II and 17 minutes on my Pentium.

Before I begin my discussion of Figs. 9.10 – 9.14, I will describe a computational convenience that I employed to simplify the interpretation of the calculations in this section. I used the same set of partial wave phase shifts for each calculation in this section. These phase shifts were computed for PbTiO_3 in a cubic perovskite structure of lattice constant $a = 3.9679 \text{ \AA}$, which is the cube root of the volume of the 300 K structure in Ref. [84]. The calculations on differently distorted structures then used these phase shifts and different atomic configurations. This puts all the calculations on a common energy scale referenced to a common interstice. To check the validity of this approximation for the distorted structures, I compared the calculation on the 300 K structure using phases calculated from that atomic configuration and from the cubic atomic configuration. The differences were much smaller than the differences between the various calculations presented in this section.

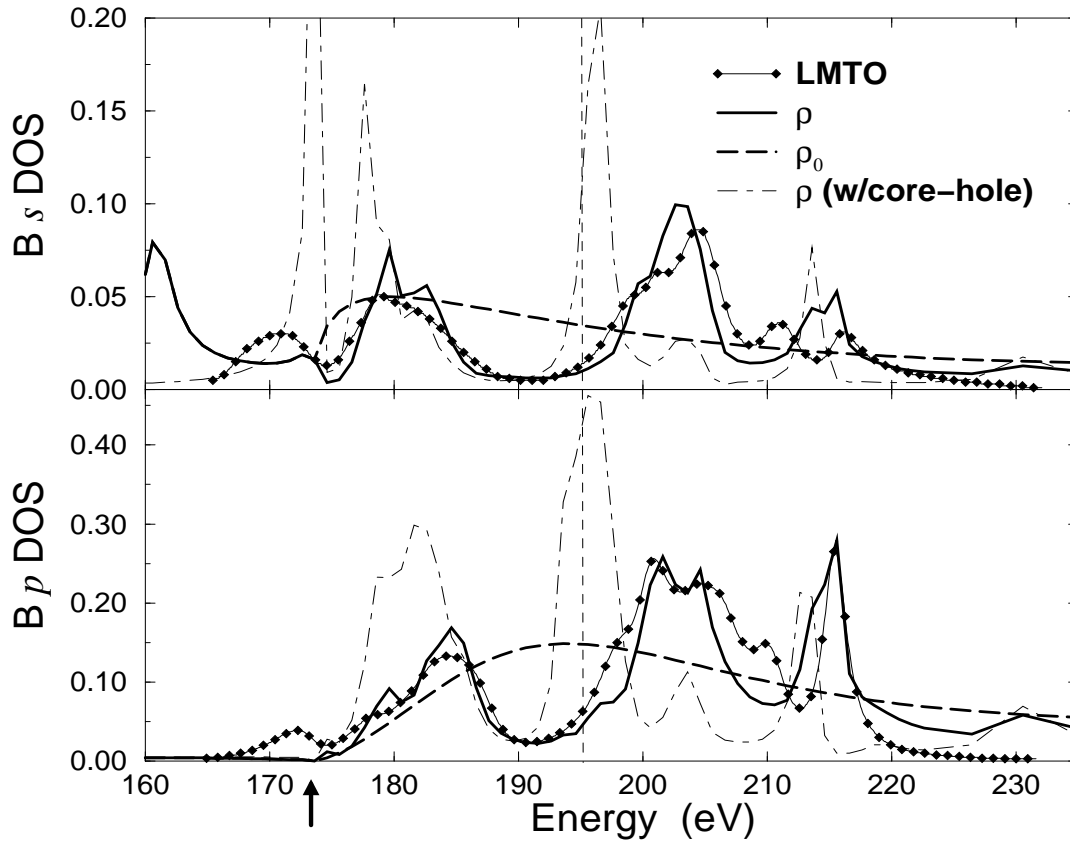


Figure 9.8: Upper panel: Boron s DOS in BN ($l = 0$). Lower panel: Boron p DOS in BN ($l = 1$). The DOS functions calculated by XANES (thick solid lines) are compared with similar functions computed by an LMTO [139] (thin solid lines with diamonds \diamond). The LMTO calculations were broadened by 1 eV for comparison with my calculations. ρ_0 (dashed lines) is the embedded neutral atom density given by Eq. (8.31). The dot-dash lines are the DOS functions for the ionized absorbing atom, which is calculated in the presence of a core-hole. The vertical dashed line is the Fermi energy calculated by the method of Sec. 8.2.6. The units on the DOS functions are $(\text{eV})^{-1}$. The arrow at 173.3 eV marks the position of the interstice (muffin tin zero).

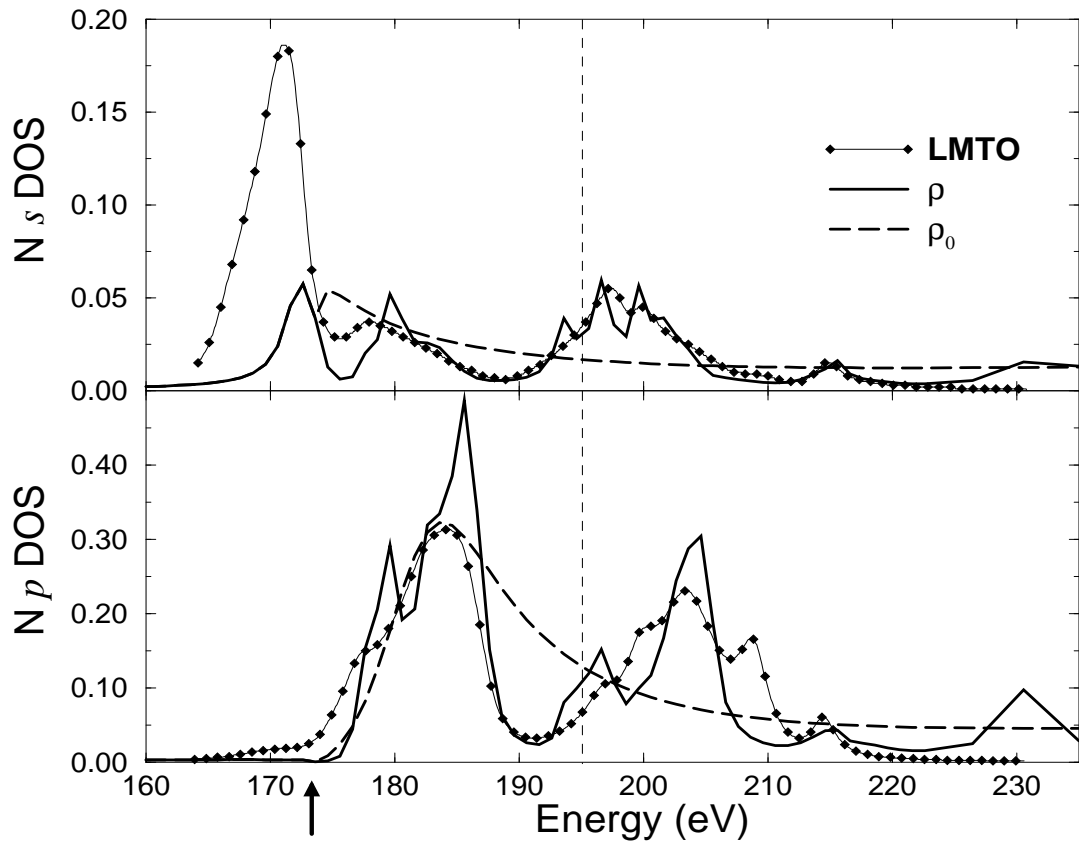


Figure 9.9: Upper panel: Nitrogen s DOS in BN ($l = 0$). Lower panel: Nitrogen p DOS in BN ($l = 1$). The DOS functions calculated by XANES (thick solid lines) are compared with similar functions computed by an LMTO [139] (thin solid lines with diamonds \diamond). The LMTO calculations were broadened by 1 eV for comparison with my calculations. ρ_0 (dashed lines) is the embedded neutral atom density given by Eq. (8.31). The vertical dashed line is the Fermi energy calculated by the method of Sec. 8.2.6. The units on the DOS functions are $(\text{eV})^{-1}$. The arrow at 173.3 eV marks the position of the interstice (muffin tin zero).

The effect of including increasing numbers of shells in the calculation is shown in Fig. 9.10. It is interesting to note that the bulk of the the peak associated in Ch. 7 with the displacement of the titanium atom from a site of point centrosymmetry is resolved by the consideration of only the oxygen octahedron. That scattering from the first oxygen shell produces this structure is the scattering theoretic equivalent to the molecular orbital theoretic statement that this peak is due to hybridization of titanium and oxygen orbitals. Including the second shell lead atoms (dashed line) adds additional structure to the spectrum. Including the third shell titanium atoms (dot-dash line) adds little new structure. Including the fourth shell oxygen atoms (thin line with diamonds \diamond) resolves the peak at 4979 eV and most of the next peak as well. Including the fifth shell titanium atoms (thin line with crosses $+$) adds no new structure to the calculation.⁷ Adding the sixth shell oxygen atoms (short dashed line) resolves the peak at 4987 eV. Beyond this energy the restriction of the angular momentum basis as indicated in Table 9.1 becomes a suspect approximation. The size of the basis required for a convergent expansion in partial waves scales according to the size of the “centrifugal barrier,” $l_{max} \approx kr_{mt}$. The peak resolved by the addition of the sixth shell is about 25 eV above the Fermi energy, or at about 2.6 \AA^{-1} . Taking the muffin tin radius of the central atom from FEFF, $r_{mt} = 1.45 \text{ \AA}$, gives $l_{max} \approx 3.7$. Data structures in XANES are currently dimensioned for consider $l \leq 3$, so $\sim 25 \text{ eV}$ is the practical limit of the calculations using the current code.

This sort of structural interpretation of the XANES is not so convenient as an analysis by path expansion. Still, this sort of analysis is useful. In this case, it underscores the importance of scattering from the oxygen atoms in determining the nature of the XANES spectrum. This is a particularly interesting result given that the contribution from oxygen atoms is weak in the EXAFS region, particularly at high k . The fourth shell oxygens contribute weakly to the EXAFS and the sixth shell even more so. Nonetheless, scattering from the oxygen atoms are the predominant source of structure in the PbTiO_3 XANES spectrum. This is understandable as the scattering of the oxygen atoms is strong at low k and weak at high k while the

⁷ Others working on the problem of computational near edge structures in titanium oxide perovskites have suggested that a cluster of 51 atoms including the central titanium, the eight surrounding lead atoms and the six surrounding titanium–oxygen octahedrons is essential to a good calculation. [140] Using the fast potential calculation of FEFF allows my code to separate the effects of muffin tin construction from the effects of different scattering contributions. The result of Fig. 9.10 shows that a spherical cluster is sufficient for computing the scattering contributions. In an explicit test, I observed only subtle differences between the 4 shell calculation and a calculation using the 51 atom cluster.

scattering from heavy atoms is much stronger at high k .

The tetragonal elongation and distortions in PbTiO_3 lead to its interesting ferroelectric and thermodynamic behavior as well as to its interesting absorption spectrum. With XANES we can alter these structural features and observe their effects on the calculated spectrum. Fig. 9.11 shows the results of three calculations. Each uses the lengths of the tetragonal axes, but varies the magnitude of the displacements of the titanium and oxygen atoms. Each is calculated using 4 shells. The solid line is for the fully distorted structure and is the same as the thin line with diamonds in Fig. 9.10. For the short dashed line the titanium and oxygen displacements were relaxed to zero. For the long dashed line, the displacements were set to $\frac{2}{3}$ of their full values. In the high energy end of the calculation, the oscillations for the undistorted structure are enhanced, as is expected in the absence of structural disorder. In contrast, the peak just above the Fermi energy is *enhanced* by the structural distortion. This is in agreement with the observed behavior of PbTiO_3 and EuTiO_3 .

Fig. 9.12 shows $\chi(E)$ as calculated by Eq. (8.21) before convolving according to Eq. (8.25). Most of the enhancement of the peak just above the Fermi energy is clearly seen as a scattering effect. The peak in χ corresponding to the peak in μ is shown to grow with the distortion.

Fig. 9.13 shows the p DOS of both the central titanium atom and of a ground state titanium atom. Again the effect of the distortion is seen both in the growth of the peak in central atom DOS in the upper panel of Fig. 9.13 and in the ground state DOS in the lower panel. The energy shift of about 9 eV between these two sets of DOS functions results from relaxation due to the presence of the core hole. The peak below the Fermi energy is presumably the top of the valence band. In most of the energy range, the effect of the distortion is to damp the oscillatory part of the DOS. The distortion clearly enhances the portion of the DOS probed by the photoelectron just above the Fermi energy.

Now I examine the effect of the tetragonal elongation on the XANES spectrum. Fig. 9.14 shows two calculations. The solid line is, once again, the calculation using the crystallographic structure. The dashed line is a calculation using a cubic structure of lattice constant $a = 3.9679 \text{ \AA}$ but with the same fractional displacements for the titanium and oxygen atoms as in the published crystal structure. The effect of the lattice constants is much less pronounced than the effect of the distortions.

Finally I demonstrate a calculation of polarized XANES spectra. Fig. 9.15 shows the polarized, single crystal PbTiO_3 data from Ch. 7 at room temperature along with the polarization dependence of the calculated spectrum on six polarization shells.

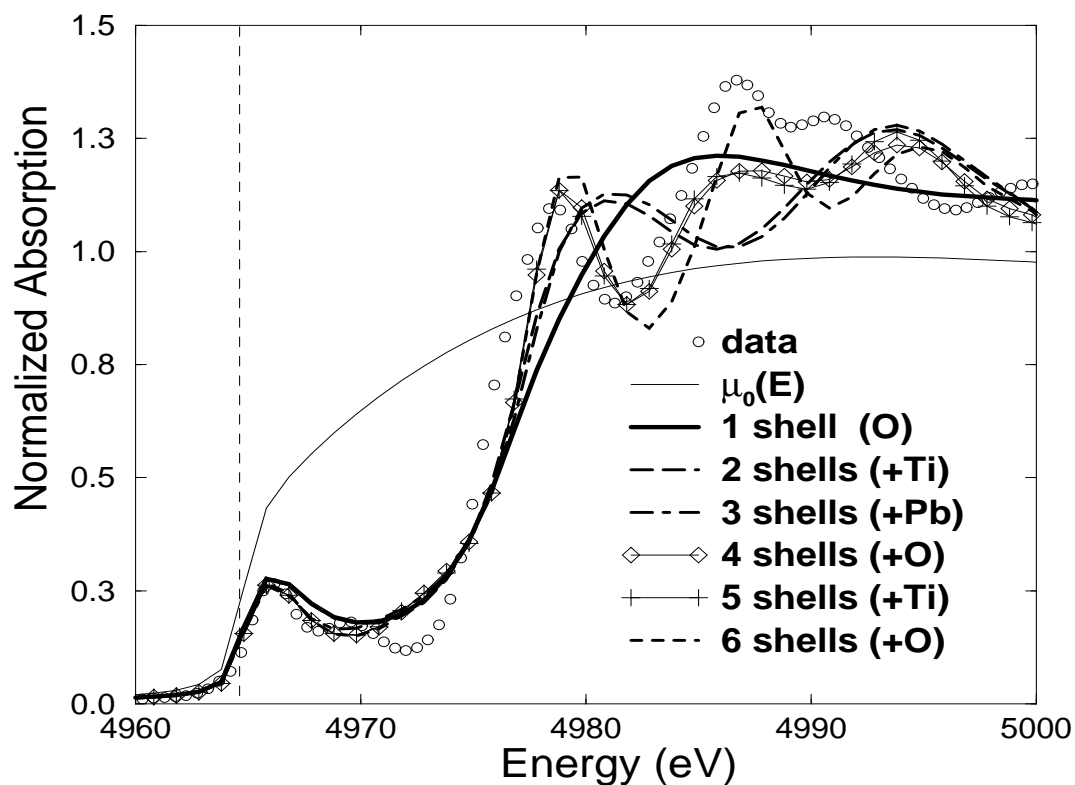


Figure 9.10: Titanium K near edge structure in PbTiO_3 . The data is transmission XAFS. Plotted in this picture are the embedded atom background and the calculations on 1–6 shells about the central atom using the structure of Ref. [84]. $\mu_0(E)$ is given by Eq. (8.23). The cluster in the 1–shell calculation is the central titanium atom and the surrounding oxygen octahedron. Each subsequent calculation includes the next coordination shell about the central titanium into the cluster. The atomic species of each shell is given in parentheses in the legend of the figure. The vertical dashed line is the Fermi energy.

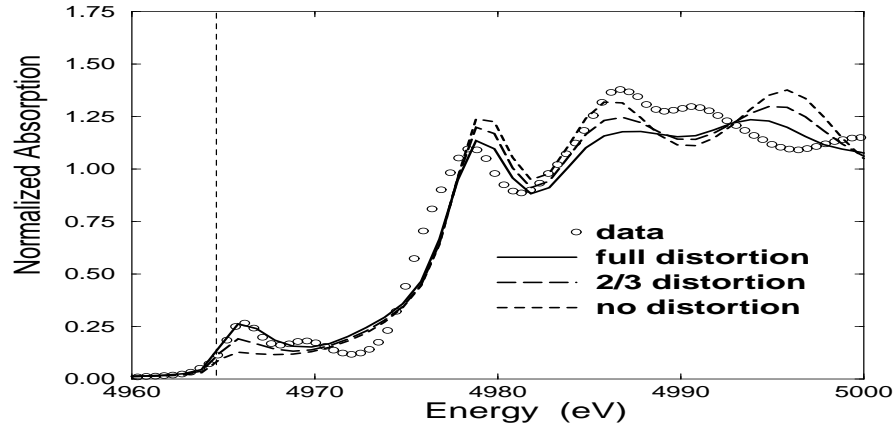


Figure 9.11: Titanium K near edge structure in PbTiO_3 . The data is transmission XAFS. The solid line is the XANES calculation using the room temperature crystallographic structure from Ref. [84]. The long dashed line is a calculation on this same structure, but with the tetragonal distortions of the titanium and oxygen atoms reduced by $\frac{1}{3}$. The short dashed line is a calculation with the tetragonal distortions set to zero. The cell axis lengths are the same in all three calculations. The vertical dashed line is the Fermi energy.

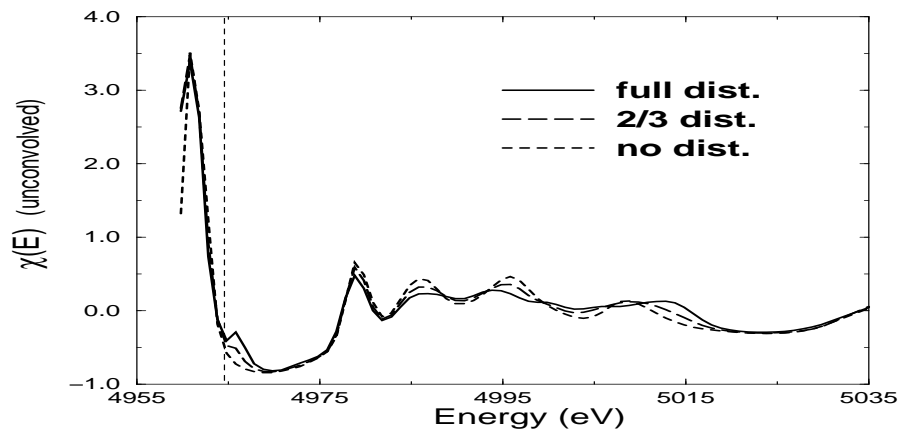


Figure 9.12: Titanium K edge $\chi(E)$ for PbTiO_3 . This is the χ function of Eq. (8.21) before convolving according to Eq. (8.25). The line types represent the same sequence of calculations as in Fig. 9.11. The vertical dashed line is the Fermi energy.

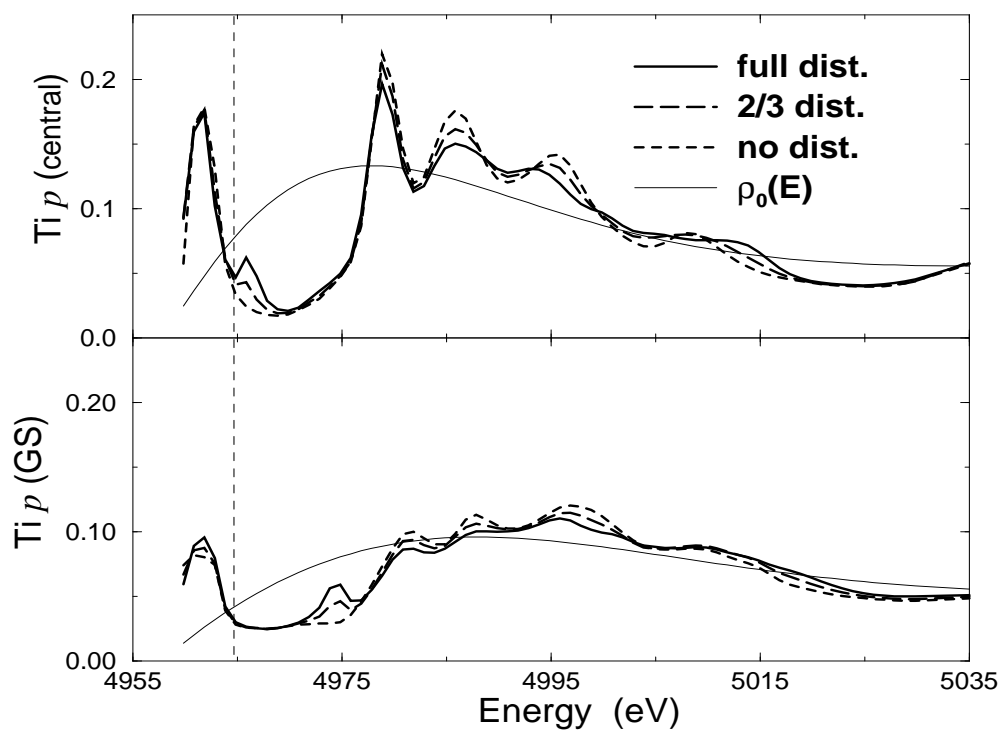


Figure 9.13: Titanium p DOS functions for the central (top) and ground state (bottom) atoms. The line types represent the same sequence of calculations as in Fig. 9.11. The thin line is the embedded atomic density. The vertical dashed line is the Fermi energy. The units on the DOS functions are $(\text{eV})^{-1}$.

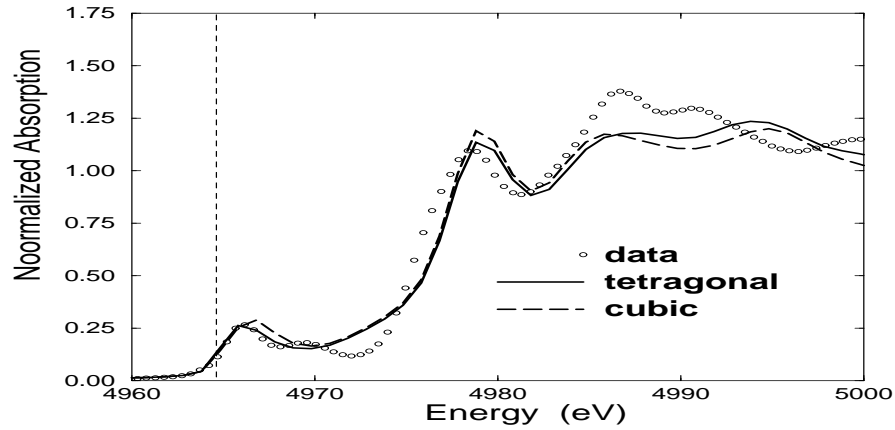


Figure 9.14: Titanium K near edge structure in PbTiO_3 . The data is transmission XAFS. The solid line is the XANES calculation using the room temperature crystallographic structure from Ref. [84]. The dashed line is a calculation using cubic cell axes but with the tetragonal distortions of the titanium and oxygen atoms. The vertical dashed line is the Fermi energy.

Since this is a K edge and linear polarization, Eq. (8.22) is used. XANES does a good job of reproducing most of the spectral features for both polarizations, including the polarization dependence of the peak just above the Fermi energy. As with the polycrystalline calculation, the peak in the data at about 4970 eV is absent from the calculation.

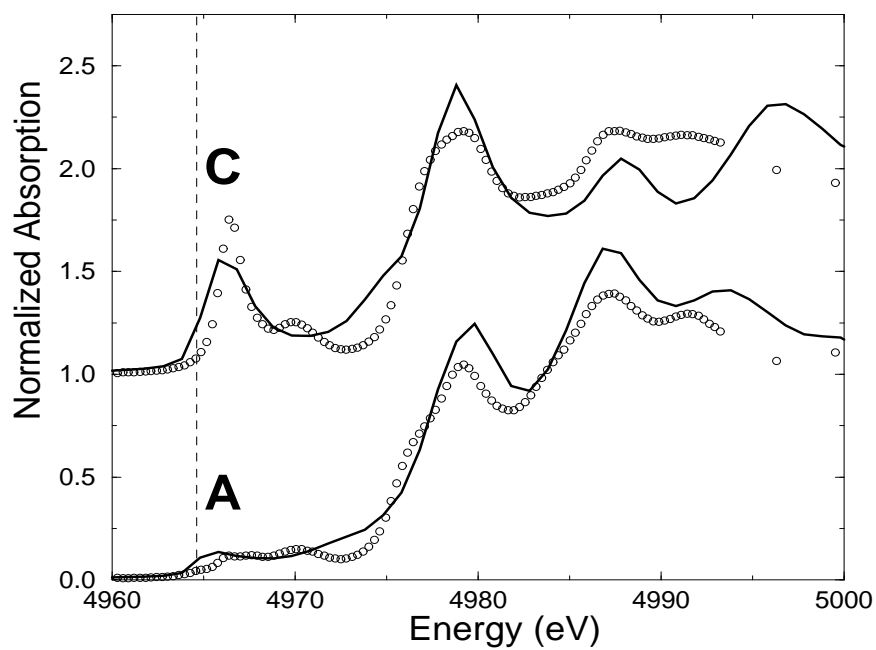


Figure 9.15: Titanium K near edge structure in single crystal PbTiO_3 . The experimental and calculated spectra for $\hat{\epsilon} \parallel c$ are shown in the upper part of the figure. The lower traces are the experimental and calculated spectra for $\hat{\epsilon} \perp c$. The data is fluorescence XAFS. The calculations use the room temperature crystallographic structure from Ref. [84] and six coordination shells. The vertical dashed line is the Fermi energy.

Chapter 10

SUMMARY AND FUTURE WORK

In the first part of this thesis I demonstrated that two oxide perovskites, PbTiO_3 and BaTiO_3 , possess a significant order–disorder component to their ferroelectric and structural phase transitions. This is a novel result as both of these materials have historically been described as being of the displacive type. In the second part of this thesis, I presented an approach to full multiple scattering (FMS) *ab initio* calculations of x–ray absorption near edge structure (XANES). The algorithms described were encoded in a computer program, XANES, and the successful use of the program on a variety of materials was shown.

In this final chapter, I will summarize my results on PbTiO_3 and BaTiO_3 and their implications to our understanding of the phenomenon of ferroelectricity. I will also discuss the role that FMS calculation of XANES can play in further understanding ferroelectric and other materials. I will conclude by discussing how the work in this thesis can be advanced and what projects I hope to work on in coming years.

10.1 The Implications of this Work to Ferroelectricity

My XAFS measurements on PbTiO_3 and BaTiO_3 demonstrate that the local structures of these two materials are dominated by an order–disorder mechanism, although both show a small displacive component as well. In PbTiO_3 the local structure remains tetragonal with its oxygen octahedron displaced relative to the lead cage and the titanium atom displaced from the midpoint of the two axial oxygen atoms. The phase transition to the cubic phase at 763 K is thus due to a disordering of the local tetragonal units over a short length scale. This length scale is longer than the 5 Å measured in my EXAFS analysis and must be shorter than about 30 Å, the approximate spatial resolution of the neutron diffraction measurement of Ref.[90]. The small displacive component of the transition is apparent in the temperature dependence of the local structure and of the distortion parameter as shown in Figs. 4.9 and 7.8. In BaTiO_3 the titanium atom remains displaced approximately in a rhombohedral $\langle 111 \rangle$ direction at all temperatures. The sequence of phase transitions are due to

the eight-site disordering as suggested by Bersuker [102] and Comes *et al.* [100]. The small displacive component to these transitions drives a slight shortening of the rhombohedral displacement as shown in Fig. 7.3.

For years, evidence has mounted suggesting that an order-disorder mechanism dominates the local structures of these and related materials. Recent EXAFS analyses of KNbO_3 [12], $\text{KTa}_{0.91}\text{Nb}_{0.09}\text{O}_3$ [13–15], NaTaO_3 [16], $\text{Na}_{0.82}\text{K}_{0.18}\text{TaO}_3$ [16] and PbZrO_3 [17] have shown that the local structures in those materials are predominantly of the order-disorder type. In PbTiO_3 several recent measurements, including refractive index measurements [87], Perturbed Angular Correlation Spectroscopy [88, 89], and single-crystal neutron diffraction [90] have shown evidence of a disordering phenomenon near the tetragonal to cubic phase transition. In BaTiO_3 , also, measurements of infrared reflectivity [7], cubic phase x-ray diffraction [8], electron spin resonance [9], and impulsive stimulated Raman scattering [10, 11] have suggested the importance of the eight-site model in that material. Furthermore, recent first principles calculations [93, 104] of the phase transitions in these materials have found theoretical evidence of disordering behavior in the high symmetry phases of both PbTiO_3 and BaTiO_3 . Lacking for both of these systems was the sort of direct measurement of the local structure with sub-Ångstrom scale spatial resolution and femtosecond temporal resolution that XAFS can provide. That direct evidence is provided in this thesis. Specifically, I have shown that the local structure of PbTiO_3 remains tetragonally distorted in its high temperature phase and that the local structure of BaTiO_3 remains rhombohedrally distorted in all of its phases. For BaTiO_3 , I have further shown that the eight-site model must be modified such that the minima in the local potential surface occupied by the titanium atoms are located slightly off the rhombohedral $\langle 111 \rangle$ axes. In particular, I found that the local displacement vector of the titanium atom in BaTiO_3 is $11.7(1.1)^\circ$ away from the $\langle 111 \rangle$ axis towards the c -axis in the tetragonal phase.

While our results clearly demonstrate the presence of local distortions both below and *well* above the ferroelectric to paraelectric transition in both PbTiO_3 and BaTiO_3 , many thermodynamic and lattice dynamic properties of these material such as the soft mode are well explained by a displacive model. This is not a contradiction. In a recent work [105], Girshberg and Yacoby present a theory of ferroelectricity which considers the coupling between local displacements and the soft mode. As observed by Stern and Yacoby [141], the soft mode is a *collective* displacement within a crystal and thus different from the *local* displacement measured by XAFS. This theory successfully explains the soft modes of PbTiO_3 and KNbO_3 in the presence of

the measured local displacements in those materials. The central peak [86] of PbTiO_3 is explained quantitatively by this theory and the soft modes of both materials are found to be normally damped and with frequencies that do not vanish at T_c , as observed in experiment. Given the many similarities between KNbO_3 and BaTiO_3 , I suggest that the model of Girshberg and Yacoby applies as well to BaTiO_3 .

It is important to understand the Raman spectrum of PbTiO_3 and BaTiO_3 in the context of these results. The temperature dependence of both Raman spectra [1, 2] clearly show the behavior expected if the local structure is the same as the average crystallographic structure in each of the phases. The critical difference between the XAFS and Raman measurements is their time scales. The lifetime of the Raman excitation is around 10^{-9} sec while the lifetime of the XAFS excitation is determined by the lifetime of the core hole vacated by the x-ray, about 1.5×10^{-15} sec. I suggest that the titanium atoms hop between the various sites allowed by the order-disorder model in each phase on a time scale between the Raman and XAFS lifetimes. Thus the XAFS measurement is a snapshot of a dynamic system that is temporally averaged by the Raman measurement. This hopping explains the observation of disordering behavior in the measurements mentioned above and does not contradict thermodynamic properties of BaTiO_3 which average over time scales much longer than the hopping time.

The thermal diffuse scattering results of Holma, et al. [142] on BaTiO_3 also merit comment. They found superior agreement to their data with Hüller's model of dynamic correlations [103] than with Comes' simple application [100] of eight-site static disorder. We suggest that dynamic correlations in the motion about the disordered atom positions coexist with hopping between the disordered sites. Recent first principles calculations [143, 144] of BaTiO_3 show exactly this behavior and may be sufficient to account for the observed profiles of the diffuse sheets. A re-examination of Holma's data in the context both of these first principles results and of the theory of Girshberg and Yacoby is merited.

The presence of distortions to the local structures of PbTiO_3 , BaTiO_3 and other materials suggests several fundamental questions about ferroelectric materials that should be addressed in the future:

- Are local distortions in high symmetry phases a universal feature of ferroelectric materials?
- Given that PbTiO_3 and BaTiO_3 are ferroelectric while EuTiO_3 is not, what is the correlation between chemistry and ferroelectricity?

- What is the role of charge transfer in the XANES structures of the perovskite materials and how is charge transfer related to ferroelectricity?
- What is the temperature dependence of the correlation between disordered local structures and what is the length scale of this correlation in the high temperature phase?
- What is the dependence of the local distortions upon hydrostatic pressure and do the local distortions persist into the pressure induced high symmetry phase?
- Do the local distortions change for very small particle size?

10.2 *The Role of FMS XANES Calculations in XAFS Research*

The XANES spectrum contains a wealth of electronic and structural information about materials. Currently, there is no systematic, rigorous way of extracting all of this information. Much of the literature on XANES measurements handles these spectra in qualitative, empirical fashion. Presented in Chs. 8 and 9 of this thesis is a new computer program, XANES, for full multiple scattering *ab initio* calculations of x-ray absorption near edge structure. XANES is by no means a finished work, but it represents a significant advance towards a goal of quantitative, rigorous analysis of XANES spectra.

The prospect of extracting electronic information from XANES spectra is quite exciting. XANES computes the absorption spectrum and the local electronic densities of state simultaneously. It uses a core-hole and performs the calculation in real space, thus does not require periodicity or any other symmetry. Electronic information such as valence, charge transfer and the location of the Fermi energy is thus available even for non-crystalline materials. Even for crystalline materials, this approach is preferable to band-structure based approaches. Since the calculation is made in the presence of the core-hole, it may be directly compared to an absorption experiment without resorting to an empirical rule-of-thumb to account for the energy shift due to the core-hole.

Ab initio calculations are of particular value for certain experimental situations where the interpretation of the XANES spectrum is particularly indirect. For example, if the absorbing atom in some experiment resides in distinct crystallographic sites, the different sites may be of different valence and even possess different Fermi energies relative to the core-hole energy. Since the XANES experiment measures a linear combination of all crystallographic sites, the interpretation of this signal can

be quite obfuscated. Independent calculations of the two sites, both in the presence of the core–hole, are of obvious value.

For many materials of highly disordered local structure, the extent of the EXAFS signal is small and, due to the large disorder, difficult to interpret. Examples of such materials are catalysts, biological materials, amorphous solids and liquids, quasicrystals, and others. Often the only source of structural information about a disordered material is its XANES spectrum. With a reliable computational tool, different local environments can be used in calculations and compared to the experiment. In this way information about coordination and symmetry can be extracted from the data.

In Ch. 7, I showed XANES spectra of PbTiO_3 and BaTiO_3 and interpreted them in terms of the local structure. Specifically, I related the area of a particular peak in the XANES spectra to the magnitude of the displacement of the titanium atom from its site of point centrosymmetry. In Sec. 9.4 I showed a direct link between the peak size and the magnitude of the displacement used in the calculation.

XANES allows the user to perform “experiments” that are not possible in nature. Varying the positions of atoms as mentioned above is one of these experiments. Changing the atomic species of the backscatterers and the ionization of the central atoms or of certain backscatterers are two others. The contributions to the spectrum due to different individual scatterers or different scattering shells can be investigated as can the contributions of differently size angular momentum bases.

In Sec. 8.2.6 I discuss calculations of charge transfer and mention the possibility of self-consistent muffin tin potentials. This may have significant impact on EXAFS analysis. In Chs. 4 – 6, I discussed the need to use phase and amplitude corrections in the EXAFS analysis to account for the error in FEFF’s fitting standards due to the use of neutral atomic sphere when constructing the muffin tin and other approximations. These corrections most often enter into the analysis as multiple E_0 variable parameters [50]. It would be quite a boon to EXAFS analysis to remove the need to introduce multiple phase corrections to the fit. Self-consistent potentials may go a long way towards fixing this source of error in the FEFF calculation.

10.3 Future Work

I wish to end this tome by describing several projects that I hope to pursue in the coming years.

Further study of BaTiO_3

In Fig. 5.1 I show the close proximity of the titanium K edge to the barium

L_{III} edge and discuss the difficulties in analyzing the titanium K edge signal due to the narrow band width. This is an unfortunate occurrence as the titanium signal, with its significant multiple scattering contribution in the third shell, would be much more sensitive to the differences between the various possible local structures used as fitting models in Sec. 5.2. Using the Diffraction Anomalous Fine Structure (DAFS) [145, 146], it is possible to separate the fine structure signals from the titanium and the barium.

DAFS has been used to separate the fine structure due to inequivalent crystallographic sites of the same atomic species [147, 148]. By modifying that approach, the fine structures from different atomic species with nearby absorption edges, as is the case in BaTiO_3 , can be isolated and analyzed separately. This will provide the final missing piece of information about the local structure of BaTiO_3 . This is a project that I will be doing in the year following my graduation as a postdoctoral fellow at the National Institute of Standards and Technology (NIST).

Further study of transition metal oxide perovskites

Fig. 10.1 shows the over-plotted XANES spectra of five titanium perovskites. There are several systematic differences among these spectra. The non ferroelectric perovskites EuTiO_3 , CaTiO_3 , and SrTiO_3 not only lack the $3d$ peak, but the swiftly rising parts of their edges are shifted about 2 eV higher in energy compared to PbTiO_3 and about 1 eV compared to BaTiO_3 . The location of the swiftly rising part of the edge is where the local electronic density of state for the $l = 1$ final state of the photoelectron becomes large. The connections between ferroelectricity, the A cation, and the width of the gap between the Fermi energy and the swiftly rising part of the edge are not currently understood. Further study, including application of my XANES code to the materials, is necessary. Also the peak around 4970 eV is different in the tetragonal PbTiO_3 compared to the other materials. The physical origin of this peak and its relation to the local structure merit further investigation.

Non-perovskite ferroelectrics

The wide-spread success of the order-disorder model in describing the behavior of the local structure in oxide perovskites suggests the possibility that order-disorder is a universal feature of ferroelectric materials. There are many ferroelectrics of non-perovskite structures. One of these, solid solutions of germa-

nium in lead telluride, has been the subject of recent first principles calculations of its ground state structure and phase diagram [149]. An earlier EXAFS study [150] found evidence of order–disorder behavior of the germanium distortion. I hope to pursue XAFS studies in this and other materials with the aim of investigating the hypothesis that disordered local structure is a common feature of the paraelectric phases of all ferroelectrics.

FMS Calculations of Hybridization

In molecular orbital (MO) theory, a hybridized state is a state arising from the overlap of atomic states, possibly of different angular momentum, of neighboring atoms in a crystal. As discussed in Sec. 7.1, hybridization can open otherwise unavailable channels for the dipole excitation by mixing character of the appropriate angular momentum from nearby atoms with empty states of the absorbing atom. In the MO picture, this is what happens in both PbTiO_3 and BaTiO_3 . Some p character from the oxygens is mixed with the large unfilled d density of the titanium atom leading to the appearance of the peak just above the Fermi energy. This hybridization is driven by the displacement of the titanium atom from a site of point centrosymmetry.

Hybridization can be calculated within the FMS formalism by using the Lippman–Schwinger equation [21]. In a scattering problem, a wave packet propagates through space and is scattered by the potentials of the neighboring atoms. If $\psi(l; \mathbf{R})$ is an atomic wave function at site \mathbf{R} and of angular momentum l , then the wave function in the presence of the scatterers is

$$\Psi(l; \mathbf{R}) = \psi(l; \mathbf{R}) + \mathbf{G}^0 \mathbf{T} \psi(l; \mathbf{R}) \quad (10.1)$$

Expressing the \mathbf{T} –matrix in terms of single site \mathbf{t} matrices as in Eq. (8.4) and solving this as a Taylor expansion yields

$$\Psi(l; \mathbf{R}) = (1 - \mathbf{G}^0 \mathbf{t})^{-1} \psi(l; \mathbf{R}) \quad (10.2)$$

As discussed in Sec. 8.2.3, the matrix $(1 - \mathbf{G}^0 \mathbf{t})$ is decomposed by a Lower–Upper decomposition as a matter of course while calculating \mathbb{G} . It is a simple task to obtain the matrix inverse from the decomposed matrix [125]. The atomic functions $\psi(l; \mathbf{R})$ are used already by XANES to compute the electronic densities of state. Thus all of the information needed to compute $\Psi(l; \mathbf{R})$ is already in

the code.

Using Eq. (10.2), $\Psi(l; \mathbf{R})$ is calculated in the full $|\mathbf{LR}\rangle$ basis of the \mathbb{G} -matrix. The hybridization amplitude ξ between state l of the central atom $\mathbf{R} = 0$ and a state of angular momentum l' of another atom at \mathbf{R}' is computed from $\Psi(l; \mathbf{R})$ by

$$\xi_\ell = \psi_\ell^* \cdot \Psi(l; \mathbf{R}) \quad (10.3)$$

Here ℓ denotes the state l' and \mathbf{R}' in the $|\mathbf{LR}\rangle$ basis. For example, in PbTiO_3 or BaTiO_3 the ℓ 's of interest might be those corresponding to the p states of the oxygens in the octahedron surrounding the central atom or the p state of the central atom itself.

With these quantities, the entire application of MO theory to x-ray absorption spectra is cast into the language of scattering. It will be interesting to observe the dependence of the hybridization intensities on the magnitudes of the atomic displacements that drive them. In particular, it will be interesting to determine in a quantitative manner which hybridizations lend significant spectral weight to the XANES features which depend strongly on atomic displacements.

Self-consistency and corrections to the muffin tin potential

As mentioned in Sec. 8.2.6, using the local electronic densities of state to compute charge transfer between the ion in the solid is the end of the first step of a self-consistency loop. The Laplace equation is solved with the charge densities of the newly populated ion to yield new ionic potentials. These ionic potentials can then be overlapped to form a new muffin tin and partial wave phase shifts can be calculated using these new muffin tin potentials. This cycle can be iterated until some level of self-consistency is attained. This work is, in fact, already under way [151]. The muffin tin potential can be further corrected by allowing for non-spherical tins. This is accomplished by allowing off-diagonal elements of the \mathbf{t} -matrix, thus allowing a wave to scatter into a state of a different angular momentum. This would significantly expand computation time. Having a diagonal \mathbf{t} -matrix allows the product $\mathbf{G}^0 \mathbf{t}$ to be computed in n^2 time, while non-spherical muffin tins would cause this calculation to take n^3 time. Fortunately the current code is sufficiently fast that adding another n^3 calculation would still allow for reasonably timed calculations.

Further Development of *ATOMS*

The program *ATOMS*, described in Appendix B, has proven to be a valuable tool for theoretical and experimental XAFS studies on crystalline materials. Its utility can be expanded in several areas.

- The part of *ATOMS* which interprets space group symbols is based upon the 1969 edition of the International Tables of X-Ray Crystallography. The 1989 edition somewhat modifies and expands the Hermann–Maguin notation to accommodate all possible settings of low symmetry space groups. *ATOMS* needs to be modified to understand all symbols offered in the 1989 edition.
- *ATOMS* can be easily modified to perform a variety of chores useful for DAFS, including the calculation of the atomic portion of the structure factor using the non-resonant scattering factors of Cromer and Mann [152] and the anomalous corrections¹ of Cromer and Lieberman [152].
- With tables of scattering factors, *ATOMS* has all of the information needed to simulate powder diffraction profiles.

¹ More modern calculations of the anomalous corrections are available. One current interest among the developers of *FEFF* is the calculation of the anomalous corrections for embedded atoms, thus anomalous scattering corrections, including valence electron effects, can be tailored to the material under study.

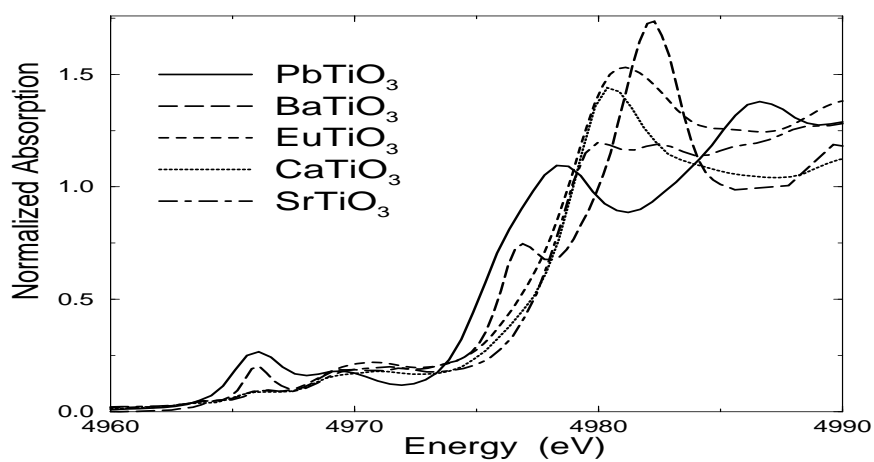


Figure 10.1: Titanium *K* edge XANES spectra of PbTiO₃, BaTiO₃, EuTiO₃, CaTiO₃, and SrTiO₃. The spectra of the non-ferroelectric materials, EuTiO₃, CaTiO₃, and SrTiO₃, not only lack the *3d* peak above the Fermi energy but also have the quickly rising parts of their edges shifted upwards by about 2 eV relative to the PbTiO₃ spectrum. Also the shape of the peak around 4970 eV is different for the tetragonal PbTiO₃ than for the other materials.

BIBLIOGRAPHY

- [1] G. Burns and F.H. Dacol. Lattice Modes in Ferroelectric Perovskites. III. Soft Modes in BaTiO₃. *Phys. Rev. B*, 18(10):5750–5755, 1978.
- [2] G. Shirane, J.D. Axe, J. Harada, and J.P. Remeika. Soft Ferroelectric Modes in Lead Titanate. *Phys. Rev. B*, 2(1):155–159, 1970.
- [3] A.M. Glazer and S.A. Mabud. Powder Profile Refinement of Lead Zirconate Titanate at Several temperatures. II. Pure PbTiO₃. *Acta Cryst.*, B34:1065–1070, 1978.
- [4] G. H. Kwei, A. C. Lawson, S. J. L. Billinge, and S. W. Cheong. Structures of the Ferroelectric Phases of Barium Titanate. *J. Phys. Chem.*, 97:2368–2377, 1993.
- [5] W. Cochran. Crystal Stability and the Theory of Ferroelectricity. *Advances in Physics*, 9:387–423, 1960.
- [6] E. Nakamura T. Mitsui, I. Tatsuzaki. *An Introduction to the Physics of Ferroelectrics*. Gordon and Breach, New York, 1976.
- [7] F. Gervais. Displacive—Order—Disorder Crossover in Ferroelectrics. *Ferroelectrics*, 53:91–98, 1984.
- [8] K. Itoh, L.Z. Zeng, E. Nakamura, and N. Mishima. Crystal Structure of BaTiO₃. *Ferroelectrics*, 63:29–37, 1985.
- [9] K.A. Muller. . In A.R. Bishop, editor, *Nonlinearity in Condensed Matter*, page 234. Springer, Heidelberg, 1986.
- [10] T. P. Dougherty, G. P. Wiederrecht, K. A. Nelson, M. H. Garret, H. P. Jenson, and C. Warde. Femtosecond Resolution of Soft Mode Dynamics in Structural Phase Transitions. *Science*, 258:770–774, 1992.

- [11] T. P. Dougherty, G. P. Wiederrecht, K. A. Nelson, M. H. Garret, H. P. Jenssen, and C. Warde. Femtosecond Time-Resolved Spectroscopy of Soft Modes in Structural Phase Transitions of Perovskites. *Phys. Rev. B*, 50(13):8996–9019, 1994.
- [12] K. H. Kim, W. T. Elam, and E. F. Skelton. Extended X-Ray Absorption Fine Structure Study of Potassium Niobate. *Mat. Res. Soc. Symp. Proc.*, 172:291–294, 1990.
- [13] O. Hanske-Petitpierre, E. A. Stern, and Y. Yacoby. EXAFS Measurements on Potassium Tantalate Niobate. *J. Phys. IV (Colloques)*, 47(12), 1986.
- [14] O. Hanske-Petitpierre, Y. Yacoby, J. Mustre de Leon, E. A. Stern, and J. J. Rehr. Off-Center Displacement of the Nb Ions Below and Above the Ferroelectric Phase Transition of $\text{KTa}_{0.91}\text{Nb}_{0.09}\text{O}_3$. *Phys. Rev. B*, 44(13):6700–6707, 1991.
- [15] O. Hanske-Petitpierre. *EXAFS and Modulated EXAFS studies on Ferroelectrics*. PhD thesis, University of Washington, 1986.
- [16] B. Rechav, Y. Yacobi, E.A. Stern, J.J. Rehr, and M. Newville. Local Structural Distortions Below and Above the Antiferrodistortive Phase Transition. *Phys. Rev. Lett.*, 72(9):1352–1355, 1994.
- [17] N. Sicron, Y. Yacoby and E.A. Stern. XAFS Study of the Antiferroelectric Phase Transition in PbZrO_3 . *J. Phys. IV (Colloques)*, to be published April 1997.
- [18] N. Sicron, B. Ravel, Y. Yacoby, E.A. Stern, F. Dogan, and J.J. Rehr. Nature of the ferroelectric phase transition in PbTiO_3 . *Phys. Rev. B*, 50:13168–13180, 1994.
- [19] B. Ravel, N. Sicron, Y. Yacoby, E.A. Stern, F. Dogan, and J.J. Rehr. Order-Disorder Behavior in the Phase Transition of PbTiO_3 . *Ferroelectrics*, 164:265–277, 1995.
- [20] J. L. Beeby. The Electronic Structure of Disorderd Systems. *Proceedings of the Royal Society*, A279:82–97, 1964.

- [21] P. Lloyd and P.V. Smith. Multiple Scattering Theory in Condensed Matter. *Adv. Phys.*, 21:69–142, 1972.
- [22] B. L. Gyorffy and M. J. Stott. A One -Electron Theory of Soft X-Ray Emission from Random Alloys. In *Band Structure Spectroscopy of Metals and Alloys*. Academic Press, London, 1973.
- [23] I. Ya. Nikiforov I. V. Bazhin, A. B. Kolpachev. Electronic Energy Structure of Substoichiometric Molybdenum Carbides in Different Crystallographic Modifications. *Phys. Stat. Sol.*, b156:309–317, 1989.
- [24] P.A. Lee and J.B. Pendry. Theory of the Extended X-Ray Absorption Fine Structure. *Phys. Rev. B*, 11(8):2795–2811, 1975.
- [25] R. C. Albers, A. K. McMahan, and J. E. Müller. Electronic and X-ray-Absorption Structure in Compressed Copper. *Phys. Rev. B*, 31(6):3435–3450, 1985.
- [26] J. E. Müller, O. Jepsen, and J. W. Wilkins. X-ray Absorption Spectra: *K*-edges of *3d* Transition Metals, *L*-edges of *3d* and *4d* Metals, and *M*-edges of Palladium. *Sol. St. Comm.*, 42(5):365–368, 1982.
- [27] S. I. Zabinsky, J. J. Rehr, A. Ankudinov, R. C. Albers, and M. J. Eller. Multiple-Scattering Calculations of X-ray-Absorption Spectra. *Phys. Rev. B*, 52(4):2995–3009, 1995.
- [28] J. J. Rehr, J. Mustre de Leon, S. I. Zabinsky, and R. C. Albers. Theoretical X-ray Absorption Fine Structure Standards. *J. Am. Chem. Soc.*, 113(14):5135–5140, 1991.
- [29] A.L. Ankudinov, S.I. Zabinsky, and J.J. Rehr. Single Configuration Dirac–Fock Atom Code. *Comp. Phys. Comm.*, 98:359–364, 1996.
- [30] J. J. Rehr and R. C. Albers. Scattering-Matrix Formulation of Curved-Wave Multiple-Scattering Theory: Application to X-ray-Absorption Fine Structure. *Phys. Rev. B*, 41(12):8139–8149, 1990.
- [31] *L^AT_EX*. <http://www.tug.org/>.

- [32] J. Fox. *University of Washington Thesis Style*. University of Washington, 1995. <http://weber.u.washington.edu/~fox/tex/thesis.html>.
- [33] R. Stallman. *The Emacs Editor*, 1997. <ftp://prep.ai.mit.edu/pub/gnu>.
- [34] K.K. Thorup and P. Abrahamson. *AUC_{TEX}: A Much Enhanced \LaTeX Mode for GNU Emacs*, 1995. <http://sunsite.auc.dk/auctex/>.
- [35] C. Dominik. *REFTEX.EL – Minor Mode for Doing \backslash label $\{\}$ \backslash ref $\{\}$ and \backslash cite $\{\}$ in \LaTeX* , 1997. <http://www.strw.leidenuniv.nl/~dominik/Tools/>.
- [36] P.S. Galbraith. *BIB-CITE.EL – Display \backslash cite, \backslash ref or \backslash label and Extract Refs from $\text{BIB}\TeX$ files.*, 1996. <ftp://ftp.phys.ocean.dal.ca/users/rhogee/elisp/>.
- [37] O. Patashnik. *BIB_{TEX}*, 1994. <http://www.tug.org/>.
- [38] T. Williams and C. Kelley. *Gnuplot: An Interactive Plotting Program*, 1993. <ftp://ftp.dartmouth.edu/pub/gnuplot/>.
- [39] P.J. Turner. *Xmgr Users Guide*, 1995. <http://plasma-gate.weizmann.ac.il/Xmgr/>.
- [40] S. Sutanthavibul, K. Yap, and B. Smith. *XFig: Facility for Interactive Generation of Figures Under X11*. <http://www.cdrom.com/pub/tex/ctan/graphics/xfig/>.
- [41] Network Computing Services, Inc. *Xmol: X Window System Molecule Viewer and Format Converter*, 1997. <http://www.msc.edu/msc/docs/xmol/XMol.html>.
- [42] K. Zhang, E.A. Stern, J.J. Rehr, and F. Ellis. Double Electron Excitation in Atomic Xe. *Phys. Rev. B*, 44(5):2030–2039, 1991.
- [43] J.J. Rehr, R.C. Alber, C.R. Natoli, and E.A. Stern. New High–Energy Approximation for X–Ray–Absorption Near–Edge Structure. *Phys. Rev. B*, 34(6):4350–4353, 1986.
- [44] S.J. Gurman, N. Binsted, I. Ross. A Rapid, Exact Curved–Wave Theory for EXAFS Calculations. *J. Phys. C: Solid State Phys.*, 17:143–151, 1984.

- [45] S.J. Gurman, N. Binsted, I. Ross. A Rapid, Exact Curved-Wave Theory for EXAFS Calculations: II. The Multiple Scattering Contributions. *J. Phys. C: Solid State Phys.*, 19:1845–1861, 1986.
- [46] A. Filliponi, A. Di Cicco, and C.R. Natoli. X-Ray-Absorption Spectroscopy and n -Body Distribution Functions in Condensed Matter. I. Theory. *Phys. Rev. B*, 52(21):15122–15134, 1995.
- [47] J. J. Sakurai. *Modern Quantum Mechanics*. Addison-Wesley, 1985.
- [48] E.A. Stern. Theory of EXAFS. In D.C. Koningsberger and R. Prins, editors, *X-Ray Absorption: Principles, Applications, Techniques of EXAFS, SEXAFS, and XANES*, volume 92 of *Chemical Analysis*, chapter 1, pages 3–51. John Wiley and Sons, New York, 1988.
- [49] G. Martens, P. Rabe, N. Schwentner, and A. Werner. Extended X-Ray-Absorption Fine-Structure Beats: A New Method to Determine Differences in Bond Lengths. *Phys. Rev. Lett.*, 39(22):1411–1414, 1977.
- [50] D. Haskel, B. Ravel, M. Newville, and E.A. Stern. Single and multiple scattering XAFS in BaZrO₃: A comparison between theory and experiment. *Physica B*, 208&209:151–153, 1995.
- [51] G. Bunker. Application of the Ratio Method of EXAFS Analysis to Disordered Systems. *Nuc. Inst. Meth.*, 207:437–444, 1983.
- [52] M. Newville. FEFFIT: Using FEFF to model XAFS in R -space. unpublished, 1994. This documentation is part of the UWXAFS3.0 package.
- [53] E. A. Stern and S. M. Heald. Basic Principles and Applications of EXAFS. In E. E. Koch, editor, *Handbook of Synchrotron Radiation*, pages 995–1014, New York, 1983. North-Holland.
- [54] M. Newville, P. Līviņš, Y. Yacoby, J. J. Rehr, and E. A. Stern. Near-edge x-ray-absorption fine structure of Pb: A comparison of theory and experiment. *Phys. Rev. B*, 47(21):14126–14131, 1993.

- [55] J.W. Cook and D.E. Sayers. Criteria for Automatic X-ray Absorption Fine Structure Background Removal. *J. Appl. Phys.*, 52(8):5024–5031, 1981.
- [56] F. Bridges, C.H. Booth, G.G. Li. An Iterative Approach to "Atomic Background" Removal in XAFS Data Analysis. *Physica B*, 208&209:121–124, 1995.
- [57] B.W. Holland, J.B. Pendry, R.F. Pettifer, and J. Bordas. Atomic Origin of Structure in EXAFS Experiments. *J. Phys. C: Solid State Phys.*, 11:633–642, 1978.
- [58] J. J. Rehr, C. H. Booth, F. Bridges, and S. I. Zabinsky. X-ray-absorption fine structure in embedded atoms. *Phys. Rev. B*, 49(17):12347–12350, 1994.
- [59] C. deBoor. *A Practical Guide to Splines*. Springer-Verlag, New York, 1978.
- [60] L. Brillouin. *Science and Information Theory*. Academic Press, New York, 1962.
- [61] B.S. Garbow, K.E. Hillstrom, J.J. Moré. MINPACK: Software for Solving Nonlinear Equations and Nonlinear Least Squares Problems. Technical report, AT&T Bell Laboratories, University of Tennessee, and Oak Ridge National Laboratories, March 1980. <http://www.netlib.org/>.
- [62] D.E. Sayers and B.A. Bunker. Data Analysis. In D.C. Koningsberger and R. Prins, editors, *X-Ray Absorption: Principles, Applications, Techniques of EXAFS, SEXAFS, and XANES*, volume 92 of *Chemical Analysis*, chapter 6, pages 443–571. John Wiley and Sons, New York, 1988.
- [63] P. R. Bevington and D. K. Robinson. *Data Reduction and Error Analysis for the Physical Sciences*. McGraw-Hill, New York, 2nd edition, 1992.
- [64] E.A. Stern. Number of Relevant Independent Points in X-Ray-Absorption Fine-Structure Spectra. *Phys. Rev. B*, 48(13):9825, 1993.
- [65] E. A. Stern, M. Newville, B. Ravel, Y. Yacoby, and D. Haskel. The UWXAFS Analysis Package: Philosophy and Details. *Physica B*, 208&209:117–120, 1995.

- [66] J.M. Cowley. *Diffraction Physics*. North-Holland, Amsterdam, fourth edition, 1990.
- [67] S.M. Heald. EXAFS with Synchrotron Radiation. In D.C. Koningsberger and R. Prins, editors, *X-Ray Absorption: Principles, Applications, Techniques of EXAFS, SEXAFS, and XANES*, volume 92 of *Chemical Analysis*, chapter 4, pages 119–161. John Wiley and Sons, New York, 1988.
- [68] E.A. Stern. Detectors for Laboratory EXAFS Facilities. In *AIP Conference Proceedings*, number 64, New York, 1980. American Institute of Physics.
- [69] E.A. Stern, W.T. Elam, B.A. Bunker and K. Lu. Ion Chambers for Fluorescence and Laboratory EXAFS Detection. *Nuc. Inst. Meth.*, 195:345–346, 1982.
- [70] W. H. McMaster, N. Kerr-Del Grande, J. H. Mallett, and J. H. Hubbell. *Compilation of X-ray Cross Sections*. Lawrence Radiation Laboratory Report UCRL-50174. National Bureau of Standards, Springfield, VA, 1969.
- [71] E.A. Stern and K. Kim. Thickness Effect on the Extended-X-ray-Absorption-Fine-Structure Amplitude. *Phys. Rev. B*, 23(8):3781–3787, 1981.
- [72] K. Q. Lu and E. A. Stern. Size Effect of Powdered Sample on EXAFS Amplitude. *Nuc. Inst. Meth.*, 212:475–478, 1983.
- [73] E.A. Stern and S.M. Heald. X-Ray Filter Assembly for Fluorescence Measurements of X-Ray Absorption Fine Structure. *Rev. Sci. Instr.*, 50:1579–, 1979.
- [74] R. I. Vedrinskii. personal communication.
- [75] Z. Li, personal communication.
- [76] I thank Steven Rubart of the University of Washington Materials Science and Engineering Department for his help with this task. A 10 mil wire saw and a slurry of water, glycerol, and silicon carbide were used to make the cut.
- [77] M. H. Garret, J. Y. Chang, H. P. Jenssen, and C. Warde. A Method for Poling Barium Titanate, BaTiO₃. *Ferroelectrics*, 120:167–173, 1991.

- [78] M. E. Lines and A. M. Glass. *Principles and Applications of Ferroelectrics and Related Materials*. Clarendon Press, Oxford, 1977.
- [79] G. Shirane, R. Pepinsky, and B.C. Frazier. X-ray and Neutron Diffraction Study of Ferroelectric PbTiO_3 . *Acta Cryst.*, 9:131–140, 1956.
- [80] S.A. Mabud and A.M. Glazer. Lattice Parameters and Birefringence in PbTiO_3 Single Crystals. *Journal of Applied Crystallography*, 12:49–53, 1979.
- [81] E.S. Gagarina, S.M. Zaitsev, M.F. Kuprianov and E. G. Fresenko. Use of Structural Refinement by Means of Powder Patterns to Study the Phase Transition in PbTiO_3 . *Soviet Physics Crystallography*, 24(3):347–349, 1979.
- [82] G. Burns and B.A. Scott. Lattice Modes in ferroelectric Perovskites: PbTiO_3 . *Phys. Rev. B*, 7(7):3088–3101, 1973.
- [83] J.A. Sanjurjo, E. Lopez-Cruz, and G. Burns. . *Phys. Rev. B*, 28(?):7260–, 1983.
- [84] R.J. Nelmes and W.F. Kuhs. The Crystal Structure of Tetragonal PbTiO_3 at Room Temperature and at 700K. *Solid State Communications*, 54(8):721–723, 1985.
- [85] M.D. Fontana, K. Wojcik, H. Idrissi, and G.E. Kugel. Ionic Disorder in the Phase Transition of PbTiO_3 . *Ferroelectrics*, 107:91–96, 1990.
- [86] M.D. Fontana, H. Idrissi, G.E. Kugel, and K. Wojcik. Raman Spectrum of PbTiO_3 Re-Examined: Dynamics of the Soft Phonon and the Central Peak. *J. Phys.: Cond. Matt.*, 3:8695–8705, 1991.
- [87] W. Kleeman, F. J. Schafer, and D. Rytz. Crystal Optical Studies of Precursor and Spontaneous Polarization in PbTiO_3 . *Phys. Rev. B*, 34(11):7873–7879, 1986.
- [88] G.L. Catchen and S.J. Wukitch and D.M. Spaar and M. Blaszkiewicz. Temperature Dependence of the Nuclear Quadrupole Interactions at Ti Sites in Ferroelectric PbTiO_3 and in Ilmenite and Perovskite CdTiO_3 : Evidence for Order-Disorder Phenomena. *Phys. Rev. B*, 42(4):1885–1894, 1990.

- [89] G. L. Catchen and S. J. Wukitch and E. M. Saylor and W. Huebner, M. Blaszkiewicz. Investigating Phase Transitions in ABO_3 Perovskites Using Perturbed Angular Correlation Spectroscopy. *Ferroelectrics*, 117:175–195, 1991.
- [90] R.J. Nelmes, R.O. Plitz, W.F. Kuhs, Z. Tun, and R. Restori. Order-Disorder Behavior in the Phase Transition of $PbTiO_3$. *Ferroelectrics*, 108:165–170, 1990.
- [91] Y. Yacoby and E.A. Stern. Disorder in Crystals Undergoing Structural Phase Transitions. *Comments Cond. Mat. Phys.*, 18(1):1–19, 1996.
- [92] R.E. Cohen. Origin of Ferroelectricity in Perovskite Oxides. *Nature*, 358(9):136–138, 1992.
- [93] A. García and D. Vanderbilt. First-Principles Study of Stability and Vibrational Properties of Tetragonal $PbTiO_3$. *Phys. Rev. B*, 54(6):3817–3824, 1996.
- [94] K.M. Rabe and U.V. Waghmare. First-Principles Model Hamiltonians for Ferroelectric Phase Transitions. *Ferroelectrics*, 136:147–156, 1992.
- [95] K.M. Rabe and U.V. Waghmare. Ferroelectric Phase Transitions: A First-Principles Approach. *Ferroelectrics*, 164:15–32, 1995.
- [96] J. Kobayashi, Y. Uesu, and Y. Sakemi. X-ray and Optical Studies on Phase Transition of $PbTiO_3$ at Low Temperatures. *Phys. Rev. B*, 28(7):3866–3872, 1983.
- [97] M.F. Kuprianov, S.M. Zaitsev, E.S. Gagarina, and E.G. Fresenko. Structural Study of $PbTiO_3$, $PbZrO_3$, and $PbHfO_3$. *Phase Transitions*, 4:55–63, 1983.
- [98] D. Haskel, E.A. Stern, B. Ravel, M. Newville, and S. Heald. Probing Valence Charge Density Distributions in $BaZrO_3$ by XAFS. to be published in *Phys. Rev. B*.
- [99] W. Wul and I.M. Goldman. ??? *C. R. Acad. Sci. Russ.*, 46:139, 1946.
- [100] R. Comes, M. Lambert and A. Guinier. The Chain Structure of $BaTiO_3$ and $KNbO_3$. *Solid State Communications*, 6:715–719, 1968.

- [101] R. Comes, M. Lambert, and A. Guinier. The Chain Structure of BaTiO₃ and KNbO₃. *Acta Crystallographica*, A26:244–250, 1970.
- [102] I.B. Bersuker. On the Origin of Ferroelectricity in Perovskite-Type Crystals. *Phys. Lett.*, 20(6):589–590, 1966.
- [103] A. Hüller. Displacement Correlation and Anomalous X-ray Scattering in BaTiO₃. *Solid State Communications*, 7:589–591, 1969.
- [104] W. Zhong, David Vanderbilt, and K.M. Rabe. First Principles Theory of Ferroelectric Phase Transitions for Perovskites: The Case of BaTiO₃. *Phys. Rev. B*, 52(9):6301–6312, 1995.
- [105] Y. Girshberg and Y. Yacoby. Ferroelectric Phase Transitions in Perovskites with Off-Center Ion Displacements. *Sol. St. Comm.*, to be published, 1997.
- [106] T.R. McGuire, M.W. Shafer, R.J. Joenk, H.A. Alperin, and S.J. Pickart. Magnetic Structure of EuTiO₃. *J. Appl. Phys.*, 37(3):981–982, 1966.
- [107] C-L. Chien, S. DeBenedetti, and F. De S. Barros. Magnetic Properties of EuTiO₃, Eu₂TiO₄, Eu₃Ti₂O₃. *Phys. Rev. B*, 10(9):3913–3922, 1974.
- [108] J. Brous, I. Fankuchen, and E. Bankes. Rare Earth Titanates with a Perovskite Structure. *Acta Cryst.*, 6:67–70, 1953.
- [109] L.A. Grunes. Study of the *K* Edges of 3*d* Transition Metals in Pure and Oxide Form by X-ray-Absorption Spectroscopy. *Phys. Rev. B*, 27(4):2111–2131, 1983.
- [110] F.W. Kutzler, C.R. Natoli, D.K. Misemer, S. Doniach, and K.O. Hodgson. Use of One Electron Theory for the Interpretation of Near Edge Structure in *K*-Shell X-ray Absorption Spectra of Transition Metal Complexes. *J. Chem. Phys.*, 73(7):3274–3288, 1980.
- [111] F. Farges, G.E. Brown Jr., and J.J. Rehr. Coordination Chemistry of Ti(IV) in Silicate Glasses and Melts: I. XAFS Study of Titanium Coordination in Oxide Model Compounds. *Geochim. Cosmochim. Acta*, 60(16):3023–3038, 1996.

- [112] R.V. Vedrinskii and V.L. Kraizman and A.A. Novakovich and S.V. Urazhdin and B. Ravel and E.A. Stern. Pre-Edge Fine Structure (PEFS) of the K-XAS for the 3D-Atoms in the Compounds: A New Tool for the Atomic Structure Determinations. *J. Phys. IV (Colloques)*, to be published April 1997.
- [113] D. Haskel. personal communication.
- [114] B. Ravel and E.A. Stern. Temperature and Polarization Dependent XANES Measurements on Single Crystal PbTiO_3 . *J. Phys. IV (Colloques)*, to be published April 1997.
- [115] J. Stohr. SEXAFS: Everything You Always Wanted to Know About SEXAFS but Were Afraid to Ask. In D.C. Koningsberger and R. Prins, editors, *X-Ray Absorption: Principles, Applications, Techniques of EXAFS, SEXAFS, and XANES*, volume 92 of *Chemical Analysis*, chapter 10, pages 443–571. John Wiley and Sons, New York, 1988.
- [116] B.I. Lundqvist. Some Numerical Results on Quasiparticle Properties in the Electron Gas. *phys. stat. sol.*, 32:273–280, 1969.
- [117] A. Messiah. *Quantum Mechanics*. John Wiley & Sons, 1966.
- [118] J. L. Beeby. The density of electrons in a perfect or imperfect lattice. *Proceedings of the Royal Society*, A302:113–136, 1967.
- [119] S. I. Zabinsky. *Multiple Scattering Theory of XAFS*. PhD thesis, University of Washington, 1993.
- [120] A.L. Ankudinov. *Relativistic Spin-dependent X-ray Absorption Theory*. PhD thesis, University of Washington, 1996.
- [121] A. R. Edmonds. *Angular Momentum in Physics*. Number 4 in Investigations in Physics. Princeton University Press, Princeton, NJ, 1957.
- [122] F. Manar and Ch. Brouder. A Fast Free Green Function Calculation in Multiple-Scattering Theory. *Physica B*, 208&209:79–80, 1995.

- [123] D. Sébilleau. New Recurrence Relations for Matrix Elements of the Propagator. *J. Phys.: Cond. Matt.*, 7:6211–6220, 1995.
- [124] J Fenlason. *GPROF: The GNU Profiler*. The Free Software Foundation, Cambridge, MA, version 2.6 edition, 1993. <ftp://prep.ai.mit.edu/pub/gnu>.
- [125] E. Anderson et al. *LAPACK Users' Guide*. Society for Industrial and Applied Mathematics, Philadelphia, second edition, 1995. <http://www.netlib.org/>.
- [126] W. H. Press, S. A. Teukolsky, W. T. Vetterling, and B. P. Flannery. *Numerical Recipes in FORTRAN*. Cambridge University Press, Cambridge, 2nd edition, 1992.
- [127] L. Mirsky. *An Introduction to Linear Algebra*. Dover Publications, Inc., New York, 1990.
- [128] J. S. Faulkner and G. M. Stocks. Calculating properties with the coherent-potential approximation. *Phys. Rev. B*, 21(8):3222–3244, 1980.
- [129] C. Kittel. *Introduction to Solid State Physics*. John Wiley & Sons, 6th edition, 1986.
- [130] E.A. Stern. Concluding remarks. Speech given at the Ninth International Conference on X-Ray Absorption Fine Structure, 1996.
- [131] G.P. Williams. Electron Binding Energies for the Elements. Technical report, National Synchrotron Light Source, 1983.
- [132] E. Hudson, D.A. Shirley, M. Domke, G. Remmers, A. Puschmann, T. Mandel, C. Xue, G. Kaindl. High-Resolution Measurements of Near-Edge Resonances in the Core-Level Photoionization Spectra of SF₆. *Phys. Rev. A*, 47(1):361–373, 1993.
- [133] R.G.W. Wyckoff. *Crystal Structures*, volume 1–6. Interscience, New York, 1964.
- [134] T.A. Tyson, K.O. Hodgson, C.R. Natoli, and M. Benfatto. General Multiple-Scattering Approach Scheme for the Computation and Interpretation of X-ray-Absorption Fine Structure in Atomic Clusters with Applications to SF₆, GeCl₄, and Br₂ Molecules. *Phys. Rev. B*, 46(10):5997–6019, 1992.

- [135] T.A. Tyson. personal communication.
- [136] K.S. Pitzer and L.S. Bernstein. Molecular Structure of XeF_6 . *J. Chem. Phys.*, 63(9):3849–3856, 1975.
- [137] H. Nakamatsu, T. Mukoyama, H. Adachi. DV- $X\alpha$ Calculation on Resonances in X-Ray Absorption Spectra of SF_6 . *Chem. Phys.*, 143:221–226, 1990.
- [138] M. Jouen. personal communication.
- [139] O.K. Anderson, O. Jepsen, and M. Sob. . In M. Yussouff, editor, *Electronic Band Structure and Its Applications*. Springer Verlag, Berlin, 1986.
- [140] V.L. Kraizman, A.A. Novakovich, R.V. Vedrinskii, and V.A. Timoshevskii. Formation of the Pre-Edge Structure and Dramatic Polarization Dependence of Ti K NEXAFS in PbTiO_3 Crystals. *Physica B*, 208&209:35–36, 1995.
- [141] E.A. Stern and Y. Yacoby. Structural Disorder in Perovskite Ferroelectric Crystals as Revealed by XAFS. *J. Phys. Chem. Solids*, 57(10):1449–1455, 1996.
- [142] M. Holma, N. Takesue, and Haydn Chen. Linear Chain Structure in Cubic KNbO_3 and BaTiO_3 . *Ferroelectrics*, 164:237–251, 1995.
- [143] J. Padilla, W. Zhong, and David Vanderbilt. First Principles Investigation fo 180° Domain Walls in BaTiO_3 . *Phys. Rev. B*, 53(10):R5969–R5973, 1996.
- [144] H. Krakauer. Precursor Structures in Ferroelectrics from First-Principles Calculations. *Ferroelectrics*, page to be published, 1997.
- [145] L.B. Sorenson, J.O. Cross, M. Newville, B. Ravel, J.J. Rehr, H. Stragier, C.E. Bouldin, J.C. Woicik. Diffraction Anomalous Fine Structure: Unifying X-ray Diffraction and X-ray Absorption with DAFS. In K. Fischer G. Materlik, C.J. Sparks, editor, *Resonant Anomalous X-ray Scattering: Theory and Applications*. North Holland, Amsterdam, 1994.
- [146] H. Stragier, J.O. Cross, J.J. Rehr, L.B. Sorenson, C.E. Bouldin, and J.C. Woicik. Diffraction Anomalous Fine Structure: A New X-Ray Structural Technique. *Phys. Rev. Lett.*, 69(21):3064–3067, 1992.

- [147] J.O. Cross. *Analysis of Diffraction Anomalous Fine Structure*. PhD thesis, University of Washington, 1996.
- [148] J.L. Hodeau, J. Vacínová, P. Wolfers, Y. Garreau, A. Fontaine, M. Hagelstein, E. Elkaïm, J.P. Lauriat, A. Collomb, J. Muller. Site Selectivity of DAFS Analysis on Hexaferrite at Fe K Edge by Using Both Monochromatic Optics and Energy Dispersive Optics. *Nuclear Instruments and Methods*, B97:115–118, 1995.
- [149] E. Cockayne and K. Rabe. . *Ferroelectrics*, 1997. to be published.
- [150] Q.T. Islam and B.A. Bunker. Ferroelectric Transition in $\text{Pb}_{1-x}\text{Ge}_x\text{Te}$: Extended X-Ray Absorption Fine-Structure Investigations of the Ge and Pb Sites. *prl*, 59(23):2701–2704, 1987.
- [151] A. Ankudinov. personal communication.
- [152] J. A. Ibers and W. C. Hamilton. *International Tables for X-ray Crystallography: volume IV Revised and Supplementary Tables*. The Kynoch Press, Birmingham, England, 1969.
- [153] M. Newville. *Local Thermodynamic Measurements of Dilute Binary Alloys Using XAFS*. PhD thesis, University of Washington, 1995.
- [154] B. Ravel. ATOMS: Crystallography and XAFS. unpublished, 1994. This documentation is part of the UWXAFS3.0 package.
- [155] H. Burzlaff and A. Hountas. Computer Programs for the Derivation of Symmetry Operations from the Space-Group Symbols. *J. Appl. Cryst.*, 15:464–467, 1982.
- [156] N. F. M. Henry and K. Lonsdale. *International Tables for X-ray Crystallography: volume I Symmetry Groups*. The Kynoch Press, Birmingham, England, 1969.
- [157] L. Tröger, D. Arvanitis, K. Baberschke, H. Michaelis, U. Grimm, and E. Zschech. Full Correction of the Self-Absorption in Soft-Fluorescence Extended X-Ray-Absorption Fine Structure. *Phys. Rev. B*, 46(6):3283–3289, 1992.

- [158] R. Hasse, 1997. personal communication.
- [159] J.J. Rehr. *Ab initio Multiple Scattering X-ray Absorption Fine Structure and X-ray Absorption Near Edge Structure Code*. University of Washington, 1995. software documentation.
- [160] B. Ravel. *XANES*. University of Washington. program documentation.

Appendix A

CRYSTALLOGRAPHY BASED FITTING MODELS IN FEFFIT

FEFF's path formalism provides a natural approach to the analysis of an EXAFS problem. FEFF computes the contribution to the EXAFS from each scattering geometry within a cluster of atoms. The total fine structure then is the sum of the contributions from all calculated scattering geometries. A fit to data using these calculations as fitting standards can be parameterized in terms of the path geometry for both single scattering (SS) and multiple scattering (MS) paths.

This appendix is *not* intended as documentation on the use of FEFFIT. For that, please consult the document[52] distributed with the program. The methods described here may be considered advanced applications of FEFF and FEFFIT. In writing this appendix, I have assumed that the reader is closely familiar with the basic operations of ATOMS, FEFF, and FEFFIT. Specifically, I have assumed that the reader understands the use of math expressions in FEFFIT, knows the purposes of the various output files from FEFF and is familiar with basic concepts of Unix filesystems.

FEFFIT [153] provides a general framework for fitting EXAFS data. In the FEFFIT input file, a path is defined by a path index and all path parameters associated with that index. Throughout this appendix, I will refer to a *path paragraph* as the set of all path parameters sharing a common index. The path parameters known to FEFFIT are shown in Table A.1. The path parameter `path` is used to denote the path to and name of the file containing FEFF's calculation of the effective scattering amplitude and phase shift for that path. `id` is a comment string that will be written to the various output files of FEFFIT. The remaining seven path parameters describe the variables in the EXAFS equation Eq. (2.10) and in Sec. 2.1.3.

This scheme suggests an immediate pitfall. As discussed in Sec. 2.3, the range of data available in an EXAFS experiment imposes a natural bandwidth limiting the information content of the signal. If seven quantities are varied for each path in a fit and many scattering paths are considered, the number of variables may vastly exceed the available information. To handle the requirements of the path parameterization, FEFFIT allows every path parameter to be described by a math expression. This

Table A.1: Path parameters available in FEFFIT.

name	symbol	description
path		The name of the <code>feffnnnn.dat</code> file for this path
id		A text string describing the path
s02	S_0^2	An amplitude
e0	E_0	A shift of the energy reference
delr	ΔR	A change in the total path length
sigma2	σ^2	A relative mean squared displacement of the path length
third	C_3	A third cumulant about the path length
fourth	C_4	A fourth cumulant about the path length
ei	E_i	A change in the effective mean free path

math expression can simply be a value or it can be a function of variables defined elsewhere in the FEFFIT input file. It is useful to think of the content of the FEFFIT input file as a macro language.¹ This appendix is not an exhaustive explanation of that syntax, but it is an example of a sophisticated use of FEFFIT for a complicated fitting problem.

The trick to using FEFFIT effectively is to choose a robust set of variables. Using the math expressions, physical constraints can be built into a fitting model. These constraints may reflect the physical and structural properties of the material under investigation and, if well chosen, will result in loosely correlated variable parameters with small uncertainties in their optimal values.

The rest of this appendix will describe my approach to fitting PbTiO_3 , BaTiO_3 , and EuTiO_3 with examples culled from the FEFFIT input files which I used to analyze the data shown in Chs. 4 – 6.

A.1 A Fitting Model for Tetragonal PbTiO_3

As discussed in Ch. 4, the purpose of the examination of PbTiO_3 in this thesis was to distinguish between the displacive and order–disorder models of its phase transition at 763 K. To do this I constructed two fitting models for analysis of the temperature

¹ In computer science, a syntax such as FEFFIT’s is called a *metalanguage*. Metalanguages are the product of a high level programming language, in this case Fortran 77, which is used to encode the syntax of the metalanguage.

dependent data. One fitting model used the crystallographic parameters of the low temperature, tetragonal phase as fitting variables. For comparison, I fit data in the high temperature phase to a model of cubic local symmetry. The method of fitting to a cubic local symmetry is described in Sec. A.3 for EuTiO_3 and is identical to that used for the cubic PbTiO_3 model.

The geometries of the various scattering paths considered in my fits to the PbTiO_3 data are entirely determined by the space group of the crystal and a set of five crystal parameters used to describe the structure of PbTiO_3 . These crystal parameters are shown in Table 4.4. Had I found that a displacive model described the local structure of PbTiO_3 through its tetragonal to cubic transition the lengths of a and c would have converged with increasing temperature and the three tetragonal displacements would have all gone to zero.

The five crystallographic parameters in Table 4.4 were the variable parameters in my fits to the data. Included in the fitting range were 18 unique scattering paths including 11 double and triple scattering paths. In this section I will describe how I related the path lengths for all 18 paths and the scattering angles of the nearly collinear scattering paths to the set of five crystal parameters. I will also discuss parameterization of phase corrections E_0 and mean square displacements σ^2 for the MS paths.

A.1.1 Evaluating the Path Parameters for PbTiO_3

Figure A.1 shows the ATOMS input file for the tetragonal phase of PbTiO_3 using the parameters in Table 4.4. From the coordinates of the four unique sites and the symmetry properties of the space group $P4MM$, the initial local configuration is determined. The lead atoms occupy the corners of a hexahedron of tetragonal symmetry. The titanium atom occupies a position near the center of the hexahedron. The planar oxygens occupy positions in the four elongated faces of the hexahedron, although they are displaced along the \hat{c} direction from the centers of those faces. The axial oxygens occupy positions near the centers of the square faces of the hexahedron, although they are displaced along \hat{c} out of the those faces. There are seven bond lengths that I must calculate using the math expressions of FEFFIT. The oxygen coordination shell is thus split into three distances: 1) a short axial path, 2) a long axial path, and 3) four planar paths. The lead and titanium coordination shells are split into two distances each. There are a variety of collinear and nearly collinear MS paths overlapping the titanium coordination shell.

```

title PbTiO3 25C
title Glazer and Mabud, Acta Cryst. B34, 1065-1070 (1978)
Space P 4 m m
a=3.905 c=4.156
rmax=5 core=ti
atom
! At.type x y z tag
Pb 0.0 0.0 0.0
Ti 0.5 0.5 0.539
O 0.5 0.5 0.1138 axial
O 0.0 0.5 0.6169 planar
-----

```

Figure A.1: The `atoms.inp` file for PbTiO_3 .

In the formalism used by FEFF and FEFFIT, the *effective path length* for a path is half of the total distance traveled by the photoelectron. For SS paths, the effective path length is simply the distance between the scatterer and the central atom. For MS paths, effective path length is half of the sum of the lengths of the legs of the path. I therefore use the five crystal parameters to compute the seven relevant bond lengths in the problem. From these I compute all SS and MS path lengths.

Fig. A.2 shows assignment of the crystallographic parameters from Table 4.4 for PbTiO_3 at room temperature. In FEFFIT, parameters which are varied to optimize the fit are specified with the `guess` keyword. The `set` keyword is used to assign constant or calculated values for use elsewhere in the input file. In each fitting iteration, FEFFIT will first assign current values to the `guess` parameters. It then evaluates all the `set` parameters, some of which may depend on current values of `guess` parameters. Then the path parameters will be evaluated given the current values of both the `guess` and `set` parameters. Finally the EXAFS equation is evaluated given the current values of the path parameters and the paths are summed for comparison to the data and determination of χ^2 .

Fig. A.3 shows the calculation of the bond lengths from the crystallographic parameters. If the math expressions in Fig. A.3 are evaluated using the initial values of the fitting parameters from Fig. A.2, then the bond lengths from Table 4.3 are ob-

```

%%% axis lengths
set    a0          3.902          %%% length of a axis
guess  delta_a     0.0
set    a           a0 + delta_a
set    c0          4.156          %%% length of c axis
% guess delta_c    0.0
% set   c          c0 + delta_c
set    vol         a0*a0*c0
set    c           vol / (a^2)
% set   delta_c    c-c0

%%% displacement parameters
guess  dti         0.0390
guess  do1         0.1138
set    do2         0.1169
%%% nominal buckling angle
set    angle0      9.41475

```

Figure A.2: Part of the FEFFIT input file for PbTiO_3 . This piece contains the crystallographic information at room temperature. The length of the c -axis is determined by holding the volume fixed and varying δ_a , as discussed in Sec. 4.2. The buckling angle is not an independent parameter. It is determined from the values of the other parameters. This is shown in Fig. A.7. Note that, by setting each of dti , do1 , and do2 to zero and delta_a to 0.083 such that $a = c = 3.985$, the cubic local structure can be obtained. Thus this fitting model has the freedom to follow the local structure of a displacive phase transition.

```

%%% short and long axial oxygen bond lengths
set      rtio1_sh      (0.5 - (do1-dti)) * c
set      rtio1_lo      (0.5 + (do1-dti)) * c
%%% planar oxygen bond length
set      rtio2          sqrt( (a/2)^2 + ((do2-dti)*c)^2 )
%%% short and long lead bond lengths
set      rtipb_sh       sqrt( a^2/2 + c^2*(0.5 - dti)^2 )
set      rtipb_lo       sqrt( a^2/2 + c^2*(0.5 + dti)^2 )
%%% short and long titanium bond lengths
set      rtiti_sh       a
set      rtiti_lo       c

```

Figure A.3: Part of the FEFFIT input file for PbTiO_3 . This piece contains the calculations of the seven bond lengths from the crystallographic information in Fig. A.2. Using the initial values of the parameters from Fig. A.2, the bond lengths from Table 4.3 are obtained.

tained. In a crystal with orthogonal axes, these distances are easily computed as sums of squares. In Sec. A.2 I discuss constructing FEFFIT input files for the rhombohedral phase of BaTiO_3 .

In FEFFIT the path parameter corresponding to the path length in the EXAFS equation, `delr`, is a measure of *change* in path length rather than the absolute path length. Fortunately FEFFIT provides a convenient shortcut. In FEFFIT, the word `reff` is a reserved word that cannot be used as a user-chosen variable name. `reff` always means the effective path length written to the `feffnnnn.dat` file from FEFF. When the path parameters for a given path are evaluated and the word `reff` is encountered in one of the math expressions, the math expression is evaluated using the effective path length of the current path as it was read from the `feffnnnn.dat` file. If `reff` is found in a math expression for a subsequent path paragraph, the effective path length from the `feffnnnn.dat` file for *that* subsequent path is used. In my input files, I computed the change in path length by summing the lengths of the legs of the scattering path, dividing by two, and subtracting `reff`. The path paragraphs for the three oxygen single scattering paths are shown in Figs. A.4. For these paths `delr` is simply the bond length minus `reff`. The descriptions of the lead and titanium single scattering paths are similar to these, substituting the titanium-lead and

titanium–titanium bond lengths into the `delr` math expressions in the appropriate path paragraphs.

```

path    1      feff/feff0001.dat
id      1      short axial 0 SS  r_eff=1.7628
delr    1      rtio1_sh - reff
sigma2  1      sigo_1 + sigmm
e0      1      e0o

path    2      feff/feff0002.dat
id      2      planar 0 SS  r_eff=1.9703
delr    2      rtio2 - reff
sigma2  2      sigo_p + sigmm
e0      2      e0o

path    3      feff/feff0003.dat
id      3      long axial 0 SS  r_eff=2.3762
delr    3      rtio1_lo - reff
sigma2  3      sigo_3 + sigmm
e0      3      e0o

```

Figure A.4: Part of the FEFFIT input file for PbTiO_3 . This part shows the oxygen SS path paragraphs. The path paragraphs for the lead and titanium SS paths are quite similar. Note that the McMaster correction `sigmm` described in Sec. B.2.2 is added to σ^2 for each path.

The parameters used to define S_0^2 , the E_0 's, and the σ^2 's in the fitting model are shown in Fig. A.5. Some of the content of Fig. A.5 seems redundant, for example the separate assignment of σ^2 's for the oxygen paths which are then set to be equal. Defining FEFFIT variables in this manner allows me to easily extend my fitting model. In the example of the oxygen σ^2 's, I was able to test the effect of allowing independent σ^2 's in the first shell without substantial editing of the FEFFIT input file².

Figure A.6 shows an example of a path paragraph describing a multiple scatter-

² It turned out that the first shell oxygen σ^2 were the same within their error bars when allowed to vary independently.

```

set      amp          0.90
set      sigmm        0.00093    %%% McMaster correction
%%% Oxygen parameters
guess    e0o          8.226
guess    sigo_p        0.004      % MSD for planar O
set      sigo_1        sigo_p      % MSD for short Ti
set      sigo_3        sigo_p      % MSD for long Ti
%%% Lead parameters
set      e0pb         -10.4
set      theta_pb_sh   227        % from PRB v.50 #18 p.13168
set      sigpb_sh      eins(temp, theta_pb_sh)
set      theta_pb_lo   204        % from PRB v.50 #18 p.13168
set      sigpb_lo      eins(temp, theta_pb_lo)
%%% Titanium parameters
set      e0ti          7.30
guess    sigti_p        0.007357   % MSD for planar Ti
set      sigti_a        sigti_p     % MSD for axial Ti

```

Figure A.5: Part of the FEFFIT input file for PbTiO_3 . This part shows the remaining guess and set parameters.

ing path. This path is a collinear, triple scattering path through the more distant axial oxygen to the axial titanium atom. This path has the same contribution to the EXAFS as the path through the shorter axial oxygen since the location of the intervening atom in a collinear path has very little effect on the EXAFS. Unfortunately, this near degeneracy slips through the degeneracy checker in FEFF's path finder. This path has four legs. The first and last leg are the long oxygen bond length. The middle two legs are the short oxygen bond length. Thus the effective path length is the sum of the short and long oxygen bond lengths. This is equivalent to the c axis length and the math expression for `delr` could have been written `c - reff` or even `delta_c`. I found it convenient, particularly for the nearly collinear paths, to maintain the more general description of the `delr`'s in terms of the lengths of the legs.

```

%%% a triple scattering, colinear path
path      27      feff/feff0023.dat
id        27      ~ -> long axial -> axial Ti -> long axial -> ~
delr      27      rtio1_lo + rtio1_sh - reff
sigma2    27      sigti_a + sigmm
e0        27      ( 2*e0o + e0ti ) / 3

```

Figure A.6: Part of the FEFFIT input file for PbTiO_3 . This part shows an example path paragraph for a collinear MS path. I use the `id` line to describe the path of the photoelectron. The symbol `~` is used to denote the central atom.

The math expressions for `sigma2` and `e0` that I used in Fig. A.6 further reflect the physics of my fitting model. I assign an E_0 and a σ^2 for each type of backscatterer. In the EXAFS equation σ^2 is the relative mean square deviation of the total path length. For a collinear multiple scattering path, the variation of the intervening atom about its site has only a tiny effect on the deviation of the total path length. In this scattering geometry, only the σ^2 of the titanium atom effects the deviation in path length. Consequently, no new σ^2 variables need to be introduced when including these MS paths.

When FEFF computes the phase shifts of the central and backscattering atoms, it constructs a muffin tin from neutral atoms. Neglecting the possibility of charge transfer between the atoms in the material may result in inaccuracies in these phase shifts. This problem should be most serious at lower energies. This mistake in

the calculation of the phase may be corrected with the correct energy dependence by introducing a shift in the energy reference of Eq. (2.10) using Eq. (2.11). One successful [50] method of parameterizing these phase corrections involves assigning a independent energy reference shift for each type of backscatterer. The phase shift for a MS path is then the average of the energy reference shifts associated with each of the backscatterers in the path. This is seen in the `e0` path parameter depicted in Fig. A.6. Again, no new fitting variables are introduced to consider MS paths.

Note that, in this section, I have not shown several parts of the input files that I used to fit PbTiO_3 . I have only shown four of the 27 path paragraphs. The remaining SS path paragraphs are very similar to those shown in Fig. A.4. The collinear MS path paragraphs are similar to the one shown in Fig. A.6. The non-collinear path paragraphs are described in the next section. Also not mentioned in this section was all of the information that goes into the header of the input file. This includes information such as Fourier transform and fitting ranges, the name of the data file, and so on. Entering this information into the FEFFIT input file is straightforward and examples are given in FEFFIT's documentation [52].

In Figs. A.4 and A.6 an additional term, `sigmm`, is added to the `sigma2` path parameter. This is the so-called McMaster correction which is computed by ATOMS and discussed in Sec. B.2.2.

One final point about the path paragraphs in the FEFFIT input file. The path parameter `path` is used to specify the name of the `feffnnnn.dat` file to be used for that scattering path. The value `path` can include a directory path³ as well as the file name. In Figs. A.4 and A.6, `feff/` is the directory path to the files `feff00nn.dat`. Using the directory structure of your operating system is a real boon for organizing the many output files of FEFF and FEFFIT.

A.1.2 Evaluating the Effect of non-collinearity in PbTiO_3

As the displacements of the titanium and planar oxygen atoms vary, the scattering angle for multiple scattering paths involving those atoms change. The embedded

³ That was the fourth distinct meaning of the word *path* in two sentences. A *scattering path* refers to the trajectory of a photoelectron. A *path parameter* is a conceptual construct used in FEFFIT. All available path parameters are given in Table A.1. `path` is the path parameter that specifies the computer file containing the a calculation by FEFF of the effective scattering amplitude and phase shift of a scattering path. A *directory path* is a conceptual construct of Unix filesystems indicating the structure of directories and subdirectories specifying the location of a file on a hard disk.

atomic backscattering amplitudes and phase shifts depend strongly on angle. I have to consider this in my fits along with variations in `delr`, `sigma2`, and `e0`. Changes in the `delr`'s are parameterized as half the sum of the lengths of the legs and the `e0`'s is parameterized as described in the preceding section. Since the planar paths are not exactly collinear assigning σ^2 's in the same manner as for the collinear path is a worse approximation, but not much worse. The additional transverse contribution to σ^2 due to the non-collinear angle will be small compared the total σ^2 .

To approximate the effect of the changing scattering angle, I used an interpolation scheme. I computed the contribution due to each planar multiple scattering path at each of three angles: 1) the angle determined from the structural parameters in Fig. 4.4, 2) $\frac{2}{3}$ of this angle, and 3) zero degrees. As the structural parameters varied in the fit, the current angle was determined as shown in Fig. A.7 and a weighting parameter, `x`, is determined for interpolation between the initial angle and the zero angle. The effect of angle must be of even parity, so an interpolation parameter of even parity is used. Fig. A.7 shows weighting coefficients for both two point and three point interpolation. Fig. A.8 shows the three path paragraphs used to model the effect of the angle.

The parameterizations of `delr`, `sigma2`, and `e0` are shown in Fig. A.8. The weighting coefficients enter as modifies of the S_0^2 term in the `s02` path parameters. Each of the three calculations at the three angles enters into the fit with the appropriate weighting coefficient for a two or three point weighting coefficient. I could use a two or three point interpolation by uncommenting the appropriate set of coefficients as shown in Fig. A.7. There was negligible difference in fit quality for the the two and three point interpolations.

There is a serious pitfall in this technique. It is critical to treat correctly both the effective phase shift and the `delr` of each path. When I calculated the paths for the $\frac{2}{3}$ and 0 angles, I took care to preserve the lengths of each leg and of the entire path such that `reff` is the same for each of these paths but the $\phi_j^{eff}(k)$ term from Eq. (2.10) is different. Thus the interpolation is used to determine the best-fit $\phi_j^{eff}(k)$ and `delr` is computed from the structural fitting parameters.

In FEFF, scattering geometries are described in a file called `paths.dat`. Normally, this file is written by FEFF's path finder and is used unedited. Special geometries, though, can be specified by editing this file. Fig. A.9 shows the `paths.dat` file that I used to generate the feff data files used in Fig. A.8. The first path, which has path index 15, is one of the nearly collinear paths found by FEFF's path finder. The scattering angle in this case is 9.41° . The coordinates in paths 115 and 215 were

```

%%% buckling angle & weighting coefficients by Lagrange's formula
%%% see Num. Rec. in Fort. 1992 ed, sec. 3.1, p. 102
set    angle      acos( a/(2*rtio2) ) * (180/pi) % in degrees
set    x          angle^2 / angle0^2
%%% two point interpolation (neglect path at 2/3 angle)
set    w_full     x
set    w_twoth   0
set    w_zero     1-x
%%% three point interpolation (include path at 2/3 angle)
% set  w_full     3*x^2 - 2*x
% set  w_twoth   (-9/2) * x * (x-1)
% set  w_zero     1.5 * (x-1) * (x-2/3)

```

Figure A.7: Part of the FEFFIT input file for PbTiO_3 . This part shows the computation of the buckling angle and the weighting parameters for the interpolation scheme of Fig. A.8 used to determine the effect of the changing angle on the signal. Note that these are all `set` values are computed from other variables in the fit, thus consideration of this angle uses no additional portion of the information content.

```

path    18      feff/feff0015.dat
id      18      ~ -> planar 0 -> planar Ti -> planar 0 -> ~
delr    18      2*rtio2 - reff
sigma2  18      sigti_p + sigmm
e0      18      ( 2*e0o + e0ti ) / 3
s02     18      w_full * amp

path    19      feff/feff0115.dat
id      19      2/3 angle
delr    19      2*rtio2 - reff
sigma2  19      sigti_p + sigmm
e0      19      ( 2*e0o + e0ti ) / 3
s02     19      w_twoth * amp

path    20      feff/feff0215.dat
id      20      zero angle
delr    20      2*rtio2 - reff
sigma2  20      sigti_p + sigmm
e0      20      ( 2*e0o + e0ti ) / 3
s02     20      w_zero * amp

```

Figure A.8: Part of the FEFFIT input file for PbTiO_3 . This part shows example path paragraphs for a multiple scattering paths involving the planar oxygen atoms. The effect of the change in bond angle on the data is determined by interpolating among two or three paths of the same length which differ only by the scattering angle through the oxygen atom. The interpolation coefficients are multiplied by S_0^2 .

chosen to keep the lengths of the legs constant and to make the angles 6.28° and 0° respectively. Running the third module of FEFF with this `paths.dat` file produces files called `feff0015.dat`, `feff0115.dat`, and `feff0215.dat` which are used in the path paragraphs shown in Fig. A.8. I chose the path indices 115 and 215 to avoid conflict with other paths yet to maintain a mnemonic connection to path 15. FEFF does not require any specific order to the choice of path indices in `paths.dat`. I have left the columns containing the leg lengths and Euler angles out of my `paths.dat` file as they are not required by FEFF.

The construction of the special `feffnnnn.dat` files for consideration of the effects of the buckling angle was a tedious and labor intensive part of preparing to run these fits. A scheme for automating this chore in a general manner would be an excellent addition to the battery of software tools developed by the FEFF and UWXAFS projects.

A.2 A Fitting Model for Rhombohedral BaTiO_3

In its low-temperature phase, BaTiO_3 is rhombohedral, thus consideration of the `delr`'s involves a rhombohedral angle $\alpha \neq 90^\circ$. The five structural parameters used in the rhombohedral model are shown in Table 5.5. Again the distinction between the displacive and order-disorder models was made by considering the local structures predicted by the two models in my fits. Much of what I did to parameterize my fits is conceptually identical to the discussion in Sec. A.1. In this section I will discuss how the `delr`'s depend upon the rhombohedral angle in the FEFFIT input file.

My analyses of BaTiO_3 data were performed on the barium edge, thus all of the examples in this section show the computation of path lengths with the barium atom as the central atom. Fig. A.10 shows the `ATOMS` input file for the rhombohedral phase of BaTiO_3 using the parameters from Table 5.5. From the symmetries of space group R3M and the five structural parameters, I know that the barium atoms reside on the corners of the rhombohedron, the titanium is displaced in a $\langle 111 \rangle$ direction from the center of the rhombohedron, and the oxygen atoms are displaced from the centers its faces. These deviations from the pure perovskite structure split the oxygen coordination shell into three distances and the titanium coordination shell into four distances. In the rhombohedral structure, the barium coordination shell is unsplit.

Fig. A.11 shows how I defined the crystallographic parameters in my FEFFIT input file. Although I performed my analysis out to the fifth coordination shell, I will only present the first three here. Note that the trigonometric functions in FEFFIT expect arguments in radians, so I convert from degrees to radians using a `math` expression.

```
PbTiO3, Glazer and Mabud, Acta Cryst. B34, 1065-1070 (1978)
Rmax 4.8868, keep limit .000, heap limit .000
Plane wave chi amplitude filter 2.50%
```

```
-----
15 4 4.000 index, nleg, degeneracy, r= 3.9583
  x      y      z      ipot label
.000000 1.952500 .323750 1 'O   '
.000000 3.905000 .000000 3 'Ti   '
.000000 1.952500 .323750 1 'O   '
.000000 .000000 .000000 0 'Ti   '
115 4 4.000 index, nleg, degeneracy, r= 3.9583
  x      y      z      ipot label
.000000 1.967290 .216370 1 'O   '
.000000 3.934570 .000000 3 'Ti   '
.000000 1.967290 .216370 1 'O   '
.000000 .000000 .000000 0 'Ti   '
215 4 4.000 index, nleg, degeneracy, r= 3.9583
  x      y      z      ipot label
.000000 1.979150 .000000 1 'O   '
.000000 3.958300 .000000 3 'Ti   '
.000000 1.979150 .000000 1 'O   '
.000000 .000000 .000000 0 'Ti   '
```

Figure A.9: A `paths.dat` file used by FEFF to generate the `feffnnnn.dat` data for PbTiO_3 at the three bond angles used in Fig. A.8. Paths 115 and 215 were constructed to have the same path length as path 15, but with angles of 6.71° and 0° respectively. Constructing paths in this manner separates the change in bond lengths from the effect on $\phi_j^{\text{eff}}(k)$ due to the change in scattering angle.

```

title Barium Titanate from Kwei et al., using 40K data
title J Phys Chem, 97, 2368, 1993
space   r 3 m
a       4.0035  alpha  89.843
rmax = 8.2      index = true
core    ba
atom
  ba    0        0        0
  ti    0.4847  0.4847  0.4847
  o     0.5088  0.5088  0.0183

```

Figure A.10: atoms.inp file for BaTiO₃.

```

set     a0          4.0035
guess   delta_a     0.0
set     a           a0 + delta_a
set     dalpha      0.157
set     alpha       (90.0-dalpha) * pi / 180  ! in radians
guess   delta_ox    0.0088
set     delta_oz    0.0183
set     doz         delta_oz * a
guess   delta_tix   -0.0153

```

Figure A.11: Part of the FEFFIT input file for BaTiO₃. This part shows the structural parameters in the rhombohedral local structure. Note that pi is a reserved word in the syntax of FEFFIT and is always equal to $\pi = 3.14159\dots$

Computing the eight bond lengths for the first three shells in this structure is messy. I use the law of cosines repeatedly to determine distances in this non-orthogonal metric. Fortunately in a rhombohedral structure, there is only one unique angle that is used in all of the law of cosines calculations. I will not describe in detail the contents of Figs. A.12 and A.14. The math is correct and the contents of the figures are well commented. The bottom line is that, through judicious use of the math expressions, very complex constraints can be built into the fitting model.

FEFFIT provides a means of “spell-checking” your input file. Inserting the `nofit` keyword into the FEFFIT input file, causes FEFFIT to evaluate all of the math expressions and path parameters using the initial values for all `guess` parameters, then stopping without performing the fit. The values of the set expressions and path parameters are written to the log file. Since the initial values of the `guess` parameters are those used in the FEFF calculation, the `delr`'s all of the paths should be zero if the math expressions are correct⁴. A second test is to set all of the guessed values of `dalpha`, `delta_ox`, `delta_oz`, and `delta_tix` in Fig. A.11 to 0 and see that the cubic structure is reproduced in a run using the `nofit` keyword. The path paragraphs shown in Fig. A.13 are for the first shell oxygen SS paths. All of the rest of the SS path paragraphs look quite similar, using the appropriate values from Figs. A.12 and A.14 for `delr` and the appropriate values for `path`, `e0` and `sigma2`.

About the barium atom, there are no MS paths which overlap the SS paths of the first three coordination shells. There are, however, significant nearly collinear MS paths overlapping the fifth coordination shell. These were included in the fit using the interpolation method described in Sec. A.1.

For the fits to the orthorhombic and tetragonal local structures of BaTiO₃, I again used the methods described in Sec. A.1. The orthorhombic case was slightly more complicated since the *a* and *b* axes were of different lengths. Ref. [4] provides the pseudo-monoclinic *a* and *c* axis lengths and α angle for the orthorhombic structure. I used these to determine the axis lengths by means of the appropriate set expressions.

A.3 A Fitting Model for Cubic EuTiO₃

Constructing a cubic fitting model in FEFFIT is vastly easier than for a lower symmetry structure. All of the tricks for parameterizing E_0 and σ^2 for MS paths discussed in

⁴ Actually roundoff error from various sources made these values in the log file slightly different from zero, typically in the fifth decimal place. This is well below the uncertainty of the EXAFS measurement.

```

%%% psi is more convenient than alpha for the law of
%%% cosines (loc) expressions below
set      psi      pi - alpha

%%% for near and far, use law of cosines to find distance
%%% along cell face, then loc again to find distance to
%%% oxygen atom
set      near1    a*(0.5-delta_ox)
set      nearp    sqrt( 2*near1**2 - 4*near1*cos(psi) )
set      dr_inear sqrt( nearp**2 + doz**2 - 2*nearp*doz*cos(psi) )

%%% half the short face diagonal is the distance from the
%%% barium to the projection of this O atom on the face.
%%% use loc with that distance, doz, and psi
set      midcorr  2*sqrt(csqr/4)*doz*cos(psi)
set      dr_omid  sqrt( csqr/4 + doz**2 - midcorr )

set      far1     a*(0.5+delta_ox)
set      farp     sqrt( 2*far1**2 - 4*far1*cos(psi) )
set      dr_ofar  sqrt( farp**2 + doz**2 - 2*farp*doz*cos(psi) )

```

Figure A.12: Part of the FEFFIT input file for BaTiO₃. This part shows the calculation of the three oxygen bond lengths.

```
path 1 ../feff/rhomb/feff0001.dat
id 1 amp=100.000      deg=3.000      nleg=2      r_eff=2.7856
delr 1 dr_inear - reff
sigma2 1 sigo + sigmm
e0 1 e0o

path 2 ../feff/rhomb/feff0002.dat
id 2 amp=100.000      deg=6.000      nleg=2      r_eff=2.8284
delr 2 dr_omid - reff
sigma2 2 sigo + sigmm
e0 2 e0o

path 3 ../feff/rhomb/feff0003.dat
id 3 amp=46.222      deg=3.000      nleg=2      r_eff=2.8859
delr 3 dr_ofar - reff
sigma2 3 sigo + sigmm
e0 3 e0o
```

Figure A.13: Part of the FEFFIT input file for BaTiO₃. This part shows the path paragraphs for the first shell oxygen SS paths using the bond lengths determined from the math expressions shown in Fig. A.12.

```

%%% compute the length of the body diagonal
%%% bsqr = long face diagonal squared
%%% csqr = short face diagonal squared
%%% gsqr = short body diagonal squared
set    bsqr    a**2 * ( 2 + 2*cos(alpha))
set    csqr    a**2 * ( 2 - 2*cos(alpha))
set    gsqr    csqr + a**2
set    cosg    (bsqr + a**2 - gsqr) / ( 2 * a * sqrt(bsqr))
set    body    sqrt( bsqr + a**2 + 2*a*sqrt(bsqr)*cosg )

%%% the nearest and farthest titaniums lie along the
%%% body diagonals
set    dr_ti1  body * ( 0.5 + delta_tix )
set    dr_ti4  body * ( 0.5 - delta_tix )

%%% consider the triangle formed by Ba atoms at opposite
%%% corners of a face and the body center.  sigma is the
%%% angle Ba-body_center-Ba. For alpha = 90 (a cube) sigma
%%% is 109.47122 deg = 1.91063 rad.  use law of cosines
set    s1      (bsqr/2) - (gsqr/4) - (body**2/4)
set    s2      body*sqrt(gsqr/4)
set    sigma   acos( s1 / s2 )

%%% now use law of cosines to get these two distances
set    ti23corr 2 * sqrt(gsqr/4) * body*delta_tix * cos(sigma)
set    dr_ti2   sqrt( gsqr/4 + (body*delta_tix)**2 - ti23corr )
set    dr_ti3   sqrt( gsqr/4 + (body*delta_tix)**2 + ti23corr )

%%% finally, an easy one!
set    dr_ba    a

```

Figure A.14: Part of the FEFFIT input file for BaTiO₃. This part shows the calculation of the four titanium bond lengths and the (very easy) barium bond length.

Sec. A.1 can be used. In the cubic perovskite structure there is no need to consider changing bond angles — all MS paths that contribute significantly to the EXAFS are collinear. Since the true perovskite structure is cubic any lattice expansion or contraction will be isotropic. This means that all `delr`'s in the fitting model can be parameterized in terms of an isotropic lattice expansion parameter η . An example of this for a SS path is shown in Fig. A.15. Parameterizing `delr` in this manner is correct for any MS path also.

```
path      1      feff/feff0001.dat
id        1      1st shell oxygen SS
delr      1      eta * reff
sigma2    1      sigo + sigmm
e0        1      e0o
```

Figure A.15: Part of the FEFFIT input file for a cubic fitting model.

Appendix B

ATOMS: HANDLING CRYSTALLINE MATERIALS IN XAFS THEORY AND EXPERIMENT

The development of a multiple scattering theory of EXAFS greatly expanded the scope of problems which could be considered by EXAFS. With FEFF5 and later versions of FEFF, distant coordination shells and multiple scattering contributions could be considered in fits to EXAFS spectra from arbitrary samples. FEFF provides a general solution to the multiple scattering problem by taking a list of atomic coordinates as its input information. From this list, it determines [119] all possible single and multiple scattering geometries within the list of atomic coordinates. While the use of an atom list makes FEFF a generally useful and powerful tool, it is a practical limitation to its use. Constructing an appropriate list of atomic coordinates can be a time consuming and error prone chore. To address this limitation to the utility of FEFF, I wrote the program ATOMS.

ATOMS automates the creation of atom lists for crystalline materials and performs several calculations useful for interpreting EXAFS measurements. In this appendix I describe the algorithms used by ATOMS and briefly describe the use of the code. ATOMS is a part of the UWXAFS analysis package [65] and is also distributed with FEFF. There is documentation [154] for ATOMS that describes all the details of the program.

B.1 The Crystallographic Algorithm

ATOMS reads its input data from a free format, plain text file. This file is called `atoms.inp`. This input file is parsed by the code and the information needed for the calculation is interpreted from its content. The parsing scheme relies on mnemonic keywords which have associated values. For example, when the parsing routine encounters the word `space` in a context where it is to be interpreted as a keyword, the characters following it are interpreted as the symbol describing the space group. Except for a few special rules discussed in the program documentation, there is no required order to the keywords in the input file. An example of this loose structure

is shown in Figure B.1. In this manner all crystallographic information as well as all other run-time parameters are entered into the program. The loose structure and English-like syntax of the input file make ATOMS easy to use and understand.

```

title PbTiO3 25C
title Glazer and Mabud, Acta Cryst. B34, 1065-1070 (1978)
core=ti      Space P 4 m m
a=3.905      nitrogen=1
rmax=3.6     c=4.156
atom
! At.type  x      y      z      tag
  Pb      0.0     0.0     0.0
  Ti      0.5     0.5     0.539
  O       0.5     0.5     0.1138  axial
  O       0.0     0.5     0.6169  planar
-----

```

Figure B.1: An example input file for ATOMS. This is for PbTiO_3 using the structural data from Ref. [3].

ATOMS uses the algorithm of Burzlaff and Hountas [155] to derive symmetry operations from Hermann–Maguin space group symbols. ATOMS understands both Hermann–Maguin and Schoenflies symbols. The Schoenflies symbols are converted internally into the corresponding Hermann–Maguin symbol for the standard setting of the space group for interpretation by the Burzlaff–Hountas algorithm. Use of the Hermann–Maguin symbols is preferred as that notation system resolves the ambiguity of spatial setting for certain low symmetry space groups [156]. For example, an orthorhombic crystal may have different symmetry elements in the three directions. The choice of which set of symmetry elements to associate with each of the Cartesian directions is arbitrary. There may be up to six different choices. The Hermann–Maguin system resolves this choice unambiguously while the Schoenflies system assigns the same symbol to each of the settings of a space group.

The Burzlaff–Hountas algorithm interprets the symmetry elements and Bravais translations from the Herman–Maguin symbol and constructs symmetry tables. The unique atomic positions specified in the input file are operated upon by these sym-

metry tables to generate the entire contents of the unit cell. The unit cell is then translated in all three directions to entirely enclose a sphere of the radius specified by the `rmax` keyword in the input file. The positions within the unit cells are translated into Cartesian coordinates using the values of the `a`, `b`, and `c` keywords. For a non-orthogonal unit cell, one or more of the cell angles `alpha`, `beta`, and `gamma` would also need to be specified. One of the atoms of the type specified by the `core` keyword is selected as the origin and a list ordered by radial distance of atom coordinates is generated. The output of `ATOMS` is written to a file called `feff.inp` which is shown in Fig. B.2. This file contains the atom list along with reasonable guesses for the rest of the information required by `FEFF`. The first three columns of the atom list are the Cartesian coordinates of the atoms. The absorbing atom is placed at $(0, 0, 0)$. The fourth column is the potential index which identifies the species of the atom at that location. The fifth and sixth column are not used by `FEFF`, but are included for the benefit of the user. The fifth column is a tag which identifies the atom as coming from a particular crystallographic site. The two oxygen atoms in the `atoms.inp` file shown in Fig. B.1 are distinguished by the tags `planar` and `axial`, which, in this case refer to the placement of the oxygen atoms relative to the \hat{c} axis and to the nearby titanium atom. The sixth column is the distance of that atom from the absorbing atom.

`FEFF` requires that each atom in the cluster be assigned a unique potential index. `FEFF` then computes the free atom potential and charge density for the atomic species of each unique potential. These free atoms are then overlapped to form the muffin tin potential used [28] by `FEFF` to compute the scattering amplitudes and phase shifts which enter into Eq. (2.10). `ATOMS` makes the simplest possible choice of potential index assignments. As shown in Fig. B.2, a potential index is assigned to the central atom and to each atomic species in the cluster. In some situations it may be advantageous to allow atoms of the same species to be handled differently by `FEFF`. It is my opinion that it should be up to the `FEFF` user to choose to run `FEFF` with potential assignments more complicated than the simple choice made by `ATOMS`.

There are several other points of interest in Fig. B.2. The comment lines indicated in the `ATOMS` input file by the keyword `title` are written to the output file. This allows for user chosen documentation to be passed from `atoms.inp` through to the output of `FEFF`. The radial extent of the cluster is chosen by the `rmax` keyword in `atoms.inp`. The `HOLE` keyword in `feff.inp` is used to specify which absorption edge will be calculated by `FEFF`. `Atoms` assumes that, if the absorbing atom is below

Figure B.2: An example input file for FEFF as generated by ATOMS. This is the output of ATOMS using the file shown in Fig. B.1. The radial extent of this cluster is truncated to include only the first two coordination shells so that it will fit on the facing page. ATOMS is typically compiled to allow clusters of up to 800 atoms.

* This feff.inp file generated by ATOMS, version 2.46b
 * ATOMS written by Bruce Ravel and copyright of The Univ. of Washington, 1994

```
* -- * -- * -- * -- * -- * -- * -- * -- * -- * -- * -- * -- * -- *
*      total mu =      5194.4 cm^-1, delta mu =      761.6 cm^-1
*      specific gravity = 7.942, cluster contains 15 atoms.
* -- * -- * -- * -- * -- * -- * -- * -- * -- * -- * -- * -- * -- *
*      mcmaster corrections: 0.00093 ang^2 and 0.165E-05 ang^4
*      self-abs. corrections: amplitude factor = 1.087
*                               0.00004 ang^2 and 0.461E-07 ang^4
*      i0 corrections:        0.00119 ang^2 and 0.121E-05 ang^4
* -- * -- * -- * -- * -- * -- * -- * -- * -- * -- * -- * -- * -- *
*      sum of corrections:    0.00216 ang^2 and 0.291E-05 ang^4
* -- * -- * -- * -- * -- * -- * -- * -- * -- * -- * -- * -- * -- *
```

TITLE PbTiO3 25C
 TITLE Glazer and Mabud, Acta Cryst. B34, 1065-1070 (1978)

HOLE 1 1.0 Ti K edge (4.965 keV), second number is S0^2

```
*      mphase,mpath,mfeff,mchi
CONTROL 1 1 1 1
PRINT 1 0 0 3
```

RMAX 3.55564

```
*CRITERIA curved plane
*DEBYE temp debye-temp
*NLEG 8
```

POTENTIALS

```
* ipot z label
* 0 22 Ti
* 1 8 0
* 2 82 Pb
```

ATOMS

```
0.00000 0.00000 0.00000 0 Ti 0.00000
0.00000 0.00000 -1.76713 1 axial 1.76713
1.95250 0.00000 0.32375 1 planar 1.97916
0.00000 -1.95250 0.32375 1 planar 1.97916
-1.95250 0.00000 0.32375 1 planar 1.97916
0.00000 1.95250 0.32375 1 planar 1.97916
0.00000 0.00000 2.38887 1 axial 2.38887
-1.95250 -1.95250 1.91592 2 Pb 3.36084
1.95250 -1.95250 1.91592 2 Pb 3.36084
-1.95250 1.95250 1.91592 2 Pb 3.36084
1.95250 1.95250 1.91592 2 Pb 3.36084
1.95250 -1.95250 -2.24008 2 Pb 3.55563
-1.95250 1.95250 -2.24008 2 Pb 3.55563
-1.95250 -1.95250 -2.24008 2 Pb 3.55563
1.95250 1.95250 -2.24008 2 Pb 3.55563
```

END

cerium on the periodic table, a K edge calculation is desired. For heavier elements, ATOMS assumes the L_{III} edge. This can be specified in `atoms.inp` by the `edge` keyword. The second argument to `HOLE` in `feff.inp` is the value of S_0^2 to be used in the calculation. ATOMS sets this to 1 on the assumption that the effect of S_0^2 will be included during the analysis of the data. For the convenience of the user, the energy of the chosen absorption edge is written as a comment on the line containing the `HOLE` keyword. Finally, the `nitrogen` keyword is one of three keywords used to specify the contents of the I_0 chamber as causes ATOMS to make the fluorescence corrections described in Secs. B.2.3 and B.2.4.

At the top of the `feff.inp` file are several lines which are commented out by the asterisk character (*). These are the various experimental corrections calculated by ATOMS and are the topic of the next section.

B.2 Calculations Using the McMaster Tables

B.2.1 The Density and Absorption Lengths

As discussed in Sec. 3.2.1 proper sample preparation for a transmission experiment is essential for collection of high quality data. In order to make appropriate choices for the composition and form of the sample it is necessary to know both the absorption length of the sample and its edge step absorption length. ATOMS approximates these quantities and reports them in the first of the commented lines at the top of the `feff.inp` file.

The absorption length is defined as the thickness x of the sample such that the intensity of the x-rays incident upon the sample at an energy 50 eV above the absorption edge is attenuated e-fold. That is, $e^{-x\mu} = 1/e$ where μ is the total absorption of the sample at that energy. The edge step absorption length, the reciprocal of which is called `delta mu` in `feff.inp` is the thickness x such that there is an e-fold change in absorption between 50 eV below and above the edge. That is, $e^{-x\cdot\delta\mu} = 1/e$, where $\delta\mu$ is the change in absorption of the absorbing atom.

ATOMS has a table of coefficients [70] for computing x-ray cross-sections of free atoms compiled into it. It computes the free atom cross-sections for each atom specified in `atoms.inp` at 50 eV above the absorption edge and for the resonant atom at 50 eV below the edge. Using the crystallographic information, it knows the size of the unit cell and how many of each species are in the unit cell. With this information the absorption length and edge step absorption length are computed. From the unit cell size and tabulated masses of the elements, the density of the crystal is also computed.

With the absorption lengths and density of the material, proper choices for sample preparation can be made.

In the example given in Fig. B.2, the absorption length is $\frac{1}{5269.6}$ cm ≈ 2 μ m and the edge step absorption length is $\frac{1}{772.6}$ cm ≈ 13 μ m. For my experiment on the titanium K edge of PbTiO_3 , I chose to make a sample which was 5 μ m thick, thus with total absorption of ~ 2.5 and an edge step of ~ 0.4 . Knowing the appropriate thickness for the sample, the dimensions of the die used to press the sample, and the density of PbTiO_3 , I was able to make an appropriate sample using the method described in Sec. 3.2.1. An example spectrum obtained with one of these samples is shown in Fig. B.3.

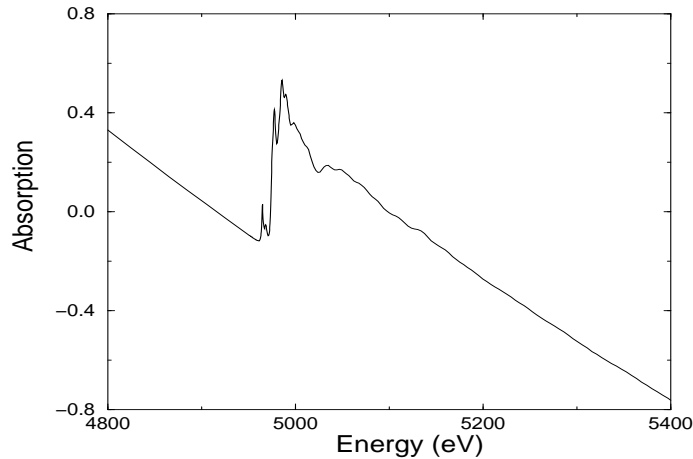


Figure B.3: Unnormalized absorption spectrum for the titanium K edge of PbTiO_3 at 300 K. The edge step for this scan is 0.413, which is very close to the predicted edge step for a 5 μ m sample.

B.2.2 The McMaster Correction

To avoid introducing systematic errors into the amplitude of the measured χ , an edge-step normalization is typically used, as discussed in Sec. 2.2. Since the true atomic background absorption, μ_0 , has energy dependence, normalization by the edge-step introduces an energy-dependent attenuation to the amplitude of χ . This attenuation is small for heavy elements, but can be of the same order as thermal effects for

light elements. ATOMS calculates an approximation to this attenuation called the *McMaster correction* [28].

Using the tables of free atoms x-ray cross-sections, ATOMS evaluates the cross-section for the free central atom in a range from 50 to 500 eV above the absorption edge. It then regresses a third order polynomial in the natural log of the energy relative to the edge to the natural log of the free atom cross-section. A regression in natural logs is how the coefficients of Ref. [70] were determined. The linear and square terms are approximations to the degree of attenuation introduced by the edge-step normalization. These terms are written to the top of `feff.inp` as second and fourth cumulants. These are intended as additive corrections to the measured σ^2 and fourth cumulants of a fit. Neglecting this correction will make the temperature dependence of σ^2 deviate from an Einstein behavior by a constant offset.

B.2.3 The I_0 Correction

In a fluorescence experiment, as described in Sec. 3.1.4, the absorption cross section is obtained from the detected intensities on the I_0 and I_F chambers (see Fig. 3.1) by measuring their ratio as a function of energy. This introduces an energy dependent error, usually an attenuation, into the amplitude of the measured χ . The secondary photon measured in the fluorescence experiment is always of the same energy. Thus there is no energy dependent part of the signal measured on I_F . There is, though, an energy response to I_0 that is neglected when I_F is normalized by the signal on I_0 . ATOMS calculates an approximation to this attenuation called the *I_0 correction*.

To enable this calculation when using ATOMS, it is necessary to specify the contents of the I_0 chamber. In Fig. B.1 this is done with the `nitrogen` keyword. ATOMS also recognizes the keywords `argon` and `krypton`. From the supplied values of these three keywords, ATOMS approximates the energy response of the I_0 chamber using the tables of free-atom x-ray cross sections. In the case shown in Fig. B.1, the I_0 chamber was entirely filled with nitrogen.

ATOMS evaluates the cross-section for the gases in the I_0 chamber in a range from 50 to 500 eV above the absorption edge. It then regresses a third order polynomial in the natural log of the energy relative to the edge to the natural log of the gas cross-section. The linear and square terms are approximations to the degree of attenuation introduced by normalizing I_F by I_0 . These terms are written to the top of `feff.inp` as second and fourth cumulants. These are intended as additive corrections to the measured σ^2 and fourth cumulants of a fit. Neglecting this correction will make the

temperature dependence of σ^2 deviate from an Einstein behavior by a constant offset.

B.2.4 The Self-Absorption Correction

The second correction required for fluorescence measurements is called the *self-absorption correction*. This calculation is also enabled when any of the **nitrogen**, **argon**, or **krypton** keywords are specified in `atoms.inp`. This form for the signal on the fluorescence detector is given in Eq. (3.7)

$$\frac{I_F}{I_0} \approx \frac{\mu_c(E)}{\mu'(E_F) + \mu_b(E) + \mu_c(E)} \quad (\text{B.1})$$

As in Sec. 3.1.4, $\mu_c(E)$ is the absorption of the resonant atom, $\mu_b(E)$ is the rest of the absorption in the material, and $\mu'(E_F)$ is the absorption of the material at the fluorescence energy of the resonant atom. The self-absorption correction is due to the $\mu_c(E)$ term in the denominator of this equation. In the limit that $\mu_c(E) \gg (\mu'(E_F) + \mu_b(E))$, the self-absorption correction is enormous, canceling the oscillatory structure of the XAFS spectrum. `ATOMS` approximates the effect of $\mu_c(E)$ term in the denominator of Eq. (B.1) given two assumptions, 1) the sample is very thick compared to the absorption length and 2) the entry angle α in Fig. 3.1 is equal to the exit angle to the fluorescence detector. This derivation could be generalized to consider a thin sample and unequal entry and exit angles.

Typically, the fluorescence experiment is performed to measure χ rather than μ . The correction presented in this section is a correction to the measured χ . The signal χ is the normalized variation in I_F/I_0 , the oscillatory part of the absorption of the resonant atom. I will now derive expressions for the variation in I_F/I_0 and for the normalization term using the notation of Eq. (B.1).

The variation in the signal, $\delta(I_F/I_0)$ is due to the variation in $\mu_c(E)$, $\delta\mu_c(E)$

$$\begin{aligned} \delta\left(\frac{I_F}{I_0}\right) &= \delta\left(\frac{\mu_c(E)}{\mu_B(E) + \mu_c(E)}\right) \\ &= \frac{\delta\mu_c(E)}{\mu_B(E) + \mu_c(E)} - \frac{\delta\mu_c(E) \cdot \mu_c(E)}{(\mu_B(E) + \mu_c(E))^2} \\ &= \frac{\delta\mu_c(E) \cdot \mu_B(E)}{(\mu_B(E) + \mu_c(E))^2} \end{aligned} \quad (\text{B.2})$$

In this equation $\mu_B(E) = (\mu'(E_F) + \mu_b(E))$.

The normalization, Δ , is the difference in I_F/I_0 below and above the edge. The

symbols $|_a$ and $|_b$ denote that the quantity is evaluated above or below the absorption edge.

$$\Delta = \frac{\mu_c(E)|_a}{\mu_c(E)|_a + \mu_B(E)} - \frac{\mu_c(E)|_b}{\mu_c(E)|_b + \mu_B(E)} \quad (\text{B.3})$$

For a fluorescence measurement where the self-absorption correction is a significant effect, $\mu_c(E)|_a$ is a large term in Eq. (B.1), but $\mu_c(E)|_b$ is assumed to be small. I need one more bit of notation,

$$\mu_c(E)|_a = \mu_c(E)|_b + \Delta\mu_c. \quad (\text{B.4})$$

Using the assumption that $\mu_c(E)|_b$ is small,

$$\begin{aligned} \Delta &= \frac{\mu_c(E)|_b + \Delta\mu_c}{\mu_c(E)|_a + \mu_B(E)} - \frac{\mu_c(E)|_b}{\mu_B(E)} \\ &= \frac{\Delta\mu_c}{\mu_c(E)|_a + \mu_B(E)} \end{aligned} \quad (\text{B.5})$$

Finally I write an expression for the normalized variation in I_F/I_0 using Eqs. (B.2) and (B.5). Since this derivation is for a correction to χ , I am only concerned with normalized variation *above* the absorption edge.

$$\begin{aligned} \frac{\delta(I_F/I_0)}{\Delta} &= \frac{\delta\mu_c(E) \cdot \mu_B(E)}{(\mu_B(E) + \mu_c(E))^2} \div \frac{\Delta\mu_c}{\mu_c(E) + \mu_B(E)} \Big|_a \\ &= \frac{\delta\mu_c(E) \cdot \mu_B(E)}{\Delta\mu_c(\mu_c(E) + \mu_B(E))} \Big|_a \end{aligned} \quad (\text{B.6})$$

The ideal measurement would be undistorted and simply expressed as $\delta\mu_c(E)/\Delta\mu_c$. The correction factor \mathcal{C}_{self} is the factor by which the measured signal must be multi-

plied to obtain the ideal signal.

$$C_{self} \cdot \frac{\delta\mu_c(E) \cdot \mu_B(E)}{\Delta\mu_c(\mu_c(E) + \mu_B(E))} = \frac{\delta\mu_c(E)}{\Delta\mu_c} \quad (\text{B.7})$$

$$\begin{aligned} C_{self} &= \frac{\mu_c(E) + \mu_B(E)}{\mu_B(E)} \\ &= 1 + \frac{\mu_c(E)}{\mu_B(E)} \end{aligned} \quad (\text{B.8})$$

ATOMS uses the free atom cross-sections to evaluate Eq. (B.8) in the energy range from 50 to 500 eV above the absorption edge¹. A third order polynomial in the natural log of the energy relative to the edge is regressed to the natural log of Eq. (B.8). The coefficients of this regression are the correction terms reported at the top of the `feff.inp` file.

The `amplitude factor` is the exponent of the constant term in the regression. This is intended as a multiplicative correction to the amplitude of the data. If this term is neglected in a fit, the measured S_0^2 will be too small by that factor.

The other two corrections are the linear and square terms of the regression and are expressed in `feff.inp` as second and fourth order cumulants [51]. These are intended as additive corrections to the measured σ^2 and fourth cumulants of a fit. Neglecting this correction will make the temperature dependence of σ^2 deviate from an Einstein behavior by a constant offset. Note that this correction is very similar to that of Ref. [157].

The effectiveness of the amplitude correction calculated by ATOMS was recently demonstrated [158] on indium fluorescence data taken on an indium alloy dilutely doped with plutonium. From crystallography, the alloy is known to be of the FCC structure. Using the amplitude correction from ATOMS and a calculated value for S_0^2 [120], fits to the indium edge data yield a coordination of 12.3 ± 0.5 for the first shell.

The approximation made before Eq. B.5 that $\mu_c(E)|_b$ is small is not necessary. Eq. B.3 can be used directly. I plan to include this in a future version of ATOMS.

¹ Care is taken in the code to avoid running into other absorption edges in the material. If there is another absorption edge within 500 eV the range is truncated appropriately.

Appendix C

THE OPERATION OF THE COMPUTER PROGRAM XANES

C.1 *Running XANES*

The algorithms described in Ch. 8 are implemented in a computer program XANES. XANES requires that the first module¹ of FEFF7 be run. These partial waves are used by XANES to calculate the single site t-matrix elements of Eq. (8.10). An example of a FEFF input file is shown in Fig. C.1. Several features have been added to FEFF to accommodate the needs of the XANES program. One of these is seen in Fig. C.1. A numeric argument is added to the FEFF7 keyword `xanes` to enable the additional calculation needed for XANES. Several other output files from FEFF are also used. These are shown in Table C.1.

Table C.1: Output files from FEFF used in XANES. The files marked as new contain new calculations by FEFF which are required by XANES.

file name	new	description
phase.bin		partial wave phase shifts
xsect.bin		embedded atom background function
potph.dat		cluster geometry and potential indexing
xrho.bin	✓	embedded atom electron densities of state
xatom.bin	✓	free atom electron configurations

After running FEFF, XANES is run to solve Eq. (8.6). The solution of the FMS \mathbb{G} -matrix is then used to solve for the site and angular momentum projected χ functions

¹ FEFF7 consists of four distinct calculations, called modules, which are usually run sequentially using a single input/output structure. It is possible to run only parts of FEFF. The first module constructs the muffin tin potential and calculates the partial wave phase shifts associated with each muffin tin. The details of the muffin tin construction and phase shift calculations are given in Refs. [27, 119, 120]. The details of running FEFF are given in Ref. [159].

```
TITLE Molecular SF6

CONTROL 1 0 0 0
PRINT   1 0 0 0

RMAX 12
XANES 12

EXCHANGE 2 0 0

POTENTIALS
*      ipot      z      tag
        0      16      S
        1       9      F

ATOMS
*      x        y        z        ipot
        0        0        0         0          S absorber
        1.56     0        0         1          6 F backscatters
        0        1.56    0         1
        0        0        1.56     1
       -1.56     0        0         1
        0       -1.56    0         1
        0        0       -1.56     1
```

Figure C.1: A sample FEFF input file for SF₆ for use with a run of XANES.

Table C.2: Output files from XANES

file name	description of contents
<code>xchi.dat</code>	μ , μ_0 , and χ convolved with the broadened step function as in Eqs. (8.24) and (8.25).
<code>xchi.raw</code>	μ and the complex χ without broadening.
<code>submat.bin</code>	The submatrix of \mathbb{G} for the central atom and the final state angular momentum for use in CORRECT.
<code>xdos_n.dat</code>	The angular momentum projected DOS function $\rho(E)$ for each unique potential \mathbf{n} .
<code>xdos_n.raw</code>	The atomic portion of the angular momentum projected DOS function $\rho_0(E)$ for each unique potential \mathbf{n} .
<code>xfermi.dat</code>	The approximations for the Fermi energy and charge transfer.

of Eqs. (8.21) and (8.30). Using FEFF's calculations of the central atom background function from `xsect.bin` and the embedded atom electron densities from `xrho.bin` along with the χ functions, XANES solves Eqs. (8.23) and (8.29). XANES uses a file called `xanes.conf` to configure various characteristics of the code at run-time. There are a large number of configuration options available for XANES which are described in the program documentation [160]. A few of the most commonly used are shown in Fig. C.2. To the end of keeping the basis small, the size of the cluster and the angular momentum basis used for each atom in the cluster is configurable in a XANES run.

The XANES run writes several files containing calculations of the absorption spectrum and of the local electron densities of state (DOS). For comparison of the calculation to experiment, it is useful to adjust various parameters affecting the calculated $\mu(E)$. These include the values of the Fermi energy and the line broadening used in Eqs. (8.24) – (8.26), the linear polarization direction, the transition channel if the calculation is on an edge of initial angular momentum $l \geq 1$, a constant shift of the absolute energy scale, and an over-all amplitude factor. An ancillary program, CORRECT, is used to apply these corrections. CORRECT reads `xsect.bin`, which contains the embedded atom background computed by FEFF, and `submat.bin`, the output file from XANES containing the central atom and $l = l_{final}$ submatrix of \mathbb{G} for each l_{final} transition channel appropriate to the chosen edge in the calculation. After reading the these files, CORRECT applies the corrections described above as indicated within

```

### xanes.conf
kmax 4.5
rmax 3.0
dryrun false true
lmax 0 2
lmax 1 1

```

Figure C.2: A sample XANES configuration file for a XANES run on SF₆. `kmax` limits the energy range of the calculation. `rmax` limits the size of the radial cluster used in the FMS calculation. `lmax` limits the size of the angular momentum basis used in the FMS calculation. In this case the basis of the fluorine atoms is restricted to *s* and *p* electrons and of the sulfur atom to *s*, *p*, and *d* electrons. When set to true, the `dryrun` keyword is used to make XANES read in all of the input files and check to see that the calculation will proceed smoothly, but stopping before computing the FMS matrix.

a configuration file, an example of which is shown in Fig. C.3. The output of this example run on SF₆ is discussed in detail in Sec. 9.2.

XANES possesses several useful features which I do not discuss in detail in this thesis. These include

- An option to use a Singular Value Decomposition for the matrix algebra.
- Computation of exact finite order scattering within the cluster up to triple scattering.
- Computation of the polarization dependence of the XANES spectrum for *K* and *L_I* edges.
- Separate computation of the $l + 1$ and $l - 1$ final states for *L_{II}* and *L_{III}* edges.
- An ancillary program for editing the configuration files for XANES and CORRECT.

For complete descriptions see the program documentation [160] and read the information files which are distributed with the source code for XANES and CORRECT.

C.2 Five Steps to a Successful XANES Run

Here is a short recipe for using XANES and (hopefully) getting a satisfactory result.

```

                                     ### file names
outfile          xchi.cor
subfile          submat.bin
xsectfile        xsect.bin

                                     ### set and guess variables
set      e0          15.0
set      efermi      6.2
set      amplitude   1.0
set      width       0.5
set      slope       0.0

                                     ### other parameters
# lfinal          both   plus   minus
# polarization   0 0 0

```

Figure C.3: A sample CORRECT configuration file for a CORRECT run on the output of XANES on SF₆. The first three keywords are used to specify the names of the input and output files. `efermi` and `width` are used to specify the sizes of those corrections. The other three are corrections to the overall amplitude of the calculated spectrum, a shift of the absolute energy scale, and the slope of a line that is added to the calculation after E_{Fermi} . The `polarization` keyword may be used to specify the linear polarization direction. The `lfinal` keyword may be used to add or to isolate the signals from the $l + 1$ and $l - 1$ final states in a calculation on an edge of initial angular momentum greater than 0.

1. *Compile XANES with appropriate parameters.* The header file `xparam.h` is included in 26 places in XANES v. 0.37. The dimensions of the problem are set there. Be sure that the parameter `nclusx`, which determines the maximum number of atoms in the cluster, is set large enough for your application. The parameter `lx` determines the maximum of the angular momentum basis. XANES does not currently work for `lx` larger than 3, although it may be prudent to set it to a smaller number if you want to run XANES on a very large cluster.
2. *Check your environment resources.* In a Unix environment, your shell has configurable limitations in its access to system resources. In CSH or TCSH these limits can be displayed by executing the shell built-in command `limit`. In BASH and equivalent shells, the equivalent built-in command is `ulimit`. Using TCSH and typing `limit` at the command line on an SGI Indigo II that I use, I see something like this:

```

cputime          unlimited
filesize         4194303 kbytes
datasize        524288 kbytes
stacksize       100000 kbytes
coredumpsize    0 kbytes
memoryuse       187444 kbytes
vmemoryuse      524288 kbytes
descriptors     200

```

The syntax for changing these limits is, for example, `limit stacksize 100000`. You might run this command from one of your login scripts. If you compile XANES to allow for large clusters (say of 80 or more atoms), you will need to set the `stacksize` to something appropriately large. It will be obvious that your system resource access is too small for the program if it dies without writing anything to the screen and dumps a core.

3. *Run FEFF.* The FEFF run should be made on a much larger cluster than what will be used in the XANES run. This will minimize the effect of the cluster boundary on the potentials of the scatterers used in the XANES calculations. If you want a XANES calculation on a crystalline material, you might start by running ATOMS. In recent versions of ATOMS there is a `xanes` keyword which, when set to true, writes cards to `feff.inp` which are useful for a subsequent XANES run. Please note that you *must* supply the XANES card in `feff.inp`

and it *must* have a positive numeric argument. You only need to run the first module of FEFF, that is to run with CONTROL 1 0 0 0 in `feff.inp`. All of the files needed by XANES are written by the first module.

4. *Run XANES.* Typically, XANES is run on a smaller cluster than FEFF. Thus the calculation of the scattering is separated from the calculation of the scattering potentials. Although all of the defaults for the keywords in the configuration file are reasonable, you might want to prepare a special configuration file. See the code documentation [160] for details about the configuration keywords. I recommend using the LU matrix decomposition option. It is faster than the SVD and I have yet to encounter a situation where the SVD was needed. I also recommend thoughtful use of the `lmax` keyword. For instance, setting `lmax` to 2 or even 1 for light atoms such as oxygen will probably result in a well converged calculation and can save considerable computation time. Also, don't set `kmax` to too large of a number. Beyond a few inverse Angstroms, a much larger angular momentum basis is required for convergence. XANES typically has a hard wired limit of $l_{max} = 3$.
5. *Run CORRECT repeatedly.* Use CORRECT to change computation parameters such as the Fermi energy, to apply polarization, and to examine different l_{final} states for L_{II} and L_{III} edges. Since CORRECT is so fast and XANES is so slow, run a generic XANES calculation and play games with CORRECT.

C.3 Using FEFF with XANES

C.3.1 New FEFF Keywords

Along with the two new output files mentioned in Table C.1, several keywords were added to the list of keywords recognized by FEFF in the `feff.inp` file. These are

XANES

The features added by me for use with XANES are enabled by adding a numerical argument to this keyword. When this keyword occurs without a numerical argument, the standard XANES functionality of FEFF is used.

EGRID

This keyword sets the knots for use in constructing a user-defined energy grid. Placing EGRID 3 10 20 30 within `feff.inp` tells FEFF to construct an energy grid with 3 knots placed 10, 20, and 30 eV above first point.

EMESH

This keyword specifies the size of the grid between the knots specified by the **EGRID** keyword. Placing **EMESH 0.5 1.0 1.5** in `feff.inp` tells **FEFF** to calculate in half volt steps between the first energy point and the first knot, in volt steps between knots 1 and 2, and in volt and a half steps between the the last two knots. Beyond that **FEFF**'s normal algorithm is used.

VINTFIX

This un-descriptive keyword is used to continue the calculation of the potentials and phase shifts below the level of **FEFF**'s interstice. It takes a real number as its value. Typically **FEFF** chooses a point a few volts above the interstice as its first energy point. The value of this keyword is *subtracted* from the default starting point.

C.3.2 FEFF Tricks

Some of the more obscure **FEFF** keywords are possibly quite useful in conjunction with **XANES**. Here are a few that I have used

EXCHANGE

Using different models for the exchange and correlation potentials may improve your calculation. As shown in Table 9.1, I find that the Hedin–Lundqvist and Ground State models are both useful.

ION

Using this card to ionize the central tends to amplify or diminish the final state DOS for the central atom. Although this is an *ad hoc* correction to the **FEFF** calculation, it can significantly improve the quality of the result.

FOLP and AFOLP

Changing the parameters on the construction of the muffin tin may yield better results. This, too, is an *ad hoc* correction.

JUMPRM

I have found that this keyword produces unsatisfactory results even though early versions of the program documentation [160] suggested that you do so.

VITA

Bruce Douglas Ravel was born in Omaha, Nebraska early in the morning of October 22, 1966 to Frances Ravel and Ira Ravel. He graduated from The Mount Tamalpais School in Ross, California in 1985. In 1989, he graduated *magna cum laude* with a B.A. in physics from Wesleyan University in Middletown, Connecticut and was inducted into Phi Beta Kappa. In the fall of 1989, Seattle, Washington became his home as he began graduate studies in physics at the University of Washington. Among other things, Bruce enjoys a glassy wave while sitting in his kayak, a diving save to stop a soccer ball from hitting the back of the net, a well written comic book, and a beautifully decorated cake.